

https://dspace.org/

Geodetic investigation of Torfajokull Volcano, Iceland

Scheiber, Stephanie Elizabeth

2009-05-29T07:30:30Z
http://hdl.handle.net/10539/6997

Downloaded from a DSpace repository. https://dspace.org/

GEODETIC INVESTIGATION OF TORFAJÖKULL VOLCANO, ICELAND

Stephanie Elizabeth Scheiber
School of Geosciences, University of the Witwatersrand

A dissertation submitted to the Faculty of Science, University of the Witwatersrand, Johannesburg, in fulfilment of the requirements for the degree of Master of Science

Johannesburg, 2008





DECLARATION

I declare that this dissertation is my own, unaided work. It is being submitted for the Degree of Master of Science at the University of the Witwatersrand, Johannesburg. It has not been submitted before for any degree or examination in any other University

_____
(Signature of candidate)

_____ day of _____ 2009

ABSTRACT

The Mid-Atlantic ridge and North Atlantic mantle plume interaction is expressed in south Iceland as two overlapping, subparallel spreading centres; the Western (WVZ) and Eastern Volcanic Zones (EVZ). The South Iceland Seismic Zone (SISZ), a transform fault, connects these systems. Plate motion is partitioned across these zones and is accommodated by repeated lateral dyke injection from central volcanoes into fissure swarms within the volcanic zones. South of the SISZ-EVZ intersection, also the location of Torfajökull volcano, the EVZ is propagating to the southwest into the Eastern Volcanic Flank Zone (EVFZ). The plate spreading south of Torfajökull appears to be partitioned across the Reykjanes Peninsula (RP) in the west and the EVFZ.

This study investigates the complex interplay between plate spreading and volcano deformation in the region surrounding Torfajökull volcano using space geodetic and modelling techniques. We present a new horizontal velocity field based on episodic GPS measurements collected between 2000 and 2006 in the southern part of the EVZ. This velocity field is compared to a GPS-derived velocity field from 1994-2003 (LaFemina et al. 2005) and elastic half-space plate spreading models. In a stable Eurasian reference frame the horizontal signal is dominated by plate spreading through the caldera, in agreement with known Holocene fissuring to the northeast along the Veidivötn fissure swarm and southwest of the caldera. It is shown that spreading is occurring across the EVFZ, with maximum strain accumulation during this inter-rifting period along the western edge of the Eldgjá fissure swarm which was last active in 934 A.D. These locations have major implications for the location of future rifting events as it is presumed that significant subsurface magma accumulation occurs along the centre of spreading.

Spreading rates for this study show along strike variations, decreasing from 10-20 mm/yr to the north of Torfajökull to 7-8 mm/yr in the south, which is in line with a simple propagating ridge model and previous studies. Locking depths for these dyke models are relatively shallow (<6 km). The horizontal velocity field also indicates the interaction of Hekla volcano situated in the northwest of the study area, as the volcano has been uplifting since its last eruption in 2000, as well as subsidence due to a possible slow cooling magma chamber in the western part of Torfajökull which is supported by InSAR and “dry-tilt” data.

ACKNOWLEDGEMENTS

Thank you to Prof Paul Dirks and Andy Nyblade for providing financial backing for a project that has been a dream of mine for a long time, and that had nothing to do with Africa. As a result of this project I have travelled to places I never dreamt I would.

Huge thanks to Peter LaFemina for being a very patient supervisor and teaching me so much...and for putting up with all of the long distance questions via email. Thank you for challenging me to write more concisely and find the answer for myself. And thanks for being such a good tour guide in Iceland.

Thanks to Susan Webb for being a very supportive local supervisor even though it wasn't your field of research. Thanks for always calming me down to a mild panic.

To Erik Sturkell for all of your assistance with "dry-tilt" data and programming. Thank you also to Gordon Cooper for your Matlab technical skills and mathematical knowledge.

To Steve, Shawn and Mark...what else can be said except I refuse to make you any more tea! But thanks for making Geophysics ridiculously fun and for teaching me so much.

To my mom and dad, thank you for all of the financial and most of all emotional support that got me through this thesis. It is only because of your encouragement and always believing in me that I am where I am today.

And finally, to an amazing boyfriend who was prepared to wait...Scott, for your patience. God's amazing grace was the only thing that got us through the last 3 years. Thank you for listening to me ramble on about the rocks in the botanical gardens...I knew from that moment I had found someone special.

CONTENTS

CONTENTS v
LIST OF FIGURES vii
LIST OF TABLES xi
LIST OF SYMBOLS AND NOMENCLATURE xiii

1 INTRODUCTION 1

2 BACKGROUND 4

2.1 TECTONIC SETTING 4
2.1.1 South-central Iceland 4
2.1.2 Reykjanes Peninsula 7
2.2 MID-ATLANTIC RIDGE SPREADING RATES IN SOUTH ICELAND 8
2.2.1 Reykjanes Peninsula 8
2.2.2 Western and Eastern Volcanic Zones 9
2.3 TORFAJÖKULL CALDERA 13
2.4 TORFAJÖKULL PETROLOGY 14
2.4.1 General Geology 14
2.4.2 Postglacial Activity 15
2.4.3 Geothermal activity 17
2.5 GEOPHYSICAL STUDIES AT TORFAJÖKULL VOLCANO 20
2.5.1 Seismic activity 20
2.5.2 Magnetotelluric data 23
2.5.3 "Dry-Tilt" Measurements 25
2.5.4 Interferometric Synthetic Aperture Radar (InSAR) 28
2.6 HEKLA VOLCANO 29
2.6.1 General 29
2.6.2 Ground deformation studies at Hekla volcano 30
2.7 KATLA VOLCANO 33
2.8 GLACIO-ISOSTATIC ADJUSTMENT 37

3 DATA COLLECTION & ANALYSIS 39

3.1 DATA ACQUISITION AND FIELD PROCEDURES 40
3.2 DATA ANALYSIS 45
3.2.1 Trimble R-utility and TEQC software 45
3.2.2 GIPSY-OASIS II Software 46
3.3 VELOCITY FIELD 48
3.3.1 ITRF-2000 Reference Frame 48
3.3.2 Stable Eurasia Reference Frame 55

4 MODELLING TECHNIQUES 62

4.1 EQUATIONS USED FOR MODELLING 63
4.1.1 Surface deformation due to a tensile fault in a half-space 63
4.1.2 Surface deformation due to a spherical body (Mogi source) 66
4.2 STATISTICAL ANALYSIS 71
4.2.1 Chi-square value 71
4.2.2 F Distribution 72

5 MODELLING RESULTS 75

5.1 MODELLING OF THE HORIZONTAL VELOCITY FIELD 75
5.2 MODELS UNCORRECTED FOR VOLCANIC DEFORMATION 77
5.3 MODELS CORRECTED FOR VOLCANIC DEFORMATION 80
5.3.1 Profile 1 80
5.3.1.1 1994-2003 Dataset 84

5.3.1.2 2001-2006 Dataset 86
5.3.2 Profile 2 90
5.3.3 Profile 3 98
5.3.3.1 1994-2003 Dataset 100
5.3.3.2 2001-2006 Dataset 101

6 DISCUSSION & CONCLUSIONS 105

6.1 DISCUSSION 105
6.1.1 Along-strike variations in spreading 106
6.1.2 Profile 1 107
6.1.3 Profile 2 109
6.1.4 Profile 3 111
6.2 CONCLUSIONS 113
6.3 FUTURE WORK 114

7 REFERENCES 116

8 APPENDICES 123

APPENDIX 1: Yearly position estimates used in Figure 3.9

APPENDIX 2: Response due to a tensile fault

APPENDIX 3: Response due to Hekla Mogi source between 2001 and 2006

APPENDIX 4: Response due to Hekla Mogi source between 1994 and 2003

APPENDIX 5: Response due to Torfajökull Mogi source between 2001 and 2006

APPENDIX 6: Response due to Katla Mogi source between 1999 and 2004

APPENDIX 7: Determining best-fit model to 1994-2003 and 2001-2006 GPS-derived velocities along profile 1

APPENDIX 8: Determining best-fit model to 1994-2003 and 2001-2006 GPS-derived velocities along profile 3

APPENDIX 9: Profile plots of the best-fit plate spreading models to the 1994-2003 and 2001-2006 GPS-derived velocities along profile 1, 2 and 3

APPENDIX 10: Determining the best-fit Mogi model to “dry-tilt” data from NAEF (or HRAF) site

APPENDIX 11: Determining the “dry-tilt response at NAEF (or HRAF) site due to a Mogi source

LIST OF FIGURES

Figure 1.1 Map of Iceland's tectonic features. 2
Figure 2.1 Map of south Iceland showing the Western Volcanic Zone (WVZ) and Eastern Volcanic Zone (EVZ) in relation to the Middle Volcanic Zone (MVZ), Hreppar block, Reykjanes Peninsula (RP), South Iceland Seismic Zone (SISZ), and Eastern Volcanic Flank Zone (EVFZ). 6
Figure 2.2 GPS velocity field relative to stable North America between 1994 and 2003. 11
Figure 2.3 Map of south Iceland showing geodetically derived spreading rates (mm/yr) determined by Hreinsdóttir et al. (2001) and LaFemina et al. (2005) across the Western Volcanic Zone (WVZ) and Eastern Volcanic Zone (EVZ), connected in the south by the South Iceland Seismic Zone (SISZ). 12
Figure 2.4 Map of south-central Iceland showing the intersection of the Eastern Volcanic Zone (EVZ), the South Iceland Seismic Zone (SISZ) and the Eastern Volcanic Flank Zone (EVFZ). 13
Figure 2.5 General outline of the geology of the Torfajökull region. 14
Figure 2.6 Basic geological map of Torfajökull volcano. 16
Figure 2.7 Diagram showing the workings of a high-temperature geothermal system, of which Torfajökull volcano is an example. 17
Figure 2.8 Geothermal activity within Torfajökull caldera. 18
Figure 2.9 Seismicity recorded at Torfajökull caldera in 2002 shown in map view, and east-west and north-south vertical sections. 22
Figure 2.10 Resistivity across Torfajökull caldera and surrounding region at 400 m below sea-level. 24
Figure 2.11 Average tilt measurements made between 2001 and 2006. 27
Figure 2.12 Interferometric Synthetic Aperture Radar (InSAR) image of Torfajökull caldera generated from SAR images taken of the caldera from 1993-2000. 28
Figure 2.13 Map of south Iceland at the junction of the Eastern Volcanic Zone (EVZ), South Iceland Seismic Zone (SISZ) and Eastern Volcanic Flank Zone (EVFZ). The locations of instrumentation used for monitoring Hekla volcano, as well as the Torfajökull volcano GPS network, are marked on the map. 32
Figure 2.14 East-west tilt data from the Næfurholt (NAEF) ''dry-tilt'' station, which is located 11.5 km west of the summit of Hekla. 33
Figure 2.15 Displacements measured at the geodetic network around Katla volcano from June 2001 to June 2004. 34
Figure 2.16 The rate of current displacement determined by Pinel et al. (2007) for the area covered by Myrdalsjökull, as well as surrounding areas. 36
Figure 2.17 Vertical velocities predicted by Pagli et al. (2007) at Vatnajökull glacier (at the centre and edge of the icecap, as well as at a distance of 80 km from the centre). 37
Figure 3.1 Episodic GPS site 3366. 41
Figure 3.2 Episodic GPS site VALA. 42
Figure 3.3 Permanent GPS site HEAL located on the flanks of Hekla volcano. 42
Figure 3.4 Field procedures and GPS instrumentation. 43
Figure 3.5 Field procedures and GPS instrumentation. 44
Figure 3.6 Field procedures and GPS instrumentation. 44
Figure 3.7 Field procedures and GPS instrumentation. 45

Figure 3.8 Map of 2001-2006 GPS sites used for this study in south-central Iceland at the intersection of the Eastern Volcanic Zone (EVZ), the South Iceland Seismic Zone (SISZ) and the Eastern Volcanic Flank Zone (EVFZ). 48
Figure 3.9a-p Coordinate time series for GPS sites in the southern EVZ used in this study. 50
Figure 3.10 GPS-derived horizontal velocity field relative to stable Eurasia for the period 2001-2006. 56
Figure 3.11 GPS-derived vertical velocity field for the period 2001-2006. 57
Figure 3.12 GPS-derived horizontal velocity field relative to stable Eurasia. 59
Figure 3.13 Map of GPS sites in south-central Iceland used in this study. 59
Figure 3.14 Horizontal (a,c,e) and vertical (b,d,f) GPS-derived velocities relative to stable Eurasia for sites within 10 km of 3 profiles taken across the EVZ (Figure 3.13) 60
Figure 4.1 Finite rectangular fault in an elastic half-space (the region of $z \leq 0$) with length $2L$ (dashed line) and width W (Okada 1985). 64
Figure 4.2 Profile and 2-D images of the vertical and horizontal displacement at the Earth's surface over a finite tensile fault. 65
Figure 4.3 Schematic of the elastic half-space model used in this study to investigate the plate spreading signal across the southern part of the EVZ. 66
Figure 4.4 Mogi-type magma reservoir in an elastic half-space with elastic shear modulus G (a measure of the rocks response to shear strains). 67
Figure 4.5 Profile and 3-D plots of the vertical and horizontal displacements at the Earth's surface over a Mogi source. 69
Figure 4.6 F distribution (continuous probability distribution). 73
Figure 5.1 Map of GPS sites in south-central Iceland and modelling profiles (P1, P2 and P3) used in this study 77
Figure 5.2 Best-fit elastic half-space plate spreading models for 1994-2003 GPS-derived site velocities relative to stable Eurasia, for sites within ~5 km of (a) profile 1 and (b) profile 3 78
Figure 5.3 Best-fit elastic half-space models for 2001-2006 GPS-derived site velocities relative to stable Eurasia along (a) profile 1, (b) profile 2 and (c) profile 3 78
Figure 5.4 Plot of the intersection of the Eastern Volcanic Zone (EVZ), the Eastern Volcanic Flank Zone (EVFZ) and South Iceland Seismic Zone (SISZ). The location of the Hekla volcano Mogi source is marked with a red star. 81
Figure 5.5 Plots of χ^2 versus extension rate for various elastic half-space plate spreading models (with x location held fixed throughout and locking depth held fixed for individual plots) fit to 1994-2003 velocities along profile 1. 84
Figure 5.6 Plots of χ^2 versus locking depth for various elastic half-space plate spreading models (with extension rate held fixed for individual plots) fit to 1994-2003 velocities along profile 1. 85
Figure 5.7 Contour plot of the χ^2 misfit for estimated extension rates and locking depths for elastic half-space plate spreading models fit to 1994-2003 velocities along profile 1. 85
Figure 5.8 Best-fit elastic half-space model for 1994-2003 GPS-derived site velocities (relative to stable Eurasia) along profile 1. Velocities are corrected for deformation due to Hekla volcano ($\Delta V_H = 0.03$ km^3). 85
Figure 5.9 Plots of χ^2 versus extension rate for various elastic half-space plate spreading models (with locking depth held fixed for individual plots) fit to 2001-2006 velocities along profile 1. 86
Figure 5.10 Plots of χ^2 versus locking depth for various elastic half-space plate spreading models (with extension rate held fixed for individual plots) fit to 2001-2006 velocities along profile 1. 87

Figure 5.11 Contour plot of the χ^2 misfit for estimated extension rates and locking depths for elastic half-space models fit to 2001-2006 velocities along profile 1. 87
Figure 5.12 Best-fit elastic half-space model for 2001-2006 GPS-derived site velocities (relative to stable Eurasia) along profile 1. Velocities are corrected for deformation due to Hekla volcano ($\Delta V_H = 0.04$ km^3). 87
Figure 5.13 Alternative elastic half-space model for 2001-2006 GPS-derived site velocities (relative to stable Eurasia) along profile 1. Velocities are corrected for deformation due to Hekla volcano ($\Delta V_H = 0.04$ km^3). 88
Figure 5.14 Best-fit elastic half-space models for 2001-2006 GPS-derived site velocities relative to stable Eurasia along profile 1, corrected for deformation due to Hekla volcano, with ΔV_H of (a) 0.05 km^3 and (b) 0.06 km^3. 89
Figure 5.15 Best-fit elastic half-space models for 2001-2006 GPS-derived site velocities (relative to stable Eurasia) along profile 2. Velocities are corrected for deformation due to Hekla volcano, with ΔV_H of (a) 0.04 km^3 and (b) 0.06 km^3..... 91
Figure 5.16 InSAR image of Torfajökull caldera generated from SAR images taken of the caldera from 1993 to 2000..... 92
Figure 5.17 Best-fit elastic half-space models for 2001-2006 GPS-derived site velocities (relative to stable Eurasia) along profile 2. Velocities are corrected for deformation due to Hekla volcano ($\Delta V_H = 0.04$ km^3), and varying deformation due to Torfajökull volcano (ΔV_T, D_T). 94
Figure 5.18 Best-fit elastic half-space models for 2001-2006 GPS-derived site velocities (relative to stable Eurasia) along profile 2. Velocities are corrected for deformation due to Hekla volcano ($\Delta V_H = 0.06$ km^3), and varying deformation due to Torfajökull volcano (ΔV_T, D_T). 94
Figure 5.19 Profile and 2-D image of the (a) "dry-tilt" response and (b) vertical displacement due to a Mogi source at 5 km depth experiencing a -0.005 km^3 change in volume. (c) The magma chamber at Torfajökull is assumed to be beneath the area of maximum subsidence as seen in the 1993-2000 InSAR image of the volcano. The extent of the area experiencing subsidence of ~-4 mm/yr is marked. 97
Figure 5.20 Plot of the intersection of the Eastern Volcanic Zone (EVZ), the Eastern Volcanic Flank Zone (EVFZ) and the South Iceland Seismic Zone (SISZ), with the location of the Mogi source below Katla volcano marked with a red star. 98
Figure 5.21 Plots of χ^2 versus extension rate for various elastic half-space plate spreading models (with locking depth held fixed for individual plots) fit to 1994-2003 velocities along profile 3. 100
Figure 5.22 Plots of χ^2 versus locking depth for various elastic half-space plate spreading models (with extension rate held fixed for individual plots) fit to 1994-2003 velocities along profile 3. 100
Figure 5.23 Contour plot of χ^2 misfit for estimated extension rates and locking depths for elastic half-space models fit to 1994-2003 velocities along profile 3. 101
Figure 5.24 Best-fit elastic half-space model for 1994-2003 GPS-derived site velocities (relative to stable Eurasia) along profile 3. Velocities are corrected for deformation due to Hekla volcano ($\Delta V_H = 0.03$ km^3). 101
Figure 5.25 Plots of χ^2 versus extension rate for various elastic half-space plate spreading models (with locking depth held fixed for individual plots) fit to 2001-2006 velocities along profile 3. 102
Figure 5.26 Plots of χ^2 versus locking depth for various elastic half-space plate spreading models (extension rate held fixed for individual plots) fit to 2001-2006 velocities along profile 3. 102
Figure 5.27 Contour plot of χ^2 misfit for estimated extension rates and locking depths for elastic half-space models fit to 2001-2006 velocities along profile 3. 103

Figure 5.28 Best-fit elastic half-space model for 2001-2006 GPS-derived site velocities (relative to stable Eurasia) along profile 3. Velocities are corrected for deformation due to Hekla volcano ($\Delta V_H = 0.04$ km^3). 103
Figure 5.29 Best-fit elastic half-space model for 2001-2006 GPS-derived site velocities (relative to stable Eurasia) along profile 3. Velocities are corrected for deformation due to Hekla volcano, due to a volume change (ΔV_H) of (a) 0.05 km^3 and (b) 0.06 km^3. 104

LIST OF TABLES

Table 2.1 Historical rifting episodes in the Eastern Volcanic Zone. 6
Table 2.2 Spreading rates and locking depths estimated by LaFemina et al. (2005) for three plate-motion parallel profiles (Figure 2.1) using elastic half-space models. Rates are compared with the REVEL and NUVEL-1a plate motion models (DeMets et al. 1994; Sella et al. 2002). 11
Table 2.3 Research conducted since 1991 into the seismic activity at Torfajökull volcano. 21
Table 2.4 Table of tilt measurements made at sites within and around Torfajökull and Hekla volcano between 2000/1 and 2006. 26
Table 2.5 Eruption duration and volumes for the four most recent eruption of Hekla volcano. 29
Table 2.6 Details of ground deformation surveys conducted at Hekla volcano since just prior to the 1981 eruption. Magma chamber parameters inferred from modelling of geodetic data are also listed. 31
Table 3.1 Table of the yearly survey record for GPS sites around and within Torfajökull caldera used in this study. 40
Table 3.2 Sites that experienced tripod movement between 2001 and 2006. 49
Table 3.3 GPS velocities for this study relative to ITRF-2000 and the Weighted RMS Scatter. 55
Table 3.4 Horizontal GPS velocities relative to stable Eurasia and vertical velocities for the period 2001-2006. 55
Table 3.5 Horizontal GPS velocities relative to stable Eurasia and vertical velocities for the period 1994-2003. 58
Table 4.1 Values of F corresponding to the probability P(F,ν1,ν2) = 0.05 of exceeding F for ν_1 versus ν_2 degrees of freedom. 73
Table 5.1 Parameter estimates for spreading models fit to 1994-2003 and 2001-2006 GPS-derived site velocities relative to stable Eurasia along profiles P1 to P3. Velocities have not been corrected for volcanic deformation. 77
Table 5.2 Table of ‘‘dry-tilt’’ measurements made at site NAEF on the western flank of Hekla volcano between 1994 and 2006, as well as the calculated change in tilt over the time periods 1994-2003 and 2001-2006. 81
Table 5.3 Site displacements and rates for the periods 1994-2003 and 2001-2006 for sites along profiles 1, 2 and 3 due to Hekla deformation. 83
Table 5.4 Parameter estimates and uncertainties for spreading models fit to 1994-2003 and 2001-2006 GPS-derived site velocities (relative to stable Eurasia) along profile 1. Velocities are corrected for various Hekla volcano deformation models (ΔV_H).. 90
Table 5.5 Parameter estimates and uncertainties for spreading models fit to 2001-2006 GPS-derived site velocities (relative to stable Eurasia) along profile 2. Velocities are corrected for various Hekla volcano deformation models (ΔV_H). 91
Table 5.6 Parameter estimates and uncertainties for spreading models fit to 2001-2006 GPS-derived site velocities (relative to stable Eurasia) along profile 2. Velocities are corrected for various Hekla (ΔV_H) and Torfajökull volcano deformation models (magma chamber depth, D_T and volume change, ΔV_T). 93
Table 5.7 Site displacements and rates for the periods 2001-2006 for sites along profile 2 due to deformation of Torfajökull volcano. 95

Table 5.8 Expected "dry-tilt" values for HRAF site (at a distance of 3.8 km from the source) and the maximum vertical subsidence rate for a range of Torfajökull Mogi source models (volume change, ΔV_T, and locking depth, D_T). 96
Table 5.9 Site displacements and rates resulting from inflation of Katla volcano over the period 1999 to 2004 for sites along Profile 3. 99
Table 5.10 Parameter estimates and uncertainties for spreading models fit to 1994-2003 and 2001-2006 GPS-derived site velocities (relative to stable Eurasia) along profile 3. Velocities are corrected for various Hekla volcano deformation models (ΔV_H). 104
Table 6.1 Parameter estimates and uncertainties for spreading models fit to 1994-2003 and 2001-2006 GPS-derived site velocities (relative to stable Eurasia) along profile 1 and 3. Models where the velocities were corrected for various Hekla volcano deformation models (ΔV_H) are also given. 106

LIST OF SYMBOLS AND NOMENCLATURE

Distance and Angles

km	kilometers
mm	millimetres
rad	radians

Power Prefixes

μ	micro (10^{-3})
M	mega (10^{6})
G	giga (10^{9})

Pressure

kbar	kilobars
Pa	Pascals

Restistivity

Ω.m	ohm-metre

Tectonic

EVFZ	Eastern Volcanic Flank Zone
EVZ	Eastern Volcanic Zone
MAR	Mid-Atlantic Ridge
NVZ	Northern Volcanic Zone
RP	Reykjanes Peninsula
SISZ	South Iceland Seismic Zone
TFZ	Tjörnes fracture zone
WVZ	Western Volcanic Zone

Time

B.P.	before present
Ma	million years (1 000 000 years)
s	seconds
yr	year

1 INTRODUCTION

Iceland sits astride the Mid-Atlantic Ridge (MAR), the plate boundary between the North American and Eurasian tectonic plates. The MAR becomes subaerial here due to its position above the North Atlantic mantle plume. This rare exposure of a slow spreading propagating ridge on land, along with other cases such as the Afar depression on the Horn of Africa, allow for detailed studies of these rifting processes.

Since ~23 Ma, west-northwest motion of the MAR relative to the mantle plume in Iceland has resulted in successive eastward migrations or jumps of the ridge, often resulting in overlapping zones of spreading (Óskarsson et al. 1985; Einarsson 1991; Hardarson et al. 1997; Garcia et al. 2003). Spreading centres in Iceland are expressed as neovolcanic zones (<0.7 Ma), consisting of central volcanoes and associated fissure swarms: the Northern Volcanic Zone (NVZ), Western Volcanic Zone (WVZ) and Eastern Volcanic Zone (EVZ) (Sæmundsson 1978) (Figure 1.1). Plate motion is accommodated across these zones by repeated lateral dyke injection from central volcanoes into fissure swarms (Walker 1960; Böðvarsson and Walker 1964; Sigurðsson and Sparks 1978; Guðmundsson 2000).

In southern Iceland plate motion is accommodated across the Western Volcanic Zone (WVZ) and Eastern Volcanic Zone (EVZ), two overlapping, subparallel ridge segments (Óskarsson et al. 1985; Hardarson et al. 1997; Garcia et al. 2003), as well as across the South Iceland Seismic Zone (SISZ) and Reykjanes Peninsula (RP) (Einarsson 1991; Sigmundsson et al. 1995) (Figure 1.1). The RP forms the plate boundary between the Reykjanes Ridge offshore in the west, and the WVZ and SISZ to the east (Einarsson 1991), while the east-west trending transform zone of the SISZ takes-up left-lateral motion between the Reykjanes Peninsula/Ridge and the EVZ (Einarsson 1991; Sigmundsson et al. 1995).

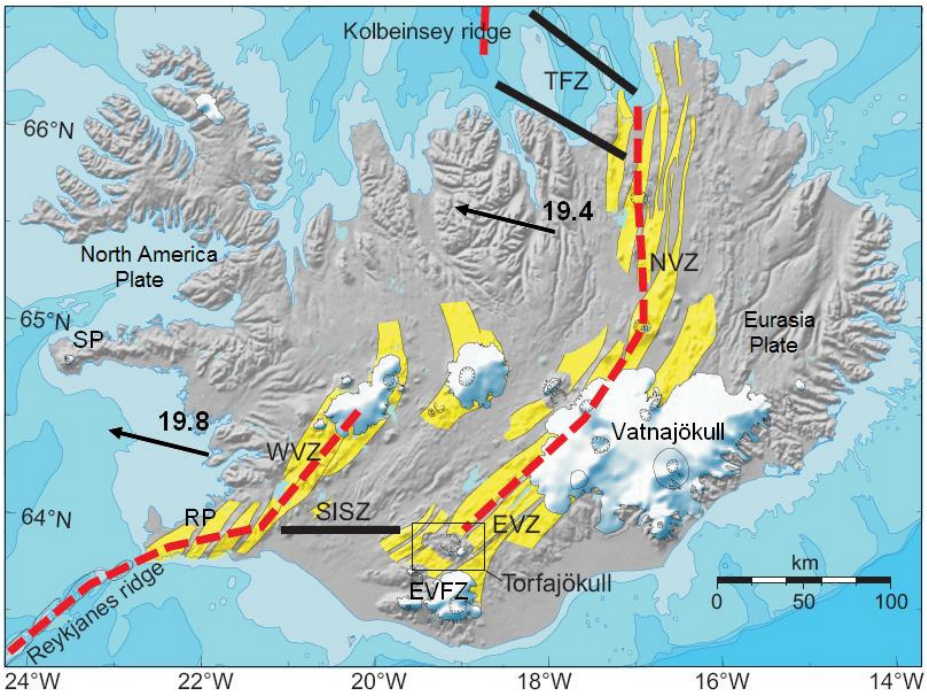


Figure 1.1 Map of Iceland's tectonic features (modified from Sturkell et al. 2006b and Borner 2007). Mid-Atlantic Ridge and North Atlantic mantle plume activity are expressed in Iceland as zones of young volcanic activity known as neovolcanic zones (in yellow, from Einarsson and Saemundsson 1987) that occur along part of the plate boundary (dashed red line). In the north the Northern Volcanic Zone (NVZ) is connected to the Kolbeinsey Ridge by the Tjörnes fracture zone (TFZ, black lines), a transform fault system that accommodates plate motion. In the south the Western Volcanic Zone (WVZ) is connected to the offshore Reykjanes Ridge by the Reykjanes Peninsula (RP). Motion between the Reykjanes Peninsula/Ridge and Eastern Volcanic Zone (EVZ) is taken up by the South Iceland Seismic Zone (SISZ) transform fault system (black line). The Snæfellsnes Peninsula (SP) marks the location of the ridge prior to the formation of the WVZ at ~7-9 Ma. The box in south-central Iceland marks the location of the Torfajökull volcanic system at the intersection of the SISZ and EVZ. Arrows show the full spreading rate (mm/yr) and direction estimated from the REVEL plate motion model (Sella et al. 2002) relative to stable Eurasia.

The total spreading rate of the Mid-Atlantic Ridge (MAR), i.e., the North American and Eurasian plates, at the latitude of Iceland is ~18-20 mm/yr in a direction N(102-104)°E. These rates are determined from the NUVEL-1A plate motion model, where spreading rates are calculated from seafloor magnetic anomalies spanning a period of ~3 Ma (DeMets et al. 1994), as well as from the more recent REVEL plate motion model which is determined from the inversion of Global Positioning System (GPS) data for rigid plate motion, and represents a decadal average (Sella et al. 2002). Geodetic studies provide support for the idea that the total rate of extension (strain accumulation) in south Iceland is partitioned between the overlapping spreading centres of the Western Volcanic Zone (WVZ) and Eastern Volcanic Zone (EVZ) (Hey 1977; Hey et al. 1980; Sigmundsson et al. 1995; Hreinsdóttir et al. 2001; LaFemina et al. 2005). LaFemina et al. (2005) shows that the western limb is deactivating towards the southwest, which is the direction of propagation of the eastern limb.

To the south of the South Iceland Seismic Zone (SISZ), geodetic studies have shown that plate motion is taken up in the west across the Reykjanes Peninsula (RP), which is oriented highly oblique to the offshore ridge and volcanic zones and across which left-lateral shear is dominant (Einarsson 1991; Sigmundsson et al. 1995; Hreinsdóttir et al. 2001; Árnadóttir et al. 2006; Keiding et al. 2008). Some of these studies suggest that the full plate spreading rate is accommodated across the RP (Árnadóttir et al. 2006; Keiding et al. 2008), while other suggest it is partitioned between the RP and the ridge further to the east that is propagating south of the intersection of the SISZ and the EVZ. (Hreinsdóttir et al. 2001; LaFemina et al. 2005). It has been suggested that this eastern limb of the ridge is propagating into the Eastern Volcanic Flank Zone (EVFZ) (LaFemina et al. 2005) (Figure 1.1), a region where rifting is less prominent. This area is one of the most poorly understood in terms of plate motion in Iceland, as well as the partitioning of rates between the RP and the eastern limb of the ridge. This study will help to improve our understanding of this system, with increased GPS coverage in the southern part of the EVZ. Data collected north and south of Torfajökull volcano, as well as within the volcano (Figure 1.1), is compared with two-dimensional elastic half-space plate spreading models in order to derive extension rate estimates for the southern part of the EVZ. Deformation of local volcanoes is taken into account during modelling.

2 BACKGROUND

2.1 Tectonic Setting

2.1.1 South-central Iceland

The Western Volcanic Zone (WVZ) has been active since a ridge jump ~7-9 Ma from the Snæfellsnes Peninsula (Sæmundsson 1978; 1979; 1992). A jump such as this occurs when the older plate boundary has migrated a certain critical distance away from the plume, at which point a new rift zone starts propagating in the crust above the plume (Einarsson 1991). Thirty-five postglacial eruptions have been recorded in the WVZ, however activity during more recent times has been characterized by rifting leading to graben subsidence, with the only historical activity in the WVZ being a non-eruptive rifting episode in 1789 A.D. (Guðmundsson 1987; Einarsson 1991; Sæmundsson 1992).

Some researchers suggest that the WVZ is becoming inactive, a theory that is supported by a number of scientific observations:

- A lack of any seismic zone connecting the northern part of the WVZ to the NVZ or EVZ (Óskarsson et al. 1985)
- The start of spreading and ridge propagation in the EVZ at ~2-3 Ma (Sæmundsson 1978; 1979)
- Historical eruptions having mainly been limited to the EVZ (Einarsson 1991)
- More recent results of geodetic studies indicating along strike variations in spreading, with rates decreasing from south to north in the WVZ (LaFemina et al. 2005).

Normal faults, fissures and dykes within the WVZ trend in a ~N30°E direction (Guðmundsson 1987), extension is therefore ~15° oblique to the N(76-78)°W spreading direction predicted by the NUVEL-1A and REVEL plate motion models relative to a stable Eurasia plate (Johannesson et al. 1990; DeMets et al. 1994; Sella et al. 2002).

The Eastern Volcanic Zone (EVZ) formed at ~2-3 Ma (Sæmundsson 1974; 1978; 1979) when the most recent eastward jump of the spreading ridge occurred, and ridge propagation began to the southwest away from the centre of the mantle plume in east-central Iceland (Pálmason 1981; Einarsson and Eiríksson 1982; Meyer et al. 1985; Óskarsson et al. 1985). The ridge in the EVZ is currently propagating at a rate of ~3.5-5.0 cm/yr to the southwest into the Eastern Volcanic Flank Zone (EVFZ) (Einarsson 1991), a zone that is dominated by a group of central volcanoes (Torfajökull, Hekla, Tindfjallajökull, Katla, Eyjafjallajökull and Vestmannaeyjar off of the coast of Iceland) and where rifting is less prominent. These evolved (silica-rich) volcanic systems of the EVFZ have formed due to remelting and reprocessing of ~10 Ma hydrothermally altered tholeiitic Tertiary crust, formed in the WVZ as the spreading ridge of the EVZ, which is the zone of highest basaltic magma flux, propagates into this region (Óskarsson et al. 1985; Gunnarsson et al. 1998; Stecher et al. 1999).

The EVZ is made up of two parallel, ~15 km wide active zones that are the location of all Holocene eruptive activity (<10,000 years) in the volcanic zone (Johannesson et al. 1990). These zones are made up of overlapping fissure swarms and associated central volcanoes, namely the Bárðarbunga (under the Vatnajökull icecap), Torfajökull and Hekla volcanic systems in the west and the Grimsvötn (under the Vatnajökull icecap) and Katla volcanic systems on the eastern side (Figure 2.1). This Holocene activity is mainly focused at the central volcanoes, with more than 190 documented events (Venzke et al. 2002) and along with five major historical rifting episodes (not including eruptions from Hekla and its associated fissure swarm) (Table 2.1). A ~20 km wide zone with no mapped Holocene eruptive fissures separates these two active zones (Johannesson et al. 1990) (Figure 2.1). The dominant trend of fissure swarms and dykes in the EVZ is N45°E. Extension along these fissure swarms is therefore ~30° oblique to the N(76-78)°W spreading direction predicted by the NUVEL-1A and REVEL plate motion models relative to a stable Eurasia plate (Johannesson et al. 1990; DeMets et al. 1994; Sella et al. 2002).

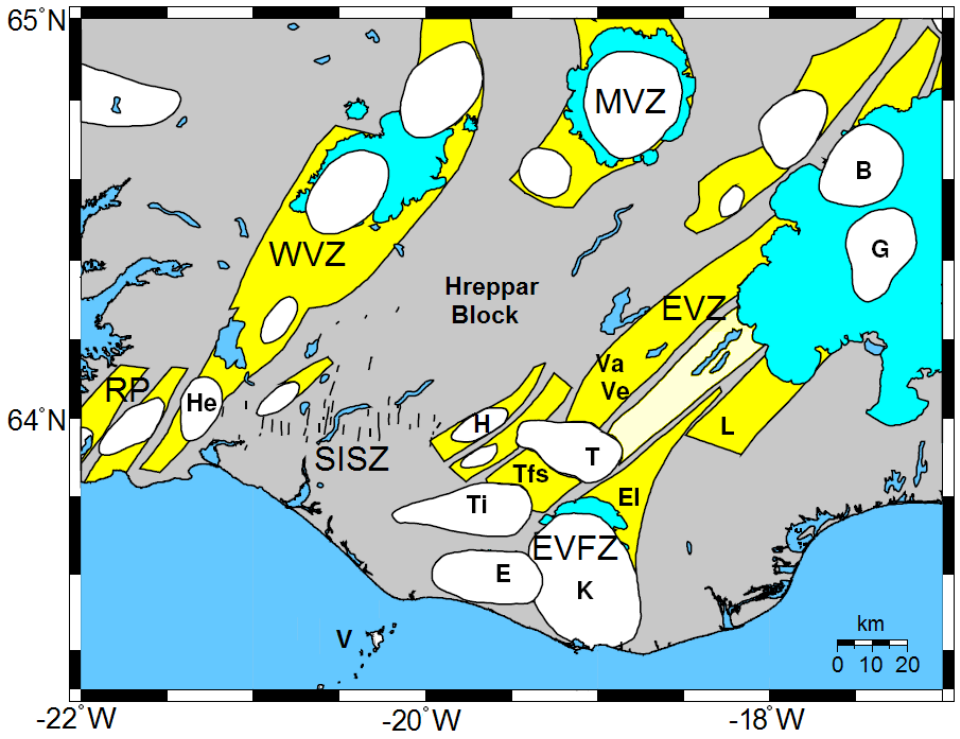


Figure 2.1 Map of south Iceland showing the Western Volcanic Zone (WVZ) and Eastern Volcanic Zone (EVZ) in relation to the Middle Volcanic Zone (MVZ), Hreppar block, Reykjanes Peninsula (RP), South Iceland Seismic Zone (SISZ), and Eastern Volcanic Flank Zone (EVFZ). Central volcanoes are outlined [Bárðarbunga (B), Grimsvötn (G), Torfajökull (T), Hekla (H), Tindfjallajökull (Ti), Katla (K), Eyjafjallajökull (E), Vestmannaeyjar (V) and Hengill (He) volcano] and fissure swarms are shaded yellow [Vatnaöldur (Va), Veidivötn (Ve), Torfajökull (Tfs), Lakagigar (L) and Eldgjá (El) fissure swarm], with the inactive fissure zone within the EVZ shaded light yellow. Glaciers and bodies of water are coloured in light and dark blue respectively.

Table 2.1 Historical rifting episodes in the Eastern Volcanic Zone.

Fissure Swarm	Year	Dyke Thickness (m)	Erupted Volume [a] (km^3)
Dómadalshraun-Tjörvahraun [b]	~150	?	0.8
Vatnaöldur [b]	871 ± 2	?	3.3
Eldgjá [c]	934	?	19.3
Veidivötn [d]	1477	10	9.1
Lakagígar [e]	1783-1784	4.5	16.0
Tröllagígar [f]	1862-1864	1.5	0.3

[a] The sum of estimated tephra and lava volumes (Jónasson et al. 1997; Venzke et al. 2002).
[b] Part of the Veidivötn fissure swarm (Larsen 1984).
[c] (Stothers 2004)
[d] (Larsen 1984; Grönvold et al. 1995)
[e] Extended from Grímsvötn caldera in Vatnajökull, with the largest erupted basaltic lava flow in historic times (Thórdarson and Self 1993)
[f] Extended from Bárðarbunga system (Thórarinsson and Sigvaldason 1972)

The WVZ and EVZ are separated by the Hreppar crustal block (Figure 2.1). The southern segments of these spreading ridges are connected by the South Iceland Seismic Zone (SISZ), whereas the northern boundary is ambiguous (LaFemina et al. 2005). Left-lateral shear across the 10-15 km wide SISZ is accommodated by right-lateral slip on a series of roughly north-south faults (Figure 2.1), and counterclockwise rotation of the blocks between them (i.e., "bookshelf" faulting) (Einarsson and Eiríksson 1982; Einarsson 1991). No similar seismic zone of this nature, characterized by continuous microearthquake activity (Einarsson 1991; Sigmundsson et al. 1995), exists to the north of the WVZ. It has however been suggested that the Middle Volcanic Zone (MVZ), which sits inbetween the northern ends of the main branches of the WVZ and EVZ (Figure 2.1), acts as a leaky transform, having accommodated relative plate motion during Quaternary time (Óskarsson et al. 1985; Foulger et al. 2003), with one documented Holocene eruption (Kjartansson 1964). The SISZ and complex Tjörnes fracture zone (TFZ) in the north act to connect the MAR to the eastward displaced rift zone in Iceland (Einarsson 1991) (Figure 1.1).

2.1.2 Reykjanes Peninsula

The Reykjanes Peninsula (RP) in southwest Iceland consists of a right-stepping en-echelon array of five northeast trending central volcanoes and associated fissure swarms (Jakobsson et al. 1978). Extensional fractures and normal faults are located within the fissure swarms and strike parallel to the eruptive fissures at N(20-40)°E, while an even larger number of fractures are located at the edge or outside the volcanic systems and strike at N(40-60)°E (Saemundsson and Einarsson 1980; Johannesson et al. 1982; Einarsson 1991; Clifton and Kattenhorn 2006). Along the southern part of the peninsula are a number of km-long north-south trending, right-lateral strike-slip faults that accommodate east-west left-lateral shear in a similar way as the "bookshelf faulting" in the SISZ (Einarsson and Saemundsson 1987; Einarsson 1991; Sigmundsson et al. 1995).

Motion across the RP is highly oblique when compared to plate motion vectors predicted by the NUVEL-1A and REVEL plate motion models for this latitude (19-20 mm/yr in a direction N(77-79)°W relative to the Eurasia plate) (DeMets et al. 1994; Sella et al. 2002; Keiding et al. 2008). Eruptive activity in the RP is cyclic with an eruptive period lasting a few hundred years and the following non-eruptive period lasting several hundred years, with the most recent eruption having occurred in the 13th century (Thórdarson and Larsen

2007). To the east, the triple junction where the Reykjanes Peninsula joins the WVZ and the SISZ is marked by high, persistent seismicity and the Hengill central volcano with its fissure swarms (Einarsson 1991) (Figure 2.1). The Hengill-Hrómundartindur volcanic system was last active in 1994 to 1998, when the system experienced increased seismicity and uplift. No eruption took place, however, the event culminated in two M>5 earthquakes (Sigmundsson et al. 1997; Feigl et al. 2000; Clifton et al. 2002).

2.2 Mid-Atlantic Ridge Spreading Rates in South Iceland

Numerous geodetic studies have been carried out in order to better constrain regional and local spreading rates within the tectonic zones of Iceland. In this section I will review these studies and results.

2.2.1 Reykjanes Peninsula

Hreinsdóttir et al. (2001) showed from analysis of GPS data collected between 1993 and 1998 in southwest Iceland and modelling studies that the RP seismic zone (a narrow zone of high seismicity along the peninsula) is the presently active central axis of the plate boundary in this area, rather than along the RP fissure swarms. Although the NUVEL and REVEL plate motion models predict spreading at a highly oblique angle to the RP seismic zone, modelling of these observed data by Hreinsdóttir et al. (2001) using a 2-D screw dislocation model showed that relative movement between the North America and Eurasia plates along the RP is being taken up by shear. Inversion of the geodetic data indicates a slip rate of ~16.5 mm/yr between the North America and Eurasia plate, parallel to the RP seismic zone (~N76ºE), below a locking depth of ~6.5 km. This slip rate correlated well with the value of the NUVEL-1A velocity component parallel to the seismic zone (DeMets et al. 1994). Hreinsdóttir et al. (2001) attributed this discrepancy between the NUVEL-1A model spreading direction and current plate motion direction as being due to a lack of magma intrusion into the crust and lack of rifting during recent times, which would otherwise be observed over the longer timescale that the NUVEL-1A plate motion model is calculated. This discrepancy implies that the remainder of the total plate spreading rate must be taken up on another plate boundary in south Iceland.

There is an additional discrepancy between the slip rate determined from modelling by Hreinsdóttir et al. (2001), and the observed left-lateral shear value across the peninsula of 11.9 (± 0.5) mm/yr, with little extension having been observed across the peninsula. This is explained by the fact that for the simple screw dislocation model used, the zone of deformation should be at least 70 km wide, while the maximum width of the peninsula is only ~40 km. The observed left-lateral shear correlates well, however, with the maximum left-lateral separation predicted by the screw dislocation model across the peninsula.

Árnadóttir et al. (2006) and Keiding et al (2008) continued the investigation into the deformation of the plate boundary in southwest Iceland by using temporally and spatially expanded GPS datasets from 1992-2000 and 2000-2006 respectively, that were modelled using 3-D dislocation and point source models. The 1992-2000 dataset was modelled by Árnadóttir et al. (2006) using a dislocation model experiencing 18 (+6/-5) mm/yr left-lateral slip parallel to the seismic zone at a locking depth of 9 ± 3 km, with significant opening of 9 ± 3 mm/yr. 2000-2006 GPS data were modelled by Keiding et al (2008) using a dislocation model experiencing 18 (+4/-3) mm/yr of left-lateral motion and opening at a rate of 7 (+3/-2) mm/yr below a locking depth of 7 (+1/-2) km. For both models it is shown that the surface deformation across the RP can be explained by deep plate boundary motion oblique to the RP seismic zone on a regional scale, which correlates with the predicted total spreading rates and directions from the NUVEL and REVEL plate motion models. According to Árnadóttir et al. (2006) and Keiding et al (2008), spreading across the RP therefore accounts for the total North America-Eurasia plate motion south of the SISZ (DeMets et al. 1994; Sella et al. 2002).

2.2.2 Western and Eastern Volcanic Zones

In order to investigate rift-transform interactions, Sigmundsson et al (1995) looked at GPS measurements made in south Iceland during the period 1986-1992. Observations showed little internal deformation of the area west of the WVZ (within the North America plate) and the southern tip of the EVZ (within the Eurasia plate). The observed velocities of these two areas relative to a stable North America plate is 2.1 (± 0.4) cm/yr in direction N(117 ± 11)ºE, and is compatible with the velocity determined using the NUVEL-1 global plate motion model (DeMets et al. 1994). Sigmundsson et al. (1995) showed that 85 ± 15% of the relative plate motion is accommodated by the SISZ, and therefore the WVZ must accommodate 15 ± 15% of the plate motion and the EVZ must

accommodate 85 ± 15%. Sigmundsson et al. (1995) also concluded that the area south of the SISZ is moving towards the east with the Eurasia plate, while the area to the north is moving towards the west with the North America plate.

Jónasson et al. (1997) extended the time period of GPS data analysed to 1986-1994, as well as extended the GPS coverage within the EVZ and included electronic distance measurements (EDM) made in the area in order to investigate extension in the EVZ. An extension rate of 12 mm/yr was calculated across a 100 km wide zone. Other investigations into spreading rates in the WVZ involved geological estimates of extension across the Þingvellir Graben in the southern WVZ, which indicate spreading rates for the WVZ that are ~40-51% of the NUVEL-1A rate (Guðmundsson 1987; Sæmundsson 1992; DeMets et al. 1994). Geodetic data collected across the graben, however, showed a slower spreading rate of 0-6.6 mm/yr, which is 0-34% of the NUVEL-1A rate (Decker et al. 1971; Gerke 1974; Brander et al. 1976; Tryggvason 1982; 1990; Sæmundsson 1992; Sigmundsson et al. 1995).

LaFemina et al. (2005) used GPS observations made in south Iceland between 1994 and 2003 to determine the partitioning of spreading rates across the WVZ and EVZ. A simple elastic half-space model of a continuously opening dyke below a locked upper crustal zone for two parallel rift zones (i.e. the WVZ and EVZ) was used to model three plate-motion parallel profiles (Figure 2.2). LaFemina et al. (2005) utilized a more complex coupling model, with a thin elastic layer representing the upper crust over a Maxwell viscoelastic half-space representing the lower crust and upper mantle, to check for the effects of post-rifting relaxation caused by the historical rifting events.

The sum of the extension rates determined by LaFemina et al. (2005) across the eastern and western limbs of the ridge in south-central Iceland equals the total plate rate, and is comparable with other estimates of North America-Eurasia relative plate motion (DeMets et al. 1994; Sella et al. 2002) (Table 2.2). LaFemina et al. (2005) show along strike variations in spreading, which matches with a propagating ridge model, with the eastern limb showing a decrease in spreading rate in the direction of propagation to the southwest, and the deactivating western limb showing an increase in rate in this direction. Modelling results by LaFemina et al. (2005) also show that the ridge is currently propagating into the EVFZ, with spreading south of Torfajökull volcano. This result implies that spreading south of the SISZ is partitioned between the ridge propagating into

the EVFZ and the RP further to the west (Hreinsdóttir et al. 2001), which is in contradiction to results by Árnadóttir et al. (2006) and Keiding et al (2008).

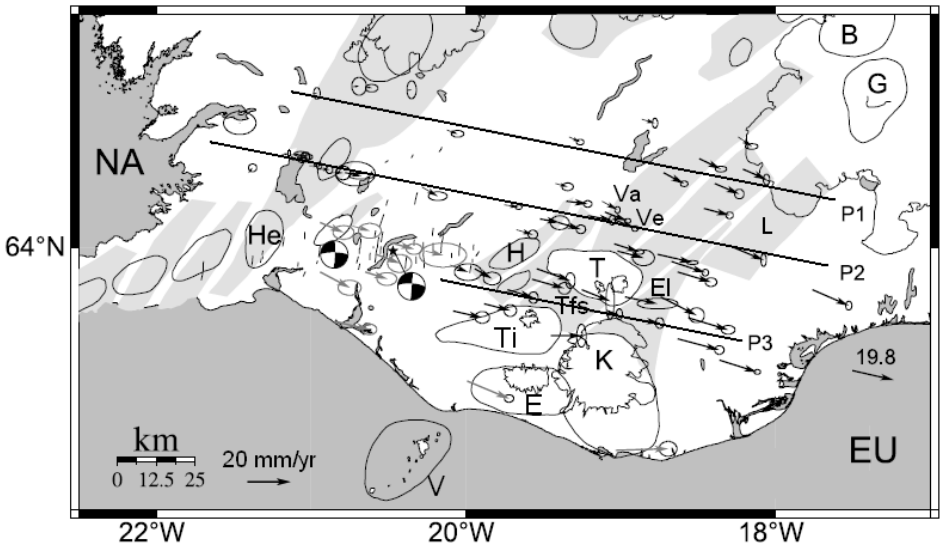


Figure 2.2 GPS velocity field relative to stable North America between 1994 and 2003 (from LaFemina et al. 2005). Plotted velocity vectors and the associated uncertainties are corrected for coseismic offsets from the June 2000 SISZ earthquakes (LaFemina et al. 2005). The focal mechanisms for these earthquakes are shown (Dziewonski et al. 2001). The location of the three profiles (P1, P2 and P3) modelled by LaFemina et al. (2005) are marked by black lines. The black arrow off of the southeast coast is the predicted North America-Eurasia (Na-Eu) plate motion vector (19.8 mm/yr) from the REVEL plate motion model (Sella et al. 2002). Names of central volcanoes (outlined) and fissure swarms (shaded grey) as in Figure 2.1.

Table 2.2 Spreading rates and locking depths estimated by LaFemina et al. (2005) for three plate-motion parallel profiles (Figure 2.2) using elastic half-space models. Rates are compared with the REVEL and NUVEL-1a plate motion models (DeMets et al. 1994; Sella et al. 2002). Model uncertainties are given in parentheses.

Profiles	Spreading Rates (mm/yr)			Locking Depth (km)		Spreading Rates (mm/yr)	
	WVZ	EVZ	Total	EVZ	WVZ	REVEL	NUVEL-1A
P1	2.6 (± 0.9)	19.8 (± 2.0)	22.4 (± 2.2)	13.0 (+7.0/-3.3)	2.5	19.7	18.4
P2	7.0 (± 0.4)	11.0 (± 0.8)	18.0 (± 0.9)	3.0 (+1.2/-0.7)	4.0 (+2.1/-1.1)	19.8	18.4
P3	?	8.0 (± 1.0)	?	7.0 (+2.5/-1.2)		19.9	18.5

The locking depths estimated by LaFemina et al. (2005) for the EVZ correspond approximately to the brittle-ductile transition depth for mafic material along the active rift axis and the maximum depth of earthquakes. LaFemina et al. (2005) attribute the maximum velocity gradient measured across the Veidivötn fissure swarm (Ve, Figure 2.2), that experienced its last major eruption in 1477 A.D. (Larsen 1984) and a smaller eruption in 1862-1864, to inter-rifting elastic strain accumulation. LaFemina et al. (2005) suggest that this fissure swarm is the current axis of spreading and will be the site of the next major fissure eruption/rifting event in the EVZ, instead of along the most recently active Lakagigar swarm (L, Figure 2.2). A summary of geodetic derived spreading rates for southern Iceland are shown in Figure 2.3.

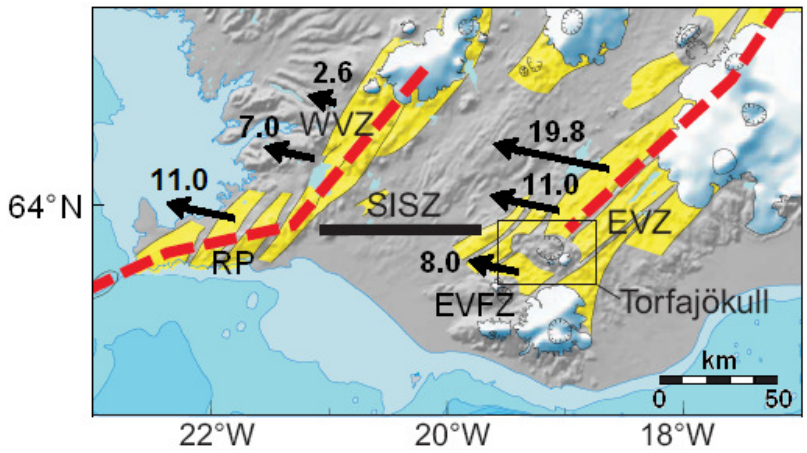


Figure 2.3 Map of south Iceland showing geodetically derived spreading rates (mm/yr) determined by Hreinsdóttir et al. (2001) and LaFemina et al. (2005) across the Western Volcanic Zone (WVZ) and Eastern Volcanic Zone (EVZ), connected in the south by the South Iceland Seismic Zone (SISZ). The model derived spreading rates correlate with a propagating ridge model, with the WVZ deactivating towards the southwest, which is the direction of propagating of the spreading ridge of the EVZ into the Eastern Volcanic Flank Zone (EVFZ).

2.3 Torfajökull Caldera

Torfajökull caldera is located at the intersection of the EVZ, SISZ and EVFZ in south-central Iceland (Figure 2.4). At Torfajökull rifting is occurring towards the southwest in the form of the volcanoes' own northeast-southwest trending fissure swarm (Tfs), while the Vatnaöldur (Va) and Veidivötn fissure (Ve) swarms associated with the Bárðarbunga central volcano are found to the northeast of the volcano and intersects the caldera's margin (Blake 1984) (Figure 2.4).

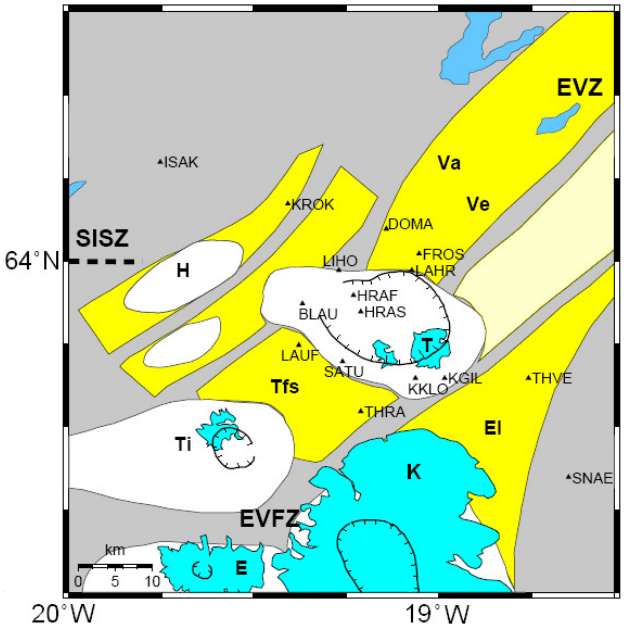


Figure 2.4 Map of south-central Iceland showing the intersection of the Eastern Volcanic Zone (EVZ), the South Iceland Seismic Zone (SISZ) and the Eastern Volcanic Flank Zone (EVFZ). Black triangles mark the location of GPS sites used for this study (labelled). Names of central volcanoes (white) and fissure swarms (yellow) as in Figure 2.1. The inactive fissure zone is marked in light yellow. Caldera outlines are marked by hatched lines. Glaciers and bodies of water are coloured in light and dark blue respectively.

An ash zone (Z-2) discovered in North Atlantic sediments and the Central Greenland ice core (GRIP) has been linked chemically, and through dating to an ancient eruption at Torfajökull ~50,000 B.P. (Grönvold et al. 1995). This provides evidence that the volcano has been active since at least the mid to late-Quaternary (Grönvold et al. 1995), with the most recent eruption in 1477 A.D. (Larsen 1984). Torfajökull is the largest rhyolitic complex in Iceland (Walker 1974; McGarvie 1984; Gunnarsson et al. 1998), with the

central volcano rising 500 m above the surrounding area, and a WNW-ESE and NNE-SSW extent of 30 km and 18 km respectively (Gunnarsson et al. 1998). The volcano's caldera, with a diameter of 12 km, is the result of one or more collapse events and subsequent refilling with younger extrusives (Gunnarsson et al. 1998).

2.4 Torfajökull Petrology

2.4.1 General Geology

In Iceland, despite the basaltic mid-ocean ridge setting, silicic rocks commonly make up more than 20–30% of the exposed rocks within large central volcanoes (≥400 km^3), and more than 50% of the central portion of these volcanoes (Walker 1974; Gunnarsson et al. 1998). The majority of the exposed rocks in the Torfajökull area were erupted during the last glaciation (>10,000 years) and are peralkalic rhyolites (McGarvie 1984). The eruption of these rhyolite lavas beneath a glacier has resulted in the formation of acid hyaloclastic deposits in the form of ridge and dome-shaped formations, as well as rhyolite breccias (MacDonald et al. 1990; McGarvie et al. 1990; Gunnarsson et al. 1998) (Figure 2.5). A small portion of the exposed rocks were erupted during several post-glacial eruptions, and are mainly subalkalic rhyolites in composition (McGarvie 1984) (Figure 2.5). Only minor amounts of transitional alkalic basaltic and intermediate extrusives have been erupted at Torfajökull (Blake 1984; Larsen 1984; McGarvie 1984) (Figure 2.5).

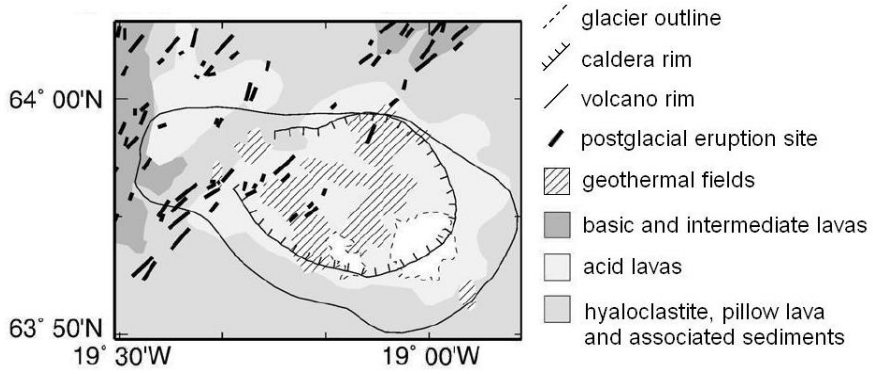


Figure 2.5 General outline of the geology of the Torfajökull region (Soosalu et al. 2006b). The volcano rim marks the extent of the Torfajökull lava flows, while the caldera rim is defined by the latest collapse features (ring fractures). Stripped regions show the extent of hydrothermal activity within the caldera (Arnórsson et al. 1987; Gunnarsson et al. 1998).

The erupted material at the volcano covers an area of 450 km^2 (Walker 1974; McGarvie 1984), with the volume of silicic extrusives averaging around 225 km^3 (Gunnarsson et al. 1998). Two small glaciers are found at the caldera's southeastern rim. The caldera hosts the most powerful high-temperature geothermal fields in Iceland, which cover an area of approximately 140 km^2 (Arnórsson et al. 1987; Gunnarsson et al. 1998) (Figure 2.5), and therefore has been the focus of ongoing geophysical and geologic investigations.

2.4.2 Postglacial Activity

In the last 2,700 years, three major basaltic eruptions along the Veidivötn fissure swarm (Ve) have triggered eruptions along a number of parallel, but discontinuous fissures within or just outside the central, western and northern parts of the Torfajökull caldera (Larsen 1984; McGarvie 1984). These eruptions have resulted from the injection of magma from the fissure swarm into the Torfajökull volcanic system (Larsen 1984; McGarvie 1984). The A.D. 1477 and A.D. 150 Veidivötn rifting episodes resulted in the eruption of thick silicic lavas and lava domes on the northern edge of the Torfajökull system (Larsen 1984; Gunnarsson et al. 1998) (Figure 2.6). The rifting episode in A.D. 870, associated with the Vatnaöldur fissure eruption (Va), resulted in the eruption of the Hrafntinnuhraun (HRAF) silicic unit in the west of Torfajökull caldera, while the Hrafntinnusker (HRAS) lavas were erupted in A.D. 1477 (Larsen 1984; Gunnarsson et al. 1998) (Figure 2.6).

Over the entire postglacial period a total of nine silicic lava units were extruded from fissures within or just outside Torfajökull caldera, parallel to the northeast-southwest trending Veidivötn fissure swarm (MacDonald et al. 1990; Gunnarsson et al. 1998). Four lava units were extruded in the northern part of the caldera and five in the southwestern (Gunnarsson et al. 1998) (Figure 2.6). Some of these postglacial silicic lavas that are older than 2,700 years may also be the result of earlier rifting in the Veidivötn fissure swarm and the extension of fissures towards the southwest, thereby allowing silicic magma from the volcanoes own magma system to erupt from vents along the fissures (Gunnarsson et al. 1998).

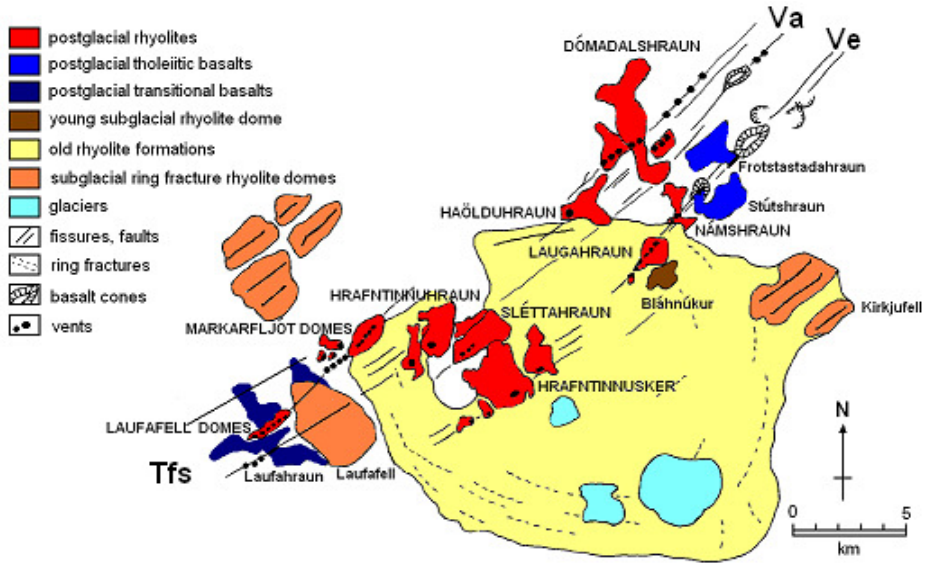


Figure 2.6 Basic geological map of Torfajökull volcano (modified from McGarvie 1984; MacDonald et al. 1990; Thórdarson and Larsen 2007). The majority of the material making up the caldera complex is older than 10,000 years. The names of the smaller postglacial rhyolitic lava fields (<10,000 years) are given in capital letters, while the names of other subglacial flows and postglacial basaltic flows are given in small letters. Ring fractures give the approximate outline of the caldera. Names of fissure swarms as in Figure 2.2.

Mechanical mixing of the tholeiitic basalts from the Veidivötn fissure swarm and the alkali rhyolites from the Torfajökull system, on the border between these two volcanic systems, is evident. Mixing is first seen in silicic extrusives erupted during the end of the last glaciation which contained a small number of tholeiitic inclusions (Blake 1984; Larsen 1984; McGarvie 1984; McGarvie 1985; McGarvie et al. 1990; Gunnarsson et al. 1998). This process has become more frequent, and the bulk degree of mixing has increased in postglacial times (Blake 1984; McGarvie 1984). Mixing is evident as discrete inclusions of basaltic magma within the rhyolitic magma, to a complete homogeneous blend of the two with a hybrid composition (McGarvie 1984). The most recently erupted Laugahraun and Dómadalshraun lavas have been contaminated by these hybrid composition magma (Blake 1984; McGarvie 1984) (Figure 2.6).

Intermediate lavas from Torfajökull's own volcanic system are mixed with postglacial rhyolites in the southern and western part of the volcano (McGarvie 1984) (Figure 2.6). In the Torfajökull system a fissure swarm of olivine basaltic magma is "trapped" at depth below the volcanoes rhyolitic magma due to its higher density, and is therefore stopped

from rising to the surface except in areas with favourable tectonics (Walker 1974; McGarvie 1984). These basalts occur mostly as inclusions in postglacial rhyolitic deposits (McGarvie 1984)

2.4.3 Geothermal activity

High-temperature geothermal fields at Torfajökull volcano are the result of groundwater being heated when coming into contact with hot rocks at depth (Figure 2.7).

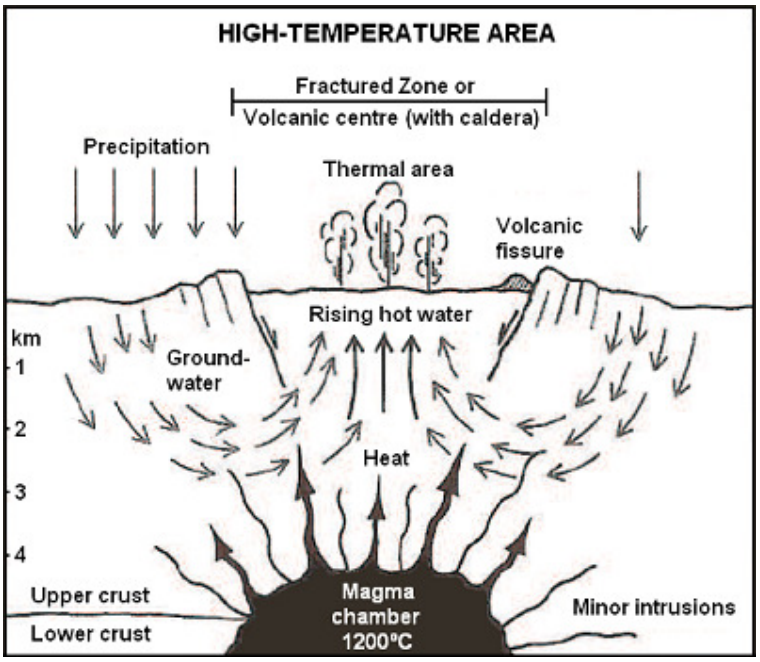


Figure 2.7 Diagram showing the workings of a high-temperature geothermal system, of which Torfajökull volcano is an example (Guðmundsson 1996; Borner 2007). As groundwater interacts with a hot body at depth it is heated and becomes more buoyant than the cold water in the surrounding rocks, causing it to rise up through cracks and fissures. Seismicity is in general associated with the geothermal activity within and around the fractured zone or volcanic centre. This seismicity is mostly due to the interaction of the hot body at depth with circulating groundwater, which results in quenching and contraction of body and the development of cracks. These cracks allow for the further penetration of the water and further cracking (i.e. swarm activity) until the rock regains its static equilibrium. This process is known as thermal cracking.

The geothermal activity at Torfajökull is manifest mainly as steaming ground, which is in turn intensely altered due to acid leaching (Arnórsson et al. 1987) (Figure 2.8). Hot springs, bubbling mud pools and fumaroles emitting sulphurous gases are also examples of activity (Figure 2.8). Thermal measurements reveal temperatures of around 300°C and greater at the Earth's surface for geothermal fields in the western and southeastern part of the caldera (Arnórsson et al. 1987; Bjarnason and Olafsson 2000; Borner 2007).



Figure 2.8 Geothermal activity within Torfajökull caldera: (a) Bubbling mud pot; (b) Boiling water and steam at the Earth's surface; (c) Fumarole emitting steam and gases, surrounded by intensely altered ground.

Research conducted at a number of volcanoes has uncovered an important interaction between magmatic systems at depth and shallower geothermal systems, and the resulting ground deformation. Campi Flegrei caldera in western Italy is an example of a caldera that experiences both thermoelastic uplift due to the migration of hot pressurised fluids in

the shallow crust, as well as surface uplift due to increases in pressure within a magma chamber at depth (Bonafede 1991; Gaeta et al. 1998; Orsi et al. 1999; De Natale et al. 2001). The inclusion of thermal fluid circulation in the deformation model for this particular volcano has helped explain the very high pressure change (~1/2 kbar or 50 MPa) that would otherwise be needed in the magma chamber in a purely elastic medium in order to account for the significant uplift that has been observed at the volcano (~1.8 m in 2 years) (Bonafede 1991). Changes in water flow in a shallow aquifer resulting from an increase in pressure and/or temperature in a magma chamber at depth, can strongly amplify the effect of the pressure increase on the uplift experienced at the Earth's surface (Gaeta et al. 1998; De Natale et al. 2001).

A very shallow depth (<2.5 km) for the magma chamber at Campi Flegrei is also needed in order to explain the ground deformation data if fluid migration is not accounted for (Bonafede 1991). Such a shallow magma chamber is not a realistic estimate however for this volcano as other studies have estimated the top of the magma chamber at a depth of ±4 km (Bonafede 1991). When accounting for geothermal activity in the deformation model this allows the additional geothermal source of deformation to be at a shallower depth than the volcanoes magma chamber (Bonafede 1991).At Torfajökull, a volcano that has been the host of long-term, high-temperature geothermal fields, part of the measured ground deformation could be due to fluid migration within the geothermal fields, as well as due to a change in pressure or volume in a magma chamber at depth.

2.5 Geophysical Studies at Torfajökull volcano

Seismicity, resistivity and tilt data collected over the last ten years at Torfajökull caldera and the surrounding region, point towards a cooling magma chamber at depth below the western part of the caldera. This proposed magma chamber coincides well with geothermal activity at the surface, and lies below the area of most recent postglacial activity within the caldera. High-temperature geothermal activity and low-frequency earthquakes are also focused in the southeast of the caldera, though the source of this activity is not clear.

2.5.1 Seismic activity

Seismicity at Torfajökull is characterized by persistent low-magnitude background activity consisting of both high and low-frequency events that do not overlap spatially or temporally (Soosalu and Einarsson 1997). High-frequency events with local magnitudes of less than M_L 3, and typical frequency ranges of 4-10 Hz, have been recorded mainly in the western and central part of the caldera as individual events and swarm activity (Einarsson 1991; Soosalu and Einarsson 1997; 2004; Lippitsch et al. 2005; Soosalu et al. 2006b). Swarm events are typically 1 or less in magnitude and many occur simply as a grouping of 3 to 5 events within a period of up to an hour, with the events being in relatively close proximity (within 1 km of each other) (Borner 2007).

The persistent, low-magnitude, low-frequency events at Torfajökull usually cluster tightly at shallow depth in the southern part of the caldera (Soosalu and Einarsson 1997; 2004; Soosalu et al. 2006b). These events have a frequency range of 1-3 Hz and magnitudes of less than M_L 1 (Soosalu and Einarsson 1997; 2004; Soosalu et al. 2006b). These low-frequency events often occur in swarms that begin abruptly, rising quickly to a level of up to a few hundred events per day, and last for a few days followed by quieter intervals (Soosalu and Einarsson 1997; Soosalu et al. 2006b). A number of studies have been conducted in order to investigate the nature and cause of the seismicity at Torfajökull (Table 2.3).

Table 2.3 Research conducted since 1991 into the seismic activity at Torfajökull volcano.

Survey Period	Observations and Interpretation
1991-1995 [a]	*Observation:* High-frequency hypocentres surround an aseismic void in the western part of the caldera. *Interpretation:* Activity is the result of thermal cracking around a cooling magma chamber at depth (diameter: ~4 km, depth: ~8 km), assisted by deep circulation of geothermal water.
	Observation: Low-frequency events in the southeastern part of the caldera. *Interpretation:* Events are the result of magma movement at depth, or some other mechanism relating to the transport of fluid in the magmatic or hydrothermal systems of the volcano.
1995-1999 [b]	*Observation:* Data showed negligible S-wave attenuation below Torfajökull. *Interpretation:* Cooling magma chamber must no longer be molten, but is instead ductile.
2002 [c]	*Observation:* High-frequency activity restricted to shallow depths (0-6 km) in the western part of the caldera (Figure 2.9). Observations show a sharp cut-off in seismicity at 3 km depth. *Interpretation:*. Sharp cut-off is possibly due to a marked temperature increase at this depth and/or a structural boundary, possibly a magma body underlying the western part of the volcano or an intrusive magma sheet.
2002 [d]	*Observation:* A closer study of the low-frequency events within the southeastern part of Torfajökull volcano that coincide well with geothermal activity. *Interpretation:*. Activity is the result of a cryptodome, "a dome-shaped structure created by the ascent of viscous magma and its accumulation at shallow depth".

[a] Soosalu and Einarsson (1997), [b] Soosalu and Einarsson (2004), [c] Lippitsch et al. (2005), [d] Soosalu et al. (2006b).

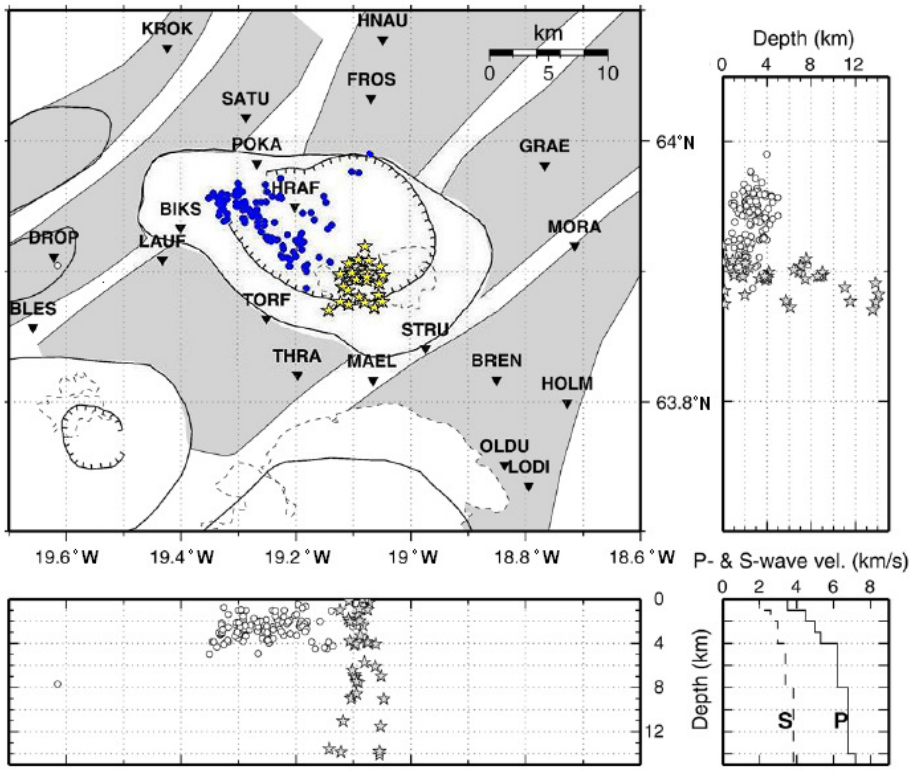


Figure 2.9 Seismicity recorded at Torfajökull caldera in 2002 shown in map view, and east-west and north-south vertical sections (modified from Soosalu et al. 2006b). High-frequency earthquakes (blue circles) were located by Lippitsch et al. (2005) and low-frequency earthquakes (yellow stars) were located by Soosalu et al. (2006b). The high-frequency events are concentrated in the central and western part of the caldera, while low magnitude, low-frequency events are located in the southeastern part of the caldera. The temporary seismic network stations are indicated by black inverted triangles. The velocity model used for the relocation of low-frequency events is shown in the lower right corner (Soosalu et al. 2006b).

When considering the origin of the low-frequency activity at Torfajökull it is important to consider activity at other volcanoes in Iceland. Seasonal low-frequency activity has been observed at Katla volcano to the south of Torfajökull (Figure 2.4), most noticeably since 1960 in an area west of the Katla caldera. Activity typically begins in late summer/early autumn with a peak in late autumn (October), and activity dying out in mid-winter (Agustsson et al. 2000; Jónsdóttir et al. 2007). Einarsson and Brandsdóttir (2000) attribute this phenomenon at Katla to increased groundwater pore pressure in the crust beneath the volcano's glacier (Mýrdalsjökull) after the summer thaw, with a possible contribution from reduced ice load after melting. More recent studies by Soosalu et al. (2006a) have led to this seismicity at Katla being attributed to a rising cryptodome.

At Torfajökull the low-frequency activity is concentrated between the volcanoes two glaciers. Seismic studies conducted at Torfajökull by Soosalu and Einarsson (1997; 2004) from 1991 to 1999 span a number of season changes, while the study conducted by Soosalu et al. (2006b) focuses on seismic activity between May and October 2002, the exact time period over which increased activity was observed at Katla volcano. Another possibility therefore for the origin of low-frequency activity at Torfajökull is glacial unloading during the summer months, as well as increased input of melt-water into the volcanoes geothermal system from its own glaciers, as well as Vatnajökull glacier and Katla's glacier.

After the eruption of Hekla volcano in 1991, Soosalu and Einarsson (1997) suggested a link between Hekla and Torfajökull volcano due to an increase in low-frequency swarm activity at Torfajökull after the eruption of Hekla from January to March 1991. Increased activity was also seen in late 1991 and early 1992, with a peak occurring in October 1991 with over 600 events on 29th and 31st October 1991 (Soosalu et al. 2006b), though as stated above this October peak could be due to, at least in part, glacial unloading and increased melt water supply. A similar increase in low-frequency swarm activity was not seen after the February-March 2000 Hekla eruption (Soosalu et al. 2006b) or the June 2000 earthquakes in the SISZ (Dziewonski et al. 2001). It must be noted, however, that continuous seismic monitoring of Hekla and Torfajökull around the time of the 1991 eruption began in 1991 and continued until 1999 (Soosalu and Einarsson 1997; 2004), while seismic monitoring at Torfajökull after the 2000 activity was limited, with a study from May to October 2002 (Lippitsch et al. 2005; Soosalu et al. 2006b). A link may therefore exist but lack of monitoring may be the reason it was not noted after the most recent Hekla eruption.

2.5.2 Magnetotelluric data

Eysteinsson and Hermance (1985) report on magnetotelluric measurements made on the outskirts of the Torfajökull caldera that revealed a low-resistivity zone (5 Ω.m) at a depth of around 15-25 km, as well as a zone of still lower resistivity (2 Ω.m) at a depth of 10-15 km (Gunnarsson et al. 1998). The deeper zone is interpreted as being due to a body of basaltic melt that separated from the mantle, while the higher zone is interpreted as being due to shallower magma chambers of this basaltic melt (Eysteinsson and Hermance 1985; Gunnarsson et al. 1998). These values correlate fairly well with crustal thickness

estimates for Iceland, which many studies have shown to be a highly variable value in this region. Darbyshire et al. (2000) compiled estimates of crustal thickness across Iceland determined by seismic refraction studies, as well as receiver function analysis and gravity modelling. Results shows that crustal thickness decreases from a maximum thickness of ~40 km above the North Atlantic mantle plume in south-central Iceland, to a minimum value of 15 km where the rift zones extend off of the northeast and southwest coasts of Iceland, with upper crustal thickness in south Iceland of between 0.7 and 11 km (Darbyshire et al. 2000; Du and Foulger 2001; Foulger et al. 2003).

More recent magnetotelluric measurements made within and outside of Torfajökull show a complicated resistivity pattern of two low-resistivity regions in the central-west and southeastern part of the caldera, separated by an area of relatively high resistivity down to a depth of one kilometer (Figure 2.10) (Karlsdóttir 2001). These low resistivity or geothermally active areas point towards a source at depth that is heating the groundwater, thus allowing the saturated bedrock to conduct electricity to a greater degree than dry, cold rock would. These data neither point toward an exact heat source location, as heated groundwater will easily migrate, nor the state of the source (i.e., ductile or molten)

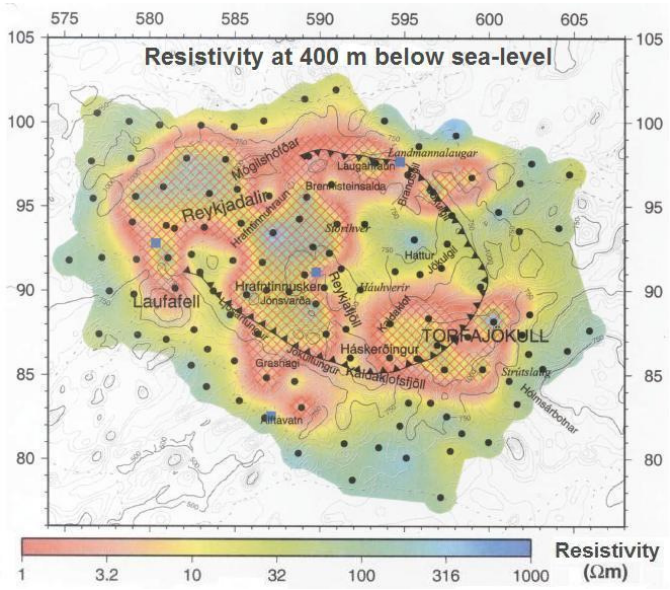


Figure 2.10 Resistivity across Torfajökull caldera and surrounding region at 400 m below sea-level (modified from Karlsdóttir 2001; Borner 2007). Two low-resistivity areas are evident; one in the southeast of the caldera under the Torfajökull glacier, and another in the central-western part of the volcano. These two areas are separated by a region of higher resistivity.

2.5.3 "Dry-Tilt" Measurements

Due to difficulties involved in using wet tilt systems, a procedure known as "dry-tilt" was developed at the Hawaiian Volcano Observatory (HVO) in 1968 (Ewert 1992; Yamashita 1992). "Dry-tilt" or tilt-levelling involves precise levelling of an array of benchmarks, and is therefore more accurately known as single-setup levelling (SSL) and is used to monitor vertical displacements (i.e. changes in ground tilt) (Yamashita 1992). SSL has been used as a monitoring technique at numerous volcanoes around the world over the years, including various volcanoes in the Cascade Range (Ewert 1992; Yamashita 1992); Hawaiian volcanoes (Heliker et al. 1986); as well as volcanoes in Iceland (Sturkell et al. 2006b and references there in).

For SSL measurements, two or three long Invar metals rods and rod stays (i.e., a metal alloy that exhibits a nearly zero coefficient of thermal expansion), a precise spirit level, and a micrometer plate are required (Ewert 1992). Bench-marks are typically arranged as an equilateral triangle with 30-40 m long sides (Heliker et al. 1986; Ewert 1992; Yamashita 1992). Station orientation and bench-mark configuration, including size and shape (linear, triangular, square, and hexagonal arrays), are flexile (Yamashita 1992). The instrument is then levelled over the centre mark of the triangle, allowing for measurement of the elevation difference between each of the three bench-mark pairs (Yamashita 1992). SSL measurements in general have a precision of ±2-3 microradians (μrad), where 1 μrad is equal to 0.0000573° and can be visualized as a 1 km long board that is elevated by 1 mm at one end (Heliker et al. 1986). One of the difficulties with SSL is that it is limited to relatively flat areas where elevation changes do not exceed 3 m (Heliker et al. 1986; Ewert 1992).

The tilt site Naefurholt (NAEF) that is on the east flank of Hekla volcano and has been measured since 1970, shows upward tilt towards the east due to the inflation of Hekla volcano since its eruption in 2000 (Sturkell et al. 2006b) (Table 2.4). Tilt measurements have been made within and around Torfajökull caldera from 2001 to 2006 (Table 2.4). The site Hrafntinnusker (HRAF) in the western part of Torfajökull caldera experienced a 7.2 μrad change in tilt over the period of this survey (between 2001 and 2006), with the direction of downward tilt being towards the southeast of the caldera (Sturkell et al. 2006b) (Figure 2.11). HRAF is the closest tilt site to the proposed cooling magma body of

Soosalu and Einarsson (1997; 2004) in the western part of Torfajökull caldera, and therefore tilt data for this site could provide support for their theory.

Table 2.4 Table of tilt measurements made at sites within and around Torfajökull and Hekla volcano between 2000/1 and 2006 (data provided by Erik Sturkell, Nordic Volcanological Centre).

Site	Date of Observation	Tilt since previous Obs (μrad)			Std error (μrad)		
		East	North	Radial	East	North	Max axis
DOMA	*September 27, 2001*						
	August 26, 2003	-4.087	2.644	**4.868**			0.621
	September 23, 2006	2.757	-1.582	**3.179**			1.102
	2001-2006	-1.33	1.062	**1.702**	1.102	1.307	
HNAU	*September 27, 2001*						
	September 23, 2006	0.041	0.645	**0.646**	0.580	0.580	0.580
NORD	*September 27, 2001*						
	September 23, 2006	1.945	-0.029	**1.945**	0.386	0.386	0.386
HRAF	*October 5, 2001*						
	September 17, 2002	-1.793	3.488	**3.922**			1.521
	August 26, 2003	0.294	-3.822	**3.833**			1.338
	September 14, 2004	-0.111	2.159	**2.162**			1.488
	September 22, 2006	-0.755	5.011	**5.068**			0.824
	2001-2006	-2.365	6.836	**7.234**	0.551	1.032	
LAUF	*October 3, 2001*						
	September 17, 2002	1.829	-1.49	**2.359**			0.530
	August 26, 2003	2.204	1.022	**2.429**			0.518
	September 14, 2004	-0.424	-1.008	**1.094**			0.812
	September 22, 2006	-3.043	0.708	**3.124**			0.598
	2001-2006	0.566	-0.768	**0.954**	0.598	0.560	
NAEF	*April 6, 2000*						
	November 21, 2000	-0.005	3.397	**3.397**			0.657
	November 6, 2001	2.425	-0.331	**2.447**			0.486
	June 14, 2002	-1.083	-0.887	**1.400**			0.640
	August 27, 2003	1.995	-0.072	**1.996**			0.461
	April 27, 2004	0.017	-0.223	**0.224**			0.560
	November 18, 2004	1.985	2.423	**3.132**			0.669
	May 24, 2005	-0.038	-3.388	**3.388**			1.026
	February 8, 2006	-1.102	0.325	**1.149**			0.642
	October 26, 2006	1.895	2.414	**3.069**			0.412
	April 26, 2007	-0.041	-0.553	**0.555**			0.533
	2001-2006				0.461	0.435	

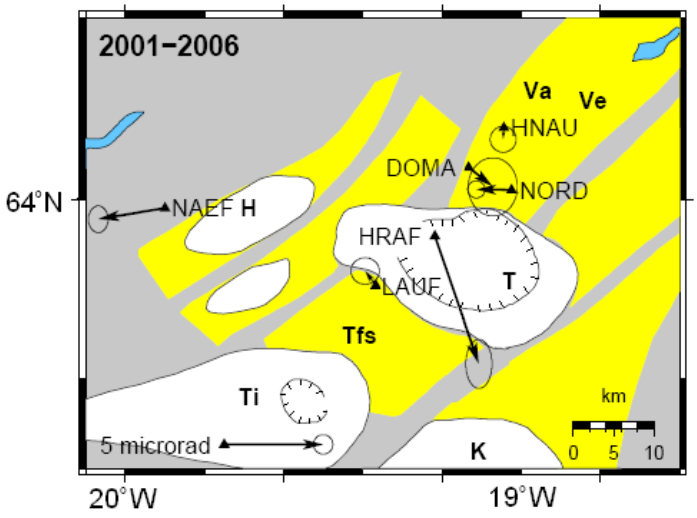


Figure 2.11 Average tilt measurements made between 2001 and 2006 (data provided by Erik Sturkell, Nordic Volcanological Centre). The tilt stations are indicated by triangles, with the tilt vectors pointing towards the direction of downward tilt and vector lengths proportional to the change in tilt. Tilt measurements made at Hrafntinnusker (HRAF) indicate subsidence of the western part of the caldera. Names of central volcanoes and fissure swarms as in Figure 2.2; bodies of water marked in blue.

Assuming that the Veidivötn fissure swarm is the current axis of spreading in the EVZ as suggested by LaFemina et al. (2005), the change in tilt measured at sites outside of the caldera [Dómadalshraun (DOMA) and Norðurnámshraun (NORD)] can be explained by the effect of the spreading ridge that passes through the caldera, with sites showing upward tilt away from the ridge (Figure 2.11). The site Hnausar (HNAU) shows no significant change in tilt from 2001 to 2006 (Figure 2.11). The location of the spreading axis to the south of Torfajökull volcano is suggested by LaFemina et al. (2005) to be in line with that to the north of the volcano, along the Veidivötn fissure swarm. However, the overall tilt measured at LAUF between 2001 and 2006 shows downward tilt away from the ridge location proposed by LaFemina et al. (2005) (Figure 2.11), which does not correspond with the direction of tilt measured at DOMA and NORD.

2.5.4 Interferometric Synthetic Aperture Radar (InSAR)

An Interferometric Synthetic Aperture Radar (InSAR) image of Torfajökull caldera was created from 1993-2000 satellite data (Figure 2.12) (A. Hooper pers comm. 2007). The InSAR image shows an elliptical subsidence pattern (northwest-southeast trending major axis) in the southwestern part of the caldera, which reaches a maximum (< -8 mm/yr) just south of the GPS site HRAS. Non-existent data coverage in the southeastern part of the volcano due to the volcanoes own glaciers, means that no conclusions can be drawn using InSAR regarding the source of low-frequency events in this part of the caldera (Soosalu and Einarsson 1997; Soosalu et al. 2006b).

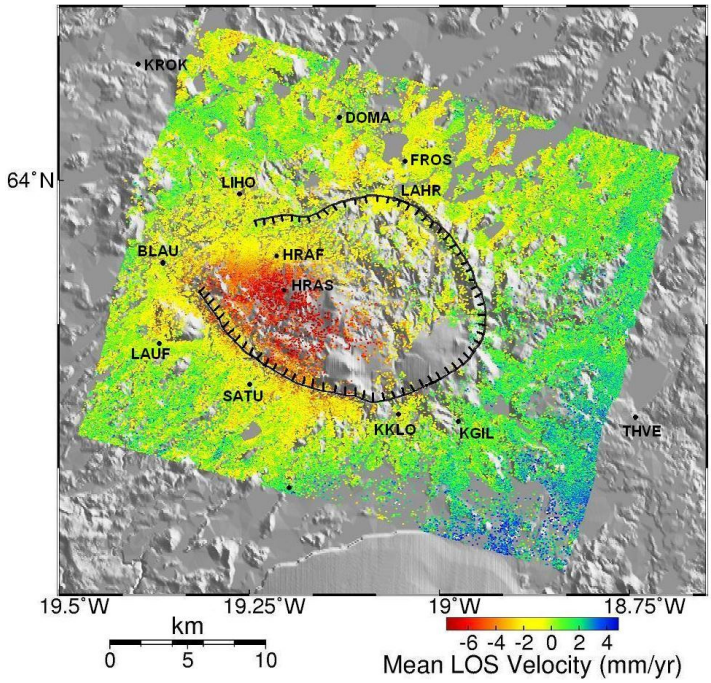


Figure 2.12 Interferometric Synthetic Aperture Radar (InSAR) image of Torfajökull caldera generated from SAR images taken of the caldera from 1993-2000 (A. Hooper pers comm. 2007). Line-of-sight (LOS) subsidence of < -8 mm/yr is seen in the western part of the volcano. The outline of the caldera is marked with a hatched line, and the locations of GPS sites used for this study are marked.

In conclusion, seismicity at Torfajökull caldera since 1991 points towards a magma source below the western part of the caldera. Some of these studies go further to define the source as a slow cooling magma chamber, a theory that is supported by the extensive

geothermal fields within Torfajökull caldera which form as a result of natural heat loss from a magma source. Tilt data collected within the caldera from 2001 to 2006 and a 1993-2000 InSAR image of the caldera both show subsidence within the western part of the caldera, supporting the idea of a cooling and contracting magma chamber at depth. The ground deformation signal is also influenced however, by the extensive high-temperature geothermal fields that dominate the western part of the caldera, and which are fed by an ever increasing flux of glacial melt-waters. The theory of a cryptodome rising below the southeastern part of Torfajökull volcano (Soosalu et al. 2006b) is not supported by the 1993-2000 SAR interferogram.

2.6 Hekla Volcano

2.6.1 General

Hekla volcano is located approximately 20 km northwest of the western-edge of the Torfajökull caldera, at the intersection of the SISZ and EVZ (Figure 2.4). Hekla is a stratovolcano that is ridge-shaped due to multiple eruptions along an approximately 8 km long southwest-northeast trending fissure at the summit of the volcano (Thórdarson and Larsen 2007). Magma compositions range from dacite to basaltic andesite (Thórdarson and Larsen 2007). Hekla is the second most active volcanic system in Iceland, having erupted 23 times since its first historical eruption in 1104 A.D. (Thórdarson and Larsen 2007). Of these 23 eruptions, 18 have occurred from the summit fissure and on radial fissures, while the remaining eruptions occurred along fissures further away from the central volcano (Thórdarson and Larsen 2007). Eruption frequency has increased in recent times, from 1-3 eruptions per century for the last 1100 years to 7 eruptions in the last century, with the most recent in 2000. Details of the four most recent eruptions of Hekla volcano are listed in Table 2.5.

Hekla is essentially aseismic between eruptions, making it difficult to constrain the location of a magma chamber(s) using seismicity (Soosalu and Einarsson 1997). Soosalu and Einarsson (2004) and Soosalu et al. (2005) were unable to find any evidence for strong S-wave attenuation at depths shallower than 14 km, and therefore suggest that any considerable molten volume must exist below this depth. This theory is supported by

Höskuldsson et al. (2007), though the idea of smaller magma pockets at depths of between 4 and 8 km is not ruled out. Soosalu and Einarsson (2004) and Soosalu et al. (2005) also state that shallower chamber depths of less than 4 km are also possible, however, a lack of significant geothermal activity and persistent seismicity at Hekla negates this theory (Soosalu and Einarsson 2004).

Table 2.5 Eruption duration and volumes for the four most recent eruption of Hekla volcano.

Year	Duration	Erupted Volume	Reference
1970	60 days	0.21 km^3	(Thórarinsson and Sigvaldason 1972; Höskuldsson et al. 2007)
1980-81	12 days	0.15 km^3	(Grönvold et al. 1983; Höskuldsson et al. 2007)
1991	54 days	0.15 km^3	(Guðmundsson et al. 1992; Höskuldsson et al. 2007)
2000	12 days	0.189 km^3	(Höskuldsson et al. 2007)

2.6.2 Ground deformation studies at Hekla volcano

Seismic unrest and changes in strain are two recorded short-term eruption precursors at Hekla volcano, the latter being measured using borehole strainmetres (Sturkell et al. 2006b; Höskuldsson et al. 2007). Additional monitoring studies conducted at Hekla volcano have shown that ground deformation monitoring is the only technique that allows for the measurement of long-term precursors to an eruption. Methods such as ‘‘dry-tilt’’ or short leveling arrays, GPS surveys and InSAR allow for the detection of ground deformation associated with magma migration at the volcano (Höskuldsson et al. 2007).

A larger number of ground deformation studies have been carried out on and around Hekla during the past several years. Table 2.6 lists the crustal deformation surveys that have been conducted since just prior to the 1981 eruption, as well as the magma chamber parameters determined from modelling of geodetic data, and Figure 2.13 shows the location of instrumentation used for these studies.

Table 2.6 Details of ground deformation surveys conducted at Hekla volcano since just prior to the 1981 eruption. Magma chamber parameters inferred from modelling of geodetic data are also listed.

Survey Type	Year	Magma Chamber Parameters	Reference
EDM [a] data	Before and after 1981 eruption	Depth: 7-8.5 km	(Kjartansson and Gronvold 1983)
GPS data	Spanning 1991 eruption	Depth: 9 km (+6,-7 km)	(Sigmundsson et al. 1992)
"Dry-tilt" data	1991 eruption and earlier	Depth: 5-6 km	(Tryggvason 1994)
Borehole Strain data	From 1991 eruption	Depth: 6.5 km (top at ca. 4-5 km)	(Linde et al. 1993)
		Considered localized strain recovery and preferred deeper location	(Jónasson et al. 2003)
Strain data	Re-interpretation	Depth: 11 km	(Sturkell et al. 2006b and references there in)
Strain data	Spanning 2000 eruption	Depth: 8 km	(Sigmundsson et al. 2001)
Strain, "dry-tilt", GPS and InSAR	Spanning 2000 eruption	Spherical source at 10 km depth, with radius of 2.1 km.	(Sturkell et al. 2007 [unpub])

[a] EDM – Electronic Distance Measurement

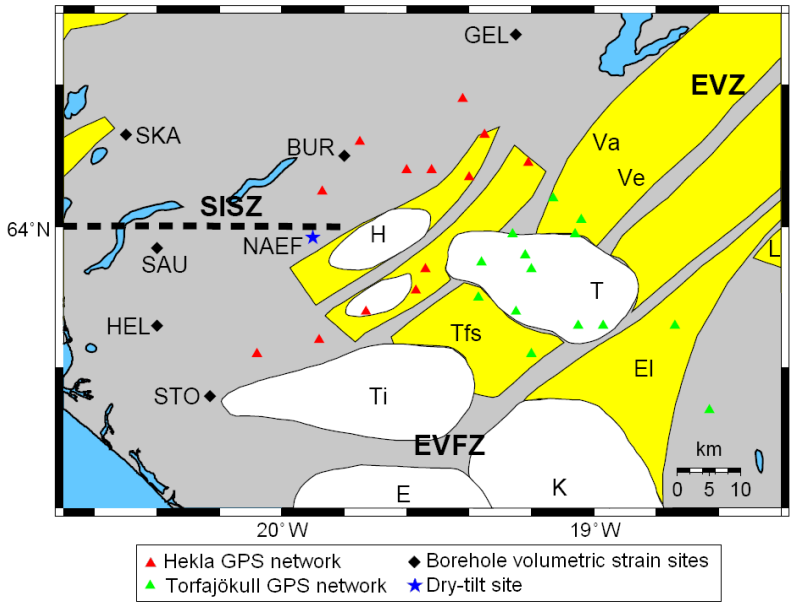


Figure 2.13 Map of south Iceland at the junction of the Eastern Volcanic Zone (EVZ), South Iceland Seismic Zone (SISZ) and Eastern Volcanic Flank Zone (EVFZ). The locations of instrumentation used for monitoring Hekla volcano, as well as the Torfajökull volcano GPS network, are marked on the map and explained in the figure key. Names of central volcanoes and fissure swarms as in Figure 2.2; bodies of water marked in blue.

Both the GPS and "dry-tilt" data collected at sites within the Hekla network have time series that indicate inflation after the 1991 eruption, followed by rapid deflation during the 2000 eruption, and re-inflation after this latest eruption (Figure 2.14) (LaFemina et al. 2005; Sturkell et al. 2006b). The study by LaFemina et al. (2005) showed that at a distance of 24 km from the Hekla volcano the radial component of displacement due to the active volcano is ~1 mm/yr, the approximate level of rate uncertainty for the 1994-2003 GPS study. It can therefore be concluded that since a number of the GPS sites used in this study are within 20-30 km of Hekla, these sites will be affected by the Hekla inflation and deflation cycles.

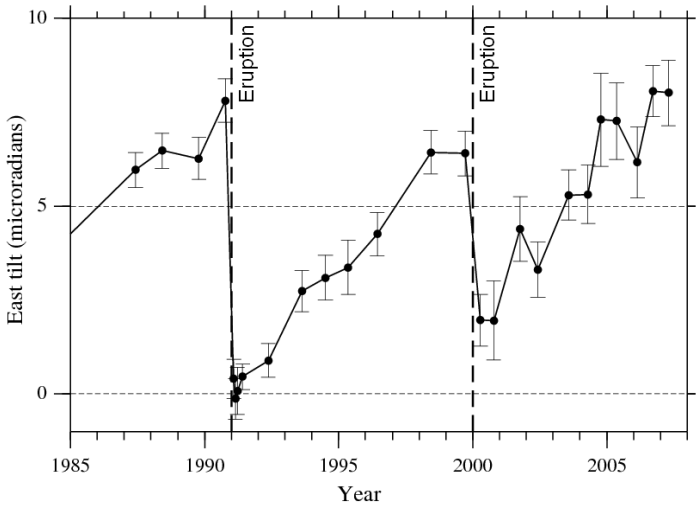


Figure 2.14 East-west tilt data from the Næfurholt (NAEF) ''dry-tilt'' station, which is located 11.5 km west of the summit of Hekla. This plot shows the radial component of deformation of the volcano (data provided by Erik Sturkell, Nordic Volcanological Centre). The tilt readings reflect mainly what is going on in a potential deep-seated magma chamber below Hekla (LaFemina et al. 2005). Repeated cycles of inflation (i.e. an increase in eastward tilt in the direction of Hekla) prior to an eruption and deflation (i.e. a decrease in tilt) during an eruption can be seen from the east-west tilt data (Sturkell et al. 2006b). Inflation occurs as the chamber below the volcano fills with magma, which is then drained during an eruption thus resulting in subsidence at the Earth's surface. The most recent tilt measurements made in 2007 show that the tilt has already exceeded the maximum value measured prior to the 1991 and 2000 eruptions.

2.7 Katla Volcano

Katla volcano which is covered by the Myrdalsjökull glacier is less than 5 km south of Torfajökull's southern-most boarder (Figure 2.4). It is one of Iceland's most active volcanoes, having experienced its last major eruption in 1918 (Larsen 2000). Katla's neighbouring volcano Eyjafjallajökull is approximately 25 km to the west of Katla (Figure 2.4), and showed an increase in seismic activity near the end of 1991, with earthquake swarms in 1994 and 1999 after a quiet period of several decades (Sturkell et al. 2003a). Katla and Eyjafjallajökull have a history of simultaneous activity, and in July 1999 a flash flood occurred from Katla's icecap along with changes in the seismicity, and the formation and deepening of ice cauldrons in the ice cap (Sigurðsson et al. 2000; Sturkell et al. 2003a). This increase in activity at these two volcanoes has led to renewed

scientific interest in the area, including regular GPS and "dry-tilt" surveys (Sturkell et al. 2003a; Sturkell et al. 2003b; Sturkell et al. 2008).

GPS measurements at points on the edge of Katla's caldera reveal steady uplift and horizontal displacement at a rate of up to 2 cm/yr between 2000 and 2004. Measurements show horizontal displacement of far field stations (>11 km) away from the caldera centre has been occurring at a rate of around 0.5 cm/yr (Sturkell et al. 2003b; Sturkell et al. 2008) (Figure 2.15). Sturkell et al. (2008) model the ground deformation at Katla as being due to a Mogi point source with a centre at 4.9 km depth beneath the northern part of the caldera. A magma chamber volume change of 0.01 km^3 is estimated due to magma accumulation between 1999 and 2004 (Sturkell et al. 2008). Sturkell et al. (2008) reiterate though that the depth estimation for the magma chamber could possibly be an overestimation due to unloading in the overlying icecap, and may be as shallow as 2-3 km.

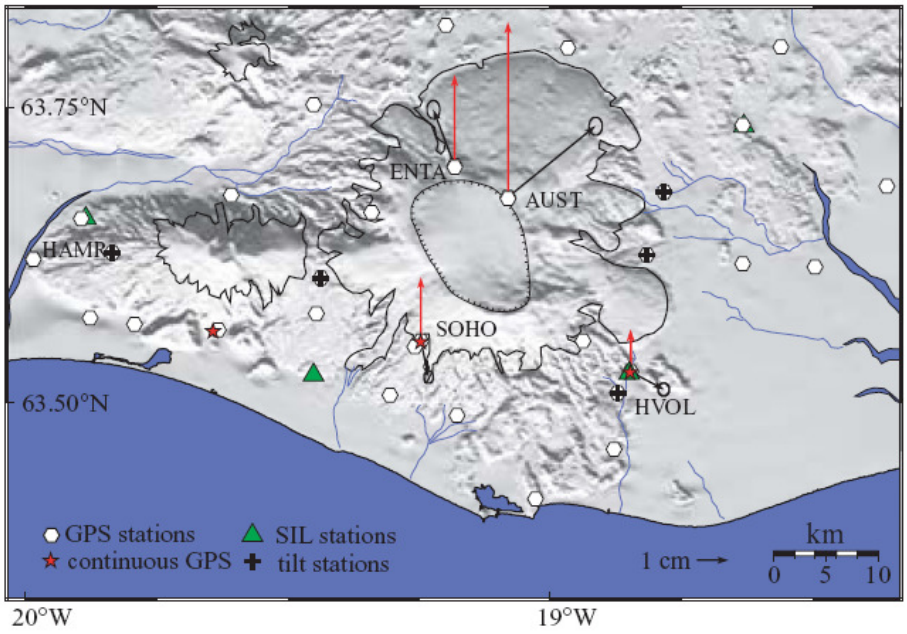


Figure 2.15 Displacements measured at the geodetic network around Katla volcano from June 2001 to June 2004 (from Pinel et al. 2007). Black arrows indicate horizontal displacements and red arrows indicate the vertical displacements of GPS sites AUST, ENTA, SOHO and HVOL, relative to HAMR. AUST experiences uplift rates of 2 cm/yr and horizontal displacements that are in general away from the volcano at rates of up to 1 cm/yr (Pinel et al. 2007). Icecaps are outlined and the Katla caldera is marked by a hatched line.

Later studies focusing on ice unloading at Katla volcano have shown that unloading alone cannot account for the observed horizontal velocities between 2000 and 2004, therefore confirming an injection of magma into the volcano plumbing system during this period (Hooper and Pedersen 2007; Pinel et al. 2007). Pinel et al. (2007) does show however that glacio-isostatic rebound due to the melting of Myrdalsjökull causes significant vertical and horizontal displacement in the area covered by the icecap, as well as surrounding areas (Figure 2.16). GPS sites to the south of Torfajökull and used in this study, such as KGIL, KKLO, SNAE and THRA, are between 15 and 30 km from the Katla caldera. Pinel et al. (2007) predict uplift rates for these sites of between 4 and 6 mm/yr due to glacio-isostatic adjustment (Figure 2.16b), and horizontal displacement rates of between 1.0 and 1.5 mm/yr (Figure 2.16c).

Sites used in this study that are situated south of Torfajökull volcano will therefore most likely have been affected by far-field ground deformation due to magma movement below Katla between 1999 and 2004, as well as by current rebound due to the melting of Myrdalsjökull. Though the rate of ground deformation and seismicity at Katla volcano has decreased significantly since 2004, the volcano is still in a state of unrest (Hooper and Pedersen 2007; Sturkell et al. 2008).

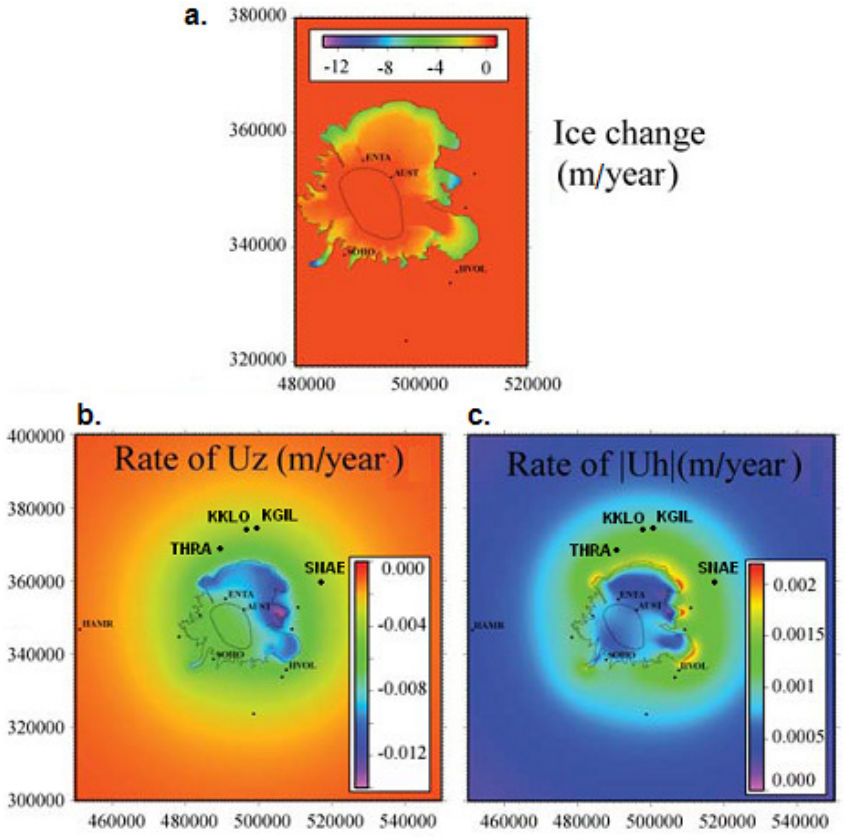


Figure 2.16 The rate of current displacement determined by Pinel et al. (2007) for the area covered by Myrdalsjökull, as well as surrounding areas. This displacement is determined by considering ice thinning over the past 115 years, and is calculated at a constant rate equal to the rate for the period 1999–2004. (a) Model used for the annual rate of ice elevation change at Myrdalsjökull; (b) Vertical displacement (Uz expressed in m/yr, the vertical axis (z) is considered to be directed downwards so unloading results in a negative vertical displacement); (c) Model of the horizontal displacement (|Uh| expressed in m/yr). The outline of Myrdalsjökull is marked, as well as the outline of the Katla caldera below the icecap. GPS sites used by Pinel et al. (2007), as well as those used in this study to the south of Torfajökull caldera are labelled.

2.8 Glacio-Isostatic Adjustment

During the last glaciation in Iceland, the Weichselian glaciation, the landmass was covered with an icecap that caused the downward flexure of the Earth's surface (Sigmundsson 1991). The ice age ended approximately 10,000 years B.P., at which stage post-glacial rebound/glacio-isostatic adjustment began to occur at a rapid rate and was completed within ~1000 years (Sigmundsson 1991). Studies by Sigmundsson (1991) of the icecap retreat and uplift history in Iceland have lead to the conclusion that Iceland is underlain by a very low viscosity asthenosphere. This observation can be explained by the fact that Iceland overlies a mantle plume on a mid-ocean ridge, and is therefore underlain by hot mantle material (Sigmundsson 1991).

It can therefore be concluded that current icecap thinning (change in mass balance) is leading to measurable elevation changes in Iceland. Sigmundsson (1991) estimates these elevation changes at 10 mm/yr around the Vatnajökull icecap. Pagli et al. (2007) predict vertical glacio-isostatic adjustment rates of ~5 mm/yr for areas 80 km away from Vatnajökull icecap (Figure 2.17a). These velocities are calculated using an axisymmetric Earth model with a 10 km thick elastic plate over a uniform viscoelastic half-space with a viscosity of 8 x 10^{18} Pa.s, and without any future changes in the rate of thinning. Slightly higher uplift rates are experienced if future changes in the rate of thinning are experienced (Figure 2.17b).

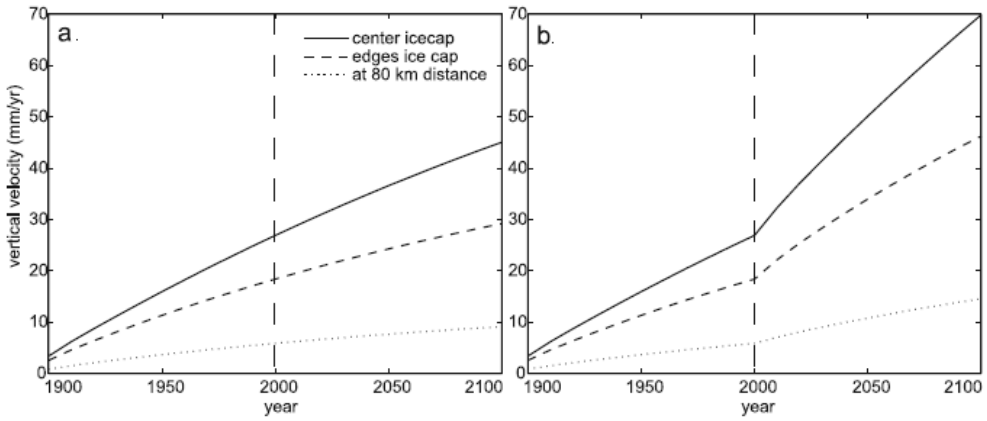


Figure 2.17 Vertical velocities predicted by Pagli et al. (2007) at Vatnajökull glacier (at the centre and edge of the icecap, as well as at a distance of 80 km from the centre). Lines show the (a) predicted vertical velocities assuming a thinning rate of 4 km^3 until 2100; and (b) the predicted velocities if thinning rates were to double in 2000 and remain constant until 2100.

Torfajökull is situated approximately 120 km from the centre of the Vatnajökull icecap, and has two of its own glaciers that are currently experiencing thinning (LaFemina pers comm. 2007). The vertical velocity signal measured at GPS sites around and within the volcano will most like be affected by this measurable glacio-isostatic adjustment.

In the following sections the collection, processing and modelling of GPS-derived site velocities is described, and conclusions are drawn by making use of information discussed in the above background chapter.

3 DATA COLLECTION & ANALYSIS

Global Positioning System (GPS) is increasingly being used to investigate plate boundary zone deformation. This monitoring technique is relatively inexpensive, and frequent measurements can be made at sites therefore making it an ideal technique. The unique on land expression of the Mid-Atlantic Ridge (MAR) in Iceland has been the focus of a number of GPS studies that are ongoing. Strain accumulation and deformation across the neovolcanic zone in northeast Iceland has been investigated by Foulger et al. (1992) and Heki et al. (1993); while episodic GPS surveys have been used by Sigmundsson et al. (1995), Jónasson et al. (1997), and LaFemina et al. (2005) to investigate strain accumulation across the WVZ and EVZ. Hreinsdóttir et al. (2001), Árnadóttir et al. (2006) and Keiding et al. (2008) used similar techniques to investigate crustal deformation and strain accumulation across the Reykjanes Peninsula plate boundary zone.

Active volcanoes and particularly calderas that are in a state of unrest are in general characterised by long-term uplift and/or subsidence over decades that can be monitored using GPS. Surface deformation is mostly the result of magmatic processes operating at depth such as the inflow or drainage of magma, or the degassing and crystallisation of magma within a chamber. The GPS data collected can provide information on the source of deformation, including the geometry and strength. High accuracy levels allow for changes due to low strain rates that mark the early stages of activity at a volcano to be measured (Dixon et al. 1997). Examples of volcanoes in Iceland that have been monitored for several years using high-precision geodetic measurements include Krafla, Askja, Grimsvötn, Hekla, Katla, Eyjafjallajökull and the Hengill-Hrómundartindur system (Sturkell et al. 2006b and references there in). Additional complex processes may, however, also contribute significantly to the ground deformation signal measured within a volcanic system. Such processes include geothermal activity within the volcanic system, the effects of which cannot be easily quantified.

3.1 Data Acquisition and Field Procedures

Episodic GPS surveys have been carried out at 16 sites around and within Torfajökull caldera between 2000 and 2006. These surveys are characterized by sampling every 15-30 seconds for an average of 3 to 5 days per year (minimum of 2 full (24 hr) UTC days) (Table 3.1). Due to the high cost of instrumentation only 2 to 3 sites are occupied at a time. As can be seen from Table 3.1**,** measurements made in 2000 for only three sites are included in the dataset, while in 2001 all sixteen sites were occupied. Therefore, for the remainder of this study these data will be referred to as the 2001-2006 dataset. I have obtained these data from Peter LaFemina at Pennsylvania State University and his colleague Erik Sturkell at the University of Iceland through a joint agreement with them and the organisation AfricaArray. Although I did not include GPS data collected in 2007 in my thesis due to time constraints, I participated in the 2007 field season (August 2007) in the Eastern Volcanic Zone (EVZ) in south Iceland in order to gain experience in carrying out a campaign GPS survey. Details of the field techniques used are outlined below.

Table 3.1 Table of the yearly survey record for GPS sites around and within Torfajökull caldera used in this study (x marks the years GPS data were collected). ISAK is a permanent site.

Sites	2000[a]	2001[b]	2002[c]	2003[d]	2004[e]	2005[f]	2006[g]
BLAU		x	x	x			x
DOMA		x	x	x			x
FROS	x	x	x	x	x		
HRAF	x	x	x	x	x		x
HRAS		x	x	x	x	x	x
ISAK		x	x	x	x	x	x
KGIL		x	x	x	x	x	x
KKLO		x	x			x	x
KROK		x	x	x			x
LAHR		x	x	x	x	x	x
LAUF		x	x	x	x		x
LIHO		x	x	x	x		x
SATU		x	x	x	x		x
SNAE		x	x	x	x	x	
THRA	x	x		x			x
THVE		x	x	x			x

GPS antennae (**A**) and receivers (**R**) used: [a] **A**: Micro (Trimble (TRM) Micro-centred L1/L2 antenna with groundplane (TRM 33429.00+gp)), Trimble 4000SST/SSE L1/L2 Geodetic (TRM14532.00); [b] **A**: Micro (Trimble (TRM) Micro-centred L1/L2 antenna with groundplane (TRM 33429.20+gp)), Choke (Trimble L1/L2 Choke Ring (TRM 29659.00)); **R**: TRM 4000 SSI & SST; [c] **A**: Micro, Choke; **R**: TRM 4000 SSI & SSE; [d] **A**: Micro, Choke, TurboRogue (AOAD/M_T Choke Ring (TurboRogue)); **R**: TRM 4000 SSI & SSE; [e] **A**: Micro, Zephyr (Zephyr Geodetic L1/L2 Antenna (TRM 41249.00)); **R**: TRM 4000 SSI, TRM 5700 ; [f] **A**: Micro, Zephyr; **R**: TRM 4000 SSI, TRM 5700 ; [g] **A**: Zephyr; **R**: TRM 4000 SSI, TRM 5700.

From 2000 to 2006, data were recorded using a number of different Trimble antennae and receivers (Table 3.1). All receivers are dual-frequency systems that can track up to 12 satellites simultaneously, and record both P code and carrier phase data (Dixon et al. 1997). For episodic GPS stations, antennae are mounted on wooden (Figure 3.1) or metal surveying tripods, or on spike mounts (a stainless steel pin with a fixed height, Figure 3.2) that are positioned and held fixed over the measuring point. In the case of semi-continuous (recording continuously for several days) and continuous GPS sites (recording continuously for several months to years), antennas are attached to metal structures that are securely anchored to the bedrock (Figure 3.3). Spikemounts and metal structures help to minimise movement, and therefore reduce the error in GPS measurements that would otherwise be introduced when using a wooden tripod that can expand and contract in the changing weather conditions, and is not always completely stable. It is important during a survey that sites be positioned on solid bedrock in order to reduce movement, with good sky visibility (Figure 3.1).



Figure 3.1 Episodic GPS site 3366 set up using a wooden tripod and antenna, with the receiver box in the foreground. GPS sites are chosen for their good sky visibility as seen in this picture, with elevation cut-offs from the surrounding topography of no more than 15º.

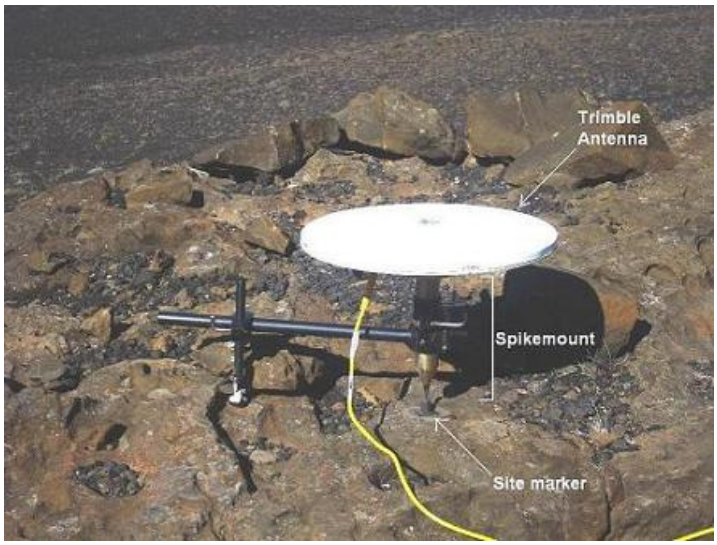


Figure 3.2 Episodic GPS site VALA. The antenna is set up on the bedrock using a spikemount, or stainless steel pin 0.08 m in height.



Figure 3.3 Permanent GPS site HEAL located on the flanks of Hekla volcano. A solar panel attached to a steel quadropod (left) and a wind generator (right) allow the GPS receiver to run continuously all year round.

Episodic sites are powered by batteries with solar panels attached, allowing the receivers to run for several days. Larger batteries are used at semi-continuous sites thus allowing the receivers to run for several days during bad weather, while wind generators are also used at continuous sites (Figure 3.3). If a loss of power is experienced due to prolonged bad weather, the system is designed to power down and up again when power becomes available (Dixon et al. 1997). Specific field procedures and instrumentation are described in Figure 3.4 - Figure 3.7 below, with sites occupied during the 2007 field season being used as examples:



Figure 3.4 Field procedures and GPS instrumentation: As at episodic GPS site BRSK, a wooden tripod is set up over the brass plate marking the location of the site, with the upper plate of the tripod set up as level as possible. The extendable legs of the tripod are securely tightened and rocks place on them in order to reduce movement. A tribrach and optical plummet are attached to the top of the tripod. The optical plummet is used to centre the tribrach over the brass plate and to level the tripod and tribrach.



Figure 3.5 Field procedures and GPS instrumentation: The GPS receiver and solar panels are attached to a power supply (i.e. battery). In the case of the episodic GPS site DROP (bottom right) only a small battery was used, while at the newly established semi-continuous site PSU001 (top left) a car battery was used due to the longer occupation time of the site.



Figure 3.6 Field procedures and GPS instrumentation: The antenna is then attached to the tripod using the tribrach, and connected to the receiver via a cable. The waterproof box that houses the receiver is kept at a distance to prevent multipathing, as seen above at episodic GPS site FAGR.



Figure 3.7 Field procedures and GPS instrumentation: The slant height from the base of the GPS antenna to the centre of the brass plate marking the site is measured at least three times using a measuring rod (as seen above for GPS site DOMA). The average height value is then used during processing. When the site is taken down, this slant height is re-measured and a check is made to see that the tripod is still levelled and centred. If the tripod has moved during the survey then the displacement is quantified and the motion accounted for during processing and analysis.

3.2 Data Analysis

3.2.1 Trimble R-utility and TEQC software

The raw GPS receiver files used in this study were in a Trimble proprietary format (dat, t00, r00 or t01) which cannot be directly inputted into the processing software, and therefore the raw files were first converted to a user-friendly format (e.g., RINEX 2). The Trimble R-utility software (UNAVCO 2005a) "runpkr00" was used to convert the *.t00, r00 and t01 data files to *.dat format, which is the input format for the software TEQC.

TEQC (UNAVCO 2007) is a free program developed by UNAVCO that allows for **T**ranslation, **E**diting and **Q**uality **C**hecking of GPS and GLONASS data. TEQC's translation function allows for *.dat GPS files to be converted to RINEX 2 (**R**eceiver **In**dependent **Ex**change) format files which in turn can be input into the GIPSY-OASIS II

software. RINEX format therefore allows for data from any receiver manufacturer (e.g., Trimble, Leica, etc.) to be converted to one format that can be used by any data processing software. TEQC also allows for RINEX files to be cut or spliced (combined) using the editing function, a useful tool when making sure one RINEX file exists per day, or when changing the header of a file. Finally, a quality check of the GPS data can be carried out using the software.

3.2.2 GIPSY-OASIS II Software

GIPSY-OASIS II software was developed at the Jet Propulsion Laboratory (JPL) and non-fiducial satellite orbit and clock files provided by JPL were used to process the data used in this study (Zumberge et al. 1997; Sella et al. 2002). **G**PS-**I**nferred **P**ositioning **Sy**stem and **O**rbit **A**nalysis **Si**mulation **S**oftware (GIPSY-OASIS II) allows for general satellite orbit analysis, accurate post-processing of collected GPS data, and exact determination of positions measured (UNAVCO 2005b). GIPSY-OASIS II corrects for a number of factors that affect the accuracy of GPS data, some of which are listed below (UNAVCO 2005b):

- The effects of the sun, moon, and planets on the satellites
- The effects of non-gravitational forces, which accounts for solar radiation pressure on the satellites
- Modelling of the known dynamics of the Earth, including solid Earth tides, precession nutation, polar motion, pole tides, and ocean loading
- General relativistic modelling of the phase and pseudorange delays which affect the GPS signal
- Wet and dry tropospheric delay modelling, including ray bending and Earth curvature, and the stochastic estimation of mapped zenith delays and clock biases
- Stochastic estimation of tropospheric gradients
- Resolving the integer cycle ambiguity in the observed carrier phases

GIPSY-OASIS II makes use of a technique called “precise point positioning”, a robust and economical method for processing GPS data and is described in detail by Zumberge et al. (1997). When using this processing method, instead of analysing all of the receiver data from a given network simultaneously, data from a globally distributed subset of

receivers (usually >45) are used to estimate receiver and transmitter parameters such as GPS orbits in an Earth-fixed frame and GPS clock corrections. These parameters are then fixed at certain predetermined values, and if the model has no spatially correlated parameters (e.g., tropospheric delay), then the transmitter parameters are broadcast in the navigation signal. These transmitter parameters in general have accuracies of a few centimetres or better, and are used to determine the parameters of the additional receivers one at a time.

These additional receivers are not included in the original subset because beyond a certain number of receivers the quality of the estimated transmitter parameters does not improve. Thus precise point positioning provides the opportunity to process a large number of GPS sites at a level of comparable accuracy, but lower computational cost than if all of the GPS data were processed simultaneously. Precise point positioning provides processed data with millimetre daily precision in the horizontal components and centimetre precision in the vertical (Zumberge et al. 1997).

The data for this study were analysed at the University of Miami via remote log-in from Pennsylvania State University, using procedures outlined by Dixon et al. (1993; 1997) as well as updated procedures from Sella et al. (2002). The important points highlighted by Sella et al. (2002) and LaFemina et al. (2005) are summarised below and in the section that follows.

The ionosphere-free combination of both undifferenced carrier phase and P code pseudorange data recorded at 30-s intervals are used for this study. A comprehensive antenna type and height file was compiled for all of the sites used in this study. This file is used during data processing. The recording time and Earth-centred position of each site (obtained from the RINEX files for each site) is also included in the change file. In order to improve the accuracy of the final velocity values calculated, an elevation angle cutoff of 10º (where data was available) and a horizontal atmospheric gradient model is used in order to improve the definition of these gradients and reduce their effect. All sites are corrected for ocean tidal loading and the carrier phase cycle ambiguities are estimated, not fixed.

3.3 Velocity Field

3.3.1 ITRF-2000 Reference Frame

Daily position estimates for sites (Figure 3.8) are generated with loose constraints using GIPSY-OASIS II, and are then transformed to the International Terrestrial Reference Frame 2000 (ITRF-2000) (Altamimi et al. 2002) using >45 collocated sites, depending on station availability, whose positions are defined in ITRF-2000 (i.e. precise point positioning). In the ITRF-2000 reference frame the horizontal velocities are relative to the NUVEL-1A no net rotation (NNR) reference frame (Argus and Gordon 1991) and the vertical velocities are relative to the centre of mass of the Earth (Dixon et al. 1997).

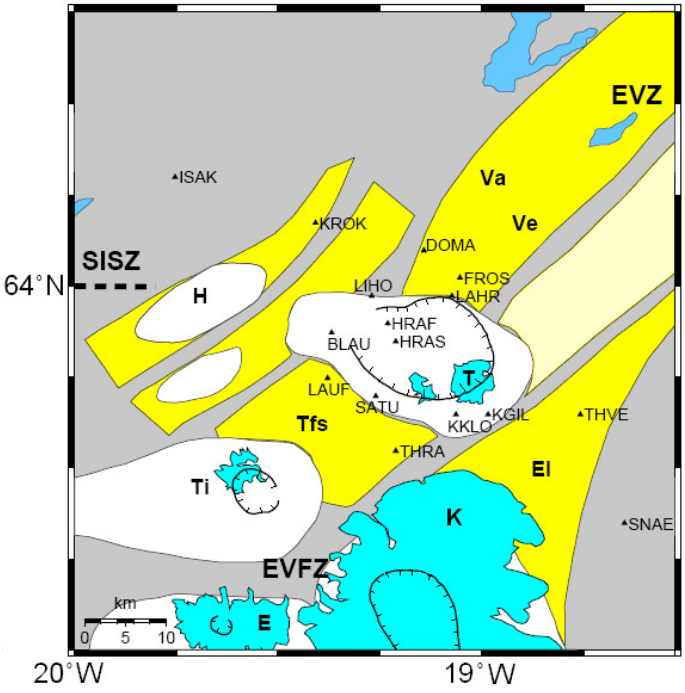


Figure 3.8 Map of 2001-2006 GPS sites used for this study (labelled black triangles) in south-central Iceland at the intersection of the Eastern Volcanic Zone (EVZ), the South Iceland Seismic Zone (SISZ) and the Eastern Volcanic Flank Zone (EVFZ). Names of central volcanoes and fissure swarms as in Figure 2.2, and detailed description as in Figure 2.4.

Position estimates with formal errors >9.9 m are removed from the database, as well as estimates that have a recording time of less than 8 hours. Daily position estimates are also corrected for any movement of the GPS antenna during a survey period by removing

the amount of movement from each estimate. This movement is quantified when an episodic site (typically a tripod) is taken down and the antenna height is re-measured and compared with the values recorded when the site was set up. Movement, if any, generally amounts to a few millimeters or less for the horizontal components. Tripods set up at sites KGIL, KKLO and LAHR moved during the 2005 survey period and site HRAS experienced movement during the 2004 survey (Table 3.2). Mean daily position uncertainties for this study are approximately 6 mm in latitude, 7 mm in longitude and 19 mm in vertical components.

Table 3.2 Sites that experienced tripod movement between 2001 and 2006. The survey year is listed, as well as the x and y-component of movement experienced (in millimetres).

	Survey	Tripod Movement	
Sites	Year	North (mm)	East (mm)
HRAS	2004	6.022	6.688
KGIL	2005	3.236	2.351
KKLO	2005	3.009	3.993
LAHR	2005	-9.500	0.000

Figure 3.9 shows time series of the ITRF-2000 daily position estimates (latitude, longitude and height) from 2000/1 to 2006 for each GPS site used in this survey (See Appendix 1 for position estimate data files for each site). Assuming that the change in position of each site is linear over time, velocity estimates (Table 3.3) are based on a weighted least squares straight line fit to the daily position estimates for a given period (black line in Figure 3.9). Points that lie off the best-fit line by more than 3 times the formal error are flagged as outliers but not removed from the database. These data are not used in the line fit. Uncertainties for these velocities are estimated using a model that accounts for the total time span over which measurements are made, the number and quality of the observation, and the existence of time-correlated ("coloured") noise (Mao et al. 1999). Mean rate uncertainties for this study are 0.8 mm/yr in latitude, 1.1 mm/yr in longitude and 2.3 mm/yr in vertical.

Data collected at ISAK in March and May 2000, and at KROK in May and October 2000 were not included in the time series for these sites (Figure 3.9f and i) as both are within 20 km of Hekla volcano and would therefore have been significantly affected by ground deformation directly after the February to March eruption. These sites would also have experienced coseismic displacement due to the June 2000 SISZ earthquakes. Data collected in 2000 at FROS, HRAF and THRA were however included in the time series

(Figure 3.9c, d and o) as the sites are >20 km from Hekla volcano and were occupied later in 2000 (FROS and HRAF were occupied in October 2000 and THRA in July 2000).

Only one position estimate for sites FROS (Figure 3.9c) and LAHR (Figure 3.9j) were determined in 2004 even though data were recorded for a number of additional days at these sites. These data were rejected during processing most likely due to a receiver clock error. The accuracies of each of these points is therefore high (i.e. small error), but the precision of the point is uncertain as it cannot be compared with any other data points for that recording period. Data collected at DOMA, HRAF and LAUF in 2006 have uncertainties that are an order of magnitude larger than those for position estimates determined during other years. This poor quality of data is most likely the result of snow on the antennae (Erik Sturkell pers. comm. 2008), and as a result these data were not included in the time series for these sites (Figure 3.9b, d and k).

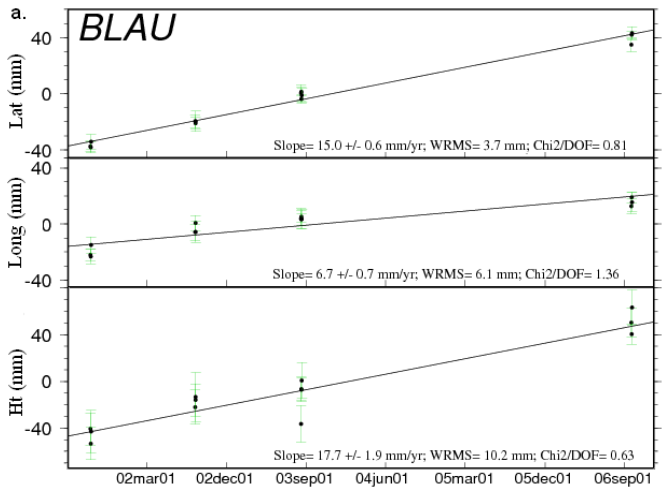


Figure 3.9a-p Coordinate time series for GPS sites in the southern EVZ used in this study (site locations shown in Figure 3.8). The time series show motion of sites in ITRF-2000 reference frame between 2000/1 and 2006. Site velocities are calculated from the slope of the weighted least squared line fit (solid line) through the data (i.e., position estimates, solid circles). Site velocity errors are determined from the uncertainties of the slope estimate, and accounts for uncorrelated and time-correlated noise, the total time span of observations, and the total number of observations (Mao et al. 1999). The time scale (x-axis) is labelled using the format YYmonthDD, where YY represents the year, DD represent the day of the month and the month of the year is abbreviated (e.g. 02mar01 represents 1st March 2002).

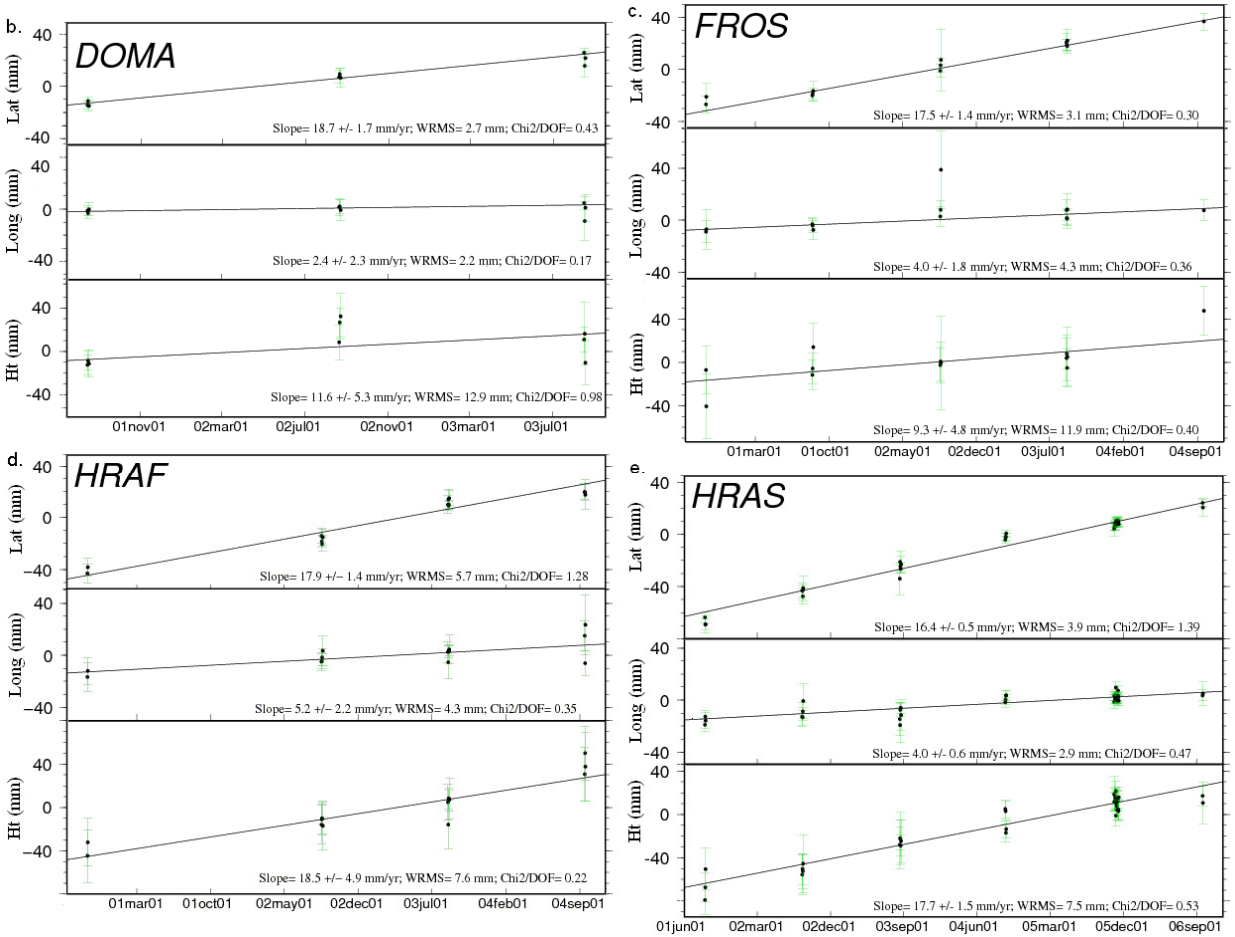


Figure 3.9a-p (continued)

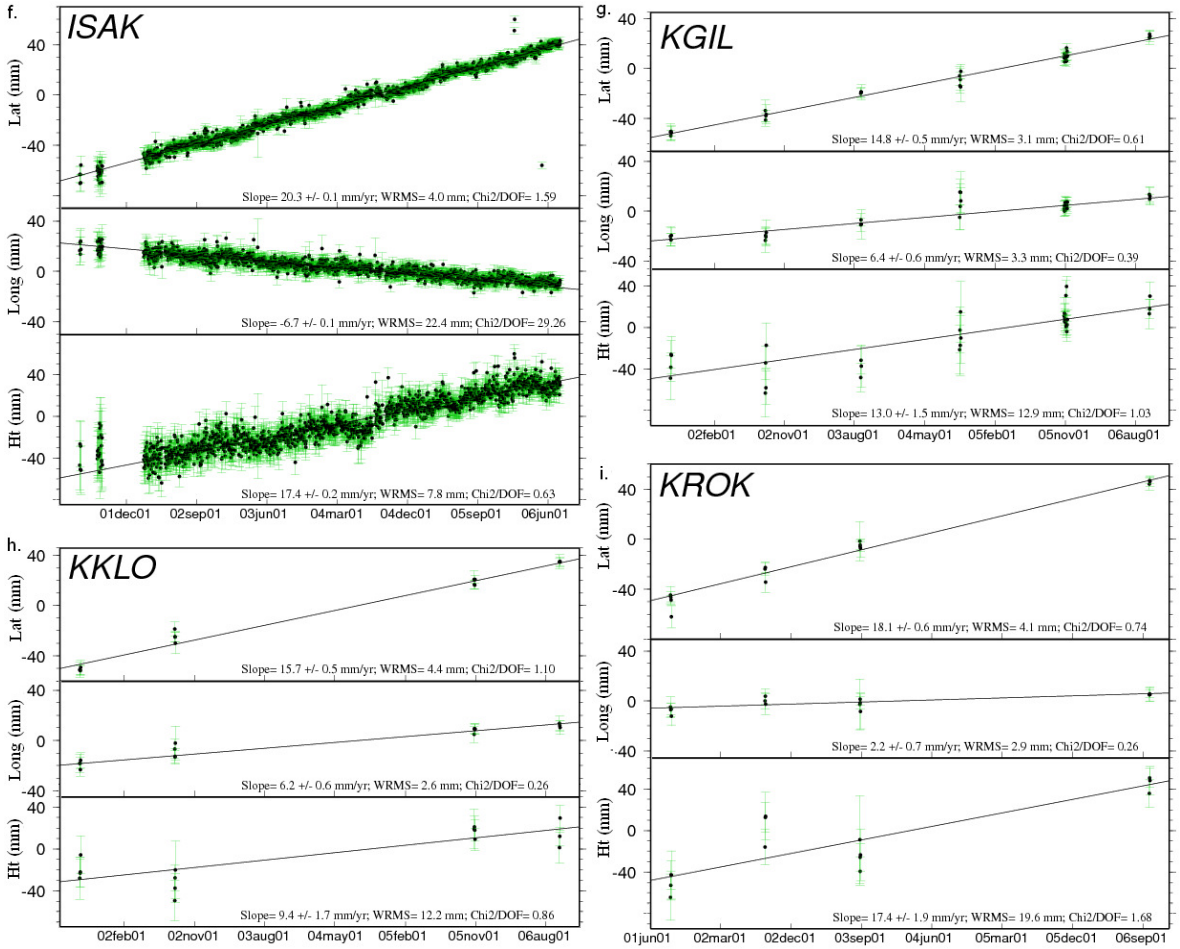


Figure 3.9a-p (continued)

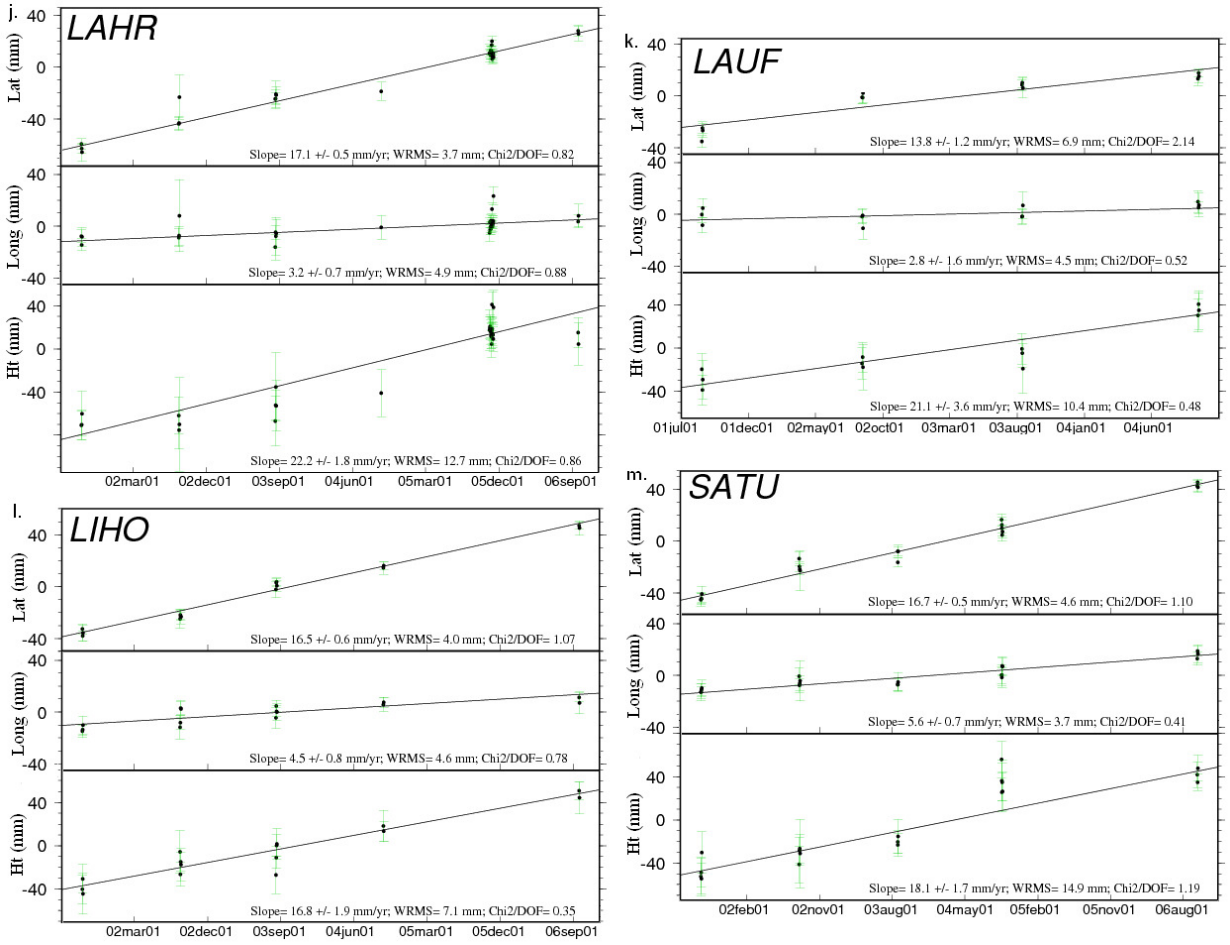


Figure 3.9a-p (continued)

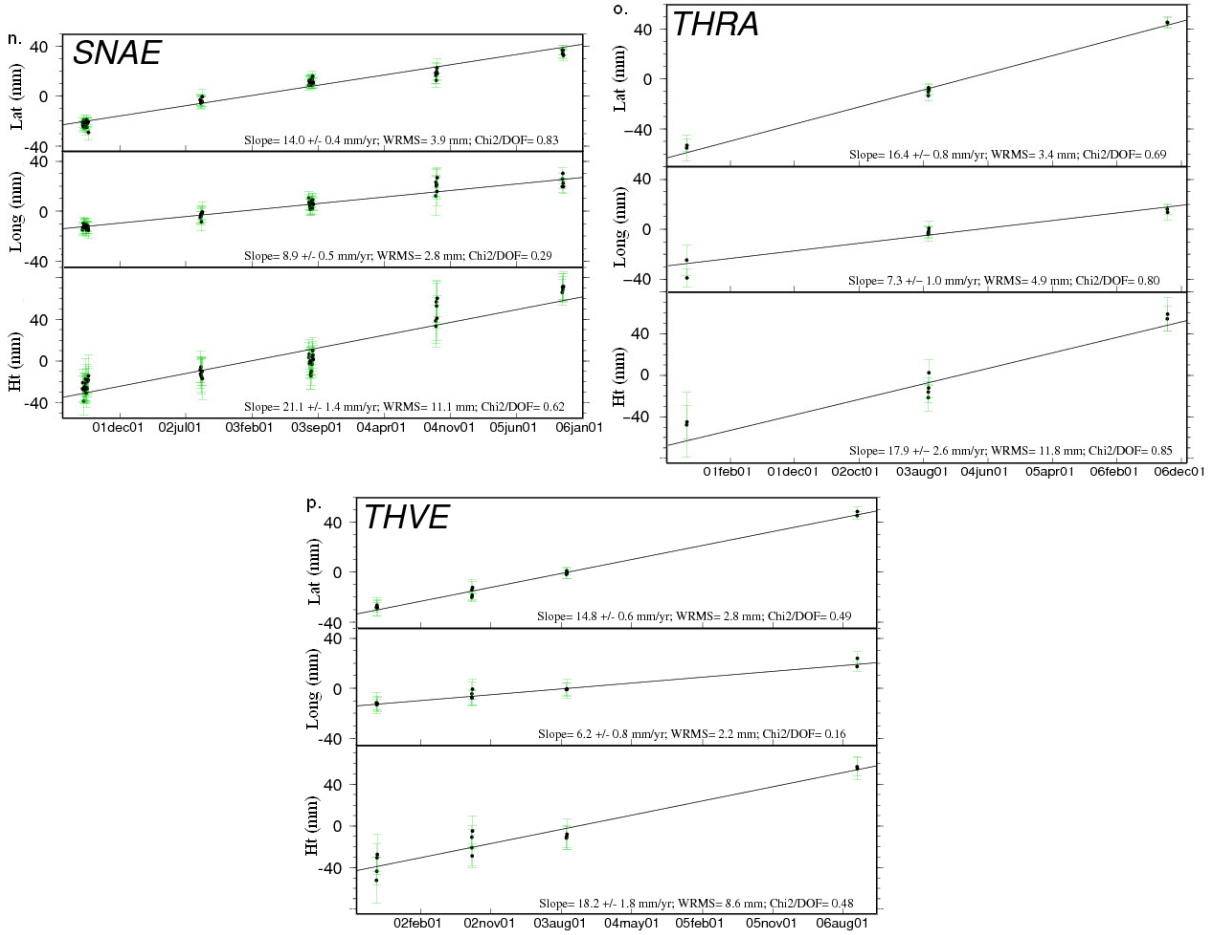


Figure 3.9a-p (continued)

Table 3.3 GPS velocities for this study relative to ITRF-2000 and the Weighted RMS Scatter.

Site	Lat (°)	Long (°)	L [a] (yrs)	N [b] (days)	Velocity [c] (mm/yr)			WRMS [d] (mm)		
					North	East	Vertical	North	East	Vertical
BLAU	63.95	-19.36	5.10	13	15.0±0.6	6.7±0.7	17.7±1.9	3.7	6.1	10.2
DOMA	64.04	-19.13	2.01	9	18.7±1.7	2.4±2.3	11.6±5.3	2.7	2.2	12.9
FROS	64.01	-19.04	3.95	13	17.5±1.4	4.0±1.8	9.3±4.8	3.1	4.3	11.9
HRAF	63.96	-19.22	3.94	14	17.9±1.4	5.2±2.2	18.5±4.9	5.7	4.3	7.6
HRAS	63.94	-19.2	5.10	36	16.8±0.5	4.3±0.6	17.7±1.5	2.4	2.7	7.5
ISAK	64.12	-19.75	5.13	1587	20.3±0.1	-6.7±0.1	17.0±0.2	4.0	22.4	7.8
KGIL	63.86	-18.97	5.12	33	14.8±0.5	6.4±0.6	13.0±1.5	3.1	3.3	12.9
KKLO[e]	63.86	-19.05	5.13	15	15.7±0.5	6.2±0.6	9.4±1.7	4.4	2.6	12.2
KROK	64.07	-19.4	5.11	13	18.1±0.6	2.2±0.7	17.4±1.9	4.1	2.9	19.6
LAHR	63.99	-19.06	5.10	28	17.1±0.5	3.2±0.7	22.2±1.8	3.7	4.9	12.7
LAUF	63.9	-19.37	3.08	12	13.8±1.2	2.8±1.6	21.1±3.6	6.9	4.5	10.4
LIHO	63.99	-19.26	5.10	15	16.5±0.6	4.5±0.8	16.8±1.9	4.0	4.6	7.1
SATU	63.88	-19.25	5.12	19	16.7±0.5	5.6±0.7	18.1±1.7	4.6	3.7	14.9
SNAE	63.74	-18.63	4.24	53	14.0±0.4	8.9±0.5	21.1±1.4	3.9	2.8	11.1
THRA	63.82	-19.2	6.21	8	16.4±0.8	7.3±1.0	17.9±2.6	3.4	4.9	11.8
THVE	63.86	-18.74	5.11	13	14.8±0.6	6.2±0.8	18.2±1.8	2.8	2.2	8.6

[a] Length of the time series; [b] Number of station days; [c] Velocity relative to ITRF-2000 ± 1 standard error;
[d] Weighted root mean squared scatter of daily position estimates about a best-fit straight line;
[e] Combination of site names KLOF (2001-2002) and KKLO (2005-2006).

3.3.2 Stable Eurasia Reference Frame

In order to better investigate local deformation signals the horizontal site velocities are plotted relative to the Euler vector for a stable Eurasian plate in ITRF-2000 (Altamimi et al. 2002) (Table 3.4 and Figure 3.10).

Table 3.4 Horizontal GPS velocities relative to stable Eurasia and vertical velocities for the period 2001-2006.

Site	Lat (°)	Long (°)	L (yrs)	N (days)	Velocity[c] (mm/yr)		
					North	East	Vertical
BLAU	63.95	-19.36	5.10	13	0.04 ± 0.64	-2.19 ± 0.71	17.7±1.9
DOMA	64.04	-19.13	2.01	9	3.73 ± 1.71	-6.52 ± 2.3	11.6±5.3
FROS	64.01	-19.04	3.95	13	2.53± 1.42	-4.95 ± 1.81	9.3±4.8
HRAF	63.96	-19.22	3.94	14	2.93 ± 1.42	-3.73 ± 2.20	18.5±4.9
HRAS	63.94	-19.2	5.10	36	1.83 ± 0.55	-4.64 ± 0.62	17.7±1.5
ISAK	64.12	-19.75	5.13	1587	5.35 ± 0.16	-15.44 ± 0.25	17.0±0.2
KGIL	63.86	-18.97	5.12	33	-0.17 ± 0.55	-2.62 ± 0.62	13.0±1.5
KKLO	63.86	-19.05	5.13	15	0.73 ± 0.55	-2.8 ± 0.62	9.4±1.7
KROK	64.07	-19.4	5.11	13	3.14 ± 0.64	-6.64 ± 0.71	17.4±1.9
LAHR	63.99	-19.06	5.10	28	2.13 ± 0.55	-5.75 ± 0.71	22.2±1.8
LAUF	63.9	-19.37	3.08	12	-1.16 ± 1.22	-6.11 ± 1.61	21.1±3.6
LIHO	63.99	-19.26	5.10	15	1.53 ± 0.64	-4.4 ± 0.81	16.8±1.9
SATU	63.88	-19.25	5.12	19	1.73 ± 0.55	-3.35 ± 0.71	18.1±1.7
SNAE	63.74	-18.63	4.24	53	-0.98 ± 0.45	-0.25 ± 0.52	21.1±1.4
THRA	63.82	-19.2	6.21	8	1.43 ± 0.83	-1.68 ± 1.01	17.9±2.6
THVE	63.86	-18.74	5.11	13	-0.18 ± 0.64	-2.88 ± 0.81	18.2±1.8

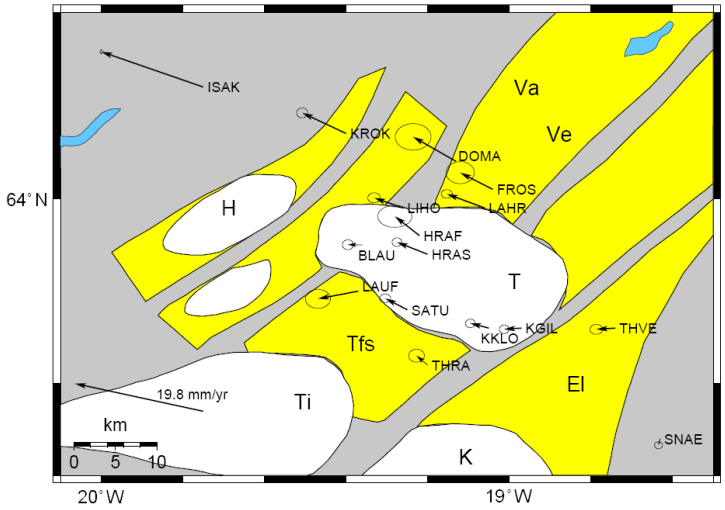


Figure 3.10 GPS-derived horizontal velocity field relative to stable Eurasia for the period 2001-2006. The far-field plate motion rate and direction relative to the Eurasia plate is indicated by the thick black arrow in the lower-left corner (i.e., 19.8 mm/yr in a direction of N78°W, Sella et al. (2002)). Central volcanoes are outlined [Torfajökull (T), Hekla (H), Tindfjallajökull (Ti), Katla (K)], and their fissure swarms are shaded yellow [Vatnaöldur (Va), Veidivötn (Ve) and Torfajökull (Tfs) and Eldgjá fissure swarm (El)]. Bodies of water are in blue.

As these velocity vectors in Figure 3.10 are plotted relative to a stable Eurasia plate, any site on the Eurasia plate would therefore show no residual motion within data uncertainties. Site SNAE to the southeast of the study area (closest to the Eurasia plate) shows some residual motion, whereas velocity vectors for other sites point in the direction of spreading (N78°W) and increase in rate as you move further away from the Eurasia plate (i.e. as you move to the northwest). This observation is in agreement with known Holocene fissuring northeast and southwest of the caldera and the results of LaFemina et al. (2005). The horizontal velocities are intermediate in rate compared to the full plate spreading rate (~18-20 mm/yr, DeMets et al.(1994) and Sella et al. (2002)), and are dominated by elastic strain accumulation across the EVZ during this interrifting period. Localized variations in horizontal rate and direction can also be seen. Velocity vectors determined for sites closest to Hekla show a deflection from predicted motion. This is most pronounced at sites BLAU and LAUF, with a variation in direction at both sites, and a significant reduction in the rate at BLAU. Site KGIL in the southeast of Torfajökull volcano also shows a deviation in angle from the predicted spreading direction.

The vertical rates plotted in Figure 3.11 on average exceed 17 mm/yr. Sites KKLO and KGIL located in the southeastern part of Torfajökull show reduced uplift rates compared to the other sites. Sites FROS and DOMA to the north of the volcano, within an active fissure swarm area, also show reduced uplift compared to the average rate, though the uncertainties for the velocity vectors for these sites are relatively large. Due to a recent discovery of a processing problem with the vertical dataset (that has no effect on the horizontal dataset), the legitimacy of the rates plotted in Figure 3.11 and listed in Table 3.4 is not certain, and therefore the vertical rates will not be discussed in the remaining chapters.

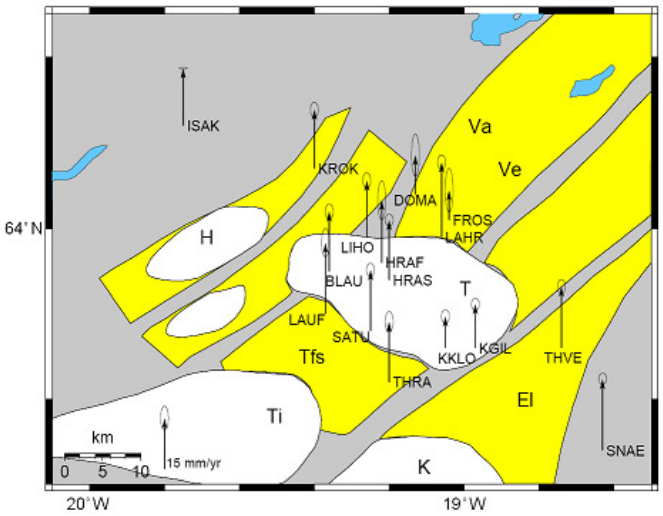


Figure 3.11 GPS-derived vertical velocity field for the period 2001-2006. Names of central volcanoes and fissure swarms as in Figure 3.10.

The horizontal rates calculated in this study for 2001-2006 are compared with rates calculated by LaFemina et al. (2005) for the period 1994-2003 (Table 3.5), and a plot of velocities for the two datasets is shown in Figure 3.12. There is a general agreement between the two datasets for velocity vectors recorded at the same site, with any discrepancies being most-likely due to changes in Hekla deformation over the two time periods. The 1994-2003 dataset spans the more complex inflation-deflation-inflation cycle of Hekla due to its eruption in 2000, while the volcano has experienced inflation during the inter-eruptive period from late 2000 to 2006. The 1994-2003 and 2001-2006 datasets are dealt with separately for the remainder of this study due to reference frame differences. For the earlier dataset, position estimates are transformed into ITRF-1997

(Boucher et al. 1999), and site velocities are calculated relative to stable Eurasia using the plate angular velocities of Sella et al (2002) which are relative to ITRF-1997, while for the later dataset the ITRF-2000 reference frame (Altamimi et al. 2002) is used.

Table 3.5 Horizontal GPS velocities relative to stable Eurasia and vertical velocities for the period 1994-2003 (data from LaFemina (2005)). Velocities are corrected for coseismic displacement caused by the June 2000 SISZ earthquakes, determined by LaFemina (2005).

Sites	Lat (°)	Long (°)	Velocity (mm/yr)		
			North	East	Vertical
BREI	64.18	-18.39	-0.69 ± 0.91	-7.63 ± 0.93	10.2 ± 2.3
BRSK	63.94	-19.54	-1.56 ± 0.91	-3.56 ± 1.52	4.1 ± 2.2
BULA	63.80	-18.56	-1.38 ± 0.83	-0.64 ± 1.31	5 ± 1.9
D350	64.18	-19.42	1.84 ± 0.73	-13.89 ± 1.11	7.7 ± 1.7
D353	64.13	-19.35	2.04 ± 0.64	-9.83 ± 0.81	8.3 ± 2.2
D356	64.09	-19.21	1.53 ± 0.61	-8.48 ± 0.93	6.3 ± 2.1
D359	64.10	-19.10	-0.07 ± 0.46	-8.6 ± 0.62	9 ± 2.4
D361	64.08	-19.05	-0.27 ± 0.55	-8.72 ± 0.62	5.8 ± 1.8
D364 (FROS)	64.01	-19.04	0.33 ± 0.46	-7.45 ± 0.91	3.8 ± 4
D365	63.99	-19.02	0.93 ± 1.52	-6.96 ± 2.1	-0.1 ± 2.3
D369	63.98	-18.76	0.42 ± 0.37	-2.83 ± 1.11	8.1 ± 3
D371	63.96	-18.67	-0.98 ± 0.61	-3.35 ± 0.64	6 ± 3.1
D372	63.93	-18.63	-0.48 ± 0.83	-3.57 ± 1.11	7.9 ± 2.5
DROP	63.91	-19.57	-0.26 ± 1.12	-4.16 ±1.21	7.6 ± 3.7
ELDH	63.68	-18.36	-1.39 ± 0.45	-1.53 ± 0.62	-2.4 ± 4.6
GALT	64.00	-18.27	-1.69 ± 0.52	-5.03 ± 1.22	9 ± 1.6
ISAK	64.12	-19.75	1.25 ± 0.46	-12.04 ± 0.62	7.7 ± 2.3
JOKU	64.31	-18.24	-0.09 ± 0.54	-12.72 ± 1.21	12.6 ± 7.6
KELD	63.82	-20.08	1.46 ± 1.12	-5.17 ± 1.41	0.7 ± 4.1
KGIL	63.86	-18.97	0.93 ± 1.02	-4.02 ± 3.9	5.7 ± 9.2
KROK	64.07	-19.40	0.04 ± 0.83	-10.14 ± 0.91	5.7 ± 4.4
KVIS	64.21	-18.72	-0.98 ± 0.55	-9.55 ± 0.71	11.1 ± 1.7
LJOS	64.25	-18.49	-0.69 ± 0.54	-8.99 ± 1.11	12.4 ± 1.8
MAEL	63.80	-18.97	0.53 ± 0.81	-3.55 ± 1.02	7.3 ± 5.3
NLAN	64.22	-18.21	-0.59 ± 0.62	-7.96 ± 1.02	8.5 ± 1.6
OD17	64.13	-19.12	0.13 ± 0.52	-11.88 ± 0.64	6.3 ± 1.5
PALA	63.88	-19.73	2.45 ± 0.91	-6.84 ± 1.12	1.7 ± 2.3
SATU	63.88	-19.25	-1.27 ± 0.81	-5.95 ± 3.51	11 ± 5.7
SKHR	63.84	-19.88	2.15 ± 1.12	-6.42 ± 1.21	2.3 ± 3.8
SLAN	64.11	-18.46	1.01 ± 0.64	-7.15 ± 0.71	3.6 ± 2.3
SNAE	63.74	-18.63	-0.98 ± 0.83	0.25 ± 0.91	12 ± 3.3
TEIG	63.88	-17.76	-3.1 ± 0.61	-2.1 ± 0.83	9.9 ± 2.8
THRA	63.82	-19.20	1.33 ± 0.61	-5.08 ± 1.02	4.8 ± 3.1
THVE	63.86	-18.74	-4.48 ± 1.42	-2.38 ± 1.51	15.5 ± 7.9
VALA	64.08	-19.52	0.94 ± 1.32	-11.01 ± 1.81	9.1 ± 1.9

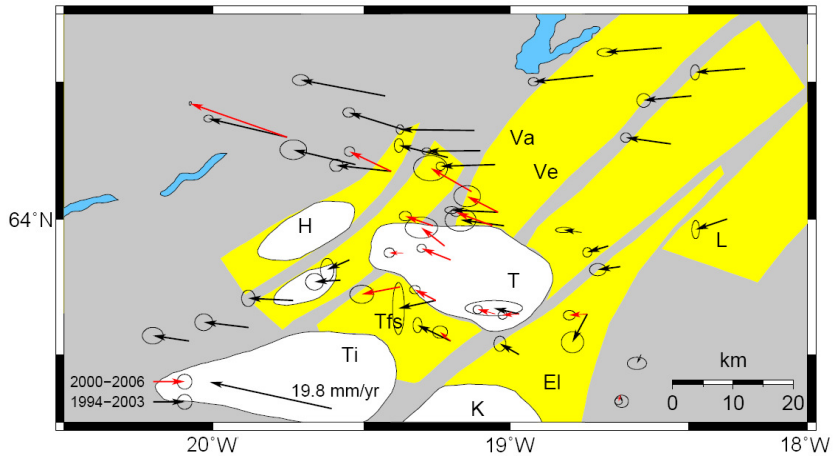


Figure 3.12 GPS-derived horizontal velocity field relative to stable Eurasia. Red arrows indicate velocities for the period 2001-2006 (this study), and black arrows the velocities for 1994-2003 corrected for coseismic displacement caused by the June 2000 SISZ earthquakes (data from LaFemina (2005)). Symbols and names of central volcanoes and fissure swarms as in Figure 3.10.

In order to better investigate the processes acting across the plate boundary in southeast Iceland, velocity profiles are considered using the component of velocity parallel to the REVEL plate motion direction, N78°W (Sella et al. 2002). Three profiles spanning the EVZ are considered (Figure 3.13).

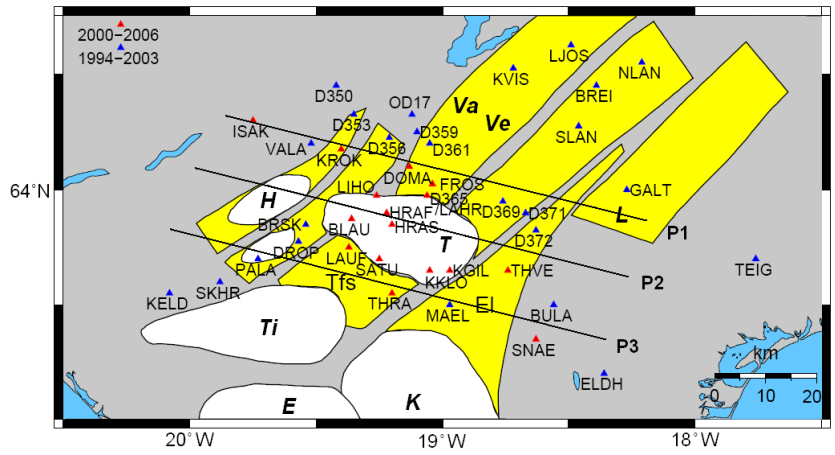


Figure 3.13 Map of GPS sites in south-central Iceland used in this study, with sites used to collect data from 1994-2003 marked by blue triangles (LaFemina et al., 2005 and this study) and sites occupied from 2001 to 2006 marked with red triangles (this study). Three profiles parallel to the spreading direction will be considered (black lines, P1, P2 and P3). Sites within 10 km of each profile are used (~5 km on either side of the profile). Names of central volcanoes and fissure swarms as in Figure 3.10.

Profile 1 shown in Figure 3.13 consists of sites located north of Torfajökull volcano within the EVZ; profile 2 spans Torfajökull volcano as well as the Eldgjá fissure swarm; and profile 3 consists of sites south of Torfajökull volcano within the EVFZ. Only sites located within 10 km of a profile are used (~5 km on either side of the profile). Data collected by LaFemina et al. (2005) for the period 1994-2003 are also considered. The vertical GPS-derived velocities and horizontal velocity components parallel to the spreading direction (N78°W) along all three profiles are shown in Figure 3.14.

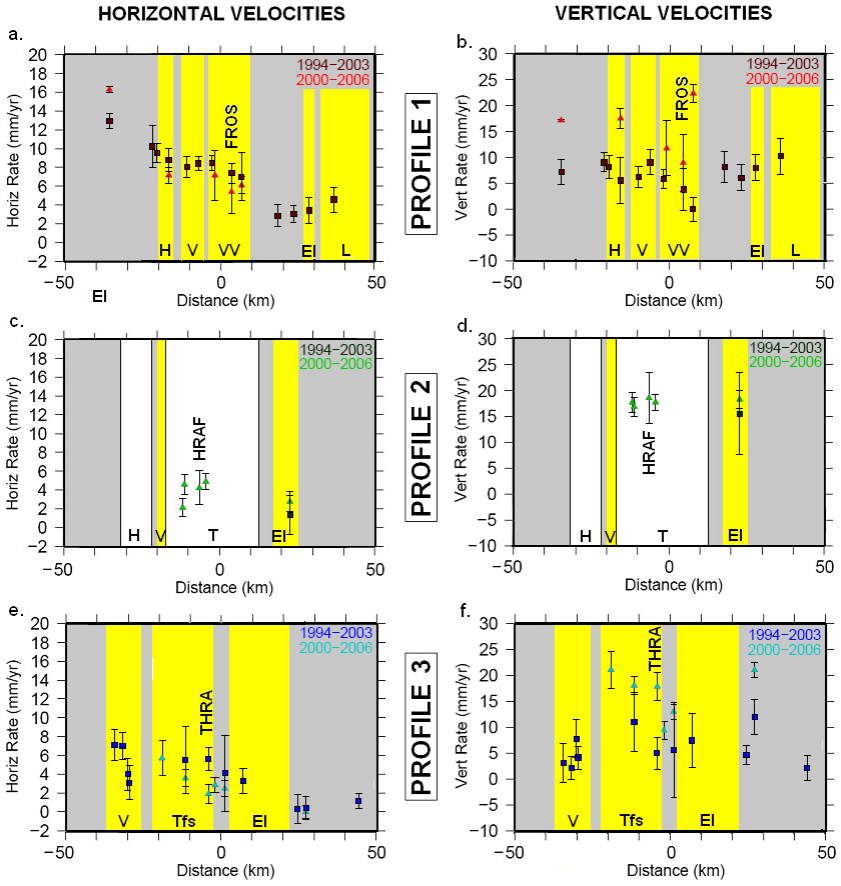


Figure 3.14 Horizontal (a,c,e) and vertical (b,d,f) GPS-derived velocities relative to stable Eurasia for sites within 10 km of 3 profiles taken across the EVZ (Figure 3.13). Data plotted includes that collected between 1994 and 2003 (LaFemina et al. 2005) and between 2001 and 2006 (this study), and is indicated by the colour of the plotted data. The horizontal velocities plotted are the rate components parallel to the plate motion direction (N78°W). Error bars are 1-sigma uncertainties for the magnitude (i.e., combined longitude and latitude components). The central sites for each profile are labelled. The location of fissure swarms is marked in yellow [Vatnaöldur and Veidivötn (VV), Eldgjá (El), Lakagigar (L), Torfajökull (Tfs), and those associated with Hekla (H) and Vatnafjöll (V) volcano], and central volcanoes in white [Torfajökull (T) and Hekla (H)].

In Figure 3.14**,** profile 1 is made up of 13 sites from the 1994-2003 dataset and 5 sites from the 2001-2006 dataset; profile 2 which passes through Torfajökull caldera contains only 5 sites from 2001-2006; and profile 3 contains 7 sites from the 1994-2003 dataset and 6 sites from the 2001-2006 dataset. The effect due to spreading is seen in the horizontal velocities plotted for profiles 1 and 3 (Figure 3.14a and e), with a general trend of increasing velocities from right (southeast) to left (northwest) on the plot, away from the stable Eurasia plate. This trend is not seen in profile 2 (Figure 3.14c) mainly due to limited data coverage over the entire length of the profile. The high rates of vertical uplift (average of 16.66 mm/yr) are evident in Figure 3.14b, d and f. These horizontal velocity profiles will be modelled in the following chapter using simple two-dimensional elastic half-space models in an attempt to interpret the observed ground deformation.

4 MODELLING TECHNIQUES

Ground deformation measurements at sites around Torfajökull volcano show the superposition of a number of different volcanic and tectonic processes. These processes include; 1) the long-term plate spreading signal across the EVZ (Einarsson 1991; Sigmundsson et al. 1995; Jónasson et al. 1997; LaFemina et al. 2005) (Section 2.2.2); 2) the continuing inflation of Hekla volcano to the northwest of Torfajökull (Sturkell et al. 2006b) (Section 2.6); 3) the inflation of Katla volcano to the south of Torfajökull from 1999 to 2004 (Sturkell et al. 2003a; Soosalu et al. 2006a; Pinel et al. 2007; Sturkell et al. 2008) (Section 2.7); and 4) subsidence within Torfajökull volcano (A. Hooper pers comm. 2007; E. Sturkell pers comm. 2007) (Section 2.5). As a result, modelling of GPS data collected from 2000/1 to 2006 will require a combination of individual models to account for all of the above mentioned processes, though limited data coverage may make distinguishing between the effects of all of these processes difficult.

Extensive geothermal activity within Torfajökull caldera is expected to add to the measured ground deformation within the volcano as has been seen at other volcanoes (e.g., Campi Flegrei, Bonafede (1991)), though the amount of which cannot be quantified due to limited data coverage within the volcano. Glacio-isostatic adjustment is not accounted for during modelling as it is assumed that sites are sufficiently far from the Vatnajökull and the Myrdalsjöull icecap covering Katla volcano that the rebound signal does not significantly affect the horizontal velocities measured. It is also assumed that melting of the two small glaciers at Torfajökull does not significantly affect the measured horizontal velocities. I will describe the modelling methods used to solve and correct for these processes in the following section.

Studies have shown that plate motion in Iceland is accommodated by repeated lateral dyke injection during rifting events (Walker 1960; Sigurðsson and Sparks 1978;

Guðmundsson 2000). The spreading ridge (fissure swarm) that passes through the study area will therefore be modelled as a tensile fault in an elastic half-space following the formulation of Okada (1985). In order to model the surface deformation associated with elastic strain accumulation associated with the spreading ridge, the data will first have to be corrected for motion caused by the deformation of active volcanoes in the study area. In most cases, ground deformation at a volcano is modelled in terms of a mathematically simple dilating spherical source, or Mogi "point" source, in a homogeneous elastic half-space (Mogi 1958). The deep magma chamber below Hekla volcano (Sturkell et al. 2006b and references there in) and shallower chamber below Katla (Sturkell et al. 2003a; Sturkell et al. 2008) will both be modelled as Mogi sources, as well as the proposed cooling chamber in the western part of Torfajökull caldera (Sæmundsson 1972; Soosalu and Einarsson 1997; 2004; Lippitsch et al. 2005).

4.1 Equations used for Modelling

4.1.1 Surface deformation due to a tensile fault in a half-space

The deformation due to the spreading ridge will be modelled using a tensile fault, i.e., a vertical fault that experiences no dip-slip or strike-slip movement but instead experiences only opening, as the displacements are the same as that due to a vertical dyke. Okada (1985) uses the displacement field due to an arbitrary dislocation across a surface in an isotropic medium to develop a set of equations for the surface displacements due to a point source. By substituting in new variables and integrating Okada (1985) also derives the equations for the surface displacements due to a finite rectangular source of length L and width W.

In the case of a tensile fault (i.e., a fault experiencing fault normal movement) with length $2L$ and width W in an isotropic homogeneous elastic half-space (Figure 4.1), the following simplified equations were derived by Okada (1985) for the surface displacements (u_x, u_y and u_z) due to a fault located at a point (0,0,z). For this study the medium constants (Lame parameters) λ and μ are taken to be equal, which is a good approximation for rocks and allows for simplification of the analytical solution, and a dip, δ of 90° is considered; the effects of which are displayed in Figure 4.2.

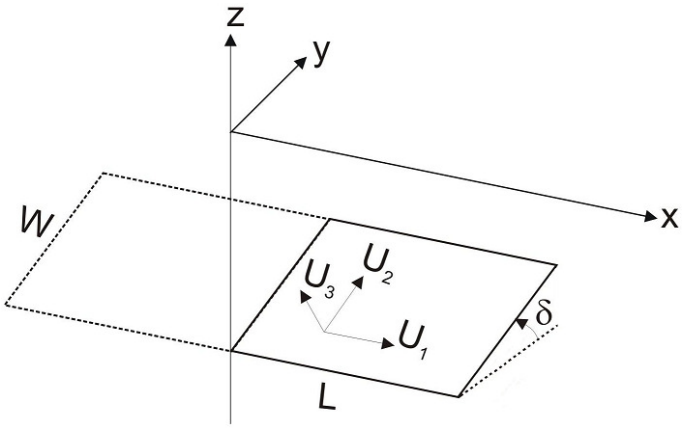


Figure 4.1 Finite rectangular fault in an elastic half-space (the region of $z \leq 0$) with length $2L$ (dashed line) and width W (Okada 1985). The fault is at a depth of $z<0$, with strike-direction parallel to the x-axis and a dip of δ. U_1, U_2 and U_3 are vectors representing the movement of the hanging-wall block relative to the foot-wall block (for a tensile fault only U_3, fault-normal movement, is considered).

$$u_x = \frac{U_3}{2\pi}\left[\frac{q^2}{R(R+\eta)} - I_3 \sin^2\delta\right] \tag{4.1}$$

$$u_y = \frac{U_3}{2\pi}\left[\frac{-\tilde{d}q}{R(R+\xi)} - \sin\delta\left\{\frac{\xi q}{R(R+\eta)} - \tan^{-1}\frac{\xi\eta}{qR}\right\} - I_1 \sin^2\delta\right] \tag{4.2}$$

$$u_z = \frac{U_3}{2\pi}\left[\frac{\tilde{y}q}{R(R+\xi)} + \cos\delta\left\{\frac{\xi q}{R(R+\eta)} - \tan^{-1}\frac{\xi\eta}{qR}\right\} - I_5 \sin^2\delta\right] \tag{4.3}$$

and

$$I_1 = \frac{\mu}{\lambda+\mu}\left[\frac{-1}{\cos\delta}\frac{\xi}{R+\tilde{d}}\right] - \frac{\sin\delta}{\cos\delta} I_5$$

$$I_2 = \frac{\mu}{\lambda+\mu}\left[-\ln(R+\eta)\right] - I_3$$

$$I_3 = \frac{\mu}{\lambda+\mu}\left[\frac{1}{\cos\delta}\frac{\tilde{y}}{R+\tilde{d}} - \ln(R+\eta)\right] + \frac{\sin\delta}{\cos\delta} I_4$$

$$I_4 = \frac{\mu}{\lambda+\mu}\frac{1}{\cos\delta}\left[\ln(R+\tilde{d}) - \sin\delta\ln(R+\eta)\right]$$

$$I_5 = \frac{\mu}{\lambda+\mu}\frac{2}{\cos\delta}\tan^{-1}\frac{\eta(X+q\cos\delta)+X(R+X)\sin\delta}{\xi(R+X)\cos\delta}$$

$$p = y\cos\delta - z\sin\delta$$

$$q = y\sin\delta + z\cos\delta$$

$$\tilde{y} = \eta\cos\delta + q\sin\delta$$

$$\tilde{d} = \eta\sin\delta - q\cos\delta;$$

$$R^2 = \xi^2 + \eta^2 + q^2 = \xi^2 + \tilde{y}^2 + \tilde{d}^2$$

$$X^2 = \xi^2 + q^2.$$

In equations 4.1-4.3 ǁ represents Chinnery's notation, and therefore the equations for u_x, u_y and u_z are expanded since:

$$f(\xi,\eta)\|_0^L = f(x+L,p) - f(x+L,p-W) - f(x-L,p) + f(x-L,p-W)$$

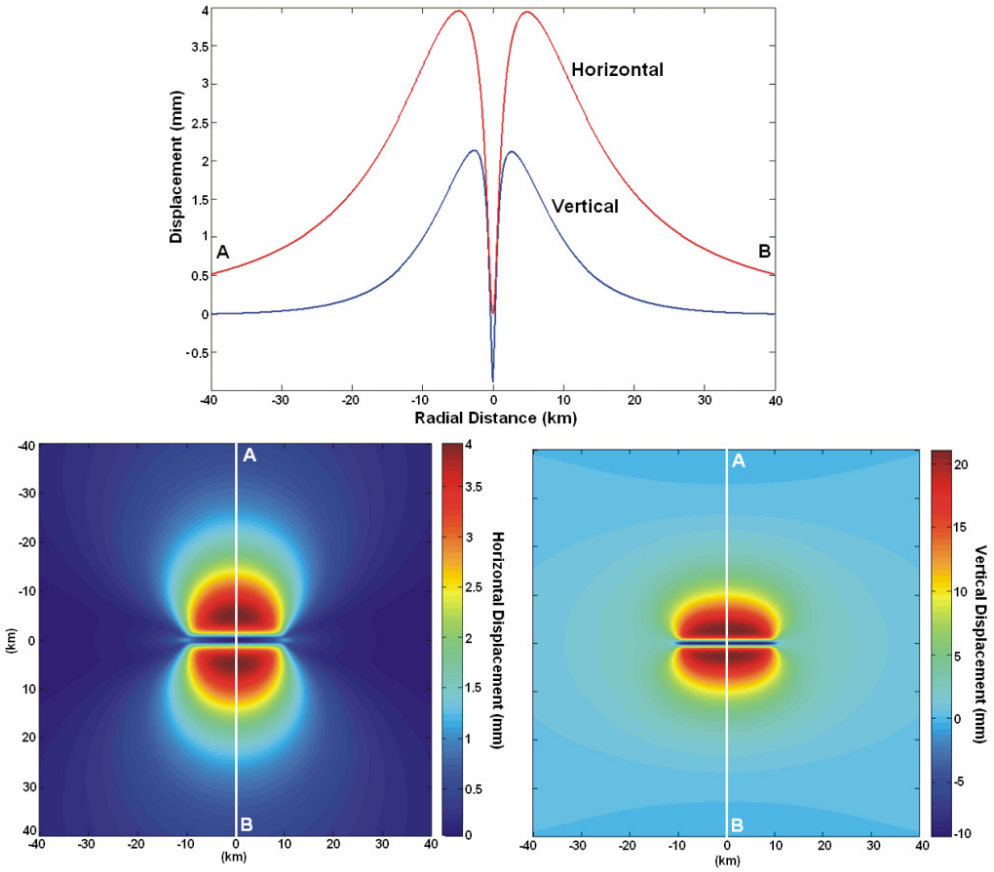


Figure 4.2 Profile and 2-D images of the vertical and horizontal displacement at the Earth's surface over a finite tensile fault at a depth of 7 km, with a width and length of 100 km and an opening of 11 mm. The location of the profile is marked on the 2-D plot.

The tensile fault, or dyke, used for modelling the spreading ridge in this study opens at a continuous rate below a certain depth. This depth is known as the locking depth since above this depth extension does not occur, which is appropriate for interrifting periods. Three variables are solved for during modelling and are displaced in Figure 4.1 and Figure 4.3; the locking depth, $-d=z+W$, the dyke-normal displacement, U_3 or u, and the horizontal location of the spreading axis, x. The length of the dyke, $2L$, and depth of the dyke, z, are assumed to be infinite in order to minimise edge effects. See Appendix 2 for the Matlab program used for this study to generate the response due to a tensile fault.

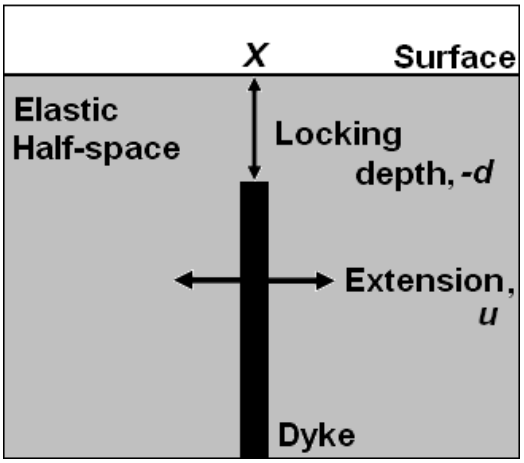


Figure 4.3 Schematic of the elastic half-space model used in this study to investigate the plate spreading signal across the southern part of the EVZ. In the model a tensile fault or dyke at location x experiences continuous opening, u, beneath a locking depth, $-d$.

4.1.2 Surface deformation due to a spherical body (Mogi source)

Mogi (1958) used the basic assumptions that: 1) the Earth's crust is an ideal semi-infinite elastic body, and 2) that sudden deformation of the crust is elastic to a first approximation, to model ground deformation at volcanoes such as Sakurazima in Japan and Kilauea caldera in Hawaii. Mogi (1958) modelled the deformation as being due to the dilation of a spherical body in a homogeneous elastic half-space (Figure 4.4). The spherical body is considered to be a point source since it is assumed that the depth of the body is significantly greater than its radius (Mogi 1958).

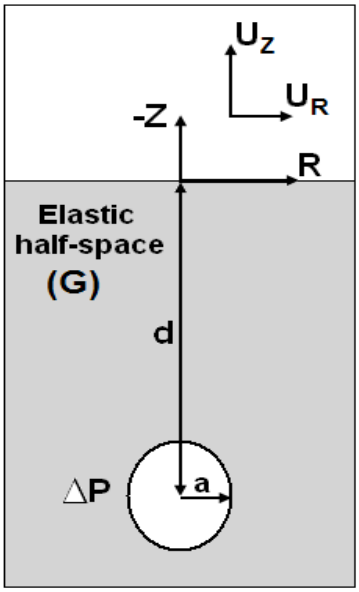


Figure 4.4 Mogi-type magma reservoir in an elastic half-space with elastic shear modulus *G* (a measure of the rocks response to shear strains) (Mogi 1958). Horizontal and vertical surface displacements (U_R and U_Z) measured at a vertical position $-Z$ ($Z<0$) and radial distance R from the sphere (where $R^2 = x^2 + y^2$) can be used to calculate the change in pressure (ΔP), or change in volume (ΔV) within a magma reservoir at a depth d, with a radius a.

According to elasticity theory, the surface deformation resulting from a change in the hydrostatic pressure of a small sphere in a semi-infinite elastic body is given by the equations (Mogi 1958)

$$U_R = -\frac{a^3 \Delta P}{4\mu}\left[\frac{R}{\left\{(Z+2d)^2+R^2\right\}^{5/2}}.\left(5Z^2+14dZ+8d^2-R^2\right)\right] + \frac{a^3 P}{4\mu}\left[\frac{R}{\left(Z^2+R^2\right)^{3/2}}+\frac{R}{\left\{(Z+2d)^2+R^2\right\}^{3/2}}\right] \quad (4.4)$$

and

$$U_Z = \frac{a^3 \Delta P}{4\mu}\left[\frac{1}{\left\{(Z+2d)^2+R^2\right\}^{5/2}}.\left(7Z^3+38dZ^2+68d^2Z+40d^3+4dR^2+ZR^2\right)\right] + \frac{a^3 P}{4\mu}\left[\frac{R}{\left(Z^2+R^2\right)^{3/2}}+\frac{Z+2d}{\left\{(Z+2d)^2+R^2\right\}^{3/2}}\right], \quad (4.5)$$

where U_R and U_Z are the radial and vertical displacements (i.e., total subsidence or uplift at the station) respectively; a is the radius of the sphere; ΔP is the pressure change within the sphere; μ is Lame's constant; d is the depth to the centre of the sphere from the surface; $-Z$ is the vertical position, and R is the radial distance of the point of measurement from the sphere (where $R^2 = x^2 + y^2$).

By replacing Z with $-d$ and μ with G, the elastic shear modulus (3×10^{10} Pa for basalt), and assuming that $a/d \ll 1$, equations 4.4 and 4.5 can be simplified and rewritten as (Mogi 1958)

$$U_R = \frac{3a^3 \Delta P R}{4G\left(d^2 + R^2\right)^{3/2}} \tag{4.6}$$

$$U_Z = \frac{3a^3 \Delta P d}{4G\left(d^2 + R^2\right)^{3/2}} \ . \tag{4.7}$$

Ground deformation can also result from a change in volume of a magma chamber (ΔV) (Mogi 1958). Since $\Delta P = \frac{G\Delta V}{\pi a^3}$ (Mogi 1958), equations 4.6 and 4.7 can be rewritten as

$$U_R = \frac{3\Delta V R}{4\pi\left(d^2 + R^2\right)^{3/2}} \tag{4.8}$$

$$U_Z = \frac{3\Delta V d}{4\pi\left(d^2 + R^2\right)^{3/2}} . \tag{4.9}$$

The horizontal and vertical displacements resulting from a Mogi source experiencing a change in pressure are shown in Figure 4.5:

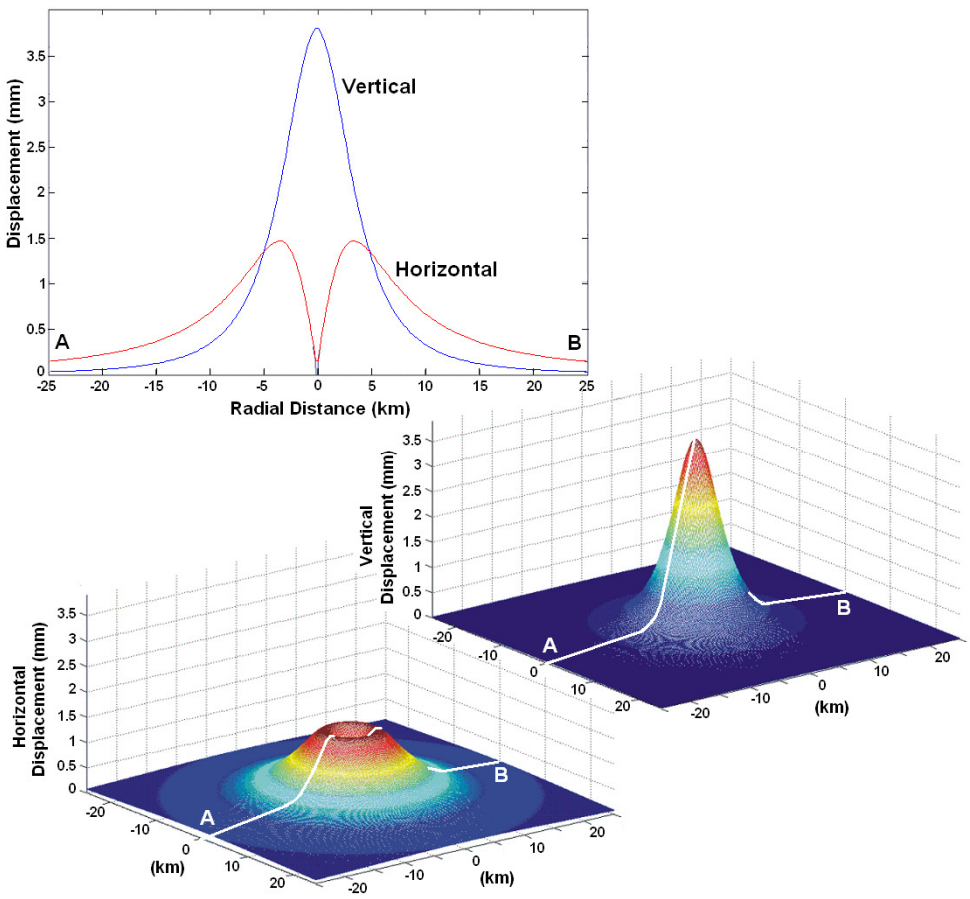


Figure 4.5 Profile and 3-D plots of the vertical and horizontal displacements at the Earth's surface over a Mogi source at a depth of 5 km, with a radius of 0.5 km, experiencing a pressure change of 30 MPa. The location of the profile is marked on the 3-D plot.

''Dry-tilt'' (Θ) (Section 2.5.3, measured in μrad) measured at a distance R from the Mogi source, can be used to calculate the volume change experienced by a magma chamber (ΔV) (Mogi 1958; McTigue 1987; Wiens et al. 2005):

$$\Theta = \frac{9}{4\pi} \frac{\Delta \mathrm{V}\, \mathrm{d}\, \mathrm{R}}{\left(\mathrm{d}^2 + \mathrm{R}^2\right)^{5/2}} \tag{4.10}$$

The volume change experienced by the Mogi source at Hekla will be broadly constrained using ''dry-tilt'' data collected at the NAEF site which is 11.5 km west of Hekla and mainly reflects displacements due to a deep-seated magma chamber (LaFemina et al. 2005). A more detailed calculation of the source volume and depth would be possible if data from more than one tilt site were available.

The Mogi model best describes magma chambers of basaltic shield volcanoes where quartz is rare or absent, and/or short-lived deformation events (a few days or less). In these instances there is insufficient time for the crust surrounding the magma body to be heated significantly, and as a result the crust responds elastically. For silicic volcanoes and/or long-lived magmatic systems in continental terrains, there is sufficient time for material surrounding the magma body to be heated. As this material is rich in quartz it reaches the brittle-ductile transition at relatively low temperatures (~300-500°C depending mainly on composition and strain rate) when compared with basaltic material, therefore resulting in deformation of the surrounding material that is characterized by viscoelastic behaviour. The ground deformation resulting from such a system cannot accurately be described using an elastic model, but instead is better described using a spherical pressure source (i.e., magma chamber) surrounded by a concentric, spherical, Maxwell viscoelastic shell of ductile material embedded in an elastic full space (Bonafede et al. 1986; Dragoni and Magnanensi 1989). Examples of long-lived volcanic systems experiencing unrest that are best described using a viscoelastic deformation model are Campi Flegrei volcanic fields in Italy (Bonafede et al. 1986; Dragoni and Magnanensi 1989) and Long Valley caldera, California in the United States of America (Newman et al. 2001; Newman et al. 2004).

The use of a viscoelastic shell model, with a lower effective viscosity than the surrounding rocks, makes it possible to account for a number of phenomena that would otherwise be poorly explained using an elastic model. The existence of a viscoelastic shell around a magma chamber results in an increase in the amplitude of displacement experienced by the surrounding material, that would otherwise only be explained by an unreasonably high pressure change in the magma chamber of an elastic model (e.g., using an elastic model, a pressure change of ~100 MPa would be needed to explain unrest at Campi Flegrei volcano between 1982 and 1984) (Bonafede et al. 1986). Viscoelastic rheology also results in a time-dependent surface response due to a change in pressure or volume within a chamber, for example, deformation measured at Long Valley caldera, which is a system that has been active for at least the last 2 Ma, has been seen to vary exponentially in time (Newman et al. 2001). Thin viscoelastic shells are characteristic of smaller and/or relatively dry magmatic systems, while thicker shells occur around larger and/or relatively wet magmatic systems as the fluids advect heat far from the magma body (Newman et al. 2001).

For this study, ground deformation due to Hekla, Katla and Torfajökull volcanoes are considered. The magmas erupted from Hekla and Katla volcano show a range of compositions. Hekla volcano erupts magmas of dacite to basaltic andesite (Thórdarson and Larsen 2007) and Katla volcano produces alkali basalt to mildly alkalic rhyolites (Lacasse et al. 2007). As a result of the fact that these volcanoes are not solely silicic systems but do erupt basaltic lavas, the assumption is made that these chambers are best modelled using an elastic Mogi model instead of a viscoelastic model. Torfajökull volcano on the other hand is a volcanic system for which approximately half of the erupted material is silicic (Gunnarsson et al. 1998), and the volcano has been active since at least ~52,000 years B.P. (Grönvold et al. 1995). The magma chamber of Torfajökull would therefore be more realistically described using a viscoelastic model, however due to the time limitations and nature of this study, as well as limited data coverage, the model is kept simple and the Torfajökull magma source is modelled as an elastic Mogi source. See Appendix 3 to 6 for the Matlab programs used to generate the response measured at GPS sites, used in this study, due to the Hekla Mogi source between 2001 and 2006 (A3), and 1994 and 2004 (A4); as well as the response due to Torfajökull (A5) and Katla deformation (A6).

4.2 Statistical Analysis

4.2.1 Chi-square value

Forward modelling using a grid search is carried out in order to estimate the optimum parameter values (i.e., opening of the dyke and locking depth). In order to determine the minimum misfit, or goodness-of-fit, of a model (estimated values) to the data (measured values), the chi-square distribution (χ^2) is used in this study. The chi-square distribution is calculated using the method of least squares, which assumes that the optimum model to fit a set of data is one which minimizes the square of the deviation of the data from the model, weighted by the square of the measured error. It is assumed that the measurements are independent of each other and follow a Gaussian distribution. For a given dataset and a number of different models, the model that gives the minimum chi-square value is considered to be the optimum model (Bevington 1969). The function is defined as

$$\chi^2 = \sum_{i=1}^{N} \left(\frac{O_i - E_i}{\sigma_i} \right)^2 , \tag{4.11}$$

where O_i is the measured value, E_i is the calculated value or model result at the same location, σ_i is the measurement uncertainty, and N is the number of data points. The reduced chi-square value (χ_v^2) is calculated by dividing χ^2 by the number of degrees of freedom (v), i.e., the number of adjustable parameters (p) minus N. A reduced chi-square value of one implies a model is a good approximation to the data, while a reduced chi-square of greater than one implies the model being used is not appropriate for describing the data. A value of less than one does not however indicate an improvement of the fit, but rather indicates an unexpectedly good fit (Bevington 1969). The reduced chi-squared value allows for comparison of models with differing numbers of adjustable parameters and total number of data points.

4.2.2 F Distribution

The F distribution is a continuous probability distribution and is designed to test whether the variances of two or more populations are equal (i.e., $F = 1$). The distribution is determined from the ratio of two independent χ^2 values, χ_1^2 and χ_2^2, divided by their respective degrees of freedom, v_1 and v_2 (Bevington 1969)

$$F = \frac{\chi_{v1}^2}{\chi_{v2}^2} = \frac{\chi_1^2 / \nu_1}{\chi_2^2 / \nu_2} = \frac{\left[\sum_{i=1}^{N} \left(\frac{O_{i1} - E_{i1}}{\sigma_{i1}} \right) \right]^2 / \nu_1}{\left[\sum_{j=1}^{N} \left(\frac{O_{j2} - E_{j2}}{\sigma_{j2}} \right) \right]^2 / \nu_2} , \tag{4.12}$$

where $\chi_{v1}^2 > \chi_{v2}^2$, i.e., the χ^2 with the larger variance should always be placed in the numerator. For each combination of v_1 and v_2 there is a different F distribution. In Figure 4.6a the F distribution for v_1 and v_2 are plotted (i.e. continuous probability distribution); for a probability of $\alpha = 0.05$, there is 5% probability in the upper tail of the plot (black section) of exceeding the critical F value (i.e., $F(v_1, v_2)$ at $P = \alpha$). A numerical example is shown in Figure 4.6b for $v_1 = 4$ and $v_2 = 12$, and using Table 4.1. For a random set of data with a correct fitting function with chi-squared χ_2^2 and degrees of

freedom v_2, the model with chi-squared χ_1^2 and degrees of freedom v_1 that results in an F value for which $P(F,v_1,v_2) = 0.05$ (equation 4.12) therefore provides a 95% correct fit to the data.

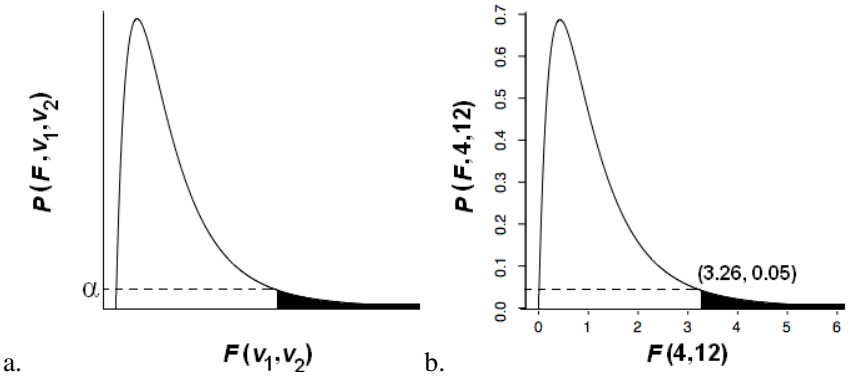


Figure 4.6 F distribution (continuous probability distribution) (Bevington 1969). (a) Theoretical plot of probability density, P, versus F distribution value for v_1 and v_2 degrees of freedom. For $P = \alpha$ there is an 'α' probability that the critical F value will be exceeded. (b) An example showing the F distribution for $v_1 = 4$ and $v_2 = 12$. There is a probability of 0.05 that the F value of 3.26 will be exceeded, i.e. from Table 4.1 for the probability level $P(F,v_1,v_2) = 0.05$, since $v_1 = 4$ and $v_2 = 12$ therefore F is equal to 3.26.

Table 4.1 Values of F corresponding to the probability $P(F,v_1,v_2) = 0.05$ of exceeding F for v_1 versus v_2 degrees of freedom (Bevington 1969).

v_2	Degrees of freedom, v_1												
	1	**2**	**3**	**4**	**5**	**6**	**7**	**8**	**9**	**10**	**11**	**12**	**…**
1	161	199	216	225	230	234	237	239	241	242	243	244	
2	18.5	19	19.2	19.2	19.3	19.3	19.4	19.4	19.4	19.4	19.4	19.41	
3	10.1	9.55	9.28	9.12	9.01	8.94	8.89	8.85	8.81	8.79	8.76	8.75	
4	7.71	6.94	6.59	6.39	6.26	6.16	6.09	6.04	6	5.96	5.94	5.91	
5	6.61	5.79	5.41	5.19	5.05	4.95	4.88	4.82	4.77	4.74	4.7	4.68	
6	5.99	5.14	4.76	4.53	4.39	4.28	4.21	4.15	4.1	4.06	4.03	4.0	
7	5.59	4.74	4.35	4.12	3.97	3.87	3.79	3.73	3.68	3.64	3.6	3.58	
8	5.32	4.46	4.07	3.84	3.69	3.58	3.5	3.44	3.39	3.35	3.31	3.28	
9	5.12	4.26	3.86	3.63	3.48	3.37	3.29	3.23	3.18	3.14	3.1	3.07	
10	4.96	4.1	3.71	3.48	3.33	3.22	3.14	3.07	3.02	2.98	2.94	2.91	
11	4.84	3.98	3.59	3.36	3.2	3.09	3.01	2.95	2.9	2.85	2.82	2.79	
12	4.75	3.89	3.49	3.26	3.11	3.0	2.91	2.85	2.8	2.75	2.72	2.69	
…													

For this study the *F* distribution is used to calculate the χ^2 misfit value corresponding to the 95% confidence interval for a model. Using the best-fit model χ^2 value (χ^2_{best}) and *F*-value for $v_{95\%}$ and v_{best} (Table 4.1, for this study $v_{95\%} = v_{best}$),

$$\chi^2_{95\%} = \frac{F\chi^2_{best}\nu_{95\%}}{\nu_{best}}. \tag{4.13}$$

As each parameter is varied independently for this study (e.g. extension rate varied from 1 to 20 mm/yr with locking depth held constant; depth varied from 1 to 15 km with rate held constant), a plot is made of the varied parameter value versus the χ^2 value for each model. The model with the minimum χ^2 value is the best-fit model. The parameter value(s) at which $\chi^2 = \chi^2_{95\%}$ provides a measure of the uncertainty level for the best-fit model parameter.

The equations discussed in chapter 4 will be used in the following chapter to model GPS-derived site velocities for the southern part of the EVZ. The velocities are first corrected for local volcanic deformation using the Mogi model (Mogi 1958), and the final velocity values are then fit to a plate spreading model (Okada 1985). The wellness of fit of the model to the data is tested using the chi-squared function, and uncertainty levels for the best-fit model parameters are determined using the *F* distribution.

5 MODELLING RESULTS

5.1 Modelling of the Horizontal Velocity Field

In order to investigate how long-term spreading across the Mid-Atlantic Ridge is accommodated in south Iceland, GPS measured surface velocities are compared to velocities predicted by a number of plate spreading models. The search area for estimated modelling parameters (spreading rate and locking depth) is constrained using ancillary data. The spreading rate is constrained by the total spreading rate for Iceland determined from the NUVEL-1A and REVEL plate motion models (DeMets et al. 1994; Sella et al. 2002), while the locking depth is constrained using estimates of the seismogenic thickness of the crust in south Iceland (Savage and Burford 1973; LaFemina et al. 2005). The location of the axis of spreading is held fixed within the mapped extent of the neovolcanic zone, which is defined by geologic studies of the extent of Holocene magmatic activity and the locations of historical rifting events (Johannesson et al. 1990).

The relative motion between North America and Eurasia at the latitude of Iceland predicted by NUVEL-1A and REVEL is ~18-20 mm/yr (DeMets et al. 1994; Sella et al. 2002). As the total plate motion is partitioned in south Iceland, north of the SISZ, between the overlapping WVZ and EVZ (Hey 1977; Hey et al. 1980; Sigmundsson et al. 1995; LaFemina et al. 2005), and across the RP and EVFZ south of the SISZ (Hreinsdóttir et al. 2001; LaFemina et al. 2005), the spreading modelled in this study accommodates only part of the plate spreading in south Iceland. Previous studies have shown a partitioning of spreading between the WVZ and EVZ, with Sigmundsson et al. (1995) estimating partitioning of 15 ± 15% and 85 ± 15%, respectively. Jónasson et al. (1997) show using GPS and EDM that across the EVZ 12 mm/yr of extension is accommodated in a zone 100 km wide. LaFemina et al. (2005) show a decrease in spreading rate along the EVZ in the direction of ridge propagation from 19.8 mm/yr just south of the Vatnajökull icecap, decreasing to 11.0 mm/yr just north of Torfajökull volcano, and 8.0 mm/yr to the south of the volcano. LaFemina et al. (2005) also show a converse increase from northeast to southwest along the WVZ (Table 2.2). A range of dyke-normal opening rates, u, between 0 and 20 mm/yr are investigated in this study.

Assuming that the locking depth for the dyke model used in this study can be equated with the seismogenic thickness of the crust in south Iceland (Savage and Burford 1973; LaFemina et al. 2005), earthquake relocations in the SISZ show an increase in seismogenic depth from 6 km in the west to 12 km near the intersection with the EVZ (Stefánsson et al. 1993). A previous geodetic study by LaFemina et al. (2005) show an increase in locking depth from 3 (+1.2/-0.7) km to the north of Torfajökull volcano to 7 (+2.5/-1.2) km to the south of the volcano. The locking depths, $-d$, for this study are varied between 0 and 15 km.

During modelling, an individual parameter (e.g., extension rate or locking depth) is varied while the other parameter and x location are held constant. Plots are made of the varied parameter versus the χ^2 value for each model (e.g. Figure 5.5 and Figure 5.6 in the following sections). The best-fit model is that with the minimum chi-squared value. The χ^2 versus parameter plots for the best-fit model and the 95% confidence level of the χ^2 function are used to determine the uncertainty interval for each parameter (see Section 4.1.4). See Appendix 7 – 9 for the Matlab programs used in this study to determine the best-fit models to profile 1 (A7) and profile 3 (A8) velocities, and the program used to generate profile plots of models and data along individual profiles (A9)

5.2 Models Uncorrected for Volcanic Deformation

We first present models for the horizontal velocity field along profiles 1 to 3 (Figure 5.1) not corrected for volcanic deformation (i.e., deformation of Hekla and Katla volcano). Best-fit model parameters for the uncorrected 1994-2003 and 2001-2006 datasets are listed in Table 5.1, and profile plots of the models and data are shown in Figure 5.2 and Figure 5.3.

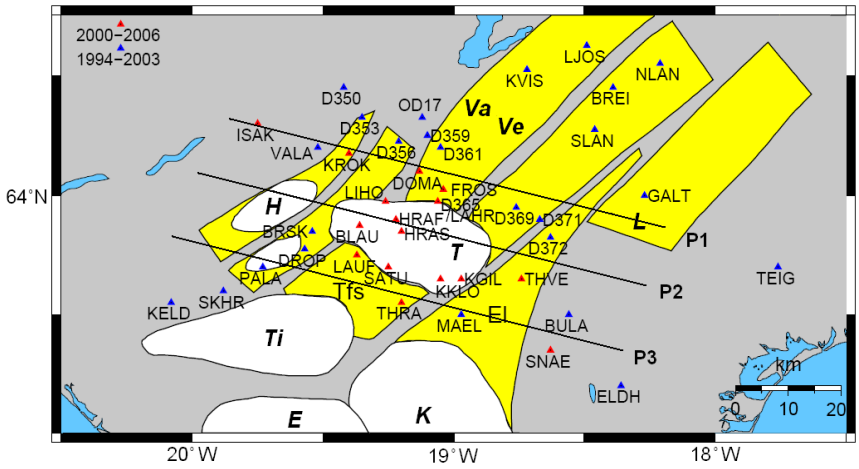


Figure 5.1 Map of GPS sites in south-central Iceland and modelling profiles (P1, P2 and P3) used in this study. Sites used to collect data from 1994-2003 are marked by blue triangles (LaFemina et al., 2005 and this study) and sites occupied from 2001 to 2006 by red triangles (this study). Names of central volcanoes and fissure swarms as in Figure 3.10.

Table 5.1 Parameter estimates for spreading models fit to 1994-2003 and 2001-2006 GPS-derived site velocities relative to stable Eurasia along profiles P1, P2 and P3. Velocities have not been corrected for volcanic deformation. Chi-squared (χ^2) and reduced chi-squared (χ^2_ν) values for each model are listed (where N is the number of data points and p the number of adjustable parameters), and model uncertainties are given in parentheses.

Dataset	P	Rate (mm/yr)	Depth (km)	Location (km)	χ^2	N	χ^2_ν (p=2)	
1994-2003	1	13.0 (+2.7/-2.5)	9.0 (+8.4/-4.7)	-2 (±6)	12.73	13	1.16	Figure 5.2a
	3	5.0 (+2.8/-2.6)	2.0 (+21.2/-2.0)	18 (-4/+8)	6.09	11	0.68	Figure 5.2b
2001-2006	1	49.0 (+5.5/-5.6)	21.0 (+6.9/-5.3)	-2 (±6)	8.70	5	2.90	Figure 5.3a
	2	6.0 (+10.0/-6.0)	13.0[a]	2	6.84	5	2.28	Figure 5.3b
	3	4.0 (+2.3/-2.2)	3.0[a]	18 (-4/+8)	0.68	5	0.23	Figure 5.3c

[a] These depth estimates cannot be constrained within reasonable values of crustal thickness.

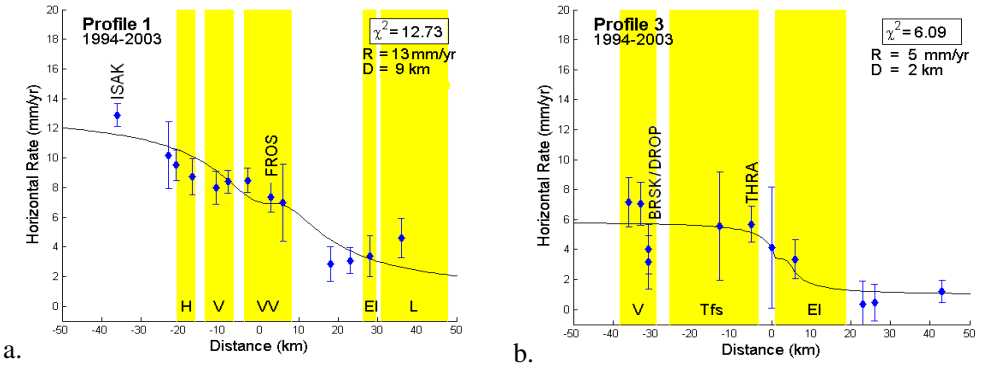


Figure 5.2 Best-fit elastic half-space plate spreading models (black line, Table 5.1) for 1994-2003 GPS-derived site velocities relative to stable Eurasia, for sites within ~5 km of (a) profile 1 and (b) profile 3. The velocity component parallel to the plate motion direction (N78°W, Sella et al. (2002)) is plotted. Velocities are left uncorrected for volcanic deformation**.** Best-fit model parameters (rate, *R* and depth, *D*) and chi-square value (χ^2) for each model are given. Names of central volcanoes and fissure swarms as in Figure 3.14.

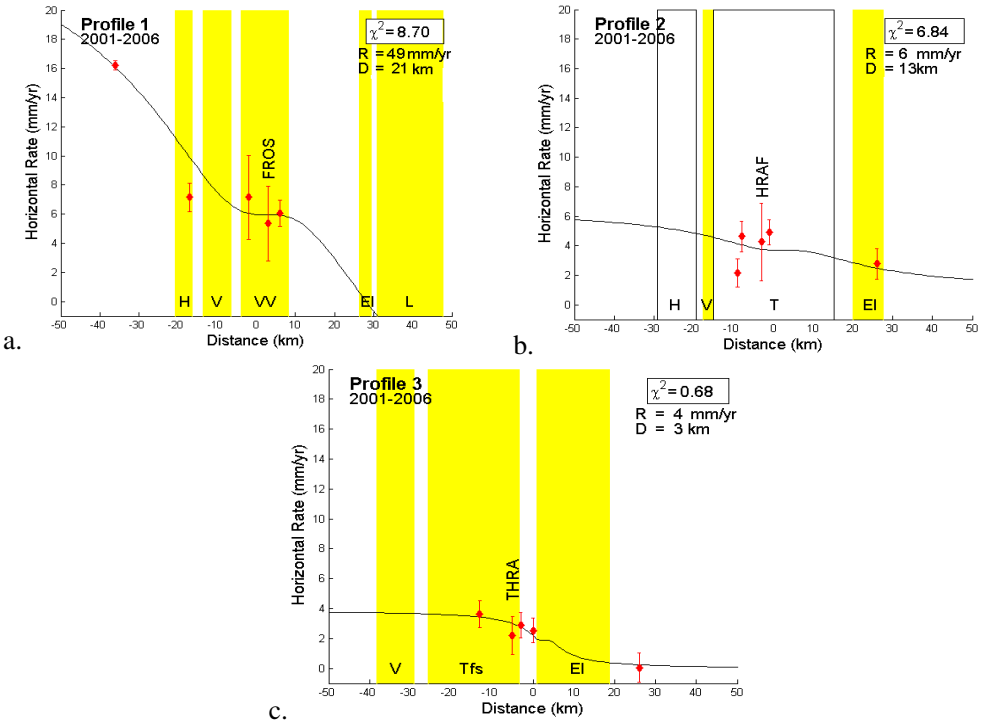


Figure 5.3 Best-fit elastic half-space models (black line, Table 5.1) for 2001-2006 GPS-derived site velocities relative to stable Eurasia along (a) profile 1, (b) profile 2 and (c) profile 3. Velocities are left uncorrected for volcanic deformation. Names of central volcanoes and fissure swarms as in Figure 3.14, and figure description as in Figure 5.2.

The best-fit model for the 1994-2003 GPS-derived velocities along profile 1 (Table 5.1 and Figure 5.2a) has an extension rate of 13.0 (+2.7/-2.5) mm/yr and locking depth of 9.0 (+8.4/-4.7) km. While the best-fit model for the 1994-2003 velocities along profile 3 (Table 5.1 and Figure 5.2b) has an extension rate of 5.0 (+2.8/-2.6) mm/yr, and a shallow locking depth of 2.0 (+21.2/-2.0) km. Velocities measured at GPS sites closest to Hekla volcano (within 15 km) show some of the largest variation from the best-fit model (e.g., ISAK along profile 1 (Figure 5.2a) and sites BRSK and DROP along profile 3 (Figure 5.2b)) suggesting that deformation due to Hekla volcano must be accounted for in order to accurately determine spreading rate and locking depth in this region.

In order to obtain any fit to the 2001-2006 profile 1 velocities, a model with an extension rate greater than the full spreading rate for Iceland (>20 mm/yr, DeMets et al.(1994) and Sella (2002)) and a locking depth greater than seismogenic crustal thickness estimates for south Iceland (>12 km, Stefánsson et al. (1993)) is needed (Table 5.1 and Figure 5.3a). Such a model is unrealistic and therefore modelling these data requires they be corrected for Hekla deformation. The best-fit model for 2001-2006 profile 2 velocities also requires a locking depth greater than the seismogenic crustal thickness determined for this region (Table 5.1 and Figure 5.3b) and is therefore also not a feasible model. The best-fit model for 2001-2006 velocities along profile 3 is a dyke experiencing opening at a rate of 4.0 (+2.3/-2.2) mm/yr below a locking depth of 3 km (Table 5.1 and Figure 5.3c).

As a result of the poor fit of realistic models to the 2001-2006 GPS-derived site velocities, in the sections that follow the data are corrected for deformation due to Hekla, Katla and Torfajökull volcanoes.

5.3 Models Corrected for Volcanic Deformation

5.3.1 Profile 1

Sites located at the western end of profile 1 are within 30 km of the currently inflating Hekla volcano (Figure 5.1). Data collected at GPS sites in the EVZ from 1994 to 2003 span the time period over which Hekla volcano experienced pre-eruption inflation (uplift), followed by a major eruption from February to March 2000 characterized by rapid subsidence, followed by renewed inflation (uplift) (Sturkell et al. 2006b; Höskuldsson et al. 2007). The 2001-2006 data span the inflation (uplift) period after the 2000 eruption. Recent tilt measurements made on the western slope of the volcano show tilting of the ground surface (here thought to represent inflation of a subsurface magma chamber) has already passed the maximum tilt value measured prior to the 1991 and 2000 eruptions (Figure 2.14).

Current estimates from tilt, InSAR and strain data place the Hekla volcano magma chamber at a depth of between 10 and 11 km (LaFemina et al. 2005; Sturkell et al. 2006a; Sturkell et al. 2006b). Seismicity studies conducted on this relatively aseismic volcano, however point to a magma chamber deeper than 14 km (or less than 4 km), with pockets of magma most likely rising to shallower depths prior to an eruption (Soosalu and Einarsson 1997; 2004; Soosalu et al. 2005; Höskuldsson et al. 2007). Surface deformation due to Hekla volcano is modelled in this study using a Mogi source at 11 km depth (Mogi 1958) below the middle point of the volcanoes eruptive fissure (Sturkell et al. 2006a; Sturkell et al. 2006b) (Figure 5.4).

The volume change experienced by the Mogi source at Hekla is broadly constrained using ‘‘dry-tilt’’ data collected at site NAEF on the western flank of the volcano (Table 5.2 and Figure 5.4). Using an overall change in tilt at NAEF of 3.0 μrad between 1994 and 2003 and 3.7 μrad between 2001 and 2006, with a magma chamber at 11 km depth, from equation 4.10 it can be determined that the Hekla magma chamber experienced a volume change of ~0.03 km^3 between 1994-2003 and ~0.04 km^3 between 2001-2006. These estimates are approximate as one tilt site is not sufficient to accurately constrain the volume or pressure change of a magma chamber.

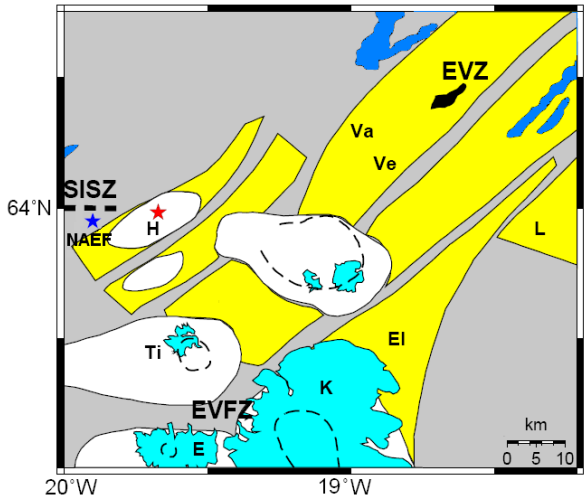


Figure 5.4 Plot of the intersection of the Eastern Volcanic Zone (EVZ), the Eastern Volcanic Flank Zone (EVFZ) and South Iceland Seismic Zone (SISZ). The location of the Hekla volcano Mogi source is marked with a red star (-19.67°W; 63.99°N, E. Sturkell pers comm. 2007) and the NAEF ''dry-tilt'' site marked with a blue star. Names of central volcanoes and fissure swarms as in Figure 3.10.

Table 5.2 Table of ''dry-tilt'' measurements made at site NAEF on the western flank of Hekla volcano between 1994 and 2006 (data provided by Erik Sturkell, Nordic Volcanological Centre), as well as the calculated change in tilt over the time periods 1994-2003 and 2001-2006.

Date of Observation	**Tilt since previous Obs (μrad)**			**Std error (μrad)**		
	East	**North**	**Radial**	**East**	**North**	**Max Axis**
July 22, 1994						
May 17, 1995	0.275	-2.379	**2.395**			0.645
June 22, 1996	0.884	2.877	**3.010**			0.711
1998	2.177	0.164	**2.183**			0.14
October 20, 1999	-0.027	1.203	**1.203**			0.344
April 6, 2000	-4.441	-1.874	**4.820**			0.546
November 21, 2000	-0.005	3.397	**3.397**			0.657
November 6, 2001	2.425	-0.331	**2.447**			0.486
June 14, 2002	-1.083	-0.887	**1.400**			0.640
August 27, 2003	1.995	-0.072	**1.996**			0.461
April 27, 2004	0.017	-0.223	**0.224**			0.560
November 18, 2004	1.985	2.423	**3.132**			0.669
May 24, 2005	-0.038	-3.388	**3.388**			1.026
February 8, 2006	-1.102	0.325	**1.149**			0.642
October 26, 2006	1.895	2.414	**3.069**			0.412
April 26, 2007	-0.041	-0.553	**0.555**			0.533
1994-2003	2.200	2.098	**3.040**	0.461	0.435	
2001-2006	3.669	0.592	**3.716**	0.412	0.564	

These volume change estimates are comparable with those determined from eruptive volumes. Studies have shown that when a volume of magma drains out of a magma chamber (ΔV_m), it is accommodated by both a change in the volume of the magma chamber (ΔV_{ch}) which is measured as deflation at the Earth's surface, as well as by volumetric decompression of the magma remaining in the chamber (Johnson et al. 2000; Delaney and McTigue 2004; de Zeeuw-van Dalfsen et al. 2005). Studies conducted at Askja volcano in Iceland (de Zeeuw-van Dalfsen et al. 2005) and on Pu'u 'O'o on Kilauea in Hawaii (Johnson 1992) have shown that since the ΔV_{ch} to ΔV_m ratio is 0.3, this means that 30% of the volume of magma drained from a chamber is accommodated by a reduction in the chamber volume, while the other 70% of magma drained is accommodated by decompression of the remaining magma in the chamber. If this theory is applied to the 2000 eruption of Hekla volcano that produced an estimated 0.189 km^3 of erupted material (Höskuldsson et al. 2007), the volcanoes magma chamber would have experienced a minimum volume decrease of ~0.06 km^3.

For the 1994-2003 time period it can be shown that at a distance of 24 km from the Hekla Mogi source the radial component of displacement is ~9 mm or 1 mm/yr, which is the approximate level of rate uncertainty for this study. 1994-2003 horizontal velocity vectors for GPS sites within 24 km of the volcano are therefore corrected for horizontal deformation due to Hekla volcano during this study, along with four sites just over 24 km from the volcano. For the 2001-2006 dataset, the volume change experienced was larger and over a shorter time period than for the 1994-2003 dataset, and therefore sites up to a distance of ~30 km were affected by and are corrected for Hekla deformation.

Table 5.3 provides a list of the sites corrected for Hekla deformation, as well as the displacements and rates experienced by the sites over the 1994-2003 and 2001-2006 time periods. The sites are corrected for Hekla inflation by removing the component of the velocities listed in Table 5.3 parallel to the plate motion direction (N78°W) from the component of the measured GPS velocities (relative to stable Eurasia) listed in Table 3.4 and Table 3.5 parallel to the plate motion direction. Deformation rates (in mm/yr) can be removed from the site velocities, instead of removing the yearly displacement due to Hekla deformation from the daily position estimates for each site, as the deformation of Hekla volcano spans the entire time period of both surveys.

Table 5.3 Site displacements and rates for the periods 1994-2003 and 2001-2006 for sites along profiles 1, 2 and 3 due to Hekla deformation. The displacements and rates for the period 2001-2006 (5 year period) are calculated using a volume change of 0.04 km^3, and the 1994-2003 displacement and rates (9 year period) are calculated using a volume change value of 0.03 km^3, as determined from ''dry-tilt'' data collected at NAEF site.

	Displacement (m)			Rate (mm/yr)		
Sites	**East**	**North**	**Vertical**	**East**	**North**	**Vertical**
1994-2003						
BRSK	0.0168	-0.0150	0.0282	1.87	-1.67	3.14
DROP	0.0104	-0.0186	0.0222	1.16	-2.07	2.47
D353	0.0075	0.0076	0.0053	0.83	0.84	0.59
D356	0.0079	0.0040	0.0039	0.88	0.44	0.44
D359	0.0059	0.0027	0.0023	0.65	0.30	0.26
D361	0.0057	0.0020	0.0021	0.63	0.22	0.23
FROS	0.0062	0.0005	0.0022	0.69	0.06	0.25
ISAK	-0.0048	0.0164	0.0129	-0.54	1.82	1.43
KGIL	0.0042	-0.0017	0.0013	0.46	-0.19	0.15
KROK	0.0132	0.0089	0.0112	1.47	0.99	1.24
LAHR	0.0060	0.0001	0.0021	0.66	0.01	0.23
PALA	-0.0038	-0.0184	0.0158	-0.42	-2.04	1.76
SATU	0.0079	-0.0046	0.0042	0.88	-0.51	0.46
SKHR	-0.0060	-0.0104	0.0066	-0.66	-1.16	0.73
THRA	0.0051	-0.0041	0.0024	0.57	-0.45	0.26
VALA	0.0117	0.0159	0.0179	1.30	1.77	1.99
2001-2006						
BLAU	0.0199	-0.0059	0.0142	4.07	-1.20	2.90
DOMA	0.0103	0.0023	0.0043	2.10	0.46	0.88
FROS	0.0126	0.0011	0.0045	2.14	0.18	0.77
HRAF	0.0204	-0.0030	0.0101	3.46	-0.50	1.71
HRAS	0.0123	-0.0029	0.0058	2.50	-0.58	1.19
ISAK	-0.0065	0.0219	0.0172	-1.32	4.46	3.50
KGIL	0.0056	-0.0022	0.0018	1.14	-0.46	0.36
KKLO	0.0065	-0.0030	0.0023	1.33	-0.61	0.47
KROK	0.0177	0.0119	0.0149	3.60	2.43	3.04
LAHR	0.0089	0.0001	0.0033	1.81	0.02	0.67
LAUF	0.0150	-0.0101	0.0110	3.07	-2.07	2.25
LIHO	0.0159	0.0000	0.0086	3.24	0.01	1.76
SATU	0.0106	-0.0062	0.0056	2.17	-1.26	1.14
THRA	0.0119	-0.0095	0.0055	1.86	-1.48	0.87

Modelling of the 1994-2003 and 2001-2006 GPS-derived site velocities along profile 1 are discussed in the following two sections. For all profile 1 models the location of the spreading axis is held fixed in line with the historically active Veidivötn fissure swarm (LaFemina et al. 2005).

5.3.1.1 1994-2003 Dataset

Figure 5.5 shows χ^2 versus extension rate plots for models with various locking depths that are fit to the 1994-2003 GPS-derived site velocities along profile 1, corrected for deformation due to Hekla volcano. Figure 5.6 shows plots of χ^2 versus locking depth for various extension/spreading rates. The minimum χ^2 values result in 10.0 (±1.7) mm/yr spreading rate and locking depth of 5.0 (+5.2/-3.0) km. It can be seen from Figure 5.5 and Figure 5.6, and for the remainder of models in this study, that estimated extension rates are well constrained (i.e., tighter curve) while locking depths are less well constrained (i.e., broader curve). This can also be seen in the extension rate versus locking depth correlation plot (Figure 5.7). Figure 5.8 shows the best-fit elastic half-space model and the component of the 1994-2003 GPS-derived site velocities parallel to the plate motion direction (relative to stable Eurasia) along profile 1.

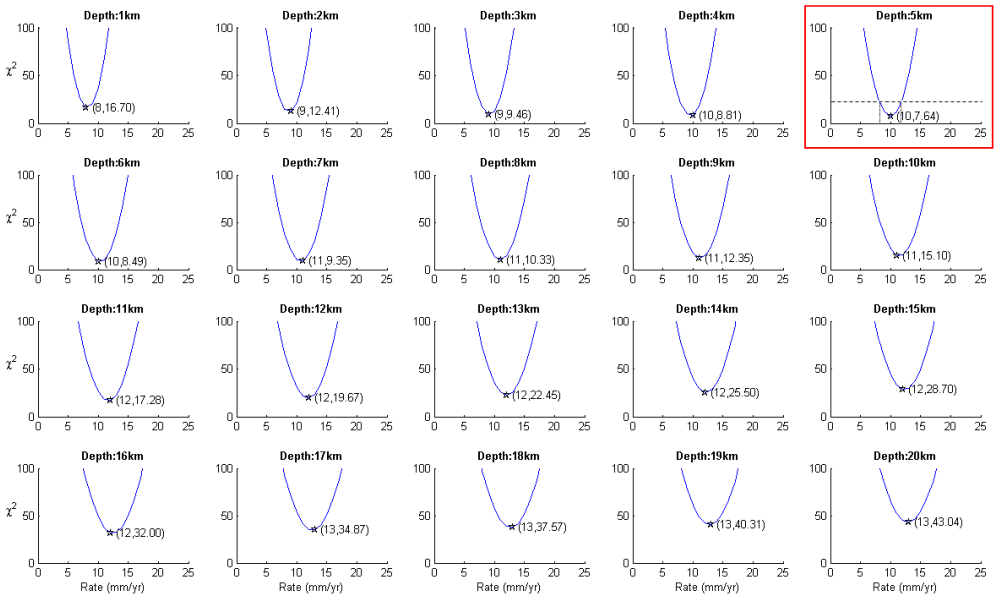


Figure 5.5 Plots of χ^2 versus extension rate for various elastic half-space plate spreading models (with x location held fixed throughout and locking depth held fixed for individual plots) fit to 1994-2003 velocities along profile 1. Minimum χ^2 values in each plot are marked with a star and (rate, χ^2) values for the point are given. The curve with the best-fit model (i.e., minimum χ^2 value) is outlined with a red box, and the χ^2 misfit value corresponding to the 95% confidence level ($\chi^2_{95\%}$, 22) for the model is indicated by a horizontal dotted line. The points of intersection of the $\chi^2_{95\%}$ line with the curve indicate the uncertainty interval for the model parameter plotted on the x-axis, and are marked by vertical lines.

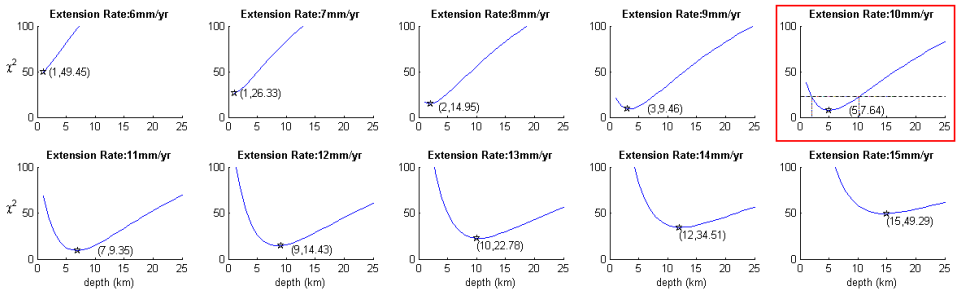


Figure 5.6 Plots of χ^2 versus locking depth for various elastic half-space plate spreading models (with extension rate held fixed for individual plots) fit to 1994-2003 velocities along profile 1. Minimum χ^2 values in each plot are marked with a star and (depth, χ^2) values for the point are given. χ^2 equal to 22 represents the approximate 95% confidence limit. See Figure 5.5 for a detailed figure description.

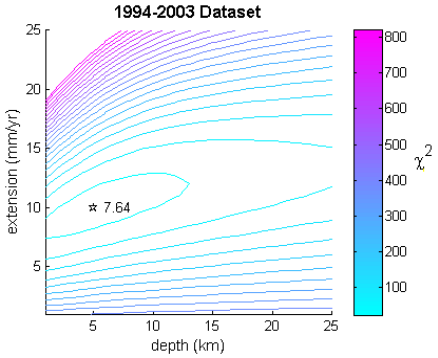


Figure 5.7 Contour plot of the χ^2 misfit for estimated extension rates and locking depths for elastic half-space plate spreading models fit to 1994-2003 velocities along profile 1. χ^2 equal to 22 (inner contour) represents the approximate 95% confidence limit. Contour interval is 40.

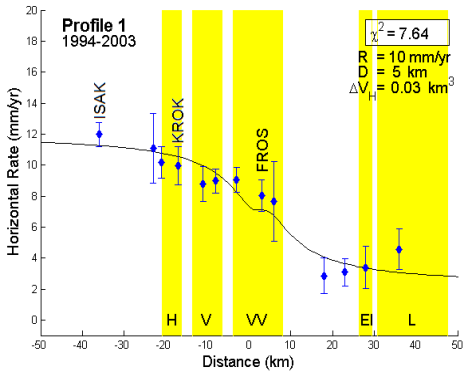


Figure 5.8 Best-fit elastic half-space model (black line) for 1994-2003 GPS-derived site velocities (relative to stable Eurasia) along profile 1. Velocities are corrected for deformation due to Hekla volcano (ΔV_H = 0.03 km^3). Names of central volcanoes and fissure swarms as in Figure 3.14, and figure description as in Figure 5.2.

A well constrained, realistic plate spreading model can therefore be fit to the 1994-2003 velocities along profile 1. In the next section the 2001 and 2006 velocities along profile 1 are investigated.

5.3.1.2 2001-2006 Dataset

Figure 5.9 shows χ^2 versus extension rate plots for models with various locking depths that are fit to the 2001-2006 GPS-derived site velocities along profile 1 corrected for deformation due to Hekla volcano. Figure 5.10 shows χ^2 versus locking depth plots for various extension rates. From Figure 5.9 - Figure 5.11 it can be seen that the minimum χ^2 values result in ≥ 25.0 mm/yr spreading rate (25 mm/yr is set as the parameter limit during modelling) and a locking depth of 19.0 (+1.8/-1.5) km. The model and data are plotted in Figure 5.12.

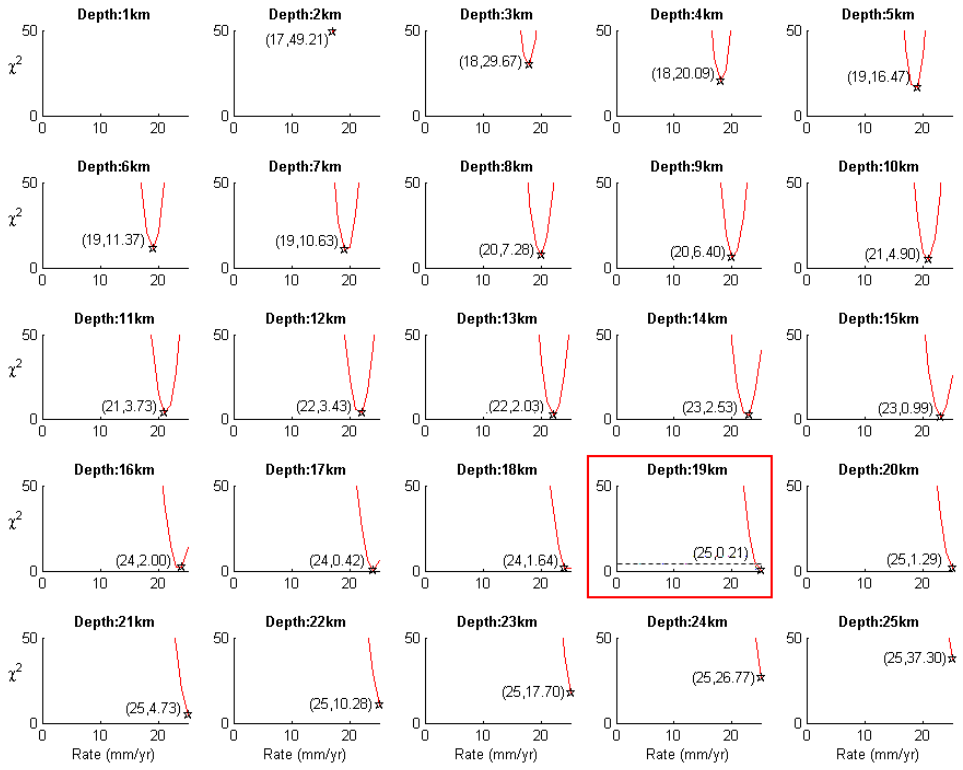


Figure 5.9 Plots of χ^2 versus extension rate for various elastic half-space plate spreading models (with locking depth held fixed for individual plots) fit to 2001-2006 velocities along profile 1. χ^2 equal to 4 represents the approximate 95% confidence limit. See Figure 5.5 for a detailed figure description.

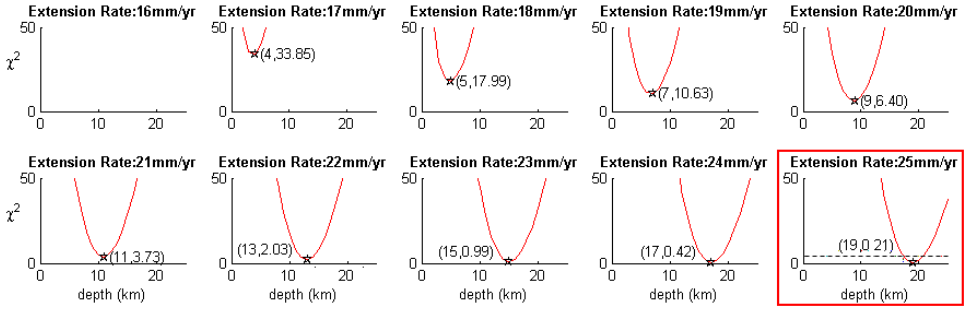


Figure 5.10 Plots of χ^2 versus locking depth for various elastic half-space plate spreading models (with extension rate held fixed for individual plots) fit to 2001-2006 velocities along profile 1. χ^2 equal to 4 represents the approximate 95% confidence limit. See Figure 5.5 and Figure 5.6 for a detailed figure description.

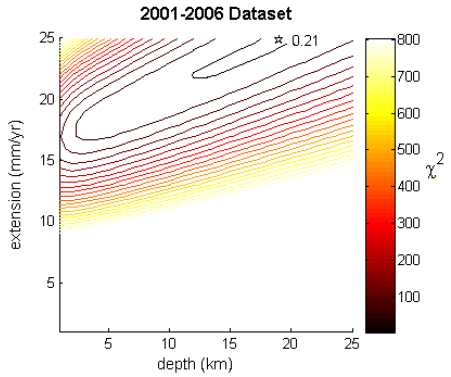


Figure 5.11 Contour plot of the χ^2 misfit for estimated extension rates and locking depths for elastic half-space models fit to 2001-2006 velocities along profile 1. χ^2 equal to 4 (inner contour) represents the approximate 95% confidence limit. Contour interval is 40.

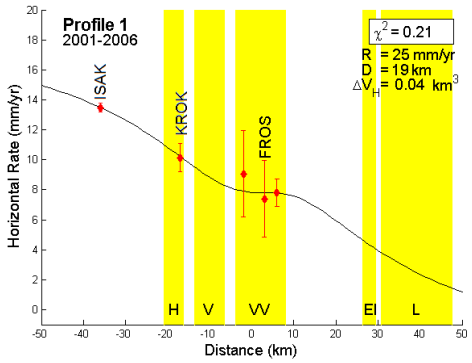


Figure 5.12 Best-fit elastic half-space model (black line) for 2001-2006 GPS-derived site velocities (relative to stable Eurasia) along profile 1. Velocities are corrected for deformation due to Hekla volcano (ΔV_H = 0.04 km^3). Names of central volcanoes and fissure swarms as in Figure 3.14, and figure description as in Figure 5.2.

For 2001-2006 velocities along profile 1 corrected for deformation due to Hekla volcano, it can be seen that the western-most site along the profile, ISAK (Figure 5.1), has a larger measured site velocity from 2001-2006 (just under 14 mm/yr, Figure 5.12) compared to the velocity for 1994-2003 (~12 mm/yr, Figure 5.8), and also has the most well constrained site velocity. Due to the low data coverage across profile 1 between 2001 and 2006, this large, well constrained velocity value at ISAK has a significant effect on modelling results as only a model with an unrealistically large spreading rate (>25 mm/yr), larger than the total spreading rate at this latitude, and locking depth (19 km) deeper than the estimated seismogenic crustal thickness for this region, can fit the ISAK site velocity as well as the remaining data points within their uncertainties.

As can be seen from the contour plot in Figure 5.11, numerous models with lower extension rates provide reasonable fits to the data, however, they have slightly larger χ^2 values compared to the best-fit model. One such model (extension rate of 16.0 mm/yr and a locking depth of 12.0 km) is plotted in Figure 5.13, however, the locking depths for this model is still not realistic thought as it is larger than the seismogenic crustal thickness measured in this region.

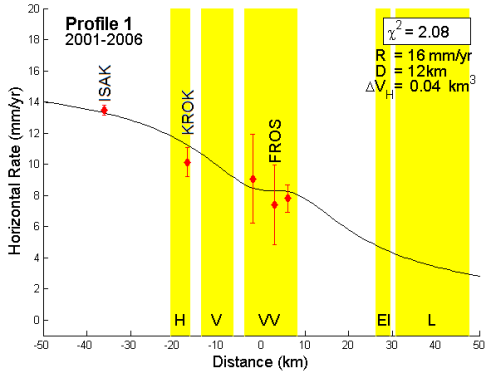
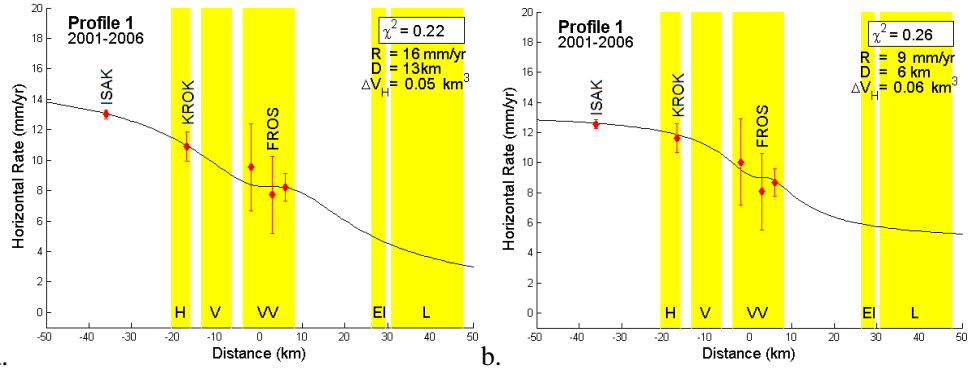


Figure 5.13 Alternative elastic half-space model (black line) for 2001-2006 GPS-derived site velocities (relative to stable Eurasia) along profile 1. Velocities are corrected for deformation due to Hekla volcano (ΔV_H = 0.04 km^3). Names of central volcanoes and fissure swarms as in Figure 3.14, and figure description as in Figure 5.2.

The effects of larger volume changes at Hekla are investigated to determine if 2001-2006 velocities along profile 1 corrected for a larger volume change give rise to more realistic spreading models. The best-fit models for data corrected for a 0.05 km^3 and 0.06 km^3 Hekla volume change are plotted in Figure 5.14a and b, respectively. As the volume change for Hekla is increased, the difference between the horizontal velocities of ISAK and KROK GPS sites along the western part of the profile decreases (best seen in Figure 5.13 compared with Figure 5.14b, as the volume change increases the velocity value for ISAK decreases while KROK increases). In the case of the 2001-2006 dataset this decrease allows for models with smaller extension rates and locking depths to fit the data. For a Hekla volume change of 0.05 km^3 the spreading rate, 16.0 (+0.7/-0.8) mm/yr, and the locking depth, 13.0 (+2.4/-2.0) km are still relatively large, especially considering the estimated seismogenic crustal thickness for this region (12 km, Stefánsson et al. (1993)). For a Hekla volume change of 0.06 km^3 the spreading rate, 9.0 (+0.6/-0.8) mm/yr, and the locking depth of 6.0 (+4.1/-2.8) km is more realistic.



a. b.

Figure 5.14 Best-fit elastic half-space models (black line) for 2001-2006 GPS-derived site velocities relative to stable Eurasia along profile 1, corrected for deformation due to Hekla volcano, with ΔV_H of (a) 0.05 km^3 and (b) 0.06 km^3. Names of central volcanoes and fissure swarms as in Figure 3.14, and figure description as in Figure 5.2.

The best-fit model parameters (extension and depth) and uncertainties for the 1994-2003 and 2001-2006 velocities along profile 1, corrected for deformation of Hekla volcano (ΔV_H), that have been discussed above are summarised in Table 5.4.

Table 5.4 Parameter estimates and uncertainties for spreading models fit to 1994-2003 and 2001-2006 GPS-derived site velocities (relative to stable Eurasia) along profile 1. Velocities are corrected for various Hekla volcano deformation models (ΔV_H). See Table 5.1 for detailed table description.

Dataset	ΔV_H (km^3)	Rate (mm/yr)	Depth (km)	χ^2	χ^2_v	
1994-2003	0.03	10.0 (±1.8)	5.0 (+5.6/-3.0)	7.64	0.69 (*N*=13, *p*=2)	Figure 5.8
2001-2006	0.04	25.0 (±0.9)	19.0 (+1.8/-1.5)	0.21	0.07 (*N*=5, *p*=2)	Figure 5.12
		16.0 (+2.3/-2.2)	12.0 (+7.2/-6.0)	2.08	0.69	Figure 5.13
	0.05	16.0 (+0.7/-0.8)	13.0 (+2.4/-2.0)	0.22	0.07	Figure 5.14a
	0.06	9.0 (+0.6/-0.8)	6.0 (+4.1/-2.8)	0.26	0.09	Figure 5.14b

While 1994-2003 velocities along profile 1 are fit with a realistic plate spreading model, the same is not the case for the 2001-2006 dataset. The effect of Hekla deformation on these velocities appears to be underestimated by "dry-tilt", and only by correcting the data for larger volume change values for Hekla are realistic spreading models able to fit the data. In the following section 2001-2006 velocities along profile 2 are investigated.

5.3.2 Profile 2

Profile 2 crosses Torfajökull volcano and the Eldgjá fissure swarm (Figure 5.1). Sites along the western part of the profile are close to Hekla volcano (~20 km from the Mogi source) and therefore are affected by the inflation-deflation cycles of this active volcano. Data collected at GPS sites along this profile are first corrected for uplift due to Hekla volcano using the volume change values explored for profile 1, and then for deflation due to a proposed cooling magma chamber below the western part of Torfajökull volcano.

Spreading rates north and south of Torfajökull volcano constrain extension rates through the centre of the volcano since, in a propagating ridge system, spreading decreases in the direction of propagation, i.e., to the southeast (Óskarsson et al. 1985; Einarsson 1991; LaFemina et al. 2005). The location of the axis of spreading for the models is assumed to be east of the HRAS and HRAF GPS site, in line with the location of the spreading centre to the north along profile 1, i.e., along the eastern edge of the Veidivötn fissure swarm (LaFemina et al. 2005 and this study). The Hrafntinnuhraun (HRAF) and Hrafntinnusker (HRAS) lavas on which the similarly named GPS sites are located, were erupted from

fissures that follow the same northeast-southwest trend as the Veidivötn fissure swarm to the north, with a possible link between activity on these fissures (Larsen 1984)

Best-fit model parameters and uncertainties for the 2001-2006 velocities along profile 2, that have been corrected for deformation due to Hekla volcano for a range of volume change values (ΔV_H = 0.04 km^3 as determined from "dry-tilt", and 0.06 km^3 as explored for profile 1, Table 5.3) are summarised in Table 5.5 and Figure 5.15. These horizontal velocity data once corrected for Hekla deformation show a clear increasing trend from the southeast of the profile to the northwest (from right to left in Figure 5.15). Sites along the western part of the profile (i.e., within the western part of the caldera) appear to be affected by additional process(es), as data show a scatter around this increasing trend due to plate motion.

Table 5.5 Parameter estimates and uncertainties for spreading models fit to 2001-2006 GPS-derived site velocities (relative to stable Eurasia) along profile 2. Velocities are corrected for various Hekla volcano deformation models (ΔV_H). See Table 5.1 for detailed table description.

ΔV_H (km^3)	Rate (mm/yr)	Depth (km)	χ^2	χ^2_ν (N=5; p=2)	
0.04	12.0 (±8.5)	11.0[a]	4.07	1.36	Figure 5.15a
0.06	9.0 (±3.0)	3.0 (+11/-3)	2.43	0.81	Figure 5.15b

[a] These depth estimates cannot be constrained within reasonable values of crustal thickness.

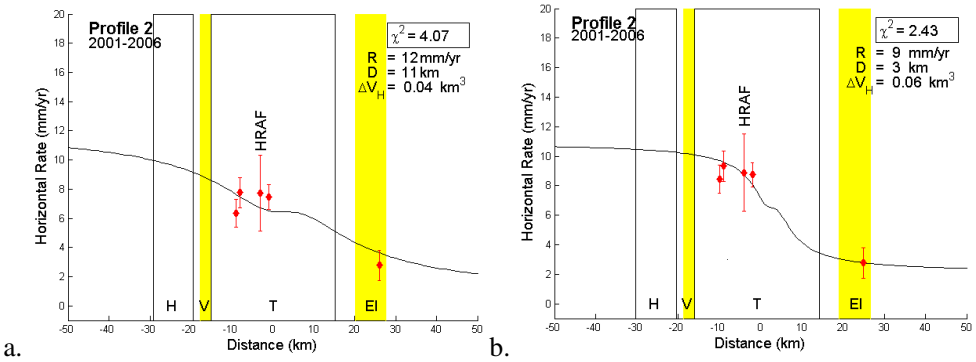


Figure 5.15 Best-fit elastic half-space models (black line, Table 5.5) for 2001-2006 GPS-derived site velocities (relative to stable Eurasia) along profile 2. Velocities are corrected for deformation due to Hekla volcano, with ΔV_H of (a) 0.04 km^3 and (b) 0.06 km^3. Names of central volcanoes and fissure swarms as in Figure 3.14, and figure description as in Figure 5.2.

Soosalu and Einarsson (1997; 2004) were the first to propose a cooling magma chamber below the western part of Torfajökull volcano based on seismicity. The location of the magma chamber was interpreted as being at a depth of 8 km at 19.23ºW and 63.97ºN, i.e., slightly north of HRAF site (Figure 5.1). Lippitsch et al. (2005) linked a sharp cut-off in seismicity at 3 km depth to the top of a magma chamber or intrusion in the western part of the volcano, with the extensive high-temperature geothermal fields within the volcano being explained as the product of natural heat loss from this shallow cooling body. A 1993-2000 InSAR image of the volcano (Figure 5.16) shows subsidence to the south of HRAF, with maximum subsidence just south of the GPS site HRAS (A. Hooper pers comm. 2007). In general the location of a magma chamber at depth below the lavas on which the HRAF and HRAS sites are placed is favourable as both sites are positioned on flows erupted during the most recent eruptive activity at the volcano in 870 A.D. and 1477 A.D., respectively (Larsen 1984; Arnórsson et al. 1987). It is assumed for this study that a magma chamber exists at depth in the region showing maximum subsidence on the InSAR image of Torfajökull caldera (19.22ºW, 63.93ºN, Figure 5.16), despite the fact that the two datasets were collected over different time periods.

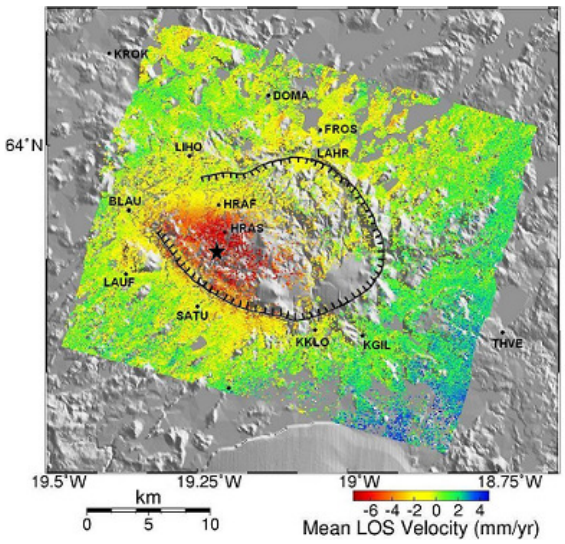


Figure 5.16 InSAR image of Torfajökull caldera generated from SAR images taken of the caldera from 1993 to 2000 (A. Hooper pers comm. 2007). GPS sites within and surrounding the caldera (hatched line) are marked, and the assumed location of the magma chamber is indicated with a black star within the area experiencing subsidence.

The sites are corrected for Torfajökull deformation by removing the velocity component due to deflation, parallel to the plate motion direction (N78°W), from the component of the measured GPS velocities (relative to stable Eurasia) listed in Table 3.4 parallel to the plate motion direction. Deformation rates (in mm/yr) can be removed from the GPS site velocities instead of yearly displacements having to be removed from the initial daily position estimates as the deformation of Torfajökull volcano spans the entire time period of both surveys.

As data coverage across profile 2 is limited, it is not possible to constrain an exact model for plate spreading through the volcano or for magmatic processes occurring at depth in the western part of Torfajökull volcano. Table 5.6 therefore provides a range of Mogi models (volume change, ΔV_T, and depth, D_T) used to correct GPS velocities along profile 2 for Torfajökull deformation (as well as for Hekla deformation), along with the best-fit plate spreading models to the corrected data. The plate spreading models fit to velocities corrected for Torfajökull deformation and a Hekla volume change of 0.04 km^3 are plotted in Figure 5.17, and for a Hekla volume change of 0.06 km^3 in Figure 5.18.

Table 5.6 Parameter estimates and uncertainties for spreading models fit to 2001-2006 GPS-derived site velocities (relative to stable Eurasia) along profile 2. Velocities are corrected for various Hekla (ΔV_H) and Torfajökull volcano deformation models (magma chamber depth, D_T and volume change, ΔV_T). See Table 5.1 for detailed table description.

ΔV_H (km^3)	ΔV_T (km^3)	D_T (km)	Rate (mm/yr)	Depth (km)	χ^2	χ^2_ν (N=5; p=2)	
0.04	-0.02	10	9.0 (+0.9/-1.0)	3.0 (+1.8/-0.9)	0.10	0.03	Figure 5.17a
	-0.01	8	9.0 (+2.3/-2.3)	4.0 (+6.4/-2.6)	0.48	0.16	Figure 5.17b
	-0.01	6	10.0 (+1.4/-1.4)	4.0 (+2.7/-1.7)	0.17	0.06	Figure 5.17c
	-0.005	4	8.0 (+1.6/-1.5)	3.0 (+3.4/-1.8)	0.27	0.09	Figure 5.17d
0.06	-0.005	6	10.0 (+1.1/-1.4)	3.0 (+2.1/-1.2)	0.17	0.06	Figure 5.18a
	-0.002	3	9.0 (+2.2/-1.8)	3.0 (+3.5/-3)	0.46	0.15	Figure 5.18b

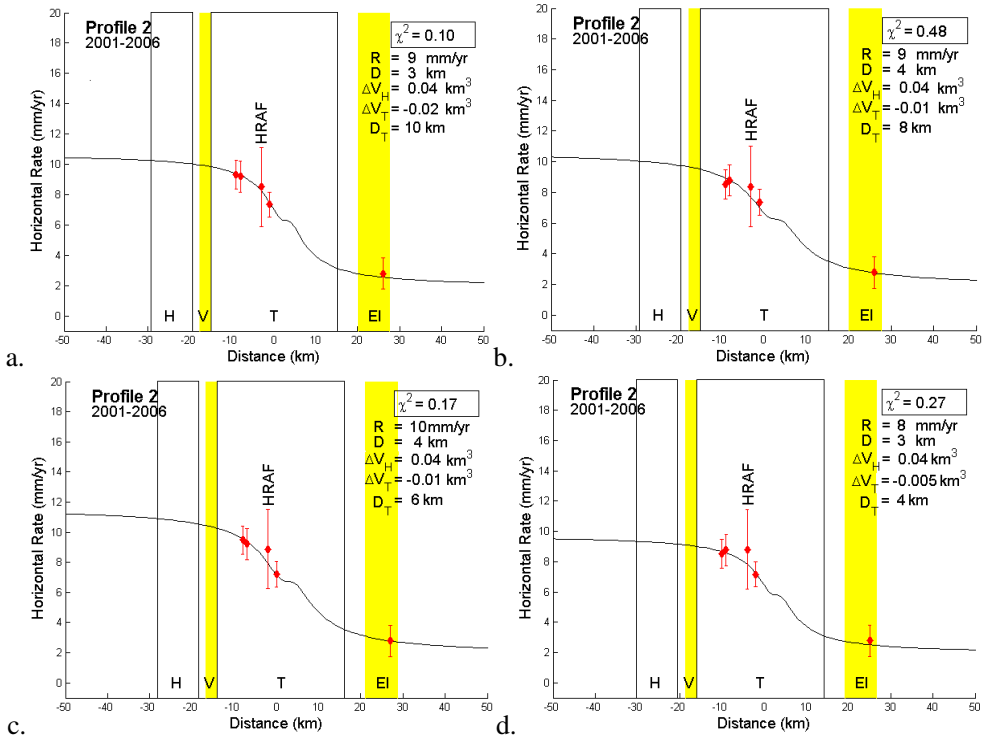


Figure 5.17 Best-fit elastic half-space models (black line, Table 5.6) for 2001-2006 GPS-derived site velocities (relative to stable Eurasia) along profile 2. Velocities are corrected for deformation due to Hekla volcano (ΔV_H = 0.04 km^3), and varying deformation due to Torfajökull volcano (ΔV_T, D_T). Names of central volcanoes and fissure swarms as in Figure 3.14, and figure description as in Figure 5.2.

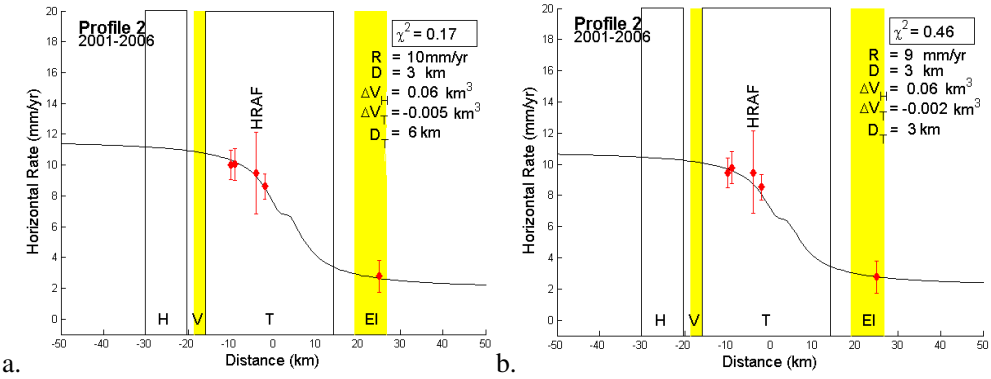


Figure 5.18 Best-fit elastic half-space models (black line, Table 5.6) for 2001-2006 GPS-derived site velocities (relative to stable Eurasia) along profile 2. Velocities are corrected for deformation due to Hekla volcano (ΔV_H = 0.06 km^3), and varying deformation due to Torfajökull volcano (ΔV_T, D_T). Names of central volcanoes and fissure swarms as in Figure 3.14, and figure description as in Figure 5.2.

For a Hekla volume change of 0.04 km^3 it can be seen that a range of Torfajökull Mogi models (Table 5.6 and Figure 5.17) improve the fit of the data to the plate spreading models when compared to the models shown in Figure 5.15. Mogi models range from deep sources (D_T = 10 km) experiencing a large volume change (ΔV_T = -0.02 km^3), to a shallow source (4 km) experiencing a smaller volume change (-0.005 km^3) (Table 5.7). In the case of the larger volume change for Hekla (0.06 km^3, Table 5.6 and Figure 5.18) only a relatively (3 to 6 km) shallow source experiencing a small volume change (-0.002 to -0.005 km^3) at Torfajökull improves the fit of the data when compared to the models shown in Figure 5.15. Extension rates fit to these GPS-derived site velocities are between 8 and 10 mm/yr, with locking depths of between 3 and 4 km.

Table 5.7 Site displacements and rates for the periods 2001-2006 for sites along profile 2 due to deformation of Torfajökull volcano. The displacements and rates are calculated using a Mogi source at a depth of 4 km, experiencing a volume change of -0.005 km^3.

	Displacement (m)			Rate (mm/yr)		
Sites	**East**	**North**	**Vertical**	**East**	**North**	**Vertical**
BLAU	0.0121	-0.0059	-0.0067	2.04	-0.99	-1.14
HRAF	0.0016	-0.0234	-0.0195	0.26	-3.94	-3.28
HRAS	-0.0077	-0.0276	-0.0422	-1.31	-4.66	-7.11
LAUF	0.0135	0.0038	-0.0073	2.28	0.64	-1.22
LIHO	0.0035	-0.0120	-0.0060	0.60	-2.03	-1.01
SATU	0.0085	0.0231	-0.0219	1.44	3.90	-3.70

Additional information such as InSAR and "dry-tilt" data can be used to constrain the source at Torfajökull volcano to some extent. Maximum line-of-site (LOS) subsidence of ~-8 mm/yr is seen on the 1993-2000 InSAR image of Torfajökull volcano (Figure 5.16). It is assumed that this rate of subsidence does not change significantly over time and therefore conclusions drawn from the 1993-2000 InSAR image may be applied to 2001-2006 GPS data. "Dry-tilt" of 7.2 μrad towards the volcano was measured at site HRAF between 2001 and 2006 (Table 2.4 and Figure 2.11), a site which is approximately 3.75 km from the Torfajökull Mogi source. Table 5.8 lists the tilt values expected at HRAF (equation 4.10, determined using Matlab programs listed in Appendix 10 and 11) and maximum vertical rate (equation 4.7) for a range of Mogi source models, including those listed in Table 5.8. These measured values are not significantly affected by activity at Hekla, with tilt measured at HRAF due to Hekla inflation amounting to <1 μrad and vertical uplift at the location of the Mogi source of ~1 mm/yr.

Table 5.8 Expected "dry-tilt" values for HRAF site (at a distance of 3.75 km from the source) and the maximum vertical subsidence rate for a range of Torfajökull Mogi source models (volume change, ΔV_T, and locking depth, D_T).

ΔV_T (km^3)	D_T (km)	Tilt at HRAF (μrad)	Maximum Subsidence Rate (mm/yr)
-0.02	10	3.8	8.0
	8	8.0	12.5
-0.01	8	4.0	6.3
	7	6.0	8.2
	6	9.1	11.1
-0.005	6	4.5	5.5
	5	7.0	8.0
	4	10.8	12.5
-0.002	4	4.4	5.0
	3	6.3	8.9
	2	7.7	20.2

The tilt and maximum rate of subsidence for the shallower, smaller Mogi source models listed in Table 5.8, for example, ΔV_T = -0.005 km^3 and D_T = 5 km (Figure 5.19a and b), fit the measured tilt value at HRAF between 2001 and 2006 and maximum subsidence rate from the 1993-2000 InSAR better than the deeper, larger sources (ΔV_T = -0.02 km^3 and D_T = 10 km). In addition, the width of the elliptical area experiencing subsidence of ~-4 mm/yr marked on the InSAR image in Figure 5.19c (5-10 km) also correlates well with the width of the vertical displacement curve at -0.024 m displacement (i.e. at a rate of -4 mm/yr) for this model in Figure 5.3b (7.6 km).

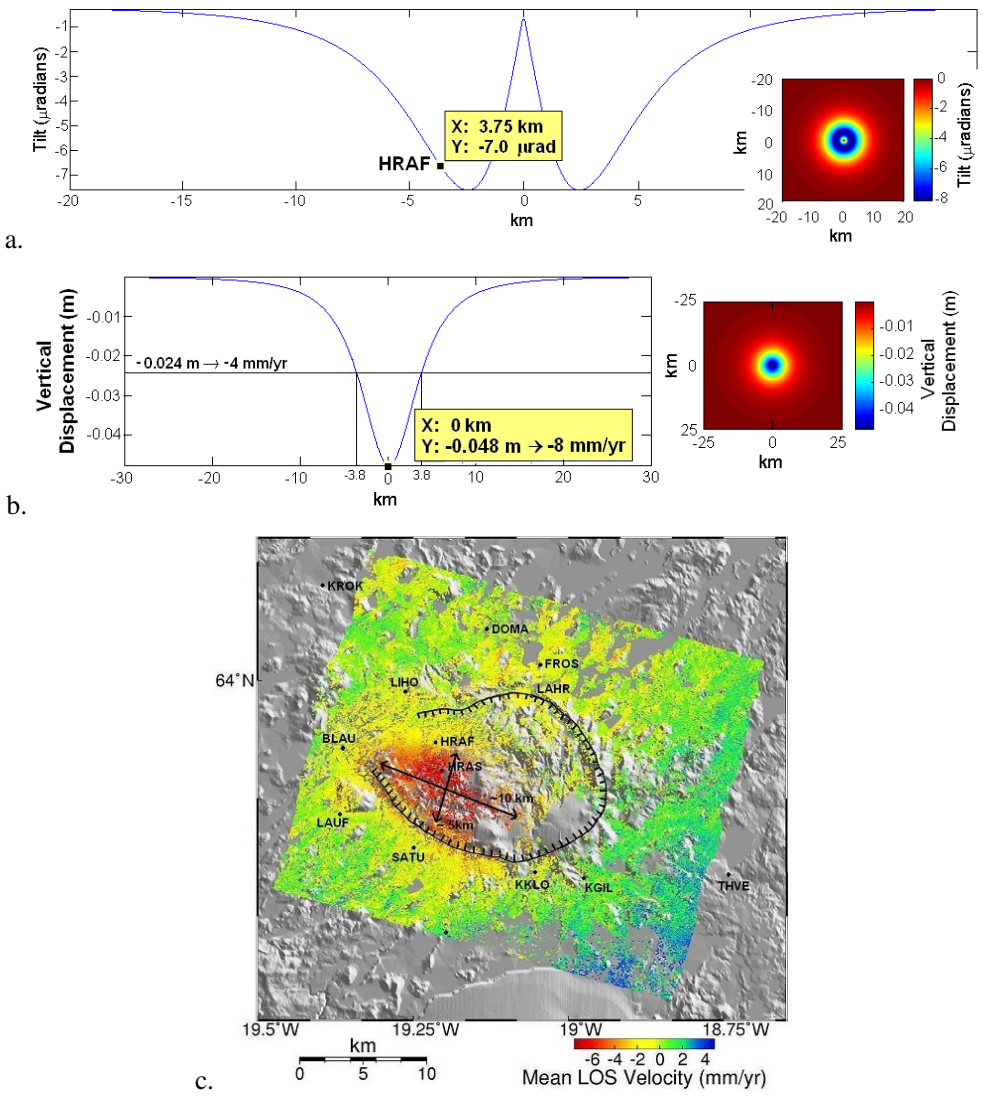


Figure 5.19 Profile and 2-D image of the (a) "dry-tilt" response and (b) vertical displacement due to a Mogi source at 5 km depth experiencing a -0.005 km^3 change in volume. The tilt experienced at HRAF site (at a distance of 3.75 km from the source) and the maximum subsidence (displacement and rate) are indicated. (c) The magma chamber at Torfajökull is assumed to be beneath the area of maximum subsidence as seen in the 1993-2000 InSAR image of the volcano. The extent of the area experiencing subsidence of ~-4 mm/yr is marked (i.e., elliptical pattern with axes between ~5 and 10 km in length).

Only limited conclusions can therefore be drawn regarding plate spreading along profile 2 due to low data coverage and local poorly constrained deformation within Torfajökull caldera. Modelling of 1994-2003 and 2001-2006 GPS-derived site velocities further south along profile 3 are discussed in the following section.

5.3.3 Profile 3

Profile 3 crosses the plate boundary south of Torfajökull volcano, across the Eastern Volcanic Flank Zone (EVFZ) (Figure 5.1). This area is dominated by a group of central volcanoes, including the recently active Katla volcano.

Increased activity at Katla volcano between 1999 and 2004 has been attributed to the accumulation of ~0.01 km^3 of magma in a chamber at 4.9 km depth over this time period (Sturkell et al. 2008). Inflation of the volcano resulted in horizontal displacement of far field sites (>11 km from the caldera centre) at a rate of around 0.5 cm/yr away from the caldera centre (Sturkell et al. 2003b; Sturkell et al. 2008). The location of the Mogi source for Katla is marked in the Figure 5.20. The above estimated chamber depth is however thought to be an overestimate due to the effect of simultaneously occurring glacio-isostatic adjustment of the crust from the melting of Myrdalsjökull icecap that covers Katla volcano (Pinel et al. 2007). Horizontal displacement of far field sites due to this rebound is on the order of ~ 1 mm/yr or less, which is the approximate level of rate uncertainty for this study, and therefore no correction is made for this process.

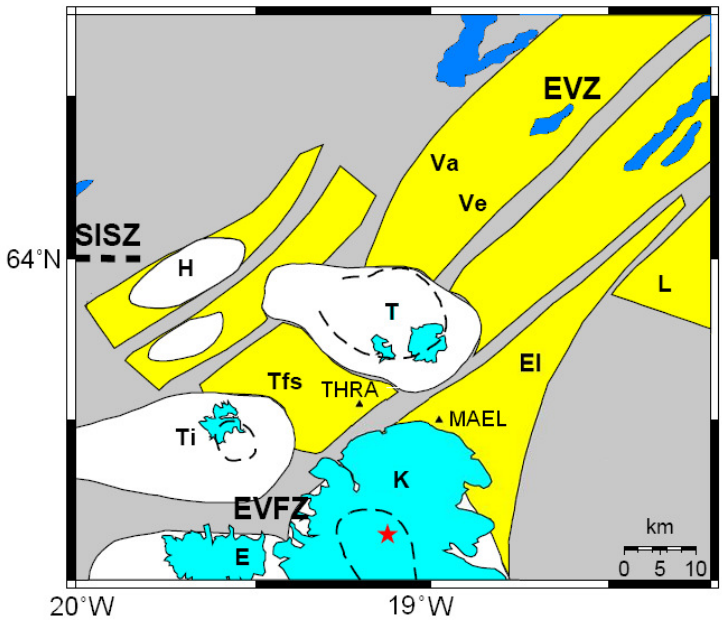


Figure 5.20 Plot of the intersection of the Eastern Volcanic Zone (EVZ), the Eastern Volcanic Flank Zone (EVFZ) and the South Iceland Seismic Zone (SISZ), with the location of the Mogi source below Katla volcano marked with a red star (approximately -19.13°W, 63.72°N, Sturkell et al. (2008)). Names of central volcanoes and fissure swarms as in Figure 3.10.

GPS site THRA which was occupied from 2000 to 2006, is within 15 km of the Katla Mogi source (Figure 5.20). The uplift experienced at THRA from 2000 to 2004 due to Katla inflation is larger than 1 mm/yr, the approximate level of rate uncertainty for this study, and therefore the time series for the site is corrected (Table 5.9). The correction for Katla inflation is applied by removing the yearly inflation rate listed in Table 5.9 from each position estimate recorded for THRA between 2000 and 2004. A new weighted least squares line is then fit to these corrected daily position estimates, from which the velocity value relative to stable Eurasia is recalculated. Data collected at MAEL and THRA (~15 km from the Katla Mogi source) between 1994 and 2003 cannot be corrected for inflation as I did not have access to the original position estimate data files for these sites. However, as can be seen from the deformation rates listed in Table 5.9, the effect of Katla inflation on far-field sites is minimal and therefore will not change the modelling results for the 1994-2003 dataset significantly.

Table 5.9 Site displacements and rates resulting from inflation of Katla volcano over the period 1999 to 2004 for sites along Profile 3. A Mogi source at 4.9 km depth experiencing a volume change of 0.01 km^3 was used to calculate the displacement (Sturkell et al. 2008).

	Displacement (m)			**Rate (mm/yr)**		
Sites	**East**	**North**	**Vertical**	**East**	**North**	**Vertical**
MAEL	0.0027	0.0060	0.0018	0.5	1.2	0.4
THRA	-0.0013	0.0060	0.0016	-0.3	1.2	0.3

Both datasets are also corrected for deformation due to Hekla volcano using the volume change values explored for profile 1 (Table 5.3). Torfajökull deflation is not taken into account when modelling profile 3 data as an exact Mogi model describing the deformation is not well constrained, and as can be seen from the 1993-2000 InSAR (Figure 5.16) subsidence is restricted to the volcanoes caldera. Modelled spreading rates along profile 3 are expected to be lower than those determined for profile 1 as the EVZ forms part of a propagating ridge system, with spreading rates decreasing in the direction of propagation to the southwest (Óskarsson et al. 1985; Einarsson 1991; LaFemina et al. 2005). In addition to this constraint, the site SNAE lies in the southeast of the study area (Figure 5.1), and although this site shows residual motion, it is one of the closest sites that represent the stable Eurasia plate. Any best-fit model should therefore not show a significant decrease in rate to the east of SNAE.

5.3.3.1 1994-2003 Dataset

χ^2 versus extension rate and χ^2 versus locking depth plots for models fit to the 1994-2003 velocities along profile 3, corrected for Hekla deformation, are shown in Figure 5.21 and Figure 5.22, respectively. These plots along with the correlation plot in Figure 5.23 show that the best-fit model is an extension rate of 7.0 (+1.5/-2.2) mm/yr below a locking depth of 3.0 (+8.2/-3.0) km. The model and data are plotted in Figure 5.24.

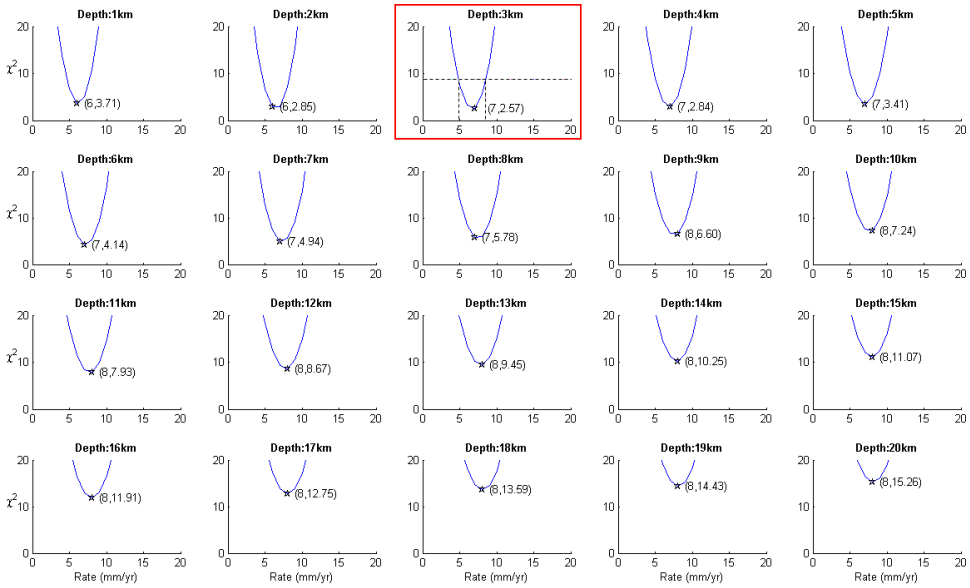


Figure 5.21 Plots of χ^2 versus extension rate for various elastic half-space plate spreading models (with locking depth held fixed for individual plots) fit to 1994-2003 velocities along profile 3. χ^2 equal to 9 represents the approximate 95% confidence limit. See Figure 5.5 for a detailed figure description.

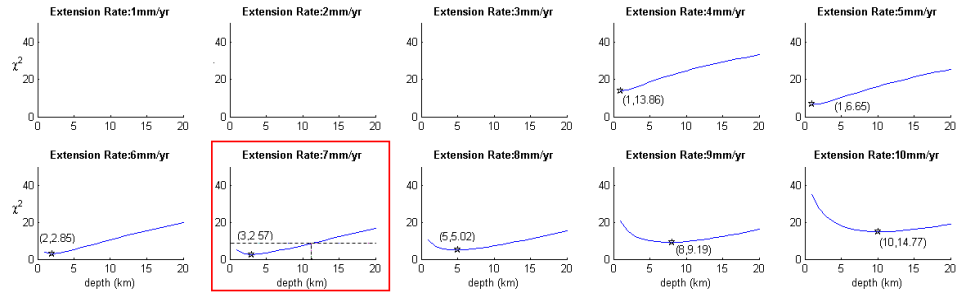


Figure 5.22 Plots of χ^2 versus locking depth for various elastic half-space plate spreading models (with extension rate held fixed for individual plots) fit to 1994-2003 velocities along profile 3. χ^2 equal to 9 represents the approximate 95% confidence limit. See Figure 5.5 and Figure 5.6 for a detailed figure description.

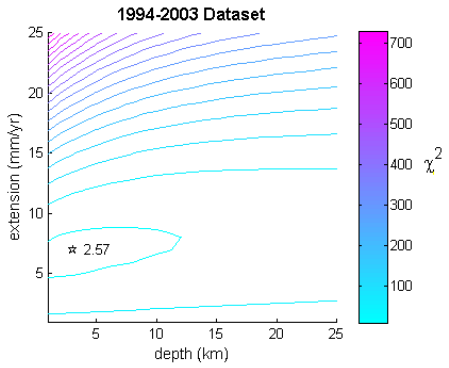


Figure 5.23 Contour plot of χ^2 misfit for estimated extension rates and locking depths for elastic half-space models fit to 1994-2003 velocities along profile 3. χ^2 equal to 9 (inner contour) represents the approximate 95% confidence limit. Contour interval is 40.

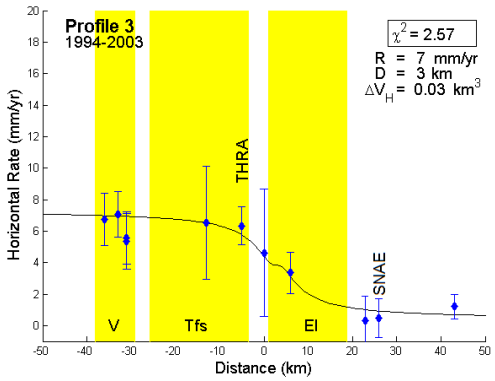


Figure 5.24 Best-fit elastic half-space model (black line) for 1994-2003 GPS-derived site velocities (relative to stable Eurasia) along profile 3. Velocities are corrected for deformation due to Hekla volcano (ΔV_H = 0.03 km^3). Names of central volcanoes and fissure swarms as in Figure 3.14, and figure description as in Figure 5.2.

5.3.3.2 2001-2006 Dataset

χ^2 versus extension rate and χ^2 versus locking depth plots for models fit to the 2001-2006 velocities along profile 3, corrected for Hekla and Katla deformation, are shown in Figure 5.25 and Figure 5.26 respectively. These plots along with the correlation plot in Figure 5.27 show that the best-fit model for the velocities is a dyke with an extension rate of 7.0 (±2.3) mm/yr below a locking depth of 4.0 (+9.9/-2.9) km. The model and data are plotted in Figure 5.28. It must be noted that the 2001-2006 GPS-derived velocity for the site LAUF (Figure 5.1) was not used during modelling as the velocity value had an

extremely poor fit to all models investigated during this study. This large deviation may either be due to a problem with the site, although the uncertainty for the site velocity is not significantly large, or due to a local deformation source that has not been accounted for.

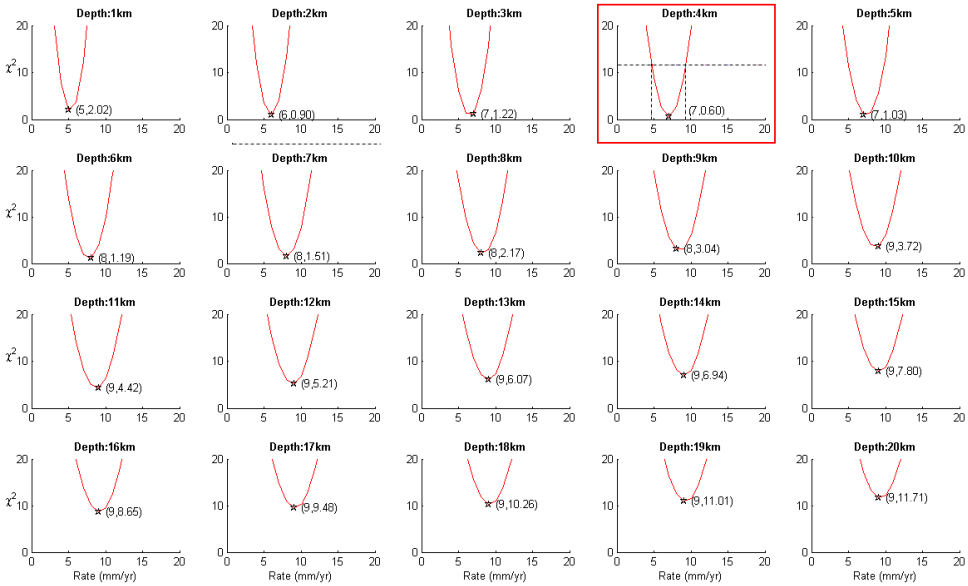


Figure 5.25 Plots of χ^2 versus extension rate for various elastic half-space plate spreading models (with locking depth held fixed for individual plots) fit to 2001-2006 velocities along profile 3. χ^2 equal to 12 represents the approximate 95% confidence limit. See Figure 5.5 for a detailed figure description.

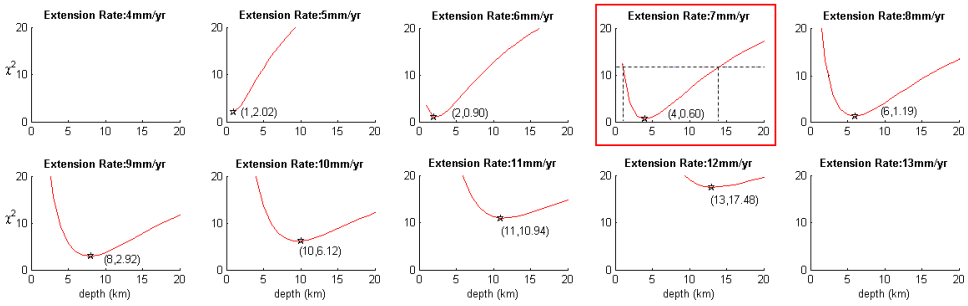


Figure 5.26 Plots of χ^2 versus locking depth for various elastic half-space plate spreading models (extension rate held fixed for individual plots) fit to 2001-2006 velocities along profile 3. χ^2 equal to 12 represents the approximate 95% confidence limit. See Figure 5.5 and Figure 5.6 for a detailed figure description.

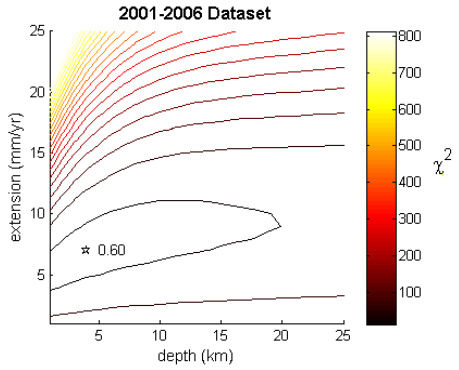


Figure 5.27 Contour plot of χ^2 misfit for estimated extension rates and locking depths for elastic half-space models fit to 2001-2006 velocities along profile 3. χ^2 equal to 12 (inner contour) represents the approximate 95% confidence limit. Contour interval is 40.

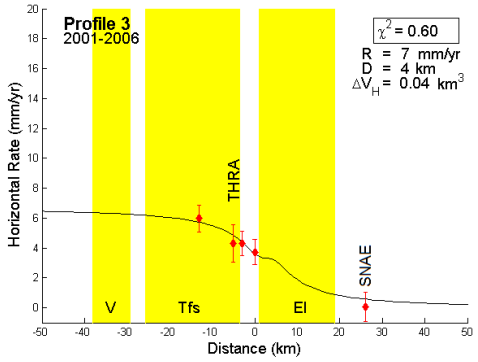


Figure 5.28 Best-fit elastic half-space model (black line) for 2001-2006 GPS-derived site velocities (relative to stable Eurasia) along profile 3. Velocities are corrected for deformation due to Hekla volcano (ΔV_H = 0.04 km^3). Names of central volcanoes and fissure swarms as in Figure 3.14, and figure description as in Figure 5.2.

Plate spreading models are also fit to GPS-derived site velocities corrected for both a 0.05 km^3 (Figure 5.29a) and 0.06 km^3 Hekla volume change (Figure 5.29b), in keeping with volume change values investigated for profile 1. The best-fit model is an extension rate of 7.0 (+2.7/-2.5) mm/yr and 8.0 (+3.4/-3.0) mm/yr, respectively, and locking depths of 3.0 (+10.8/-2.6) km and 4.0 (+13.5/-3.4) km, respectively.

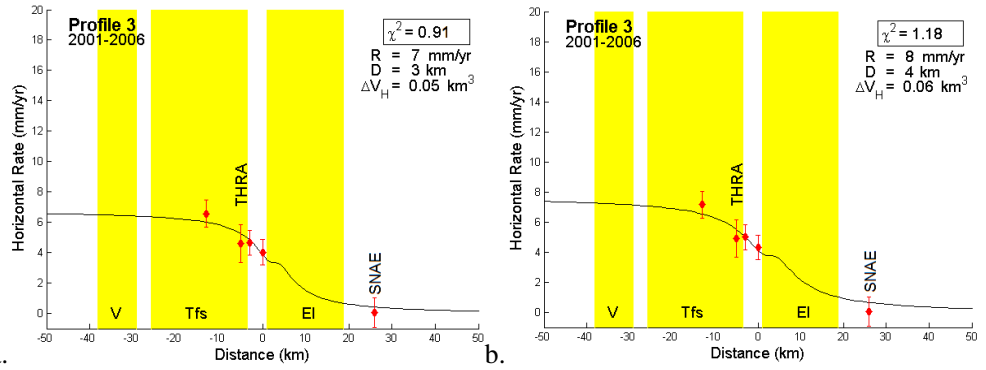


Figure 5.29 Best-fit elastic half-space model (black line) for 2001-2006 GPS-derived site velocities (relative to stable Eurasia) along profile 3. Velocities are corrected for deformation due to Hekla volcano, due to a volume change (ΔV_H) of (a) 0.05 km^3 and (b) 0.06 km^3. Names of central volcanoes and fissure swarms as in Figure 3.14, and figure description as in Figure 5.2.

As can be seen from the location of the centre of spreading in the above plots (Figure 5.24, Figure 5.28 and Figure 5.29), which was held constant, the axis of spreading is along the western edge of the Eldgjá fissure swarm which was last active in 934 A.D. (Table 2.1and Figure 5.1, Stothers (2004)). The best-fit dyke model parameters (extension and depth) and uncertainties for the 1994-2003 and 2001-2006 velocities along profile 3, corrected for deformation due to Hekla (ΔV_H) and Katla volcano are summarised in Table 5.10.

Table 5.10 Parameter estimates and uncertainties for spreading models fit to 1994-2003 and 2001-2006 GPS-derived site velocities (relative to stable Eurasia) along profile 3. Velocities are corrected for various Hekla volcano deformation models (ΔV_H). See Table 5.1 for detailed table description.

Dataset	ΔV_H	Rate (mm/yr)	Depth (km)	χ^2	χ^2_v	
1994-2003	0.03	7.0 (+1.5/-2.2)	3.0 (+8.2/-3.0)	2.57	0.29 (N=11, p=2)	Figure 5.24
2001-2006	0.04	7.0 (±-2.3)	4.0 (+9.9/-2.9)	0.61	0.20 (N=5, p=2)	Figure 5.28
	0.05	7.0 (+2.7/-2.5)	3.0 (+10.8/-2.6)	0.91	0.30	Figure 5.29a
	0.06	8.0 (+3.4/-3.0)	4.0 (+13.5/-3.4)	1.18	0.39	Figure 5.29a

Realistic plate spreading models are fit to both the 1994-2003 and 2001-2006 GPS-derived site velocities along profile 3, and the two models are in agreement within uncertainties. In the following chapter the above modelling results are discussed and compared with results from previous studies, and conclusions drawn are summarised.

6 DISCUSSION & CONCLUSIONS

6.1 Discussion

Due to the complex interaction between the Mid-Atlantic Ridge (MAR) and North Atlantic mantle plume at the latitude of Iceland, the spreading centre has experienced successive eastward migrations or jumps since ~23 Ma (Óskarsson et al. 1985; Hardarson et al. 1997; Garcia et al. 2003). The west-northwest motion of the ridge relative to the mantle plume in east-central Iceland (Pálmason 1981; Einarsson and Eiríksson 1982; Meyer et al. 1985; Óskarsson et al. 1985) led to the last ridge jump ~2-3 Ma which resulted in the formation of the Eastern Volcanic Zone (EVZ) (Sæmundsson 1974; 1978; 1979). The earlier formed Western Volcanic Zone (WVZ) and EVZ form an overlapping, subparallel ridge system in south Iceland (Óskarsson et al. 1985; Hardarson et al. 1997; Garcia et al. 2003) that accommodates a large portion of plate motion, with the eastern limb propagating towards the southwest, and the western limb deactivating in the same direction (Óskarsson et al. 1985; Einarsson 1991; LaFemina et al. 2005).

South of the intersection of the South Iceland Seismic Zone (SISZ) and EVZ the ridge is propagating to the southwest into the Eastern Volcanic Flank Zone (EVFZ), a zone dominated by central volcanoes (Einarsson 1991). Further to the west, plate motion is accommodated across the Reykjanes Peninsula (RP) which forms the transition between the Reykjanes Ridge offshore and the WVZ and SISZ, and is oriented highly oblique to the offshore ridge and volcanic zones (Einarsson 1991). The observations from this study have implications for spreading across the EVZ, and the partitioning of spreading between it and the WVZ, as well as partitioning of spreading between the RP and the more recent location of rifting in the EVFZ.

6.1.1 Along-strike variations in spreading

In an overlapping ridge system such as in south Iceland, it has been shown that strain and therefore the full plate rate (~18-20 mm/yr in a direction N(102-104)°E, (DeMets et al. 1994; Sella et al. 2002)) is partitioned between spreading centres (Hey 1977; Hey et al. 1980), with spreading increasing on the deactivating limb (WVZ) and decreasing on the propagating limb (EVZ) in the direction of propagation (i.e., to the southwest in south Iceland). LaFemina et al. (2005) demonstrated this latitude-dependence of spreading in the neovolcanic zones in south Iceland, and showed that rifting is occurring south of the SISZ-EVZ intersection into the EVFZ, with the remaining extension south of the SISZ supposedly being taken up across the RP (Hreinsdóttir et al. 2001). Spreading rates determined during this study show along strike variations in the EVZ, with the extension decreasing from north to south into the EVFZ (Table 6.1).

Table 6.1 Parameter estimates and uncertainties for spreading models fit to 1994-2003 and 2001-2006 GPS-derived site velocities (relative to stable Eurasia) along profile 1 and 3. Models where the velocities were corrected for various Hekla volcano deformation models (ΔV_H) are also given. See Table 5.1 for detailed table description.

	Dataset	ΔV_H (km^3)	Rate (mm/yr)	Depth (km)	χ^2	*N*	χ^2_ν (*p*=2)	
Profile 1	1994-2003	0	13.0 (+2.7/-2.5)	9.0 (+8.4/-4.7)	12.73	13	1.16	Figure 5.2a
		0.03	10.0 (±1.8)	5.0 (+5.6/-3.0)	7.64		0.69	Figure 5.8
	2001-2006	0	49.0 (+5.5/-5.6)	21.0 (+6.9/-5.3)	8.70	5	2.90	Figure 5.3a
		0.04	25.0 (±0.9)	19.0 (+1.8/-1.5)	0.21		0.07	Figure 5.13a
			16.0 (+2.3/-2.2)	12.0 (+7.2/-6.0)	2.08		0.69	Figure 5.13b
		0.05	16.0 (+0.7/-0.8)	13.0 (+2.4/-2.0)	0.22		0.07	Figure 5.14a
		0.06	9.0 (+0.6/-0.8)	6.0 (+4.1/-2.8)	0.26		0.09	Figure 5.14b
Profile 3	1994-2003	0	5.0 (+2.8/-2.6)	2.0 (+21.2/-2.0)	6.09	11	0.68	Figure 5.2b
		0.03	7.0 (+1.5/-2.2)	3.0 (+8.2/-3.0)	2.57		0.29	Figure 5.24
	2001-2006	0	4.0 (+2.3/-2.2)	3.0[a]	0.68	5	0.23	Figure 5.3c
		0.04	7.0 (±2.3)	4.0 (+9.9/-2.9)	0.61		0.20	Figure 5.28
		0.05	7.0 (+2.7/-2.5)	3.0 (+10.8/-2.6)	0.91		0.30	Figure 5.29a
		0.06	8.0 (+3.4/-3.0)	4.0 (+13.5/-3.4)	1.18		0.39	Figure 5.29a

[a] These depth estimates cannot be constrained within reasonable values of crustal thickness.

The majority of chi-squared (χ^2) values listed in Table 6.1 have a magnitude of less than one. Although the χ^2 value is a measure of the goodness-of-fit of a model to data, with a low value implying a better fit (Bevington 1969), the above low values are rather a sign of limited data coverage as it is often easier to fit a model to fewer data points. This is

also seen for the reduced chi-squared values $\left(\chi_\nu^2\right)$ in Table 6.1, as a value of one implies a model is a good approximation to the data, while a value of less than one does not necessarily indicate an improvement of the fit (Bevington 1969). Very small χ^2 and χ_ν^2 values can therefore imply "too good" a fit or in other words an unrealistic model.

6.1.2 Profile 1

For sites within ~30 km of the Hekla volcano along all three profiles it is evident that a component of the measured GPS velocities is due to the continuous deformation of Hekla volcano. If no correction for Hekla inflation after the 2000 eruption is made to the 2001-2006 velocities along profile 1, then spreading rates (>49 mm/yr) and locking depths (~21 km) that are unrealistically large considering the total plate spreading rate for Iceland (~18-20 mm/yr, DeMets et al. (1994) and Sella et al. (2002)), and the estimated seismogenic thickness of the crust at the intersection of the SISZ and EVZ (12 km, Stefánsson et al. (1993)), are needed to model the data (Table 6.1). The location of the axis of spreading for all profile 1 models is held fixed along the Veidivötn fissure swarm, which was last active in 1477 A.D. (Larsen 1984) and is in agreement with the location proposed by LaFemina et al. (2005).

The 1994-2003 dataset spans the inflation period before the major eruption of Hekla in 2000 which was characterised by rapid subsidence, as well as the re-inflation period after the eruption. Best-fit models for this dataset are realistic even if velocity values are not corrected for deformation due to Hekla volcano, though in this case velocities measured at GPS sites closest to the volcano show significant deviation from the best-fit curve (e.g., ISAK, DROP and BRSK). The best-fit model for these uncorrected 1994-2003 GPS-derived velocities along profile 1 is an extension rate of 13.0 (+2.7/-2.5) mm/yr (Table 6.1), which is within the limit of the total plate spreading rate for Iceland. This estimate is similar to previously determined rates of ~12 mm/yr (Jónasson et al. 1997) and 11.0 (± 0.8) mm/yr (LaFemina et al. 2005) within model uncertainties. The best-fit model locking depth is 9.0 (+8.4/-4.7) km (Table 6.1), which is within the limits of the seismogenic crustal thickness estimated for this region, and is deeper than the previous estimate by LaFemina et al. (2005) of 3.0 (+1.2/-0.7) km.

It is therefore clear from "dry-tilt" measurements made on the flank of Hekla, and GPS-derived velocities for sites close to the volcano, that Hekla volcano has been actively deforming over the time period of both survey. As a result modelled data must first be corrected for this deformation using volume change values determined from the tilt data. In the case of the 2001-2006 dataset corrected for a Hekla volume change of 0.04 km^3, the best-fit model is an extension rate of 25.0 (±0.9) mm/yr below a locking depth of 19.0 (+1.8/-1.5) km (Table 6.1). These model parameters are still unrealistically large. With the limited data coverage that exists for the 2001-2006 dataset, particularly along the eastern part of the profile, we are unable to draw any further conclusions about the best-fit model for this profile. For this study, in general, the accuracy level of models fit to 2001-2006 velocities is reduced due to low data coverage.

It must therefore be assumed that either previous studies have underestimated the extension rate and locking depth at this latitude along the EVZ, or that the volume change value calculated from "dry-tilt" for Hekla volcano between 2001 and 2006 is underestimated, a likely scenario as one "dry-tilt" site is not sufficient to constrain accurately processes taking place at depth. It is shown in this study that accounting for a larger volume change value for Hekla volcano (0.05 km^3 and 0.06 km^3) between 2001 and 2006 allows modelling of GPS-derived site velocities using more realistic plate spreading models. For a Hekla volume change of 0.05 km^3 the best-fit spreading rate, 16.0 (+0.7/-0.8) mm/yr (Table 6.1), is in-line with the estimate by Sigmundsson et al. (1995) that 85 ± 15% of spreading is taken up across the EVZ (i.e., 15-21 mm/yr, LaFemina et al. (2005)), but is larger than previous estimates by Jónasson et al. (1997) and LaFemina et al. (2005). The estimated locking depth, 13.0 (+2.4/-2.0) km (Table 6.1), is only slightly larger than the seismogenic crustal thickness estimated for the SISZ-EVZ intersection. For a volume change of 0.06 km^3, the best-fit model is a dyke experiencing extension of 9.0 (+0.6/-0.8) mm/yr below a locking depth of 6.0 (+4.1/-2.8) km (Table 6.1), which is more realistic and in line with previous estimates for this profile (Jónasson et al. 1997; LaFemina et al. 2005).

For the 1994-2003 dataset corrected for Hekla deformation (ΔV_H=0.03 km^3) the best-fit spreading model is a dyke experiencing extension of 10.0 (±1.8) mm/yr below a locking depth of 5.0 (+5.6/-3.0) km (Table 6.1). This model is realistic and is in agreement with previous estimates for this profile (Jónasson et al. 1997; LaFemina et al. 2005).

6.1.3 Profile 2

For GPS-derived site velocities collected at sites along profile 2, through Torfajökull volcano, it is not possible to fit a realistic plate spreading model to the data without correcting for deformation due to Hekla volcano first. After correcting for a Hekla volume change of between 0.04 and 0.06 km^3 it can be seen that the GPS-derived site velocities increase from the southeast to the northwest along the profile. This increasing trend is indicative of the increase in plate spreading rates away from the stable Eurasia plate, and shows ridge propagation and therefore spreading is taking place through Torfajökull volcano.

Correcting these GPS-derived site velocities for deflation due to a cooling and contracting magma source below the western part of Torfajökull volcano, with the location of the source constrained by InSAR data, also improves the fit of the dyke model to the data. It is however not possible to determine one well-constrained spreading and Torfajökull Mogi source model as data coverage along profile 2 is limited, though constraints can be placed on the solution. More GPS sites are needed at locations outside of Torfajökull volcano in order for background plate spreading to be modelled, therefore allowing the signal due to Torfajökull deflation measured at the existing sites within the volcano to be constrained.

For this study the Hekla volume change values investigated for profile 1 (i.e. 0.04 km^3 and 0.06 km^3) are used to determine the range of Mogi source models for Torfajökull that improve the fit of the velocity data to the plate spreading model. For a Hekla source volume change of 0.04 km^3, the Torfajökull model range includes source depths from 4 km to 10 km and volume changes from -0.005 km^3 to -0.02 km^3. For larger volume changes at Hekla volcano (0.06 km^3) only a relatively shallow source (3 to 6 km) and small volume change (-0.002 to -0.005 km^3) for Torfajökull deformation result in a fit of realistic plate spreading models.

A shallower, smaller source at Torfajökull volcano is more realistic as the volcano has not been active since 1477 A.D. (Larsen 1984) and is most likely experiencing slow cooling and contraction of a magma chamber at depth (Dzurisin et al. 2002). Extensive high-temperature geothermal fields within the volcano (Arnórsson et al. 1987; Bjarnason and

Olafsson 2000) mean that a slowly contracting source would have to be shallow enough for the natural heat loss during cooling to feed the geothermal system. A shallow source is also supported by seismic studies, with Lippitsch et al.(2005) recognising a sharp cut-off in seismicity at 3 km depth below the western part of the volcano, possibly indicative of the roof of a magma source. Tilt and InSAR data collected within the volcano also support a shallow, small source. Extension rates for plate spreading models fit to these GPS-derived site velocities corrected for Hekla deformation and a range Torfajökull Mogi source models are between 8 and 10 mm/yr, which are within the spreading rate interval determined from profile 1 and 3 spreading rates. The best-fit locking depths are between 3 and 4 km.

It must be noted however that due to the limited data coverage (GPS and "dry-tilt") along profile 2, the above model results cannot be confirmed and the accuracy level cannot be precisely determined. In addition, other complex processes such as geothermal activity and gravitational loading of the crust are operating within Torfajökull volcano, and could be affecting the measured GPS signal therefore calling into question the legitimacy of the above models. The extensive geothermal activity within Torfajökull caldera could be adding to the measured ground deformation as has been seen at other volcanoes (e.g., Campi Flegrei, Bonafede (1991)), leading to an overestimate of the volume change experienced by a chamber at depth. It has also been shown that subsidence at volcanoes may not necessarily be due only to thermal contraction or magma crystallization at depth, but instead be caused mainly by gravitational loading of the thermally weakened crust by the mass of the volcano, as well as thinning of this weakened crust by rifting (e.g., Medicine Lake volcano in northern California where unrealistically large Mogi source models were needed to explain observed levels of subsidence, Dzurisin et al. (2002)). Sites HRAF and HRAS are both situated on ~20 m thick silicic lava flows erupted during the most recent activity at Torfajökull (1477 and 871 A.D., Larsen (1984)); therefore subsidence in the western part of the caldera could be due to crustal loading from these flows.

The proposal by Soosalu et al. (2006b) that a rising cryptodome is causing the low-frequency activity in the southeastern part of the caldera cannot be tested by our study as the GPS network in this area is too sparse. The 1993-2000 InSAR images of the caldera (A. Hooper pers comm. 2007) also provides no indication as to the source of the activity, as data coverage in this area is low due to the presence of Torfajöull's two glaciers. One

would, however, expect high-frequency events to be observed in addition to these low-frequency events as magma rising through the crust to shallow levels should cause brittle fracturing of the surrounding rock mass (Schmincke 2004), but significant levels of this activity have not been recorded as of yet. A peak in low-frequency activity in late autumn (October) in 2002 could be linked to increased melt water supply to the volcano's geothermal system, and possibly reduced loading after glacial melting during the summer months. It is unclear therefore whether these low-frequency events are magmatic in origin, or relates to the circulation of water in Torfajökull's extensive geothermal system.

6.1.4 Profile 3

Spreading along profile 3 to the south of Torfajökull volcano is constrained by rates to the north, as the rate of spreading decreases in a propagating ridge system (EVZ) in the direction of propagation (LaFemina et al. 2005). The location of the maximum strain accumulation (axis of spreading) along this profile does not correlate with previous geodetic studies across the EVFZ, which place the centre of spreading on a Holocene fissure south of Torfajökull that is aligned with the Veidivötn fissure to the north (LaFemina et al. 2005). Instead this study shows that the spreading axis is aligned along the western edge of the Eldgjá fissure swarm that was last active in 934 A.D. (Table 2.1, Stothers (2004)). This location could have implications for activity at Katla volcano or vice versa.

The best-fit model for 2001-2006 velocities along profile 3, not corrected for volcanic deformation, is an extension rate of 4.0 (+2.3/-2.2) mm/yr below a locking depth of 3 km (Table 6.1). This spreading rate and locking depth is less than that predicted from previous studies (i.e., 8.0 (± 1.0) mm/yr below a locking depth of 7.0 (+2.5/-1.2) km, LaFemina et al. (2005)), though both rates are similar within uncertainties. The best-fit model for the 1994-2003 velocities along profile 3 not corrected for volcanic deformation has an extension rate of 5.0 (+2.8/-2.6) mm/yr and a shallow locking depth of 2.0 (+21.2/-2.0) km (Table 6.1)

For the 2001-2006 dataset velocities along profile 3 corrected for Hekla deformation (ΔV_H=0.04 km^3), the best-fit model is a dyke with an extension rate of 7.0 (+2.3/-2.3) mm/yr below a locking depth of 4.0 (+9.9/-2.9) km (Table 6.1). The best-fit models do not change significantly for larger volume changes of Hekla volcano (0.05 and 0.06 km^3)

as was the case for profile 1, as only a few sites along profile 3 are close enough to the volcano. These best-fit models have extension rates ranging from 7.0 (+2.7/-2.5) mm/yr to 8.0 (+3.4/-3.0) mm/yr, and locking depths ranging from 3.0 (+10.8/-2.6) to 4.0 (+13.5/-3.4) km (Table 6.1). For the 1994-2003 velocities along profile 3 corrected for Hekla deformation (ΔV_H=0.03 km^3), the best-fit model is a dyke with an extension rate of 7.0 (+1.5/-2.2) mm/yr below a locking depth of 3.0 (+8.2/-3.0) km (Table 6.1). The best-fit model parameters for the two datasets compare well within uncertainties and show a decrease from those rates determined for profile 1, as well as being in agreement with those determined by LaFemina et al. (2005) except with shallower locking depths. Locking depths for the two datasets are within the limits of the seismogenic crustal thickness estimated for this region (Stefánsson et al. 1993).

At the latitude of profile 3, total plate motion has been shown to be partitioned between the overlapping spreading centres of the RP and rifting into the EVFZ (Hreinsdóttir et al. 2001; LaFemina et al. 2005). The full plate spreading rate at this latitude determined using the REVEL plate motion model is 19.9 mm/yr, and the NUVEL-1A plate motion model is 18.5 mm/yr (DeMets et al. 1994; Sella et al. 2002). Previous studies conducted along the RP have estimated spreading across the peninsula of ~11 mm/yr (Hreinsdóttir et al. 2001), while more recent studies by Árnadóttir et al. (2006) and Keiding et al. (2008) have shown that the majority of the plate motion (~20 mm/yr) south of the SISZ is taken up across the RP. These larger spreading rates for the RP would therefore imply that little to no spreading is taking place south of Torfajökull. This study shows that this is not the case, and is supported by geological evidence in the form of Torfajökull's own fissure swarm that extends to the southwest of the volcano and the Eldgjá fissure swarm.

6.2 Conclusions

Modelling of plate spreading using GPS-derived horizontal velocities for this study show along strike variation in spreading rate in the EVZ, with modelled extension rates decreasing over the study area from between 10 and 20 mm/yr north of Torfajökull volcano, to 7-8 mm/yr across the EVFZ in the south. These results are consistent with a propagating ridge model for south Iceland, with the EVZ propagating to the southwest. Results also show relatively shallow locking depths (<6 km) for plate spreading models.

The location of the spreading axis to the north of Torfajökull volcano for this study is in agreement with previous studies, with the location of maximum strain accumulation along the Veidivötn fissure swarm. GPS-derived velocity data collected within Torfajökull volcano show ridge propagation and therefore plate spreading is taking place through the volcano, in line with the axis of spreading to the north. This location for the spreading axis correlates well with fissure swarms and the most recent eruptive activity within the volcano. South of the volcano it appears the axis of spreading "jumps" to the southeast along the western edge of the Eldgjá fissure swarm that was last active in 934 A.D. These locations have implications for future rifting events as the axis of spreading is presumably the location of significant subsurface magma accumulation.

Hekla volcano is shown to have a significant effect on sites within the study area. ''Dry-tilt'' measurements made on the flank of the volcano appear to underestimate the volume of magma accumulating beneath the volcano since its last eruption in 2000. Subsidence of the ground surface in the western part of Torfajökull volcano as seen from InSAR and "dry-tilt" data is modelled using GPS-derived horizontal velocity data. The modelling results support the idea of a cooling and contracting magma chamber at depth, though due to limited data coverage an exact model for the source cannot be constrained.

6.3 Future Work

As with almost every study, increased data coverage would allow for more tightly constrained models. For the 2001-2006 dataset, increased coverage is needed along profile 1 in the eastern part of the EVZ so that sites not affected by Hekla deformation can be used to constrain the background plate spreading rate along this profile. This would then allow deformation due to Hekla volcano to be better constrained for sites along the western part of the profile. Along profile 2, increased coverage is needed both east and west of Torfajökull to help constrain plate spreading as the existing sites within the caldera are affected by additional processes (e.g., thermoelastic deformation due to the high-temperature geothermal fields within Torfajökull caldera, and deformation due to possible magmatic processes at depth in the western part of the caldera). Along profile 3, increased coverage is needed both along the western and eastern parts of the profile as the current GPS sites are concentrated at the centre. However, increased data coverage though ideal, is not always realistic due to the high cost of instrumentation and intensive field work necessary if sites are to be revisited yearly. The establishment of continuous sites would help reduce the amount of field work necessary, though would increase the cost.

Increased data coverage in the southeastern part of Torfajökull caldera would also help determine whether the source of the low-frequency events measured in this part of the volcano is magmatic, or relates to the circulation of water in the geothermal system, though this part of the volcano is not easily accessible. Additional studies at Torfajökull, including seismicity studies with extensive site coverage within the volcano for a sufficiently long period of time, and studies investigating loading and the crustal flexure response due to lava flows within Torfajökull volcano, would help to constrain the source causing subsidence within the western part of the volcano.

Mogi sources on average provide a 95% fit to ground deformation data collected at volcanoes, however more realistic complex magma source geometries may provide a better fit to the data. A more complex model such as an ellipsoidal source could be explored when modelling deformation due to Hekla, Katla and Torfajökull volcanoes, especially considering the elliptical subsidence signal seen on the 1993-2000 InSAR image of Torfajökull volcano. The long-lived silicic magma source at Torfajökull

volcano would also be better modelled as a magma source surrounded by a viscoelastic shell. The plate spreading model used in this study is also a simplified model as the tensile fault is assumed to have an infinite length and depth within an elastic medium, which is an over simplified rheology for the Earth's crust. However, due to limited data coverage for this study, the number of GPS sites within the study area would need to be increased, for sufficiently long period of time, before more complex modelling can be successfully carried out.

More focused studies are currently underway using the extensive GPS time-series from the numerous sites surrounding Hekla volcano (Sturkell et al. 2007). As the volcano is effectively aseismic, ground deformation data is one of the few datasets that can be used to better constrain the exact depth of the volcanoes magma source, and therefore these studies need to be continued. Additional "dry-tilt" sites set up around Hekla volcano would also help to constrain the volume change of the magma chamber at depth, as one site cannot give an accurate estimation. A well constrained source at Hekla volcano would allow for more accurate modelling of plate spreading.

7 REFERENCES

Agustsson, K., R. Stefansson, A. T. Linde, P. Einarsson and I. S. Sacks (2000). "Successful prediction and warning of the 2000 eruption of Hekla based on seismicity and strain changes." Eos Trans. AGU: Fall Meet Suppl., Abstr. 11B: 30.

Altamimi, Z., P. Sillard and C. Boucher (2002). "ITRF2000: A new release of the International Terrestrial Reference Frame for earth sciences applications." Journal of Geophysical Research **107**(B10): 2214.

Argus, D. F. and R. G. Gordon (1991). "No-net-rotation model of current plate velocities incorporating plate motion model NUVEL-1." Geophysical Research Letters **18**: 2039–2042.

Árnadóttir, T., W. Jiang, K. L. Feigl, H. Geirsson and E. Sturkell (2006). "Kinematic models of plate boundary deformation in southwest Iceland derived from GPS observations." Journal of Geophysical Research **111(B07402)**: doi:10.1029/2005JB003907.

Arnórsson, S., G. Ivarsson, K. Cuff and K. Saemundsson (1987). "Geothermal activity in the Torfajökull field, South Iceland: Summary of geochemical studies." Jökull **37**: 1-10.

Bevington, P. R. (1969). Data Reduction and Error Analysis for the Physical Sciences. New York, McGraw-Hill.

Bjarnason, J. O. and M. Olafsson (2000). "Chemical composition of geothermal steam and hot water at Torfajökull." National Energy Authority of Iceland **Report OS-2000/030**: 91 (in Icelandic).

Blake (1984). "Magma mixing and hybridization processes at the alkali, silicic Torfajökull central volcano triggered by tholeiitic Veiðivötn fissure, South Iceland." Journal of Volcanology and Geothermal Research **22**(1-2): 1-31.

Böðvarsson, R. and G. P. L. Walker (1964). "ral drift in Iceland." The Geophysical Journal of the Royal Astronomical Society **8**(3): 285-300.

Bonafede, M. (1991). "Hot fluid migration: an efficient source of ground deformation: application to the 1982-1985 crisis at Campi Flegrei-Italy." Journal of Volcanology and Geothermal Research **48**: 187-198.

Bonafede, M., M. Dragoni and F. Quareni (1986). "Displacement and stress fields produced by a centre of dilation and by a pressure source in a viscoelastic half-space: application to the study of ground deformation and seismic activity at Campi Flegrei, Italy." Geophysical Journal International **87**: 455-485.

Borner, N. (2007). Seismicity of the Torfajökull central volcano, Iceland: A geothermal and geological interpretation, Pembroke College. **Phd:** 69.

Boucher, C., Z. Altamimi and P. Sillard (1999). "The 1997 International Terrestrial Reference Frame (ITRF-97)." IERS Technical Note **27**: Paris, Observatory de Paris.

Brander, J. L., R. G. Mason and R. W. Calvert (1976). "Precise distance measurements in Iceland." Tectonophysics **31**(3-4): 193-206.

Clifton, A. E. and S. A. Kattenhorn (2006). "Structural architecture of a highly oblique divergent plate boundary segment." Tectonophysics **419**: 27–40.

Clifton, A. E., F. Sigmundsson, K. L. Feigl, G. Gudmundsson and T. Arnadottir (2002). "Surface effects of faulting and deformation resulting from magma accumulation at the Hengill triple junction, SW Iceland, 1994-1998." Journal of Volcanology and Geothermal Research **115**(1-2): 233-255.

Darbyshire, F. A., R. S. White and K. F. Priestley (2000). "Structure of the crust and uppermost mantle of Iceland from a combined seismic and gravity study." Earth and Planetary Science Letters **181**: 409-428.

De Natale, G., C. Troise and F. Pingue (2001). "A mechanical fluid-dynamical model for ground movements at Campi Flegrei caldera." Journal of Geodynamics **32**: 487-517.

de Zeeuw-van Dalfsen, E., H. Rymer, F. Sigmundsson and E. Sturkell (2005). "Net gravity decrease at Askja volcano, Iceland: constrainst on processes responsible for continuous caldera deflation, 1988-2003." Journal of Volcanology and Geothermal Research **139**: 227-239.

Decker, R. W., P. Einarsson and P. A. Mohr (1971). "Rifting in Iceland; new geodetic data." Science **173**(3996): 530-533.

Delaney, P. T. and D. F. McTigue (2004). "Volume of magma accumulation or withdrawal estimated from surface uplift or subsidence, with application to the 1960 collapse of Kilauea." Bulletin of Volcanology **56**(6-7): 417-424.

DeMets, C., R. G. Gordon, D. F. Argus and S. Stein (1994). "Effect of recent revisions to the geomagnetic reversal time scale on estimates of current plate motions." Geophysical Research Letters **21**(20): 2191-2194.

Dixon, T. H., M. Bursik, S. K. Wolf, M. Heflin, F. Webb, F. Farina and S. Robaudo (1993). Constraints on deformation of the resurgent dome, Long Valley caldera, California from space geodesy. Space Geodesy and Geodynamics, Geodyn. Ser. D. Smith and p. D. Turcotte. Washington, D.C., AGU. **23:** 193-214.

Dixon, T. H., A. Mao, M. Bursik, M. Heflin, J. Langbein, R. Stein and F. Webb (1997). "Continuous monitoring of surface deformation at Long Valley Caldera, California, with GPS." Journal of Geophysical Research **102**: 12017-12034.

Dragoni, M. and C. Magnanensi (1989). "Displacement and stress produced by a pressurized, spherical magma chamber, surrounded by a viscoelastic shell." Physics of the Earth and Planetary Interiors **56**: 316—328.

Du, Z. and G. R. Foulger (2001). "Variation in the crustal structure across Iceland." Geophysical Journal International **145**: 246-264.

Dziewonski, A. M., G. Ekstroem and N. N. Maternovskaya (2001). "Centroid-moment tensor solutions for April-June 2000." Physics of the earth and Planetary Interiors **123**(1): 1-14.

Dzurisin, D., M. P. Poland and R. Burgmann (2002). "Steady subsidence of Medicine Lake volcano, northern California, revealed by repeated leveling surveys." Journal of Geophysical Research **107**(B12): 2372, doi:10.1029/2001JB000893.

Einarsson, P. (1991). "Earthquakes and present-day tectonism in Iceland." Tectonophysics **189**: 261-279.

Einarsson, P. and B. Brandsdottir (2000). "Earthquakes in the Mýrdalsjökull area, Iceland, 1978–1985: Seasonal correlation and connection with volcanoes." Jökull **49**: 59–73.

Einarsson, P. and J. Eiríksson (1982). "Earthquake fractures in the districts Land and Rangárvellir in the SISZ." Jökull **32**: 113-120.

Einarsson, P. and K. Saemundsson (1987). Earthquake epicentres 1982-1985 and volcanic systems in Iceland (map). I hlutarins eðli, Festschrift for Þorbjorn Sigurgeirsson. I. Sigfusson. Reykjavık, Menningarsjoður.

Ewert (1992). A Single-Setup Trigonometric Leveling Method for Monitoring Ground-Tilt Changes. Monitoring Volcanoes: Techniques and Strategies Used by the Staff of the Cascades Volcano Observatory, 1980-90. Ewert and Swanson, USGS Bulletin 1966**:** 151.

Eysteinsson, H. and J. F. Hermance (1985). "Magnetotelluric measurements across the eastern neovolcanic zone in south Iceland." Journal of Geophysical Research **90**: 10093-10103.

Feigl, K. L., J. Gasperi, F. Sigmundsson and A. Rigo (2000). "Crustal deformation near Hengill volcano, Iceland 1993–1998: Coupling between magmatic activity and faulting inferred from elastic modeling of satellite radar interferograms." Journal of Geophysical Research **105**(B11): 25 655–25 670.

Foulger, G., C.-H. Jahn, G. Seeber, P. Einarsson, B. R. Julian and K. Heki (1992). "Post-rifting stress relaxation at the divergent plate boundary in Northeast Iceland." Nature **358**: 488-490.

Foulger, G. R., Z. Du and B. R. Julian (2003). "Icelandic-type crust." Geophysical Journal International **155**(2): 567-590.

Gaeta, F. S., G. De Natale, F. Peluso, G. Mastrolorenzo, D. Castagnolo, C. Troise, F. Pingue, D. G. Mita and S. Rossano (1998). "Genesis and evolution of unrest episodes at Campi Flegrei caldera: The role of thermal fluid-dynamical processes in the geothermal system." Journal of Geophysical Research **103**(B9): 20921-20933.

Garcia, S., N. O. Arnaud, J. Angelier, F. Bergerat and C. Homberg (2003). "Rift jump process in Northern Iceland since 10 Ma from 40Ar/39Ar geochronology." Earth and Planetary Science Letters **214**: 529-544.

Gerke, K., Ed. (1974). Crustal movements in the Myvatn- and Thingvallavatn-area, both horizontal and vertical. Geodynamics of Iceland and the North Atlantic Area Reidel Publishing Corporation.

Grönvold, K., G. Larsen, P. Einarsson, S. Thorarinsson and K. Sæmundsson (1983). "The Hekla eruption 1980-1981." The Bulletin of Volcanology **46**: 349-363.

Grönvold, K., N. Oskarsson, S. J. Johnsen, H. B. Clausen, C. U. Hammer, G. Bond and E. Bard (1995). "Ash layers from Iceland in the Greenland GRIP ice core correlated with oceanic and land sediments." Earth and Planetary Science Letters **135**: 149-155.

Guðmundsson, A. (1987). "Tectonics of the Thingvellir fissure swarm, SW Iceland." Journal of Structural Geology **9**(1): 61-69.

Guðmundsson, A. (2000). "Dynamics of volcanic systems in Iceland: example of tectonism and volcanism at juxtaposed hot spot and mid-ocean ridge systems." Annual Reviews of Earth and Planetary Sciences **28**: 107-140.

Guðmundsson, A., N. Oskarsson, K. Gronvold, K. Sæmundsson, O. Sigurdsson, R. Stefansson, S. R. Gislason, P. Einarsson, B. Brandsdottir, G. Larsen, H. Johannesson and T. Thordarson (1992). "The 1991 eruption of Hekla, Iceland." The Bulletin of Volcanology **54**: 238-246.

Guðmundsson, A. T. (1996). Earth in Action. The Essential Guide to the Geology of Iceland. Reykjavik, Vaka-Helgafell.

Gunnarsson, B., B. D. Marsh and H. P. Taylor Jr (1998). "Generation of Icelandic rhyolites: silicic lavas from the Torfajökull central volcano." Journal of Volcanology and Geothermal Research **83**: 1-45.

Hardarson, B. S., J. G. Fitton, R. M. Ellam and M. S. Pringle (1997). "Rift relocation - a geochemical and geochronological investigation of a palaeo-rift in northwest Iceland." Earth and Planetary Science Letters **153**: 181-196.

Heki, K., G. Foulger, B. R. Julian and C.-H. Jahn (1993). "Plate dynamics near divergent boundaries: geophysical implications of post-rifting crustal deformation in NE Iceland." Journal of Geophysical Research **98**: 14,279-14,297.

Heliker, Griggs, Takahashi and Wright (1986). "Volcano Monitoring at the U.S.Geological Survey's Hawaiian Volcano Observatory." Earthquakes and Volcanoes **18**(1): 38.

Hey, R. (1977). "A new class of pseudofaults and their bearing on plate tectonics: A propagating rift model." Earth and Planetary Science Letters **37**: 321-325.

Hey, R., F. K. Duennebier and J. W. Morgan (1980). "Propagating Rifts on Midocean Ridges." Journal of Geophysical Research **85**(B7): 3647-3658.

Hooper, A. and R. Pedersen (2007). Deformation due to magma movement and ice unloading at Katla volcano, Iceland, detected by persistent scatterer InSAR. ENVISAT Symposium. Montreux, Switzerland.

Höskuldsson, Á., N. Óskarsson, R. Pedersen, K. Grönvold, K. Vogfjörð and R. Ólafsdóttir (2007). "The millennium eruption of Hekla in February." The Bulletin of Volcanology **70**(2): 169-182.

Hreinsdóttir, S., P. Einarsson and F. Sigmundsson (2001). "Crustal deformation at the oblique spreading Reykjanes Peninsula, SW Iceland; GPS measurements from 1993 to 1998." Journal of Geophysical Research **106**(7): 13,803-13,816.

Jakobsson, S. P., J. Jónsson and F. Shido (1978). "Petrology of the Western Reykjanes Peninsula, Iceland." Journal of Petrology **19**(4): 669–705.

Johannesson, H., S. P. Jakobsson and K. Sæmundsson (1990). Geological map of Iceland, sheet 6, South Iceland. Reykjavı´k, Icelandic Museum of Natural History and Iceland Geodetic Survey.

Johannesson, H., S. P. Jakobsson and K. Saemundsson (1982). Geological map of Iceland. Sheet 6, South-Iceland. Reykjavik, Icelandic Museum of Natural History and Iceland Geodetic Survey.

Johnson, D. J. (1992). "Dynamics of magma storage in the summit reservoir of Kilauea volcano, Hawaii." Journal of Geophysical Research **97**(B2): 1807-1820.

Johnson, D. J., F. Sigmundsson and P. T. Delaney (2000). "Comment on "Volume of magma accumulation or withdrawal estimated from surface uplift or subsidence, with application to the 1960 collapse of Kilauea volcano" by P.T. Delaney and D.F. McTigue."" Bulletin of Volcanology **61**: 491-493.

Jónasson, S., P. Einarsson and F. Sigmundsson (1997). "Extension across a divergent plate boundary, the Eastern Volcanic rift zone, South Iceland, 1967-1994, observed with GPS and electronic distance measurements." Journal of Geophysical Research **102**(6): 11,913-11,929.

Jónasson, S., P. Segall, K. Agustsson and D. Agnew (2003). "Local fluid flow and borehole strain in the south Iceland Seismic Zone." Eos Trans. AGU **84(46)**: Fall Meet. Suppl., Abstract G31B-0717.

Jónsdóttir, K., A. Tryggvason, R. Roberts, B. Lund, H. Soosalu and R. Böðvarsson (2007). "Habits of a glacier-covered volcano: Seismicity patterns and velocity structure of Katla volcano, Iceland." Annals of Glaciology **45**: 169-177.

Karlsdóttir, R. (2001). "TEM resistivity measurements at Torfajökull." Orkustofnun **report OS-2001/031**: 131 (in Icelandic).

Keiding, M., T. Árnadóttir, E. Sturkell, H. Geirsson and B. Lund (2008). "Strain accumulation along an oblique plate boundary: the Reykjanes Peninsula, southwest Iceland." Geophysical Journal International **172**: 861-872.

Kjartansson, E. and K. Gronvold (1983). "Location of a magma reservoir beneath Hekla volcano, Iceland." Nature **301**: 139-141.

Kjartansson, G. (1964). Geological Map of Iceland, Sheet 5, central Iceland. Reykjavik, Museum of Natural History, Department of Geology and Geography.

Lacasse, C., H. Sigurdsson, S. N. Carey, H. Johannesson, L. E. Thomas and N. W. Rogers (2007). "Bimodal volcanism at the Katla subglacial caldera, Iceland: Insight into the geochemistry and petrogenesis of rhyolitic magmas." Bulletin of Volcanology **69**: 373 - 399, doi:10.1007/s00445-006-0082-5.

LaFemina, P. C. (2005). Plate Boundary Zone Deformation Measured by GPS and Implications for Long-term Geologioc Processes. Division of Marine Geology and Geophysics. Miami, FL, University of Miami - Rosenstiel School of Marine and Atmospheric Sciences. **PhD:** 200.

LaFemina, P. C., T. H. Dixon, R. Malservisi, T. Arnadottir, E. Sturkell, F. Sigmundsson and P. Einarsson (2005). "Geodetic GPS measurements in south Iceland: Strain accumulation and partitioning in a propagating ridge system." Journal of Geophysical Research **110**: B11405.

Larsen, G. (1984). "Recent volcanic history of the Veiðivötn fissure swarm, southern Iceland - an approach to volcanic risk assessment." Journal of Volcanology and Geothermal Research **22**: 33-58.

Larsen, G. (2000). "Holocene eruptions within the Katla volcanic system, south Iceland: Characteristics and environmental impact." Jökull **49**: 1–28.

Linde, A. T., K. Agustsson, I. S. Sacks and R. Stefansson (1993). "Mechanism of the 1991 eruption of Hekla from continuous borehole strain monitoring." Nature **365**: 737–740.

Lippitsch, R., R. S. White and H. Soosalu (2005). "Precise hypocentre relocation of microearthquakes in a high-temperature geothermal field: the Torfajökull central volcano, Iceland." Geophysical Journal International **160**: 370-387.

MacDonald, R., D. W. McGarvie, H. Pinkerton and R. L. Smith (1990). "Petrogenic evolution of the Torfajokul volcanic complex, Iceland. I. Relationship between the magma types." Journal of Petrology **31**(2): 429-459.

Mao, A., C. G. A. Harrison and T. H. Dixon (1999). "Noise in GPS coordinate time series." Journal of Geophysical Research **104**: 2797–2816.

McGarvie, D. (1984). "Torfajökull: a volcano dominated by magma mixing." Geology **12**: 685-688.

McGarvie, D. M., R. Macdonald, H. Pinkerton and R. L. Smith (1990). "Petrologic evolution of the Torfajökull Volcanic Complex, Iceland. II. The role of magma mixing." Journal of Petrology **31**: 461-481.

McGarvie, D. W. (1985). "Volcanology and petrology of mixed magmas and rhyolites from the Törfajokull Volcano, Iceland." PhD dissertation, The Johns Hopkins University.

McTigue, D. F. (1987). "Elastic stress and deformation near a finite spherical magma body: Resolution of the point source paradox." Journal of Geophysical Research **92**: 12,931–12,940.

Meyer, P. S., H. Sigurdsson and J. G. Schilling (1985). "Petrological and geochemical variations along Iceland's neovolcanic zones." Journal of Geophysical Research **90**: 10043-10072.

Mogi, K. (1958). "Relations between the eruptions of various volcanoes and the deformations of the ground surfaces around them." Bulletin of Earthquake Research Institute **36**: 99-134.

Newman, A. V., T. H. Dixon and N. Gourmelen (2004). "A Four-Dimensional Viscoelastic Deformation Model for Long Valley Caldera, California, between 1995 and 2000." Journal of Volcanology and Geothermal Research **150**: 244-269.

Newman, A. V., T. H. Dixon, G. I. Ofoegbu and J. E. Dixon (2001). "Geodetic and seismic constraints on recent activity at Long Valley Caldera, California: evidence for viscoelastic rheology." Journal of Volcanology and Geothermal Research **105**: 183-206.

Okada, Y. (1985). "Surface Deformation due to shear and tensile faults in a half-space." Bulletin of Seismological Society of America **75**(4): 1135-1154.

Orsi, G., S. M. Petrazzuoli and K. Wohletz (1999). "Mechanical and thermo-fluid behaviour during unrest at the Campi Flegrei caldera (Italy)." Journal of Volcanology and Geothermal Research **91**: 453-470.

Óskarsson, N., S. Steinthorsson and G. E. Sigvaldason (1985). "Iceland geochemical anomaly: origin, volcanotectonics, chemical fractionation and isotope evolution of the crust." Journal of Geophysical Research **90**: 10011-10025.

Pagli, C., F. Sigmundsson, B. Lund, R. Sturkell, H. Geirsson, P. Einarsson, T. Árnadóttir and S. Hreinsdóttir (2007). "Glacio-isostatic deformation around the Vatnajökull ice cap, Iceland, induced by recent climate warming: GPS observations and finite element modelling." Journal of Geophysical Research **112**(B08405): doi:10,1029/2006/B004421.

Pálmason, G. (1981). "Crustal rifting, and related thermo-mechanical processes in the lithosphere beneath Iceland." Geol. Rundsch. **70**: 244-260.

Pinel, V., F. Sigmundsson, E. Sturkell, H. Geirsson, P. Einarsson, M. T. Gudmundsson and T. Högnadóttir (2007). "Discriminating volcano deformation due to magma movements and variable surface loads: application to Katla subglacial volcano, Iceland." Geophysical Journal International **169**: 325-338.

Sæmundsson, K. (1972). "Geological notes on the Torfajökull area." Natturufraedingurinn **42**: 81-99 (in Icelandic).

Sæmundsson, K. (1974). "Evolution of the axial rifting zone in northern Iceland and the Tjörnes Fracture Zone." Geological Society of America Bulletin **85**: 495–504.

Sæmundsson, K. (1978). "Fissure swarms and central volcanoes of the neovolcanic zones of Iceland." Geological Journal Special Issue **10**: 415-432.

Sæmundsson, K. (1979). "Outline of the geology of Iceland." Jökull **29**: 7-28.

Sæmundsson, K. (1992). "Geology of the Thingvallavatn area." Oikos **64**(1-2): 40-68.

Saemundsson, K. and S. Einarsson (1980). "Geological map of Iceland, sheet 3, SW Iceland." Icelandic Geodetic Survey and Museum of Natural History.

Savage, J. C. and R. O. Burford (1973). "Geodetic determination of relative plate motion in central California." Journal of Geophysical Research **78**(5): 832-845.

Schmincke, H. (2004). Volcanism, Springer.

Sella, G. F., T. H. Dixon and A. Mao (2002). "REVEL: A model for Recent plate velocities from space geodesy." Journal of Geophysical Research **107**(B4): 2081.

Sigmundsson, F. (1991). "Post-glacial Rebound and Asthenosphere Viscosity in Iceland." Geophysical Research Letters **18**: 1131-1134.

Sigmundsson, F., P. Einarsson and R. Bilham (1992). "Magma chamber deflation recorded by the Global Positioning System: the Hekla 1991 eruption " Geophysical Research Letters **19**: 1483– 1486.

Sigmundsson, F., P. Einarsson, R. Bilham and E. Sturkell (1995). "Rift-transform kinematics in South Iceland; deformation from Global Positioning System measurements, 1986 to 1992." Journal of Geophysical Research **100**(4): 6235-6248.

Sigmundsson, F., P. Einarsson, S. T. Rognvaldsson, G. R. Foulger, K. M. Hodgkinson and G. Thorbergsson (1997). "The 1994-1995 seismicity and deformation at the Hengill triple junction, Iceland; triggering of earthquakes by minor magma injection in a zone of horizontal shear stress." Journal of Geophysical Research **102**(7): 15-15,161.

Sigmundsson, F., R. Pedersen, K. Feigl, E. Sturkell, P. Einarsson, S. Jonsson, K. Agustsson, A. Linde and F. Bretar (2001). "Joint interpretation of geodetic data for volcano studies: evaluation of pre- and co-eruptive deformation for the Hekla 2000 eruption from InSAR, tilt, GPS and strain data." Eos Trans. AGU **82**(**47**): Fall Meet. Suppl., Abstract V21E-07.

Sigurðsson, H. and S. R. J. Sparks (1978). "Lateral magma flow within rifted Icelandic crust." Nature **274**: 126-130.

Sigurðsson, O., S. Zóphoníasson and E. Ísleifsson (2000). "The jökulhlaup from Sólheimajökull July 18th 1999." Jökull **49**: 75-80 (in Icelandic with English summary).

Soosalu, H. and P. Einarsson (1997). "Seismicity around the Hekla and Torfajökull volcanoes, Iceland, during a volcanically quiet period, 1991-1995." The Bulletin of Volcanology **59**: 36-48.

Soosalu, H. and P. Einarsson (2004). "Seismic constraints on magma chambers at Hekla and Torfajökull volcanoes, Iceland." The Bulletin of Volcanology **66**: 276-286.

Soosalu, H., P. Einarsson and B. ó. S. Þorbjarnardóttir (2005). "Seismic activity related to the 200 eruption of the Hekla volcano, Iceland." The Bulletin of Volcanology **68**: 21-36.

Soosalu, H., K. Jonsdottir and P. Einarsson (2006a). "Seimicity crisis at the Katla volcano, Iceland - signs of a cryptodome." Journal of Volcanology and Geothermal Research **153**: 177-186.

Soosalu, H., R. Lippitsch and P. Einarsson (2006b). "Low-frequency earthquakes at the Torfajökull volcano, south Iceland." Journal of Volcanology and Geothermal Research **153**: 187-199.

Stecher, O., R. W. Carlson and B. Gunnarsson (1999). "Torfajökull: a radiogenic end-member of the Iceland Pb-isotropic array." Earth and Planetary Science Letters **165**: 117-127.

Stefánsson, R., R. Bodvarsson, R. Slunga, P. Einarsson, S. Jakobsdóttir, H. Bungum, S. Gregersen, J. Havskov, J. Hjelme and H. Korhonen (1993). "Earthquake prediction research in the South Iceland seismic zone and the SIL Project." Bulletin of the Seismological Society of America **83**(3): 696-716.

Stothers, R. B. (2004). "Far Reach of the Tenth Century Eldgjá Eruption, Iceland " Climatic Change **39**(4): 715-726.

Sturkell, E., K. Agustsson, A. T. Linde, S. I. Sacks, P. Einarsson, F. Sigmundsson, H. Geirsson, H. Olafsson, R. Pedersen and P. C. LaFemina (2006a). Current magma accumulation in the deep magma chamber under the Hekla volcano, Iceland. Raunvísindaþing 2006, Háskóli Íslands.

Sturkell, E., K. Agustsson, A. T. Linde, S. I. Sacks, P. Einarsson, F. Sigmundsson, H. Geirsson, R. Pedersen, P. C. LaFemina and H. Olafsson (2007). "Hekla revealed: new insight into volcanic activity from strain and other deformation data." (unpublished).

Sturkell, E., P. Einarsson, M. J. Roberts, H. Geirsson, M. T. Gudmundsson, F. Sigmundsson, V. Pinel, G. B. Guðmundsson, H. Ólafsson and R. Stefánsson (2008). "Seismic and geodetic insights into magma accumulation at Katla subglacial volcano, Iceland: 1999 to 2005." Journal of Geophysical Research **113**(B03212): 10.129.

Sturkell, E., P. Einarsson, F. Sigmundsson, H. Geirsson, H. Olafsson, R. Pedersen, E. de Zeeuw-van Dalfsen, A. T. Linde, S. I. Sacks and R. Stefansson (2006b). "Volcano geodesy and magma dynamics in Iceland." Journal of Volcanology and Geothermal Research **150**: 14-34.

Sturkell, E., F. Sigmundsson and P. Einarsson (2003a). "Recent unrest and magma movements at Eyjafjallajökull and Katla volcanoes, Iceland." Journal of Geophysical Research **DOI 10.1029/2001JB000917**.

Sturkell, E., F. Sigmundsson, P. Einarsson, H. Geirsson and M. J. Roberts (2003b). "Magma inflow into Katla, one of Iceland's most hazardous volcanoes." Eos Trans. AGU: Fall Meet. Suppl., Abstract V12G-07, F1503.

Thórarinsson, S. and G. E. Sigvaldason (1972). "The Hekla eruption of 1970." The Bulletin of Volcanology **36**: 269-288.

Thórdarson, T. and G. Larsen (2007). "Volcanism in Iceland in historical time: Volcano types, eruption styles and eruptive history." Journal of Geodynamics **43**: 118-152.

Thórdarson, T. and S. Self (1993). "The Laki (Skaftar Fires) and Grimsvotn eruptions in 1783-1785." Bulletin of Volcanology **55**: 233-263.

Tryggvason, E. (1982). "Recent ground deformation in continental and oceanic rift zones; Continental and oceanic rifts." Geodynamics Series **8**: 17-29.

Tryggvason, E. (1990). Hoggun Almanagjar. Maelingar a Thingvollum 1990 [Displacement of Almannagja. Measurements at Thingvellir 1990]. Nordic Volcanological Institute Report 9001. Reykjavik, Nordic Volcanological Institute.

Tryggvason, E. (1994). "Observed ground deformation at Hekla, Iceland prior to and during the eruptions of 1970, 1980– 1981 and 1991: Internal structure of volcanoes and geophysical precursors of eruptions." Journal of Volcanology and Geothermal Research **61**: 281– 291.

UNAVCO. (2005a). "Data Download & Transfer - Trimble Receivers. [WWW]. http://facility.unavco.org/software/download_transfer/trimble/trimble.html." Retrieved 11th April, 2008.

UNAVCO. (2005b). "GIPSY-OASIS II Overview. [WWW]. http://facility.unavco.org/software/processing/gipsy/gipsy_info.html." Retrieved 17th May, 2007.

UNAVCO. (2007). "Teqc. [WWW]. http://facility.unavco.org/software/teqc/teqc.html." Retrieved 15th Feb, 2007.

Venzke, E., R. W. Wunderman, L. McClelland, T. Simkin, J. F. Luhr, L. Siebert and G. Mayberry (2002). "Global Volcanism, 1968 to the Present." Smithsonian Institution Global Volcanism Program Digital Information Series **GVP-4**: http://www.volcano.si.edu/gvp/reports/.

Walker, G. P. L. (1960). "Zeolite zones and dyke distribution in relation to the structure of the basalts in Eastern Iceland." Journal of Geology **69**: 515-528.

Walker, G. P. L. (1974). Eruptive mechanisms in Iceland. Geodynamics of Iceland and the North Atlantic Area. L. Kristjansson. Dordrect, Holland, Reidel**:** 189-202.

Wiens, D. A., S. H. Pozgay, P. J. Shore, A. W. Sauter and R. A. White (2005). "Tilt recorded by a portable broadband seismograph: The 2003 eruption of Anatahan Volcano, Mariana Islands." Geophysical Research Letters **32**(L18305): doi:10.1029/2005GL023369.

Yamashita (1992). Single-Setup Leveling Used to Monitor Vertical Displacement (Tilt) on Cascades Volcanoes. Monitoring Volcanoes: Techniques and Strategies Used by the Staff of the Cascades Volcano Observatory, 1980-90. Ewert and Swanson, USGS Bulletin 1966**:** 143.

Zumberge, J. F., M. B. Heflin, D. C. Jefferson, M. M. Watkins and F. H. Webb (1997). "Precise point positioning for the efficient and robust analysis of GPS data from large networks." Journal of Geophysical Research **102**: 5005–5017.

8 APPENDICES

APPENDIX 1: Yearly position estimates used in Figure 3.9

BLAU

DATE	GD	Lat(deg)+/-Sigma(m)	Lon(deg)+/-Sigma(m)	Height(m)+/Sigma(m)
01AUG20	GD	63.951694335 0.0039	-19.363856555 0.0044	846.9158 0.0137
01AUG21	GD	63.951694329 0.0041	-19.363856579 0.0050	846.9032 0.0139
01AUG22	GD	63.951694365 0.0052	-19.363856410 0.0060	846.9135 0.0181
02AUG15	GD	63.951694495 0.0048	-19.363856224 0.0057	846.9345 0.0146
02AUG16	GD	63.951694483 0.0041	-19.363856090 0.0055	846.9407 0.0137
02AUG17	GD	63.951694495 0.0072	-19.363856218 0.0074	846.9432 0.0209
03AUG14	GD	63.951694677 0.0059	-19.363856024 0.0072	846.9202 0.0157
03AUG15	GD	63.951694684 0.0031	-19.363855995 0.0044	846.9501 0.0100
03AUG16	GD	63.951694639 0.0031	-19.363856037 0.0042	846.9494 0.0101
03AUG17	GD	63.951694661 0.0049	-19.363856032 0.0067	846.9575 0.0153
06SEP24	GD	63.951694985 0.0048	-19.363855842 0.0055	847.0071 0.0125
06SEP25	GD	63.951695048 0.0028	-19.363855715 0.0037	846.9971 0.0088
06SEP26	GD	63.951695059 0.0048	-19.363855786 0.0068	847.0199 0.0150

DOMA

DATE	GD	Lat(deg)+/-Sigma(m)	Lon(deg)+/-Sigma(m)	Height(m)+/-Sigma(m)
01AUG15	GD	64.035212874 0.0029	-19.130415820 0.0040	650.9248 0.0092
01AUG16	GD	64.035212905 0.0029	-19.130415858 0.0039	650.9287 0.0090
01AUG17	GD	64.035212870 0.0042	-19.130415799 0.0051	650.9260 0.0127
02AUG21	GD	64.035213069 0.0048	-19.130415761 0.0066	650.9459 0.0161
02AUG22	GD	64.035213090 0.0042	-19.130415754 0.0055	650.9640 0.0135
02AUG23	GD	64.035213064 0.0075	-19.130415810 0.0077	650.9697 0.0211
03AUG17	GD	64.035213236 0.0035	-19.130415702 0.0047	650.9483 0.0113
03AUG18	GD	64.035213146 0.0090	-19.130415982 0.0147	650.9537 0.0290
03AUG19	GD	64.035213198 0.0058	-19.130415774 0.0105	650.9269 0.0201

FROS

DATE	GD	Lat(deg)+/-Sigma(m)	Lon(deg)+/-Sigma(m)	Height(m)+/-Sigma(m)
00OCT10	GD	64.010033094 0.0064	-19.044383069 0.0083	713.8919 0.0222
00OCT11	GD	64.010033146 0.0104	-19.044383029 0.0154	713.8584 0.0301
01AUG14	GD	64.010033155 0.0040	-19.044382949 0.0047	713.8874 0.0139
01AUG15	GD	64.010033165 0.0042	-19.044382972 0.0051	713.8935 0.0140
01AUG16	GD	64.010033185 0.0074	-19.044383040 0.0071	713.9131 0.0223
02AUG19	GD	64.010033324 0.0050	-19.044382830 0.0073	713.8965 0.0162
02AUG20	GD	64.010033362 0.0052	-19.044382724 0.0073	713.8998 0.0178
02AUG21	GD	64.010033401 0.0237	-19.044382095 0.0296	713.8988 0.0435
03AUG19	GD	64.010033523 0.0065	-19.044382727 0.0081	713.9030 0.0209
03AUG20	GD	64.010033505 0.0042	-19.044382854 0.0054	713.9070 0.0144
03AUG21	GD	64.010033495 0.0052	-19.044382861 0.0074	713.8940 0.0171
03AUG22	GD	64.010033534 0.0084	-19.044382717 0.0125	713.9042 0.0278
04SEP20	GD	64.010033665 0.0065	-19.044382732 0.0081	713.9467 0.0225

HRAF

DATE	GD	Lat(deg)+/-Sigma(m)	Lon(deg)+/-Sigma(m)	Height(m)+/-Sigma(m)
00OCT10	GD	63.959090966 0.0074	-19.217554797 0.0109	949.9896 0.0244
00OCT11	GD	63.959091009 0.0067	-19.217554701 0.0103	950.0021 0.0221
02AUG17	GD	63.959091225 0.0056	-19.217554557 0.0071	950.0186 0.0178
02AUG18	GD	63.959091188 0.0043	-19.217554549 0.0056	950.0234 0.0138
02AUG19	GD	63.959091167 0.0050	-19.217554487 0.0066	950.0243 0.0151
02AUG20	GD	63.959091215 0.0064	-19.217554384 0.0112	950.0174 0.0226
03AUG17	GD	63.959091441 0.0068	-19.217554404 0.0080	950.0390 0.0164
03AUG18	GD	63.959091473 0.0083	-19.217554565 0.0123	950.0184 0.0224
03AUG19	GD	63.959091434 0.0030	-19.217554400 0.0043	950.0427 0.0098
03AUG20	GD	63.959091441 0.0029	-19.217554382 0.0041	950.0407 0.0096
03AUG21	GD	63.959091485 0.0057	-19.217554364 0.0111	950.0422 0.0189
04SEP15	GD	63.959091529 0.0062	-19.217554148 0.0114	950.0652 0.0249
04SEP16	GD	63.959091523 0.0060	-19.217554580 0.0096	950.0846 0.0250
04SEP17	GD	63.959091508 0.0116	-19.217553975 0.0231	950.0721 0.0317

HRAS

DATE	GD	Lat(deg)+/-Sigma(m)	Lon(deg)+/-Sigma(m)	Height(m)+/-Sigma(m)
01AUG18	GD	63.936408329 0.0043	-19.204847176 0.0049	1075.5480 0.0135
01AUG19	GD	63.936408281 0.0040	-19.204847045 0.0048	1075.5594 0.0134
01AUG20	GD	63.936408280 0.0064	-19.204847106 0.0062	1075.5764 0.0194
02AUG17	GD	63.936408513 0.0059	-19.204847045 0.0073	1075.5714 0.0186
02AUG18	GD	63.936408511 0.0048	-19.204847062 0.0057	1075.5766 0.0143
02AUG19	GD	63.936408473 0.0061	-19.204846965 0.0067	1075.5743 0.0159
02AUG20	GD	63.936408530 0.0095	-19.204846800 0.0133	1075.5815 0.0269
03AUG17	GD	63.936408596 0.0122	-19.204847085 0.0127	1075.5989 0.0226
03AUG18	GD	63.936408712 0.0085	-19.204847182 0.0135	1075.6048 0.0241
03AUG19	GD	63.936408681 0.0031	-19.204846939 0.0047	1075.6047 0.0105
03AUG20	GD	63.936408663 0.0030	-19.204846908 0.0042	1075.5981 0.0099
03AUG21	GD	63.936408694 0.0062	-19.204847020 0.0116	1075.6023 0.0199
04SEP15	GD	63.936408863 0.0027	-19.204846820 0.0038	1075.6319 0.0084
04SEP16	GD	63.936408884 0.0028	-19.204846784 0.0040	1075.6301 0.0088
04SEP17	GD	63.936408883 0.0028	-19.204846722 0.0040	1075.6100 0.0085
04SEP18	GD	63.936408907 0.0028	-19.204846710 0.0037	1075.6133 0.0085
05OCT27	GD	63.936408937 0.0055	-19.204846810 0.0056	1075.6458 0.0160
05OCT28	GD	63.936408952 0.0027	-19.204846718 0.0033	1075.6385 0.0081
05OCT29	GD	63.936408972 0.0027	-19.204846727 0.0035	1075.6393 0.0082
05OCT30	GD	63.936408954 0.0027	-19.204846772 0.0034	1075.6445 0.0082
05OCT31	GD	63.936408965 0.0030	-19.204846702 0.0043	1075.6423 0.0091
05NOV01	GD	63.936408958 0.0029	-19.204846746 0.0039	1075.6415 0.0092
05NOV02	GD	63.936408996 0.0028	-19.204846777 0.0038	1075.6485 0.0090
05NOV03	GD	63.936408976 0.0032	-19.204846589 0.0047	1075.6258 0.0098
05NOV04	GD	63.936408995 0.0029	-19.204846761 0.0038	1075.6395 0.0090
05NOV05	GD	63.936408976 0.0028	-19.204846765 0.0037	1075.6365 0.0088
05NOV06	GD	63.936408988 0.0028	-19.204846769 0.0036	1075.6346 0.0090
05NOV07	GD	63.936408991 0.0028	-19.204846768 0.0036	1075.6311 0.0091
05NOV08	GD	63.936408993 0.0028	-19.204846741 0.0035	1075.6407 0.0088
05NOV09	GD	63.936408973 0.0028	-19.204846798 0.0036	1075.6390 0.0092
05NOV10	GD	63.936408997 0.0028	-19.204846638 0.0036	1075.6314 0.0092
05NOV11	GD	63.936408982 0.0027	-19.204846718 0.0035	1075.6316 0.0086
05NOV12	GD	63.936408985 0.0027	-19.204846745 0.0036	1075.6301 0.0091
05NOV13	GD	63.936408972 0.0028	-19.204846797 0.0039	1075.6427 0.0095
06SEP23	GD	63.936409118 0.0029	-19.204846713 0.0041	1075.6441 0.0091
06SEP24	GD	63.936409086 0.0071	-19.204846689 0.0091	1075.6376 0.0193

ISAK

DATE	GD	Lat(deg)+/-Sigma(m)	Lon(deg)+/-Sigma(m)	Height(m)+/-Sigma(m)
01JUN02	GD	64.119326916 0.0064	-19.747176740 0.0110	319.2133 0.0237
01JUN03	GD	64.119326852 0.0065	-19.747176611 0.0096	319.2338 0.0225
01JUN04	GD	64.119326916 0.0068	-19.747176800 0.0089	319.2093 0.0219
01JUN05	GD	64.119326857 0.0068	-19.747176588 0.0104	319.2318 0.0234
01JUN06	GD	64.119326983 0.0072	-19.747176724 0.0097	319.2086 0.0231
01AUG09	GD	64.119326943 0.0076	-19.747176595 0.0072	319.2195 0.0219
01AUG10	GD	64.119326975 0.0082	-19.747176584 0.0074	319.2268 0.0230
01AUG11	GD	64.119326962 0.0079	-19.747176742 0.0073	319.2231 0.0227
01AUG12	GD	64.119326903 0.0083	-19.747176717 0.0080	319.2226 0.0239
01AUG13	GD	64.119326879 0.0098	-19.747176802 0.0109	319.2276 0.0260
01AUG14	GD	64.119326950 0.0079	-19.747176598 0.0074	319.2263 0.0228
01AUG15	GD	64.119326926 0.0096	-19.747176752 0.0088	319.2398 0.0256
01AUG16	GD	64.119326958 0.0089	-19.747176718 0.0077	319.2295 0.0232
01AUG17	GD	64.119326925 0.0091	-19.747176546 0.0080	319.2219 0.0241
01AUG18	GD	64.119326910 0.0113	-19.747176675 0.0084	319.2067 0.0250
01AUG19	GD	64.119326855 0.0108	-19.747176742 0.0083	319.2535 0.0246
01AUG20	GD	64.119326938 0.0077	-19.747176584 0.0069	319.2485 0.0232
01AUG21	GD	64.119327004 0.0088	-19.747176847 0.0080	319.2244 0.0236
01AUG22	GD	64.119326947 0.0080	-19.747176757 0.0073	319.2115 0.0237
01AUG23	GD	64.119326913 0.0093	-19.747176807 0.0089	319.2513 0.0266
01AUG24	GD	64.119326927 0.0077	-19.747176611 0.0069	319.2423 0.0232
01AUG25	GD	64.119326938 0.0084	-19.747176680 0.0078	319.2321 0.0233
01AUG26	GD	64.119326943 0.0107	-19.747176720 0.0083	319.2166 0.0275
01AUG27	GD	64.119326979 0.0086	-19.747176690 0.0085	319.2178 0.0251
01AUG28	GD	64.119326859 0.0094	-19.747176559 0.0116	319.2395 0.0290
01AUG29	GD	64.119326974 0.0077	-19.747176674 0.0073	319.2137 0.0235
02FEB06	GD	64.119327062 0.0049	-19.747176771 0.0081	319.2186 0.0155
02FEB07	GD	64.119327067 0.0043	-19.747176844 0.0074	319.2107 0.0142
02FEB08	GD	64.119327066 0.0045	-19.747176845 0.0065	319.2224 0.0150
02FEB09	GD	64.119327044 0.0046	-19.747176792 0.0077	319.2109 0.0151
02FEB10	GD	64.119327038 0.0044	-19.747176747 0.0059	319.2271 0.0147

02FEB11	GD	64.119327033	0.0042	-19.747176798	0.0059	319.2164 0.0142
02FEB12	GD	64.119327024	0.0049	-19.747176782	0.0067	319.2103 0.0152
02FEB13	GD	64.119327017	0.0045	-19.747176784	0.0067	319.2133 0.0140
02FEB14	GD	64.119327019	0.0043	-19.747176600	0.0061	319.2210 0.0140
02FEB15	GD	64.119326995	0.0043	-19.747176657	0.0061	319.2205 0.0143
02FEB16	GD	64.119326961	0.0047	-19.747176732	0.0061	319.2302 0.0144
02FEB17	GD	64.119327008	0.0047	-19.747176636	0.0067	319.2314 0.0141
02FEB18	GD	64.119327011	0.0041	-19.747176779	0.0055	319.2238 0.0139
02FEB19	GD	64.119327039	0.0049	-19.747176768	0.0073	319.2351 0.0150
02FEB20	GD	64.119327062	0.0045	-19.747176775	0.0069	319.2189 0.0142
02FEB21	GD	64.119327025	0.0045	-19.747176784	0.0060	319.2208 0.0140
02FEB22	GD	64.119327078	0.0050	-19.747176692	0.0077	319.2200 0.0161
02FEB23	GD	64.119327083	0.0044	-19.747176719	0.0059	319.2157 0.0146
02FEB24	GD	64.119327050	0.0045	-19.747176883	0.0064	319.2010 0.0149
02FEB25	GD	64.119327048	0.0046	-19.747176821	0.0061	319.2131 0.0149
02FEB26	GD	64.119327087	0.0049	-19.747176842	0.0063	319.2124 0.0151
02FEB27	GD	64.119327023	0.0044	-19.747176865	0.0055	319.2191 0.0142
02FEB28	GD	64.119327015	0.0047	-19.747176910	0.0067	319.2138 0.0155
02MAR01	GD	64.119327064	0.0053	-19.747176959	0.0086	319.2039 0.0165
02MAR02	GD	64.119326993	0.0042	-19.747176819	0.0057	319.2286 0.0131
02MAR03	GD	64.119327004	0.0043	-19.747176722	0.0064	319.2179 0.0136
02MAR04	GD	64.119327074	0.0047	-19.747176782	0.0066	319.2266 0.0146
02MAR05	GD	64.119327041	0.0051	-19.747176770	0.0074	319.2339 0.0164
02MAR06	GD	64.119327058	0.0044	-19.747176777	0.0056	319.2185 0.0131
02MAR07	GD	64.119327065	0.0033	-19.747176826	0.0048	319.2301 0.0108
02MAR08	GD	64.119327087	0.0044	-19.747176787	0.0058	319.2095 0.0133
02MAR09	GD	64.119327067	0.0042	-19.747176816	0.0053	319.2205 0.0128
02MAR10	GD	64.119327073	0.0035	-19.747176855	0.0045	319.2199 0.0117
02MAR11	GD	64.119327064	0.0043	-19.747176864	0.0055	319.2129 0.0128
02MAR12	GD	64.119327001	0.0043	-19.747176857	0.0053	319.2312 0.0130
02MAR13	GD	64.119327048	0.0044	-19.747176849	0.0051	319.2148 0.0129
02MAR14	GD	64.119327016	0.0038	-19.747176808	0.0047	319.2186 0.0120
02MAR15	GD	64.119327056	0.0040	-19.747176707	0.0048	319.2066 0.0123
02MAR16	GD	64.119327042	0.0032	-19.747176881	0.0039	319.2231 0.0104
02MAR17	GD	64.119327029	0.0035	-19.747176832	0.0043	319.2318 0.0110
02MAR18	GD	64.119327055	0.0039	-19.747176925	0.0047	319.2300 0.0116
02MAR19	GD	64.119327056	0.0047	-19.747177018	0.0065	319.2205 0.0163
02MAR20	GD	64.119327071	0.0037	-19.747176929	0.0045	319.2254 0.0113
02MAR21	GD	64.119327085	0.0034	-19.747176817	0.0042	319.2147 0.0108
02MAR22	GD	64.119327094	0.0036	-19.747176835	0.0045	319.2058 0.0113
02MAR23	GD	64.119327094	0.0042	-19.747176907	0.0048	319.2306 0.0130
02MAR24	GD	64.119327152	0.0071	-19.747176785	0.0093	319.2312 0.0178
02MAR25	GD	64.119327045	0.0037	-19.747176691	0.0046	319.2219 0.0123
02MAR26	GD	64.119327063	0.0044	-19.747176847	0.0050	319.2215 0.0131
02MAR27	GD	64.119327035	0.0043	-19.747176794	0.0052	319.2233 0.0127
02MAR28	GD	64.119327048	0.0035	-19.747176847	0.0044	319.2233 0.0105
02MAR29	GD	64.119327045	0.0039	-19.747176911	0.0047	319.2117 0.0129
02MAR30	GD	64.119327034	0.0046	-19.747176845	0.0054	319.2398 0.0138
02MAR31	GD	64.119327106	0.0035	-19.747176836	0.0048	319.2327 0.0110
02APR01	GD	64.119327053	0.0049	-19.747176752	0.0058	319.2193 0.0134
02APR02	GD	64.119327052	0.0037	-19.747176872	0.0049	319.2284 0.0116
02APR03	GD	64.119327045	0.0045	-19.747176691	0.0053	319.2356 0.0130
02APR04	GD	64.119327068	0.0036	-19.747176806	0.0042	319.2149 0.0113
02APR05	GD	64.119327039	0.0043	-19.747176691	0.0049	319.2020 0.0136
02APR06	GD	64.119327045	0.0041	-19.747176625	0.0049	319.2208 0.0127
02APR07	GD	64.119327009	0.0040	-19.747176793	0.0050	319.2186 0.0123
02APR08	GD	64.119327056	0.0042	-19.747176703	0.0048	319.2016 0.0125
02APR09	GD	64.119327056	0.0038	-19.747176690	0.0045	319.2241 0.0115
02APR10	GD	64.119327047	0.0036	-19.747176760	0.0046	319.2191 0.0116
02APR11	GD	64.119327048	0.0032	-19.747176800	0.0040	319.2290 0.0100
02APR12	GD	64.119327063	0.0042	-19.747176771	0.0049	319.2240 0.0126
02APR13	GD	64.119327054	0.0038	-19.747176762	0.0047	319.2105 0.0115
02APR14	GD	64.119327058	0.0035	-19.747176780	0.0043	319.2287 0.0112
02APR15	GD	64.119327127	0.0038	-19.747176841	0.0045	319.2367 0.0119
02APR16	GD	64.119327064	0.0037	-19.747176694	0.0049	319.2155 0.0124
02APR17	GD	64.119327078	0.0046	-19.747176792	0.0056	319.1964 0.0135
02APR18	GD	64.119327068	0.0073	-19.747177007	0.0094	319.2301 0.0208
02APR19	GD	64.119327080	0.0047	-19.747176598	0.0062	319.2301 0.0134
02APR30	GD	64.119327053	0.0032	-19.747176760	0.0043	319.2299 0.0103
02MAY01	GD	64.119327095	0.0041	-19.747176806	0.0048	319.2292 0.0123
02MAY02	GD	64.119327088	0.0032	-19.747176716	0.0042	319.2144 0.0100
02MAY03	GD	64.119327099	0.0031	-19.747176685	0.0040	319.2264 0.0097
02MAY04	GD	64.119327094	0.0034	-19.747176752	0.0044	319.2215 0.0113
02MAY05	GD	64.119327084	0.0037	-19.747176684	0.0046	319.2109 0.0118

02MAY06	GD	64.119327078	0.0035	-19.747176718	0.0045	319.2286 0.0108
02MAY07	GD	64.119327040	0.0039	-19.747176802	0.0047	319.2197 0.0122
02MAY08	GD	64.119327102	0.0034	-19.747176726	0.0045	319.2184 0.0109
02MAY09	GD	64.119327069	0.0034	-19.747176750	0.0044	319.2141 0.0110
02MAY10	GD	64.119327098	0.0032	-19.747176811	0.0042	319.2181 0.0100
02MAY11	GD	64.119327121	0.0039	-19.747176807	0.0046	319.2182 0.0114
02MAY12	GD	64.119327111	0.0035	-19.747176899	0.0048	319.2304 0.0110
02MAY13	GD	64.119327090	0.0033	-19.747176865	0.0043	319.2267 0.0104
02MAY14	GD	64.119327105	0.0045	-19.747176835	0.0059	319.2227 0.0125
02MAY15	GD	64.119327108	0.0035	-19.747176795	0.0045	319.2175 0.0107
02MAY16	GD	64.119327099	0.0031	-19.747176769	0.0040	319.2194 0.0094
02MAY17	GD	64.119327111	0.0031	-19.747176816	0.0041	319.2154 0.0096
02MAY18	GD	64.119327089	0.0033	-19.747176725	0.0043	319.2247 0.0102
02MAY19	GD	64.119327040	0.0037	-19.747176752	0.0052	319.2318 0.0120
02MAY20	GD	64.119327123	0.0033	-19.747176730	0.0045	319.2232 0.0114
02MAY21	GD	64.119327090	0.0034	-19.747176819	0.0045	319.2231 0.0112
02MAY22	GD	64.119327114	0.0031	-19.747176740	0.0041	319.2362 0.0102
02MAY23	GD	64.119327121	0.0043	-19.747176874	0.0048	319.2165 0.0119
02MAY24	GD	64.119327100	0.0031	-19.747176875	0.0041	319.2275 0.0099
02MAY25	GD	64.119327088	0.0031	-19.747176723	0.0040	319.2195 0.0098
02MAY26	GD	64.119327119	0.0031	-19.747176818	0.0040	319.2281 0.0096
02MAY27	GD	64.119327089	0.0034	-19.747176613	0.0049	319.2273 0.0105
02MAY28	GD	64.119327096	0.0032	-19.747176804	0.0040	319.2251 0.0097
02MAY29	GD	64.119327112	0.0033	-19.747176789	0.0044	319.2237 0.0113
02MAY30	GD	64.119327098	0.0031	-19.747176781	0.0039	319.2215 0.0096
02MAY31	GD	64.119327114	0.0033	-19.747176686	0.0044	319.2241 0.0111
02JUN01	GD	64.119327112	0.0034	-19.747176657	0.0045	319.2196 0.0115
02JUN02	GD	64.119327078	0.0034	-19.747176747	0.0045	319.2190 0.0100
02JUN03	GD	64.119327108	0.0032	-19.747176839	0.0042	319.2263 0.0102
02JUN04	GD	64.119327162	0.0032	-19.747176853	0.0042	319.2260 0.0099
02JUN05	GD	64.119327115	0.0033	-19.747176831	0.0041	319.2265 0.0099
02JUN06	GD	64.119327040	0.0034	-19.747176750	0.0045	319.2422 0.0113
02JUN07	GD	64.119327137	0.0034	-19.747176682	0.0046	319.2295 0.0112
02JUN08	GD	64.119327115	0.0033	-19.747176788	0.0043	319.2404 0.0103
02JUN09	GD	64.119327106	0.0037	-19.747176756	0.0048	319.2160 0.0111
02JUN10	GD	64.119327089	0.0036	-19.747176824	0.0046	319.2287 0.0104
02JUN11	GD	64.119327125	0.0032	-19.747176828	0.0041	319.2279 0.0098
02JUN12	GD	64.119327097	0.0033	-19.747176772	0.0042	319.2242 0.0099
02JUN13	GD	64.119327119	0.0032	-19.747176838	0.0041	319.2141 0.0098
02JUN14	GD	64.119327077	0.0034	-19.747176776	0.0042	319.2195 0.0100
02JUN15	GD	64.119327122	0.0033	-19.747176786	0.0041	319.2160 0.0099
02JUN16	GD	64.119327113	0.0033	-19.747176842	0.0043	319.2226 0.0101
02JUN17	GD	64.119327106	0.0037	-19.747176669	0.0047	319.2376 0.0105
02JUN18	GD	64.119327102	0.0038	-19.747176681	0.0049	319.2303 0.0113
02JUN19	GD	64.119327128	0.0032	-19.747176837	0.0041	319.2355 0.0098
02JUN20	GD	64.119327107	0.0035	-19.747176842	0.0045	319.2230 0.0111
02JUN21	GD	64.119327116	0.0032	-19.747176744	0.0040	319.2240 0.0096
02JUN22	GD	64.119327118	0.0034	-19.747176740	0.0042	319.2264 0.0100
02JUN23	GD	64.119327127	0.0033	-19.747176794	0.0040	319.2260 0.0098
02JUN24	GD	64.119327101	0.0032	-19.747176744	0.0042	319.2157 0.0105
02JUN25	GD	64.119327125	0.0032	-19.747176828	0.0040	319.2027 0.0100
02JUN26	GD	64.119327136	0.0032	-19.747176852	0.0044	319.2170 0.0105
02JUN27	GD	64.119327132	0.0033	-19.747176819	0.0044	319.2180 0.0102
02JUN28	GD	64.119327113	0.0033	-19.747176856	0.0043	319.2317 0.0104
02JUN29	GD	64.119327114	0.0033	-19.747176743	0.0042	319.2232 0.0104
02JUN30	GD	64.119327131	0.0036	-19.747176970	0.0047	319.2283 0.0104
02JUL01	GD	64.119327109	0.0033	-19.747176856	0.0044	319.2293 0.0104
02JUL02	GD	64.119327125	0.0032	-19.747176800	0.0040	319.2315 0.0098
02JUL03	GD	64.119327146	0.0031	-19.747176904	0.0041	319.2218 0.0097
02JUL04	GD	64.119327151	0.0034	-19.747176885	0.0045	319.2413 0.0107
02JUL05	GD	64.119327091	0.0034	-19.747176869	0.0044	319.2230 0.0109
02JUL06	GD	64.119327118	0.0035	-19.747176902	0.0047	319.2300 0.0110
02JUL07	GD	64.119327117	0.0030	-19.747176893	0.0039	319.2280 0.0095
02JUL08	GD	64.119327131	0.0032	-19.747176875	0.0040	319.2201 0.0097
02JUL09	GD	64.119327108	0.0034	-19.747176807	0.0045	319.2170 0.0105
02JUL10	GD	64.119327116	0.0033	-19.747176949	0.0042	319.2119 0.0102
02JUL11	GD	64.119327128	0.0031	-19.747176810	0.0040	319.2203 0.0097
02JUL12	GD	64.119327122	0.0034	-19.747176813	0.0046	319.2222 0.0106
02JUL13	GD	64.119327132	0.0035	-19.747176740	0.0045	319.2314 0.0113
02JUL14	GD	64.119327109	0.0033	-19.747176776	0.0042	319.2231 0.0107
02JUL15	GD	64.119327115	0.0033	-19.747176797	0.0042	319.2222 0.0107
02JUL16	GD	64.119327141	0.0034	-19.747176879	0.0043	319.2243 0.0103
02JUL17	GD	64.119327126	0.0034	-19.747176850	0.0044	319.2213 0.0109
02JUL18	GD	64.119327130	0.0031	-19.747176791	0.0042	319.2278 0.0099

02JUL19	GD	64.119327150	0.0035	-19.747176827	0.0042	319.2147 0.0101
02JUL20	GD	64.119327144	0.0037	-19.747176784	0.0051	319.2199 0.0117
02JUL21	GD	64.119327108	0.0034	-19.747176896	0.0049	319.2257 0.0111
02JUL22	GD	64.119327096	0.0032	-19.747176832	0.0040	319.2217 0.0100
02JUL23	GD	64.119327119	0.0036	-19.747176822	0.0045	319.2193 0.0108
02JUL24	GD	64.119327122	0.0035	-19.747176798	0.0044	319.2197 0.0113
02JUL25	GD	64.119327098	0.0037	-19.747176787	0.0048	319.2290 0.0117
02JUL26	GD	64.119327050	0.0035	-19.747176862	0.0042	319.2322 0.0108
02JUL27	GD	64.119327069	0.0035	-19.747176911	0.0049	319.2230 0.0112
02JUL28	GD	64.119327135	0.0032	-19.747176859	0.0042	319.2286 0.0099
02JUL29	GD	64.119327127	0.0032	-19.747176835	0.0041	319.2258 0.0099
02JUL30	GD	64.119327114	0.0031	-19.747176862	0.0040	319.2299 0.0097
02JUL31	GD	64.119327120	0.0031	-19.747176903	0.0040	319.2208 0.0096
02AUG01	GD	64.119327119	0.0034	-19.747176809	0.0042	319.2210 0.0102
02AUG02	GD	64.119327128	0.0035	-19.747176784	0.0052	319.2337 0.0117
02AUG03	GD	64.119327118	0.0034	-19.747176833	0.0043	319.2261 0.0106
02AUG04	GD	64.119327150	0.0035	-19.747176758	0.0052	319.2222 0.0115
02AUG05	GD	64.119327122	0.0032	-19.747176873	0.0040	319.2191 0.0098
02AUG06	GD	64.119327135	0.0032	-19.747176898	0.0039	319.2232 0.0098
02AUG07	GD	64.119327178	0.0032	-19.747176879	0.0039	319.2279 0.0098
02AUG08	GD	64.119327126	0.0031	-19.747176851	0.0039	319.2265 0.0095
02AUG09	GD	64.119327137	0.0031	-19.747176790	0.0040	319.2298 0.0095
02AUG10	GD	64.119327137	0.0033	-19.747176930	0.0047	319.2276 0.0107
02AUG11	GD	64.119327175	0.0034	-19.747176892	0.0044	319.2327 0.0107
02AUG12	GD	64.119327138	0.0032	-19.747176879	0.0041	319.2330 0.0100
02AUG13	GD	64.119327122	0.0031	-19.747176790	0.0042	319.2368 0.0100
02AUG14	GD	64.119327154	0.0031	-19.747176846	0.0040	319.2276 0.0096
02AUG15	GD	64.119327159	0.0034	-19.747176838	0.0046	319.2354 0.0104
02AUG16	GD	64.119327141	0.0032	-19.747176771	0.0043	319.2342 0.0101
02AUG17	GD	64.119327162	0.0031	-19.747176898	0.0040	319.2341 0.0094
02AUG18	GD	64.119327155	0.0033	-19.747176864	0.0044	319.2346 0.0099
02AUG19	GD	64.119327167	0.0039	-19.747176750	0.0056	319.2252 0.0123
02AUG20	GD	64.119327107	0.0038	-19.747176910	0.0053	319.2303 0.0118
02AUG21	GD	64.119327122	0.0037	-19.747176890	0.0055	319.2145 0.0118
02AUG22	GD	64.119327149	0.0034	-19.747176828	0.0050	319.2317 0.0108
02AUG23	GD	64.119327208	0.0033	-19.747176880	0.0041	319.2425 0.0101
02AUG24	GD	64.119327140	0.0031	-19.747176795	0.0041	319.2268 0.0101
02AUG25	GD	64.119327136	0.0032	-19.747176765	0.0043	319.2419 0.0106
02AUG26	GD	64.119327138	0.0035	-19.747176861	0.0046	319.2273 0.0110
02AUG27	GD	64.119327160	0.0034	-19.747176840	0.0051	319.2332 0.0113
02AUG28	GD	64.119327140	0.0035	-19.747176846	0.0044	319.2324 0.0110
02AUG29	GD	64.119327116	0.0030	-19.747176898	0.0041	319.2323 0.0096
02AUG30	GD	64.119327141	0.0032	-19.747176897	0.0043	319.2313 0.0104
02AUG31	GD	64.119327160	0.0035	-19.747176832	0.0047	319.2292 0.0111
02SEP01	GD	64.119327110	0.0035	-19.747176784	0.0048	319.2271 0.0109
02SEP02	GD	64.119327132	0.0032	-19.747176855	0.0048	319.2264 0.0107
02SEP03	GD	64.119327120	0.0036	-19.747176828	0.0047	319.2265 0.0120
02SEP04	GD	64.119327144	0.0041	-19.747176839	0.0065	319.2200 0.0140
02SEP05	GD	64.119327158	0.0034	-19.747176897	0.0046	319.2318 0.0114
02SEP06	GD	64.119327142	0.0031	-19.747176861	0.0041	319.2238 0.0096
02SEP07	GD	64.119327186	0.0038	-19.747176879	0.0059	319.2417 0.0117
02SEP08	GD	64.119327162	0.0038	-19.747176923	0.0056	319.2293 0.0119
02SEP09	GD	64.119327149	0.0033	-19.747176822	0.0046	319.2345 0.0104
02SEP10	GD	64.119327162	0.0036	-19.747176702	0.0055	319.2529 0.0117
02SEP11	GD	64.119327124	0.0035	-19.747176769	0.0049	319.2326 0.0106
02SEP12	GD	64.119327120	0.0033	-19.747176789	0.0050	319.2269 0.0107
02SEP13	GD	64.119327138	0.0033	-19.747176885	0.0047	319.2252 0.0106
02SEP14	GD	64.119327164	0.0033	-19.747176814	0.0045	319.2287 0.0105
02SEP15	GD	64.119327143	0.0033	-19.747176836	0.0043	319.2131 0.0105
02SEP16	GD	64.119327154	0.0032	-19.747176898	0.0043	319.2157 0.0106
02SEP17	GD	64.119327158	0.0031	-19.747176869	0.0041	319.2211 0.0099
02SEP18	GD	64.119327174	0.0031	-19.747176812	0.0045	319.2141 0.0106
02SEP19	GD	64.119327184	0.0032	-19.747176821	0.0042	319.2305 0.0101
02SEP20	GD	64.119327164	0.0031	-19.747176778	0.0042	319.2360 0.0106
02SEP21	GD	64.119327125	0.0031	-19.747176793	0.0041	319.2176 0.0104
02SEP22	GD	64.119327129	0.0032	-19.747176919	0.0043	319.2292 0.0103
02SEP23	GD	64.119327136	0.0029	-19.747176762	0.0038	319.2266 0.0094
02SEP24	GD	64.119327121	0.0031	-19.747176873	0.0042	319.2352 0.0106
02SEP25	GD	64.119327155	0.0033	-19.747176876	0.0045	319.2319 0.0115
02SEP26	GD	64.119327115	0.0036	-19.747176960	0.0049	319.2365 0.0114
02SEP27	GD	64.119327136	0.0037	-19.747176738	0.0054	319.2305 0.0118
02SEP28	GD	64.119327139	0.0032	-19.747176860	0.0043	319.2332 0.0106
02SEP29	GD	64.119327126	0.0034	-19.747176809	0.0048	319.2383 0.0113
02SEP30	GD	64.119327138	0.0035	-19.747176850	0.0053	319.2274 0.0109

02OCT01	GD	64.119327228	0.0044	-19.747176714	0.0077	319.2449 0.0146
02OCT02	GD	64.119327210	0.0038	-19.747176561	0.0054	319.2324 0.0118
02OCT03	GD	64.119327125	0.0038	-19.747176886	0.0059	319.2349 0.0122
02OCT04	GD	64.119327174	0.0047	-19.747176767	0.0061	319.2288 0.0135
02OCT05	GD	64.119327244	0.0037	-19.747176838	0.0053	319.2390 0.0108
02OCT06	GD	64.119327202	0.0035	-19.747176971	0.0050	319.2562 0.0107
02OCT07	GD	64.119327204	0.0051	-19.747176903	0.0078	319.2489 0.0139
02OCT08	GD	64.119327137	0.0037	-19.747176960	0.0057	319.2332 0.0120
02OCT09	GD	64.119327130	0.0040	-19.747176852	0.0064	319.2415 0.0119
02OCT10	GD	64.119327143	0.0039	-19.747176736	0.0054	319.2443 0.0114
02OCT11	GD	64.119327225	0.0035	-19.747176759	0.0050	319.2281 0.0121
02OCT12	GD	64.119327224	0.0036	-19.747176876	0.0053	319.2207 0.0121
02OCT13	GD	64.119327130	0.0034	-19.747176924	0.0048	319.2323 0.0111
02OCT14	GD	64.119327179	0.0039	-19.747176809	0.0069	319.2214 0.0127
02OCT15	GD	64.119327133	0.0041	-19.747176880	0.0056	319.2275 0.0123
02OCT16	GD	64.119327145	0.0037	-19.747176921	0.0048	319.2220 0.0111
02OCT17	GD	64.119327175	0.0034	-19.747176965	0.0047	319.2255 0.0110
02OCT18	GD	64.119327181	0.0037	-19.747176969	0.0052	319.2282 0.0122
02OCT19	GD	64.119327134	0.0034	-19.747176976	0.0050	319.2301 0.0111
02OCT20	GD	64.119327153	0.0032	-19.747176964	0.0046	319.2334 0.0109
02OCT21	GD	64.119327142	0.0033	-19.747176892	0.0046	319.2378 0.0108
02OCT22	GD	64.119327158	0.0032	-19.747176988	0.0043	319.2327 0.0103
02OCT23	GD	64.119327126	0.0034	-19.747176852	0.0048	319.2270 0.0114
02OCT24	GD	64.119327125	0.0052	-19.747176950	0.0088	319.2408 0.0151
02OCT25	GD	64.119327133	0.0045	-19.747177111	0.0064	319.2401 0.0132
02OCT26	GD	64.119327124	0.0045	-19.747177004	0.0063	319.2382 0.0142
02OCT27	GD	64.119327138	0.0040	-19.747176972	0.0054	319.2288 0.0122
02OCT28	GD	64.119327148	0.0041	-19.747177020	0.0061	319.2318 0.0140
02OCT29	GD	64.119327134	0.0039	-19.747176858	0.0055	319.2255 0.0126
02OCT30	GD	64.119327167	0.0036	-19.747176803	0.0050	319.2314 0.0112
02OCT31	GD	64.119327161	0.0034	-19.747176941	0.0050	319.2281 0.0112
02NOV01	GD	64.119327160	0.0036	-19.747176862	0.0055	319.2398 0.0122
02NOV02	GD	64.119327216	0.0036	-19.747176858	0.0053	319.2456 0.0114
02NOV03	GD	64.119327163	0.0045	-19.747176865	0.0060	319.2402 0.0134
02NOV04	GD	64.119327149	0.0041	-19.747176807	0.0056	319.2437 0.0122
02NOV05	GD	64.119327114	0.0038	-19.747176913	0.0057	319.2247 0.0124
02NOV06	GD	64.119327144	0.0037	-19.747176881	0.0058	319.2435 0.0128
02NOV07	GD	64.119327147	0.0034	-19.747176883	0.0050	319.2401 0.0111
02NOV08	GD	64.119327147	0.0034	-19.747176813	0.0047	319.2263 0.0115
02NOV09	GD	64.119327156	0.0034	-19.747176793	0.0048	319.2323 0.0114
02NOV10	GD	64.119327161	0.0036	-19.747176905	0.0051	319.2344 0.0115
02NOV11	GD	64.119327179	0.0037	-19.747176967	0.0053	319.2356 0.0125
02NOV12	GD	64.119327169	0.0038	-19.747176945	0.0051	319.2228 0.0120
02NOV13	GD	64.119327179	0.0037	-19.747176941	0.0054	319.2347 0.0118
02NOV14	GD	64.119327163	0.0037	-19.747176807	0.0052	319.2424 0.0122
02NOV15	GD	64.119327159	0.0040	-19.747176890	0.0056	319.2383 0.0126
02NOV16	GD	64.119327193	0.0039	-19.747176980	0.0056	319.2382 0.0130
02NOV17	GD	64.119327132	0.0036	-19.747176928	0.0053	319.2500 0.0125
02NOV18	GD	64.119327233	0.0039	-19.747177007	0.0058	319.2517 0.0128
02NOV19	GD	64.119327129	0.0037	-19.747176597	0.0052	319.2424 0.0122
02NOV20	GD	64.119327121	0.0039	-19.747176763	0.0056	319.2433 0.0126
02NOV21	GD	64.119327200	0.0052	-19.747176667	0.0077	319.2349 0.0151
02NOV22	GD	64.119327156	0.0033	-19.747177013	0.0047	319.2426 0.0109
02NOV23	GD	64.119327189	0.0036	-19.747176810	0.0053	319.2405 0.0121
02NOV24	GD	64.119327172	0.0035	-19.747176856	0.0051	319.2284 0.0117
02NOV25	GD	64.119327148	0.0035	-19.747176816	0.0048	319.2353 0.0113
02NOV26	GD	64.119327133	0.0036	-19.747176829	0.0048	319.2485 0.0115
02NOV27	GD	64.119327188	0.0038	-19.747176813	0.0051	319.2413 0.0117
02NOV28	GD	64.119327186	0.0034	-19.747176909	0.0047	319.2367 0.0114
02NOV29	GD	64.119327176	0.0033	-19.747176773	0.0047	319.2517 0.0108
02NOV30	GD	64.119327193	0.0033	-19.747176871	0.0048	319.2478 0.0111
02DEC01	GD	64.119327199	0.0038	-19.747176790	0.0052	319.2413 0.0125
02DEC02	GD	64.119327155	0.0034	-19.747176848	0.0050	319.2406 0.0116
02DEC03	GD	64.119327160	0.0034	-19.747176859	0.0046	319.2451 0.0116
02DEC04	GD	64.119327136	0.0035	-19.747176865	0.0048	319.2359 0.0119
02DEC05	GD	64.119327143	0.0034	-19.747176860	0.0047	319.2541 0.0112
02DEC06	GD	64.119327128	0.0034	-19.747176839	0.0051	319.2305 0.0117
02DEC07	GD	64.119327164	0.0040	-19.747176720	0.0054	319.2192 0.0129
02DEC08	GD	64.119327170	0.0037	-19.747176861	0.0054	319.2353 0.0125
02DEC09	GD	64.119327166	0.0033	-19.747176749	0.0045	319.2207 0.0110
02DEC10	GD	64.119327194	0.0034	-19.747176837	0.0045	319.2349 0.0109
02DEC11	GD	64.119327199	0.0033	-19.747176794	0.0045	319.2434 0.0111
02DEC12	GD	64.119327184	0.0033	-19.747176750	0.0047	319.2385 0.0111
02DEC13	GD	64.119327193	0.0034	-19.747176818	0.0049	319.2316 0.0112

02DEC14	GD	64.119327193	0.0036	-19.747176829	0.0056	319.2321 0.0123
02DEC15	GD	64.119327209	0.0036	-19.747176822	0.0051	319.2284 0.0124
02DEC16	GD	64.119327204	0.0036	-19.747176787	0.0049	319.2320 0.0118
02DEC17	GD	64.119327170	0.0034	-19.747176848	0.0048	319.2335 0.0117
02DEC18	GD	64.119327175	0.0034	-19.747176863	0.0045	319.2345 0.0117
02DEC19	GD	64.119327203	0.0040	-19.747176796	0.0072	319.2333 0.0128
02DEC20	GD	64.119327207	0.0037	-19.747176773	0.0051	319.2263 0.0124
02DEC21	GD	64.119327202	0.0040	-19.747176809	0.0051	319.2222 0.0128
02DEC22	GD	64.119327182	0.0034	-19.747176768	0.0046	319.2309 0.0114
02DEC23	GD	64.119327161	0.0037	-19.747176969	0.0054	319.2407 0.0120
02DEC24	GD	64.119327203	0.0034	-19.747176540	0.0048	319.2628 0.0111
02DEC25	GD	64.119327217	0.0034	-19.747176725	0.0048	319.2484 0.0116
02DEC26	GD	64.119327198	0.0036	-19.747176825	0.0050	319.2437 0.0117
02DEC27	GD	64.119327191	0.0051	-19.747176897	0.0068	319.2340 0.0143
02DEC28	GD	64.119327216	0.0036	-19.747176780	0.0054	319.2336 0.0124
02DEC29	GD	64.119327202	0.0034	-19.747176906	0.0048	319.2422 0.0117
02DEC30	GD	64.119327231	0.0033	-19.747176929	0.0045	319.2322 0.0111
02DEC31	GD	64.119327185	0.0033	-19.747176895	0.0045	319.2354 0.0110
03JAN01	GD	64.119327224	0.0035	-19.747176833	0.0048	319.2321 0.0121
03JAN02	GD	64.119327199	0.0035	-19.747176873	0.0048	319.2370 0.0121
03JAN03	GD	64.119327184	0.0040	-19.747176851	0.0060	319.2341 0.0129
03JAN04	GD	64.119327205	0.0040	-19.747176829	0.0056	319.2289 0.0128
03JAN05	GD	64.119327177	0.0035	-19.747176877	0.0048	319.2339 0.0119
03JAN06	GD	64.119327185	0.0034	-19.747176743	0.0044	319.2281 0.0114
03JAN07	GD	64.119327194	0.0035	-19.747176724	0.0043	319.2331 0.0115
03JAN08	GD	64.119327214	0.0034	-19.747176803	0.0041	319.2275 0.0107
03JAN09	GD	64.119327198	0.0035	-19.747176802	0.0043	319.2317 0.0107
03JAN10	GD	64.119327199	0.0036	-19.747176810	0.0046	319.2295 0.0109
03JAN11	GD	64.119327205	0.0035	-19.747176832	0.0041	319.2341 0.0109
03JAN12	GD	64.119327211	0.0034	-19.747176835	0.0042	319.2349 0.0110
03JAN13	GD	64.119327159	0.0035	-19.747176787	0.0043	319.2206 0.0113
03JAN14	GD	64.119327146	0.0036	-19.747176728	0.0046	319.2255 0.0115
03JAN15	GD	64.119327172	0.0035	-19.747176820	0.0042	319.2281 0.0110
03JAN16	GD	64.119327195	0.0037	-19.747176774	0.0042	319.2379 0.0114
03JAN17	GD	64.119327183	0.0035	-19.747176893	0.0042	319.2280 0.0108
03JAN18	GD	64.119327185	0.0034	-19.747176893	0.0043	319.2287 0.0110
03JAN19	GD	64.119327180	0.0035	-19.747176897	0.0044	319.2237 0.0112
03JAN20	GD	64.119327190	0.0036	-19.747176936	0.0045	319.2241 0.0113
03JAN21	GD	64.119327192	0.0036	-19.747176935	0.0046	319.2335 0.0112
03JAN22	GD	64.119327156	0.0039	-19.747176859	0.0048	319.2287 0.0117
03JAN23	GD	64.119327220	0.0037	-19.747176783	0.0044	319.2512 0.0112
03JAN24	GD	64.119327197	0.0037	-19.747176825	0.0042	319.2489 0.0108
03JAN25	GD	64.119327172	0.0039	-19.747176885	0.0050	319.2465 0.0120
03JAN26	GD	64.119327180	0.0034	-19.747176924	0.0042	319.2426 0.0108
03JAN27	GD	64.119327163	0.0039	-19.747176858	0.0042	319.2364 0.0110
03JAN28	GD	64.119327188	0.0038	-19.747176807	0.0045	319.2370 0.0115
03JAN29	GD	64.119327196	0.0038	-19.747176817	0.0045	319.2274 0.0110
03JAN30	GD	64.119327194	0.0042	-19.747176979	0.0058	319.2335 0.0145
03JAN31	GD	64.119327181	0.0036	-19.747176858	0.0047	319.2404 0.0115
03FEB01	GD	64.119327164	0.0036	-19.747176808	0.0043	319.2407 0.0110
03FEB02	GD	64.119327190	0.0052	-19.747176934	0.0089	319.2445 0.0141
03FEB03	GD	64.119327196	0.0035	-19.747176939	0.0045	319.2367 0.0109
03FEB04	GD	64.119327162	0.0042	-19.747176859	0.0051	319.2510 0.0122
03FEB05	GD	64.119327195	0.0036	-19.747176864	0.0044	319.2349 0.0114
03FEB06	GD	64.119327185	0.0037	-19.747176918	0.0046	319.2509 0.0109
03FEB07	GD	64.119327162	0.0034	-19.747176880	0.0045	319.2482 0.0108
03FEB08	GD	64.119327168	0.0038	-19.747176843	0.0048	319.2464 0.0117
03FEB09	GD	64.119327188	0.0039	-19.747176784	0.0050	319.2461 0.0119
03FEB10	GD	64.119327226	0.0039	-19.747176876	0.0052	319.2454 0.0124
03FEB11	GD	64.119327197	0.0035	-19.747176938	0.0047	319.2388 0.0120
03FEB12	GD	64.119327176	0.0036	-19.747176968	0.0046	319.2235 0.0112
03FEB13	GD	64.119327202	0.0036	-19.747176801	0.0045	319.2337 0.0107
03FEB14	GD	64.119327199	0.0036	-19.747176964	0.0044	319.2228 0.0113
03FEB18	GD	64.119327246	0.0100	-19.747176858	0.0145	319.2427 0.0247
03FEB19	GD	64.119327212	0.0033	-19.747176822	0.0040	319.2399 0.0101
03FEB20	GD	64.119327179	0.0036	-19.747176848	0.0043	319.2421 0.0104
03FEB21	GD	64.119327205	0.0047	-19.747176792	0.0058	319.2218 0.0134
03FEB23	GD	64.119327240	0.0049	-19.747176873	0.0080	319.2567 0.0160
03FEB24	GD	64.119327202	0.0031	-19.747176867	0.0040	319.2313 0.0096
03FEB25	GD	64.119327218	0.0032	-19.747176899	0.0039	319.2326 0.0101
03FEB26	GD	64.119327207	0.0034	-19.747176902	0.0040	319.2400 0.0099
03FEB27	GD	64.119327265	0.0045	-19.747176920	0.0063	319.2424 0.0132
03FEB28	GD	64.119327210	0.0036	-19.747176730	0.0043	319.2493 0.0105
03MAR01	GD	64.119327194	0.0037	-19.747176868	0.0044	319.2276 0.0106

03MAR02	GD	64.119327222	0.0038	-19.747176969	0.0046	319.2434 0.0115
03MAR03	GD	64.119327185	0.0036	-19.747176864	0.0043	319.2356 0.0101
03MAR04	GD	64.119327201	0.0038	-19.747176986	0.0049	319.2369 0.0110
03MAR05	GD	64.119327200	0.0035	-19.747176922	0.0044	319.2307 0.0111
03MAR06	GD	64.119327241	0.0042	-19.747176968	0.0063	319.2347 0.0118
03MAR07	GD	64.119327182	0.0033	-19.747176828	0.0041	319.2444 0.0101
03MAR08	GD	64.119327204	0.0038	-19.747176866	0.0043	319.2421 0.0104
03MAR09	GD	64.119327203	0.0041	-19.747176933	0.0049	319.2374 0.0122
03MAR10	GD	64.119327222	0.0036	-19.747176889	0.0047	319.2428 0.0105
03MAR11	GD	64.119327228	0.0032	-19.747176869	0.0042	319.2375 0.0102
03MAR12	GD	64.119327208	0.0033	-19.747176821	0.0042	319.2269 0.0102
03MAR13	GD	64.119327193	0.0034	-19.747176881	0.0044	319.2258 0.0107
03MAR14	GD	64.119327224	0.0036	-19.747176939	0.0049	319.2267 0.0110
03MAR15	GD	64.119327224	0.0036	-19.747176903	0.0047	319.2290 0.0110
03MAR16	GD	64.119327196	0.0037	-19.747176835	0.0046	319.2291 0.0109
03MAR17	GD	64.119327221	0.0038	-19.747176789	0.0052	319.2301 0.0109
03MAR18	GD	64.119327249	0.0033	-19.747176908	0.0045	319.2422 0.0105
03MAR19	GD	64.119327218	0.0032	-19.747176918	0.0045	319.2364 0.0111
03MAR20	GD	64.119327258	0.0039	-19.747176999	0.0046	319.2408 0.0111
03MAR21	GD	64.119327212	0.0033	-19.747176831	0.0042	319.2381 0.0108
03MAR22	GD	64.119327213	0.0031	-19.747176887	0.0042	319.2382 0.0099
03MAR23	GD	64.119327217	0.0032	-19.747176831	0.0042	319.2440 0.0101
03MAR24	GD	64.119327192	0.0030	-19.747176785	0.0040	319.2382 0.0096
03MAR25	GD	64.119327224	0.0031	-19.747176837	0.0041	319.2205 0.0100
03MAR26	GD	64.119327234	0.0033	-19.747176891	0.0042	319.2368 0.0108
03MAR27	GD	64.119327195	0.0033	-19.747176819	0.0047	319.2271 0.0109
03MAR28	GD	64.119327199	0.0038	-19.747176867	0.0051	319.2284 0.0113
03MAR29	GD	64.119327248	0.0046	-19.747176780	0.0056	319.2330 0.0126
03MAR30	GD	64.119327208	0.0039	-19.747176991	0.0048	319.2308 0.0118
03MAR31	GD	64.119327248	0.0039	-19.747176921	0.0051	319.2351 0.0118
03APR01	GD	64.119327223	0.0035	-19.747176857	0.0046	319.2377 0.0109
03APR02	GD	64.119327240	0.0036	-19.747176933	0.0045	319.2297 0.0115
03APR03	GD	64.119327247	0.0034	-19.747176819	0.0043	319.2326 0.0109
03APR04	GD	64.119327225	0.0037	-19.747176859	0.0052	319.2316 0.0128
03APR05	GD	64.119327254	0.0038	-19.747176834	0.0047	319.2394 0.0112
03APR06	GD	64.119327273	0.0032	-19.747177066	0.0042	319.2383 0.0101
03APR07	GD	64.119327215	0.0032	-19.747176797	0.0042	319.2298 0.0105
03APR08	GD	64.119327234	0.0034	-19.747176821	0.0045	319.2367 0.0109
03APR09	GD	64.119327245	0.0035	-19.747176785	0.0047	319.2328 0.0111
03APR10	GD	64.119327229	0.0034	-19.747176564	0.0051	319.2490 0.0108
03APR11	GD	64.119327267	0.0033	-19.747176886	0.0042	319.2265 0.0103
03APR12	GD	64.119327282	0.0031	-19.747176809	0.0039	319.2242 0.0100
03APR13	GD	64.119327277	0.0029	-19.747176904	0.0039	319.2271 0.0096
03APR14	GD	64.119327267	0.0030	-19.747176881	0.0039	319.2340 0.0096
03APR15	GD	64.119327279	0.0030	-19.747176894	0.0042	319.2362 0.0099
03APR16	GD	64.119327333	0.0033	-19.747176881	0.0044	319.2594 0.0104
03APR17	GD	64.119327307	0.0033	-19.747176883	0.0042	319.2290 0.0100
03APR18	GD	64.119327267	0.0031	-19.747176879	0.0041	319.2354 0.0100
03APR19	GD	64.119327281	0.0030	-19.747176890	0.0039	319.2313 0.0100
03APR20	GD	64.119327246	0.0030	-19.747176923	0.0041	319.2347 0.0097
03APR21	GD	64.119327266	0.0034	-19.747176899	0.0047	319.2357 0.0103
03APR22	GD	64.119327276	0.0035	-19.747176951	0.0049	319.2306 0.0111
03APR23	GD	64.119327285	0.0031	-19.747176947	0.0043	319.2280 0.0099
03APR24	GD	64.119327293	0.0033	-19.747176914	0.0047	319.2227 0.0106
03APR25	GD	64.119327270	0.0033	-19.747176933	0.0043	319.2306 0.0103
03APR26	GD	64.119327279	0.0031	-19.747176955	0.0041	319.2354 0.0099
03APR27	GD	64.119327209	0.0194	-19.747176688	0.0227	319.2415 0.0408
03APR28	GD	64.119327293	0.0054	-19.747176880	0.0068	319.2354 0.0169
03APR29	GD	64.119327278	0.0033	-19.747176969	0.0044	319.2321 0.0105
03APR30	GD	64.119327267	0.0036	-19.747176931	0.0047	319.2266 0.0118
03MAY01	GD	64.119327268	0.0034	-19.747176910	0.0048	319.2327 0.0106
03MAY02	GD	64.119327270	0.0032	-19.747177013	0.0042	319.2306 0.0105
03MAY03	GD	64.119327270	0.0029	-19.747176900	0.0037	319.2301 0.0095
03MAY04	GD	64.119327267	0.0029	-19.747176912	0.0036	319.2258 0.0093
03MAY05	GD	64.119327276	0.0030	-19.747176866	0.0041	319.2265 0.0095
03MAY06	GD	64.119327277	0.0034	-19.747176968	0.0045	319.2330 0.0114
03MAY07	GD	64.119327239	0.0034	-19.747176917	0.0044	319.2256 0.0109
03MAY08	GD	64.119327265	0.0031	-19.747176884	0.0043	319.2268 0.0099
03MAY09	GD	64.119327270	0.0032	-19.747177001	0.0044	319.2399 0.0109
03MAY10	GD	64.119327283	0.0042	-19.747176914	0.0059	319.2390 0.0121
03MAY11	GD	64.119327295	0.0032	-19.747176916	0.0046	319.2336 0.0103
03MAY12	GD	64.119327282	0.0031	-19.747176870	0.0040	319.2374 0.0096
03MAY13	GD	64.119327286	0.0030	-19.747176897	0.0040	319.2443 0.0097
03MAY14	GD	64.119327283	0.0034	-19.747176867	0.0045	319.2407 0.0100

03MAY15	GD	64.119327257	0.0031	-19.747176963	0.0039	319.2384	0.0099
03MAY16	GD	64.119327264	0.0031	-19.747176951	0.0041	319.2385	0.0097
03MAY17	GD	64.119327285	0.0030	-19.747176867	0.0038	319.2309	0.0097
03MAY18	GD	64.119327226	0.0031	-19.747176932	0.0040	319.2418	0.0103
03MAY19	GD	64.119327272	0.0033	-19.747177007	0.0042	319.2315	0.0115
03MAY20	GD	64.119327268	0.0030	-19.747176881	0.0038	319.2419	0.0093
03MAY21	GD	64.119327303	0.0035	-19.747176853	0.0047	319.2462	0.0113
03MAY22	GD	64.119327270	0.0032	-19.747176899	0.0039	319.2344	0.0099
03MAY23	GD	64.119327269	0.0034	-19.747176919	0.0042	319.2381	0.0101
03MAY24	GD	64.119327308	0.0032	-19.747176851	0.0039	319.2364	0.0098
03MAY25	GD	64.119327266	0.0032	-19.747176876	0.0040	319.2386	0.0105
03MAY26	GD	64.119327270	0.0042	-19.747176923	0.0049	319.2313	0.0127
03MAY30	GD	64.119327277	0.0049	-19.747176991	0.0077	319.2370	0.0162
03MAY31	GD	64.119327273	0.0035	-19.747176938	0.0043	319.2276	0.0113
03JUN01	GD	64.119327274	0.0033	-19.747176955	0.0044	319.2331	0.0101
03JUN02	GD	64.119327253	0.0039	-19.747176920	0.0054	319.2308	0.0125
03JUN03	GD	64.119327268	0.0032	-19.747177013	0.0040	319.2261	0.0102
03JUN04	GD	64.119327282	0.0031	-19.747176951	0.0039	319.2304	0.0102
03JUN05	GD	64.119327255	0.0029	-19.747176933	0.0036	319.2348	0.0094
03JUN06	GD	64.119327282	0.0031	-19.747177002	0.0040	319.2369	0.0100
03JUN07	GD	64.119327307	0.0032	-19.747176987	0.0041	319.2388	0.0098
03JUN08	GD	64.119327306	0.0036	-19.747176987	0.0048	319.2391	0.0106
03JUN09	GD	64.119327321	0.0032	-19.747177013	0.0041	319.2455	0.0099
03JUN10	GD	64.119327287	0.0030	-19.747177016	0.0037	319.2391	0.0093
03JUN11	GD	64.119327286	0.0029	-19.747176913	0.0037	319.2354	0.0093
03JUN12	GD	64.119327298	0.0029	-19.747176951	0.0036	319.2237	0.0094
03JUN13	GD	64.119327282	0.0030	-19.747176921	0.0036	319.2267	0.0096
03JUN14	GD	64.119327281	0.0032	-19.747176963	0.0043	319.2301	0.0097
03JUN15	GD	64.119327265	0.0034	-19.747176929	0.0043	319.2282	0.0101
03JUN16	GD	64.119327298	0.0037	-19.747176966	0.0050	319.2232	0.0117
03JUN17	GD	64.119327297	0.0038	-19.747177030	0.0052	319.2294	0.0120
03JUN18	GD	64.119327291	0.0038	-19.747176851	0.0055	319.2421	0.0121
03JUN19	GD	64.119327283	0.0031	-19.747176976	0.0040	319.2338	0.0095
03JUN20	GD	64.119327290	0.0029	-19.747176891	0.0036	319.2319	0.0092
03JUN21	GD	64.119327298	0.0032	-19.747176922	0.0045	319.2353	0.0101
03JUN22	GD	64.119327332	0.0030	-19.747176949	0.0037	319.2363	0.0094
03JUN23	GD	64.119327313	0.0030	-19.747176939	0.0040	319.2355	0.0099
03JUN24	GD	64.119327285	0.0034	-19.747176956	0.0047	319.2301	0.0114
03JUN25	GD	64.119327277	0.0031	-19.747177069	0.0039	319.2368	0.0097
03JUN26	GD	64.119327330	0.0031	-19.747177009	0.0041	319.2313	0.0099
03JUN27	GD	64.119327277	0.0036	-19.747176919	0.0044	319.2261	0.0107
03JUN28	GD	64.119327273	0.0036	-19.747176997	0.0049	319.2254	0.0116
03JUN29	GD	64.119327280	0.0032	-19.747177043	0.0042	319.2361	0.0101
03JUN30	GD	64.119327279	0.0031	-19.747177051	0.0040	319.2325	0.0096
03JUL01	GD	64.119327285	0.0031	-19.747176859	0.0040	319.2408	0.0102
03JUL02	GD	64.119327307	0.0031	-19.747176818	0.0040	319.2392	0.0103
03JUL03	GD	64.119327300	0.0031	-19.747176869	0.0039	319.2358	0.0096
03JUL04	GD	64.119327288	0.0032	-19.747176902	0.0042	319.2332	0.0097
03JUL05	GD	64.119327326	0.0032	-19.747176969	0.0042	319.2398	0.0101
03JUL06	GD	64.119327307	0.0030	-19.747176963	0.0037	319.2390	0.0095
03JUL07	GD	64.119327303	0.0031	-19.747176904	0.0039	319.2333	0.0098
03JUL08	GD	64.119327296	0.0029	-19.747176870	0.0037	319.2359	0.0092
03JUL09	GD	64.119327320	0.0032	-19.747176930	0.0039	319.2298	0.0101
03JUL10	GD	64.119327302	0.0031	-19.747176969	0.0038	319.2308	0.0100
03JUL11	GD	64.119327239	0.0044	-19.747177173	0.0061	319.2412	0.0116
03JUL12	GD	64.119327293	0.0035	-19.747177019	0.0047	319.2310	0.0114
03JUL13	GD	64.119327281	0.0031	-19.747176981	0.0039	319.2237	0.0097
03JUL14	GD	64.119327310	0.0030	-19.747177018	0.0039	319.2283	0.0094
03JUL15	GD	64.119327325	0.0034	-19.747176987	0.0047	319.2441	0.0107
03JUL16	GD	64.119327318	0.0041	-19.747177086	0.0059	319.2397	0.0122
03JUL18	GD	64.119327257	0.0062	-19.747177006	0.0073	319.2258	0.0169
03JUL19	GD	64.119327306	0.0034	-19.747176942	0.0043	319.2448	0.0102
03JUL20	GD	64.119327292	0.0032	-19.747176866	0.0040	319.2413	0.0098
03JUL21	GD	64.119327307	0.0031	-19.747176957	0.0039	319.2368	0.0100
03JUL22	GD	64.119327289	0.0030	-19.747176913	0.0038	319.2389	0.0094
03JUL23	GD	64.119327299	0.0030	-19.747176925	0.0039	319.2367	0.0097
03JUL24	GD	64.119327295	0.0030	-19.747176956	0.0037	319.2394	0.0096
03JUL25	GD	64.119327305	0.0029	-19.747177014	0.0038	319.2404	0.0095
03JUL26	GD	64.119327305	0.0032	-19.747176955	0.0044	319.2474	0.0107
03JUL27	GD	64.119327292	0.0033	-19.747176939	0.0045	319.2285	0.0106
03JUL28	GD	64.119327310	0.0030	-19.747176923	0.0037	319.2398	0.0095
03JUL29	GD	64.119327318	0.0035	-19.747176885	0.0057	319.2372	0.0123
03JUL30	GD	64.119327306	0.0031	-19.747176977	0.0045	319.2424	0.0102
03JUL31	GD	64.119327290	0.0032	-19.747176843	0.0045	319.2544	0.0105

03AUG01	GD	64.119327354	0.0035	-19.747176954	0.0052	319.2628 0.0111
03AUG02	GD	64.119327321	0.0030	-19.747176892	0.0042	319.2495 0.0098
03AUG03	GD	64.119327317	0.0031	-19.747176937	0.0043	319.2483 0.0102
03AUG04	GD	64.119327320	0.0029	-19.747176958	0.0040	319.2464 0.0100
03AUG05	GD	64.119327331	0.0029	-19.747176959	0.0037	319.2474 0.0092
03AUG06	GD	64.119327333	0.0033	-19.747177006	0.0046	319.2421 0.0106
03AUG07	GD	64.119327350	0.0032	-19.747176990	0.0041	319.2470 0.0100
03AUG08	GD	64.119327307	0.0034	-19.747176970	0.0047	319.2421 0.0110
03AUG09	GD	64.119327225	0.0032	-19.747176919	0.0042	319.2404 0.0103
03AUG10	GD	64.119327327	0.0030	-19.747176968	0.0039	319.2375 0.0095
03AUG11	GD	64.119327330	0.0032	-19.747176856	0.0040	319.2389 0.0097
03AUG12	GD	64.119327343	0.0032	-19.747176968	0.0045	319.2406 0.0103
03AUG13	GD	64.119327352	0.0030	-19.747177020	0.0042	319.2445 0.0096
03AUG14	GD	64.119327321	0.0033	-19.747176869	0.0043	319.2482 0.0100
03AUG15	GD	64.119327345	0.0031	-19.747176972	0.0040	319.2350 0.0098
03AUG16	GD	64.119327314	0.0031	-19.747176925	0.0041	319.2460 0.0101
03AUG17	GD	64.119327334	0.0032	-19.747176956	0.0040	319.2416 0.0099
03AUG18	GD	64.119327396	0.0068	-19.747176995	0.0101	319.2415 0.0191
03AUG19	GD	64.119327292	0.0031	-19.747176970	0.0043	319.2449 0.0101
03AUG20	GD	64.119327317	0.0031	-19.747176916	0.0040	319.2415 0.0098
03AUG21	GD	64.119327305	0.0037	-19.747177116	0.0054	319.2493 0.0111
03AUG22	GD	64.119327326	0.0033	-19.747177007	0.0045	319.2378 0.0101
03AUG23	GD	64.119327342	0.0033	-19.747176922	0.0046	319.2361 0.0107
03AUG24	GD	64.119327329	0.0031	-19.747176991	0.0039	319.2350 0.0096
03AUG25	GD	64.119327334	0.0030	-19.747176998	0.0039	319.2322 0.0096
03AUG26	GD	64.119327346	0.0031	-19.747176976	0.0042	319.2415 0.0100
03AUG27	GD	64.119327330	0.0030	-19.747177013	0.0040	319.2374 0.0095
03AUG28	GD	64.119327342	0.0032	-19.747176922	0.0046	319.2354 0.0106
03AUG29	GD	64.119327325	0.0031	-19.747176947	0.0039	319.2355 0.0098
03AUG30	GD	64.119327342	0.0033	-19.747176913	0.0046	319.2464 0.0109
03AUG31	GD	64.119327303	0.0032	-19.747176905	0.0040	319.2480 0.0105
03SEP01	GD	64.119327320	0.0032	-19.747176933	0.0042	319.2307 0.0104
03SEP02	GD	64.119327276	0.0030	-19.747176931	0.0040	319.2401 0.0100
03SEP03	GD	64.119327313	0.0031	-19.747176885	0.0042	319.2510 0.0099
03SEP04	GD	64.119327284	0.0034	-19.747176965	0.0046	319.2524 0.0105
03SEP05	GD	64.119327328	0.0030	-19.747176996	0.0040	319.2495 0.0096
03SEP06	GD	64.119327310	0.0030	-19.747176894	0.0038	319.2422 0.0095
03SEP07	GD	64.119327338	0.0029	-19.747176908	0.0037	319.2438 0.0093
03SEP08	GD	64.119327333	0.0031	-19.747176987	0.0040	319.2376 0.0096
03SEP09	GD	64.119327348	0.0033	-19.747176951	0.0042	319.2342 0.0102
03SEP10	GD	64.119327353	0.0042	-19.747176906	0.0064	319.2503 0.0141
03SEP15	GD	64.119327335	0.0050	-19.747176918	0.0071	319.2431 0.0143
03SEP16	GD	64.119327319	0.0035	-19.747176987	0.0049	319.2426 0.0111
03SEP17	GD	64.119327303	0.0037	-19.747177023	0.0052	319.2379 0.0117
03SEP18	GD	64.119327337	0.0036	-19.747177030	0.0051	319.2329 0.0116
03SEP19	GD	64.119327363	0.0038	-19.747177116	0.0055	319.2313 0.0126
03SEP20	GD	64.119327320	0.0037	-19.747176878	0.0051	319.2162 0.0122
03SEP21	GD	64.119327312	0.0032	-19.747176928	0.0044	319.2468 0.0111
03SEP22	GD	64.119327320	0.0031	-19.747176990	0.0045	319.2373 0.0102
03SEP23	GD	64.119327318	0.0037	-19.747177075	0.0052	319.2324 0.0124
03SEP24	GD	64.119327348	0.0041	-19.747177001	0.0056	319.2432 0.0131
03SEP25	GD	64.119327352	0.0035	-19.747176899	0.0046	319.2472 0.0106
03SEP26	GD	64.119327364	0.0037	-19.747176954	0.0050	319.2465 0.0124
03SEP27	GD	64.119327355	0.0034	-19.747176903	0.0046	319.2427 0.0117
03SEP28	GD	64.119327352	0.0034	-19.747176978	0.0046	319.2453 0.0118
03SEP29	GD	64.119327331	0.0031	-19.747176984	0.0041	319.2442 0.0104
03SEP30	GD	64.119327352	0.0036	-19.747176973	0.0049	319.2373 0.0124
03OCT01	GD	64.119327338	0.0037	-19.747177048	0.0051	319.2358 0.0124
03OCT02	GD	64.119327311	0.0034	-19.747177048	0.0046	319.2443 0.0114
03OCT03	GD	64.119327321	0.0032	-19.747176920	0.0042	319.2443 0.0105
03OCT04	GD	64.119327342	0.0032	-19.747177023	0.0044	319.2385 0.0112
03OCT05	GD	64.119327339	0.0032	-19.747176993	0.0044	319.2382 0.0113
03OCT06	GD	64.119327343	0.0034	-19.747177014	0.0049	319.2412 0.0122
03OCT07	GD	64.119327336	0.0038	-19.747176987	0.0054	319.2506 0.0130
03OCT08	GD	64.119327328	0.0032	-19.747176990	0.0044	319.2561 0.0112
03OCT09	GD	64.119327322	0.0032	-19.747176925	0.0043	319.2486 0.0110
03OCT10	GD	64.119327337	0.0029	-19.747176960	0.0039	319.2468 0.0100
03OCT11	GD	64.119327356	0.0030	-19.747176998	0.0039	319.2382 0.0099
03OCT12	GD	64.119327429	0.0033	-19.747176953	0.0043	319.2612 0.0112
03OCT13	GD	64.119327338	0.0033	-19.747176997	0.0045	319.2481 0.0107
03OCT14	GD	64.119327402	0.0035	-19.747176955	0.0049	319.2463 0.0111
03OCT15	GD	64.119327353	0.0035	-19.747176918	0.0047	319.2404 0.0117
03OCT16	GD	64.119327357	0.0030	-19.747176929	0.0042	319.2398 0.0098
03OCT17	GD	64.119327328	0.0032	-19.747176974	0.0042	319.2427 0.0098

03OCT18	GD	64.119327348	0.0033	-19.747177000	0.0048	319.2387 0.0113
03OCT19	GD	64.119327332	0.0038	-19.747177007	0.0052	319.2390 0.0123
03OCT20	GD	64.119327343	0.0031	-19.747176876	0.0044	319.2393 0.0103
03OCT21	GD	64.119327345	0.0039	-19.747177058	0.0055	319.2419 0.0130
03OCT22	GD	64.119327354	0.0041	-19.747177062	0.0057	319.2482 0.0137
03OCT23	GD	64.119327335	0.0034	-19.747176990	0.0047	319.2486 0.0118
03OCT24	GD	64.119327361	0.0037	-19.747177056	0.0055	319.2364 0.0128
03OCT25	GD	64.119327345	0.0034	-19.747177014	0.0046	319.2454 0.0113
03OCT26	GD	64.119327298	0.0032	-19.747177025	0.0044	319.2400 0.0109
03OCT27	GD	64.119327280	0.0040	-19.747176955	0.0052	319.2475 0.0129
03OCT28	GD	64.119327311	0.0036	-19.747176952	0.0051	319.2447 0.0120
03OCT29	GD	64.119327338	0.0051	-19.747176846	0.0082	319.2539 0.0155
03OCT30	GD	64.119327330	0.0043	-19.747177127	0.0056	319.2337 0.0131
03OCT31	GD	64.119327331	0.0039	-19.747177130	0.0051	319.2307 0.0127
03NOV01	GD	64.119327339	0.0036	-19.747177151	0.0052	319.2366 0.0122
03NOV02	GD	64.119327343	0.0034	-19.747177059	0.0047	319.2510 0.0108
03NOV03	GD	64.119327356	0.0033	-19.747177034	0.0043	319.2526 0.0108
03NOV04	GD	64.119327348	0.0037	-19.747177066	0.0062	319.2506 0.0127
03NOV05	GD	64.119327370	0.0032	-19.747177154	0.0044	319.2513 0.0111
03NOV06	GD	64.119327342	0.0037	-19.747176969	0.0048	319.2467 0.0112
03NOV12	GD	64.119327318	0.0080	-19.747176818	0.0109	319.2622 0.0189
03NOV13	GD	64.119327408	0.0037	-19.747177123	0.0055	319.2552 0.0124
03NOV14	GD	64.119327351	0.0044	-19.747176860	0.0055	319.2403 0.0123
03NOV15	GD	64.119327342	0.0033	-19.747176968	0.0049	319.2496 0.0103
03NOV16	GD	64.119327338	0.0039	-19.747176979	0.0058	319.2411 0.0124
03NOV17	GD	64.119327356	0.0041	-19.747176961	0.0059	319.2501 0.0129
03NOV18	GD	64.119327357	0.0034	-19.747177038	0.0048	319.2591 0.0115
03NOV19	GD	64.119327372	0.0033	-19.747176973	0.0044	319.2478 0.0108
03NOV20	GD	64.119327342	0.0042	-19.747177063	0.0067	319.2526 0.0127
03NOV21	GD	64.119327347	0.0033	-19.747176999	0.0044	319.2547 0.0101
03NOV22	GD	64.119327346	0.0041	-19.747177008	0.0053	319.2556 0.0123
03NOV23	GD	64.119327343	0.0038	-19.747177080	0.0050	319.2562 0.0123
03NOV24	GD	64.119327333	0.0034	-19.747176965	0.0045	319.2496 0.0112
03NOV25	GD	64.119327324	0.0034	-19.747176897	0.0048	319.2520 0.0115
03NOV26	GD	64.119327336	0.0033	-19.747177000	0.0046	319.2464 0.0112
03NOV27	GD	64.119327344	0.0033	-19.747177021	0.0044	319.2442 0.0112
03NOV28	GD	64.119327329	0.0034	-19.747177059	0.0048	319.2443 0.0119
03NOV29	GD	64.119327369	0.0032	-19.747177012	0.0042	319.2483 0.0107
03NOV30	GD	64.119327374	0.0036	-19.747177036	0.0049	319.2481 0.0112
03DEC01	GD	64.119327371	0.0035	-19.747177043	0.0047	319.2567 0.0112
03DEC02	GD	64.119327339	0.0032	-19.747177017	0.0041	319.2564 0.0108
03DEC03	GD	64.119327344	0.0031	-19.747177033	0.0040	319.2553 0.0104
03DEC04	GD	64.119327355	0.0032	-19.747177014	0.0042	319.2546 0.0108
03DEC05	GD	64.119327318	0.0045	-19.747177021	0.0073	319.2483 0.0123
03DEC06	GD	64.119327352	0.0034	-19.747177030	0.0042	319.2335 0.0101
03DEC07	GD	64.119327325	0.0032	-19.747176996	0.0042	319.2524 0.0104
03DEC08	GD	64.119327324	0.0033	-19.747177037	0.0045	319.2469 0.0108
03DEC09	GD	64.119327357	0.0032	-19.747177036	0.0041	319.2408 0.0104
03DEC10	GD	64.119327364	0.0036	-19.747177079	0.0047	319.2357 0.0111
03DEC11	GD	64.119327341	0.0035	-19.747177077	0.0046	319.2400 0.0117
03DEC12	GD	64.119327344	0.0033	-19.747177026	0.0045	319.2501 0.0115
03DEC13	GD	64.119327353	0.0032	-19.747177012	0.0040	319.2468 0.0105
03DEC14	GD	64.119327362	0.0034	-19.747177067	0.0044	319.2493 0.0110
03DEC15	GD	64.119327379	0.0033	-19.747177113	0.0043	319.2489 0.0115
03DEC16	GD	64.119327358	0.0031	-19.747176997	0.0039	319.2467 0.0098
03DEC17	GD	64.119327380	0.0032	-19.747176962	0.0040	319.2507 0.0103
03DEC18	GD	64.119327359	0.0032	-19.747176994	0.0041	319.2560 0.0107
03DEC19	GD	64.119327369	0.0034	-19.747177039	0.0042	319.2420 0.0112
03DEC20	GD	64.119327367	0.0036	-19.747177074	0.0048	319.2328 0.0113
03DEC21	GD	64.119327372	0.0041	-19.747177056	0.0053	319.2433 0.0132
03DEC22	GD	64.119327332	0.0033	-19.747176979	0.0040	319.2469 0.0101
03DEC23	GD	64.119327337	0.0033	-19.747176992	0.0041	319.2512 0.0105
03DEC24	GD	64.119327335	0.0034	-19.747176948	0.0043	319.2446 0.0108
03DEC25	GD	64.119327340	0.0032	-19.747176897	0.0039	319.2490 0.0102
03DEC26	GD	64.119327360	0.0034	-19.747177030	0.0042	319.2425 0.0107
03DEC27	GD	64.119327380	0.0035	-19.747176980	0.0043	319.2391 0.0105
03DEC28	GD	64.119327363	0.0035	-19.747177049	0.0043	319.2405 0.0113
03DEC29	GD	64.119327367	0.0032	-19.747176986	0.0039	319.2593 0.0104
03DEC30	GD	64.119327356	0.0033	-19.747176883	0.0039	319.2420 0.0099
03DEC31	GD	64.119327361	0.0034	-19.747176946	0.0043	319.2547 0.0102
04JAN01	GD	64.119327384	0.0037	-19.747176945	0.0046	319.2471 0.0118
04JAN02	GD	64.119327349	0.0072	-19.747176707	0.0105	319.2686 0.0218
04JAN03	GD	64.119327382	0.0033	-19.747176976	0.0039	319.2509 0.0102
04JAN04	GD	64.119327364	0.0032	-19.747176901	0.0040	319.2494 0.0101

04JAN05	GD	64.119327356	0.0034	-19.747176891	0.0041	319.2397 0.0105
04JAN06	GD	64.119327348	0.0034	-19.747176900	0.0040	319.2394 0.0101
04JAN07	GD	64.119327400	0.0035	-19.747176968	0.0047	319.2568 0.0104
04JAN08	GD	64.119327390	0.0035	-19.747176942	0.0041	319.2554 0.0103
04JAN09	GD	64.119327388	0.0036	-19.747177027	0.0044	319.2553 0.0105
04JAN10	GD	64.119327368	0.0038	-19.747176906	0.0049	319.2437 0.0109
04JAN11	GD	64.119327380	0.0032	-19.747177031	0.0040	319.2524 0.0101
04JAN12	GD	64.119327357	0.0035	-19.747176951	0.0040	319.2608 0.0102
04JAN13	GD	64.119327351	0.0037	-19.747177073	0.0043	319.2550 0.0105
04JAN14	GD	64.119327352	0.0035	-19.747176989	0.0041	319.2570 0.0108
04JAN15	GD	64.119327415	0.0038	-19.747177002	0.0048	319.2531 0.0122
04JAN16	GD	64.119327382	0.0039	-19.747176977	0.0045	319.2451 0.0119
04JAN17	GD	64.119327367	0.0033	-19.747176894	0.0039	319.2523 0.0103
04JAN18	GD	64.119327348	0.0036	-19.747176909	0.0042	319.2497 0.0111
04JAN19	GD	64.119327414	0.0034	-19.747177012	0.0042	319.2482 0.0104
04JAN20	GD	64.119327403	0.0034	-19.747176950	0.0041	319.2550 0.0106
04JAN21	GD	64.119327395	0.0035	-19.747177011	0.0042	319.2508 0.0107
04JAN22	GD	64.119327380	0.0041	-19.747176965	0.0059	319.2600 0.0120
04JAN23	GD	64.119327389	0.0036	-19.747176889	0.0051	319.2716 0.0107
04JAN24	GD	64.119327371	0.0034	-19.747176971	0.0039	319.2486 0.0106
04JAN25	GD	64.119327419	0.0044	-19.747177081	0.0057	319.2494 0.0116
04JAN26	GD	64.119327376	0.0035	-19.747177062	0.0040	319.2527 0.0111
04JAN27	GD	64.119327375	0.0034	-19.747177031	0.0042	319.2511 0.0111
04JAN28	GD	64.119327383	0.0033	-19.747177048	0.0041	319.2524 0.0108
04JAN29	GD	64.119327410	0.0032	-19.747177104	0.0038	319.2442 0.0102
04JAN30	GD	64.119327375	0.0033	-19.747177049	0.0037	319.2495 0.0102
04JAN31	GD	64.119327374	0.0031	-19.747177035	0.0037	319.2431 0.0102
04FEB01	GD	64.119327391	0.0032	-19.747177073	0.0039	319.2454 0.0104
04FEB02	GD	64.119327372	0.0031	-19.747177022	0.0037	319.2476 0.0098
04FEB03	GD	64.119327383	0.0032	-19.747177006	0.0041	319.2471 0.0103
04FEB04	GD	64.119327383	0.0030	-19.747176966	0.0040	319.2493 0.0099
04FEB05	GD	64.119327378	0.0033	-19.747177023	0.0041	319.2477 0.0107
04FEB06	GD	64.119327365	0.0032	-19.747176996	0.0039	319.2515 0.0103
04FEB07	GD	64.119327386	0.0032	-19.747177000	0.0038	319.2476 0.0102
04FEB08	GD	64.119327373	0.0035	-19.747177044	0.0041	319.2449 0.0107
04FEB09	GD	64.119327370	0.0033	-19.747176997	0.0038	319.2641 0.0100
04FEB10	GD	64.119327397	0.0030	-19.747176945	0.0038	319.2501 0.0096
04FEB11	GD	64.119327373	0.0035	-19.747176956	0.0042	319.2471 0.0101
04FEB12	GD	64.119327350	0.0036	-19.747177030	0.0045	319.2527 0.0104
04FEB13	GD	64.119327387	0.0036	-19.747177057	0.0044	319.2479 0.0106
04FEB14	GD	64.119327369	0.0035	-19.747177044	0.0043	319.2507 0.0103
04FEB15	GD	64.119327408	0.0033	-19.747177038	0.0043	319.2498 0.0104
04FEB16	GD	64.119327398	0.0032	-19.747177044	0.0042	319.2430 0.0108
04FEB17	GD	64.119327410	0.0032	-19.747176951	0.0038	319.2490 0.0100
04FEB18	GD	64.119327378	0.0033	-19.747177133	0.0039	319.2513 0.0097
04FEB19	GD	64.119327394	0.0031	-19.747177017	0.0039	319.2472 0.0098
04FEB20	GD	64.119327379	0.0032	-19.747177015	0.0041	319.2420 0.0104
04FEB21	GD	64.119327392	0.0030	-19.747176968	0.0039	319.2431 0.0096
04FEB22	GD	64.119327364	0.0035	-19.747177036	0.0043	319.2461 0.0115
04FEB23	GD	64.119327357	0.0030	-19.747176883	0.0038	319.2487 0.0094
04FEB24	GD	64.119327380	0.0035	-19.747177040	0.0045	319.2470 0.0111
04FEB25	GD	64.119327384	0.0034	-19.747177084	0.0041	319.2433 0.0113
04FEB26	GD	64.119327394	0.0031	-19.747177080	0.0040	319.2437 0.0103
04FEB27	GD	64.119327405	0.0036	-19.747177072	0.0041	319.2513 0.0114
04FEB28	GD	64.119327380	0.0032	-19.747177039	0.0039	319.2571 0.0100
04FEB29	GD	64.119327386	0.0032	-19.747176992	0.0041	319.2531 0.0100
04MAR01	GD	64.119327398	0.0034	-19.747177130	0.0040	319.2613 0.0103
04MAR02	GD	64.119327357	0.0031	-19.747176874	0.0041	319.2437 0.0098
04MAR03	GD	64.119327374	0.0031	-19.747176967	0.0039	319.2544 0.0097
04MAR04	GD	64.119327405	0.0031	-19.747176969	0.0042	319.2591 0.0111
04MAR05	GD	64.119327387	0.0030	-19.747177042	0.0039	319.2512 0.0097
04MAR06	GD	64.119327397	0.0032	-19.747177053	0.0041	319.2553 0.0100
04MAR07	GD	64.119327408	0.0030	-19.747177054	0.0039	319.2574 0.0100
04MAR08	GD	64.119327422	0.0031	-19.747177067	0.0040	319.2538 0.0100
04MAR09	GD	64.119327445	0.0037	-19.747177252	0.0046	319.2649 0.0111
04MAR10	GD	64.119327351	0.0037	-19.747176746	0.0051	319.2555 0.0115
04MAR11	GD	64.119327420	0.0036	-19.747176966	0.0044	319.2576 0.0103
04MAR12	GD	64.119327427	0.0033	-19.747177027	0.0041	319.2543 0.0105
04MAR13	GD	64.119327398	0.0032	-19.747176962	0.0041	319.2608 0.0107
04MAR14	GD	64.119327409	0.0033	-19.747177017	0.0040	319.2541 0.0099
04MAR15	GD	64.119327412	0.0030	-19.747176920	0.0041	319.2557 0.0097
04MAR16	GD	64.119327397	0.0030	-19.747176870	0.0041	319.2511 0.0095
04MAR17	GD	64.119327403	0.0032	-19.747176950	0.0043	319.2467 0.0102
04MAR18	GD	64.119327403	0.0037	-19.747177032	0.0046	319.2470 0.0126

04MAR19	GD	64.119327445	0.0033	-19.747177012	0.0042	319.2505 0.0102
04MAR20	GD	64.119327418	0.0035	-19.747176964	0.0041	319.2559 0.0102
04MAR21	GD	64.119327431	0.0031	-19.747177026	0.0040	319.2500 0.0101
04MAR22	GD	64.119327424	0.0032	-19.747176993	0.0042	319.2482 0.0102
04MAR23	GD	64.119327417	0.0032	-19.747177010	0.0040	319.2503 0.0101
04MAR24	GD	64.119327395	0.0031	-19.747176906	0.0039	319.2540 0.0098
04MAR25	GD	64.119327409	0.0032	-19.747176911	0.0041	319.2460 0.0108
04MAR26	GD	64.119327414	0.0036	-19.747176849	0.0044	319.2591 0.0115
04MAR27	GD	64.119327384	0.0033	-19.747176910	0.0043	319.2529 0.0102
04MAR28	GD	64.119327395	0.0036	-19.747176930	0.0046	319.2485 0.0118
04MAR29	GD	64.119327425	0.0030	-19.747176951	0.0038	319.2502 0.0097
04MAR30	GD	64.119327383	0.0033	-19.747176962	0.0045	319.2480 0.0118
04MAR31	GD	64.119327424	0.0032	-19.747176959	0.0042	319.2485 0.0107
04APR01	GD	64.119327428	0.0030	-19.747176881	0.0038	319.2513 0.0099
04APR02	GD	64.119327526	0.0030	-19.747177056	0.0038	319.2655 0.0096
04APR03	GD	64.119327431	0.0038	-19.747177056	0.0045	319.2643 0.0111
04APR04	GD	64.119327404	0.0031	-19.747176995	0.0041	319.2515 0.0107
04APR05	GD	64.119327436	0.0034	-19.747176936	0.0042	319.2547 0.0102
04APR06	GD	64.119327439	0.0033	-19.747177019	0.0044	319.2435 0.0103
04APR07	GD	64.119327434	0.0034	-19.747177002	0.0043	319.2493 0.0106
04APR08	GD	64.119327421	0.0030	-19.747177030	0.0038	319.2492 0.0095
04APR09	GD	64.119327440	0.0032	-19.747177007	0.0040	319.2360 0.0096
04APR10	GD	64.119327433	0.0033	-19.747176908	0.0043	319.2506 0.0112
04APR11	GD	64.119327438	0.0033	-19.747176908	0.0042	319.2503 0.0108
04APR12	GD	64.119327420	0.0031	-19.747176972	0.0039	319.2475 0.0098
04APR13	GD	64.119327434	0.0031	-19.747177011	0.0039	319.2413 0.0097
04APR14	GD	64.119327477	0.0031	-19.747176980	0.0038	319.2474 0.0096
04APR15	GD	64.119327419	0.0031	-19.747177035	0.0041	319.2518 0.0104
04APR16	GD	64.119327440	0.0032	-19.747177024	0.0042	319.2521 0.0096
04APR17	GD	64.119327431	0.0029	-19.747177105	0.0036	319.2485 0.0091
04APR18	GD	64.119327436	0.0030	-19.747177084	0.0037	319.2389 0.0091
04APR19	GD	64.119327443	0.0031	-19.747177067	0.0039	319.2473 0.0091
04APR20	GD	64.119327418	0.0030	-19.747176998	0.0037	319.2535 0.0093
04APR21	GD	64.119327409	0.0030	-19.747176991	0.0038	319.2513 0.0094
04APR22	GD	64.119327433	0.0030	-19.747177030	0.0037	319.2517 0.0091
04APR23	GD	64.119327463	0.0031	-19.747177069	0.0039	319.2410 0.0100
04APR24	GD	64.119327486	0.0030	-19.747176953	0.0038	319.2512 0.0095
04APR25	GD	64.119327483	0.0030	-19.747177091	0.0039	319.2541 0.0092
04APR26	GD	64.119327438	0.0029	-19.747177005	0.0036	319.2480 0.0091
04APR27	GD	64.119327452	0.0030	-19.747177021	0.0037	319.2452 0.0095
04APR28	GD	64.119327477	0.0030	-19.747176975	0.0038	319.2421 0.0095
04APR29	GD	64.119327470	0.0030	-19.747176977	0.0037	319.2476 0.0094
04APR30	GD	64.119327430	0.0032	-19.747177020	0.0042	319.2475 0.0100
04MAY01	GD	64.119327451	0.0031	-19.747177066	0.0038	319.2591 0.0094
04MAY02	GD	64.119327432	0.0030	-19.747177066	0.0038	319.2616 0.0096
04MAY03	GD	64.119327437	0.0031	-19.747177061	0.0039	319.2622 0.0096
04MAY04	GD	64.119327427	0.0032	-19.747177071	0.0042	319.2546 0.0098
04MAY05	GD	64.119327429	0.0031	-19.747177013	0.0041	319.2397 0.0101
04MAY06	GD	64.119327422	0.0032	-19.747177005	0.0039	319.2515 0.0102
04MAY07	GD	64.119327424	0.0033	-19.747177017	0.0043	319.2456 0.0102
04MAY08	GD	64.119327475	0.0031	-19.747177040	0.0038	319.2443 0.0094
04MAY09	GD	64.119327471	0.0031	-19.747177013	0.0039	319.2476 0.0099
04MAY10	GD	64.119327457	0.0035	-19.747177006	0.0040	319.2451 0.0102
04MAY11	GD	64.119327486	0.0032	-19.747176938	0.0040	319.2479 0.0097
04MAY12	GD	64.119327518	0.0034	-19.747177069	0.0042	319.2511 0.0106
04MAY13	GD	64.119327458	0.0035	-19.747177033	0.0042	319.2618 0.0098
04MAY14	GD	64.119327445	0.0033	-19.747177046	0.0040	319.2513 0.0100
04MAY15	GD	64.119327478	0.0032	-19.747177024	0.0038	319.2550 0.0101
04MAY16	GD	64.119327442	0.0032	-19.747177011	0.0040	319.2517 0.0097
04MAY17	GD	64.119327462	0.0031	-19.747177047	0.0037	319.2437 0.0094
04MAY18	GD	64.119327472	0.0030	-19.747177071	0.0037	319.2430 0.0091
04MAY19	GD	64.119327453	0.0029	-19.747177070	0.0036	319.2458 0.0090
04MAY21	GD	64.119327424	0.0044	-19.747177123	0.0058	319.2296 0.0137
04MAY22	GD	64.119327503	0.0050	-19.747177077	0.0056	319.2456 0.0157
04MAY23	GD	64.119327401	0.0062	-19.747177134	0.0067	319.2313 0.0165
04MAY24	GD	64.119327460	0.0029	-19.747177053	0.0036	319.2402 0.0090
04MAY25	GD	64.119327462	0.0031	-19.747177018	0.0038	319.2505 0.0096
04MAY26	GD	64.119327439	0.0031	-19.747176980	0.0038	319.2453 0.0098
04MAY27	GD	64.119327473	0.0033	-19.747176997	0.0041	319.2406 0.0103
04MAY28	GD	64.119327489	0.0054	-19.747176806	0.0064	319.2531 0.0145
04MAY29	GD	64.119327487	0.0032	-19.747176916	0.0042	319.2466 0.0099
04JUN01	GD	64.119327486	0.0056	-19.747177121	0.0065	319.2319 0.0159
04JUN03	GD	64.119327470	0.0058	-19.747177061	0.0063	319.2350 0.0157
04JUN04	GD	64.119327454	0.0029	-19.747177044	0.0037	319.2368 0.0093

04JUN05	GD	64.119327438	0.0030	-19.747177025	0.0039	319.2458	0.0097
04JUN06	GD	64.119327457	0.0031	-19.747177014	0.0038	319.2457	0.0097
04JUN07	GD	64.119327481	0.0030	-19.747176954	0.0039	319.2463	0.0095
04JUN08	GD	64.119327459	0.0030	-19.747177014	0.0038	319.2466	0.0095
04JUN09	GD	64.119327462	0.0030	-19.747176964	0.0036	319.2503	0.0092
04JUN10	GD	64.119327474	0.0030	-19.747177036	0.0037	319.2430	0.0093
04JUN11	GD	64.119327464	0.0030	-19.747177018	0.0037	319.2453	0.0092
04JUN12	GD	64.119327474	0.0029	-19.747177032	0.0036	319.2496	0.0093
04JUN13	GD	64.119327417	0.0030	-19.747177014	0.0037	319.2389	0.0094
04JUN14	GD	64.119327451	0.0030	-19.747177097	0.0038	319.2441	0.0097
04JUN15	GD	64.119327480	0.0031	-19.747177071	0.0038	319.2443	0.0095
04JUN16	GD	64.119327494	0.0031	-19.747177079	0.0038	319.2400	0.0096
04JUN17	GD	64.119327490	0.0030	-19.747176966	0.0038	319.2472	0.0097
04JUN18	GD	64.119327463	0.0031	-19.747176983	0.0038	319.2477	0.0097
04JUN19	GD	64.119327456	0.0029	-19.747177037	0.0036	319.2391	0.0091
04JUN20	GD	64.119327487	0.0030	-19.747176990	0.0037	319.2453	0.0094
04JUN21	GD	64.119327471	0.0031	-19.747177035	0.0037	319.2425	0.0095
04JUN22	GD	64.119327483	0.0032	-19.747177002	0.0040	319.2472	0.0098
04JUN23	GD	64.119327488	0.0030	-19.747176994	0.0037	319.2444	0.0093
04JUN24	GD	64.119327481	0.0030	-19.747177028	0.0037	319.2518	0.0096
04JUN25	GD	64.119327505	0.0031	-19.747177127	0.0038	319.2580	0.0096
04JUN26	GD	64.119327560	0.0031	-19.747177112	0.0037	319.2787	0.0092
04JUN27	GD	64.119327486	0.0031	-19.747177081	0.0037	319.2433	0.0093
04JUN28	GD	64.119327482	0.0032	-19.747177026	0.0040	319.2499	0.0096
04JUN29	GD	64.119327474	0.0032	-19.747177031	0.0040	319.2504	0.0095
04JUN30	GD	64.119327494	0.0030	-19.747177162	0.0036	319.2542	0.0092
04JUL01	GD	64.119327511	0.0030	-19.747177073	0.0037	319.2517	0.0091
04JUL02	GD	64.119327491	0.0030	-19.747177023	0.0037	319.2462	0.0091
04JUL03	GD	64.119327482	0.0029	-19.747176990	0.0036	319.2432	0.0090
04JUL04	GD	64.119327495	0.0030	-19.747176968	0.0037	319.2432	0.0092
04JUL05	GD	64.119327482	0.0031	-19.747177014	0.0038	319.2456	0.0094
04JUL06	GD	64.119327510	0.0029	-19.747177018	0.0036	319.2512	0.0092
04JUL07	GD	64.119327490	0.0030	-19.747176964	0.0037	319.2521	0.0093
04JUL08	GD	64.119327517	0.0031	-19.747176962	0.0039	319.2509	0.0095
04JUL09	GD	64.119327515	0.0030	-19.747177031	0.0038	319.2547	0.0092
04JUL10	GD	64.119327493	0.0031	-19.747177001	0.0039	319.2482	0.0094
04JUL11	GD	64.119327465	0.0030	-19.747177092	0.0039	319.2587	0.0095
04JUL12	GD	64.119327514	0.0030	-19.747177050	0.0037	319.2449	0.0093
04JUL13	GD	64.119327469	0.0031	-19.747176981	0.0041	319.2451	0.0097
04JUL14	GD	64.119327487	0.0029	-19.747176998	0.0036	319.2512	0.0089
04JUL15	GD	64.119327516	0.0029	-19.747177048	0.0038	319.2393	0.0094
04JUL16	GD	64.119327478	0.0029	-19.747177081	0.0039	319.2521	0.0094
04JUL27	GD	64.119327478	0.0091	-19.747176819	0.0139	319.2650	0.0199
04JUL28	GD	64.119327508	0.0030	-19.747177080	0.0039	319.2526	0.0091
04JUL29	GD	64.119327567	0.0030	-19.747177128	0.0039	319.2929	0.0094
04JUL30	GD	64.119327507	0.0030	-19.747177067	0.0039	319.2724	0.0096
04JUL31	GD	64.119327513	0.0029	-19.747177093	0.0036	319.2556	0.0091
04AUG01	GD	64.119327574	0.0030	-19.747177056	0.0039	319.2579	0.0096
04AUG02	GD	64.119327526	0.0030	-19.747177125	0.0038	319.2624	0.0092
04AUG03	GD	64.119327501	0.0030	-19.747177041	0.0039	319.2514	0.0097
04AUG04	GD	64.119327484	0.0029	-19.747177036	0.0037	319.2612	0.0093
04AUG05	GD	64.119327505	0.0031	-19.747176932	0.0039	319.2573	0.0096
04AUG06	GD	64.119327536	0.0030	-19.747177069	0.0039	319.2613	0.0094
04AUG07	GD	64.119327499	0.0030	-19.747177056	0.0040	319.2708	0.0096
04AUG08	GD	64.119327494	0.0030	-19.747177050	0.0039	319.2650	0.0094
04AUG09	GD	64.119327477	0.0032	-19.747177062	0.0043	319.2667	0.0100
04AUG10	GD	64.119327492	0.0032	-19.747177084	0.0042	319.2697	0.0100
04AUG11	GD	64.119327535	0.0030	-19.747177140	0.0038	319.2496	0.0096
04AUG12	GD	64.119327513	0.0031	-19.747177136	0.0038	319.2489	0.0094
04AUG13	GD	64.119327511	0.0032	-19.747177032	0.0041	319.2550	0.0098
04AUG14	GD	64.119327500	0.0030	-19.747177168	0.0039	319.2543	0.0094
04AUG15	GD	64.119327492	0.0029	-19.747177012	0.0036	319.2585	0.0090
04AUG16	GD	64.119327477	0.0030	-19.747177063	0.0041	319.2646	0.0102
04AUG17	GD	64.119327484	0.0029	-19.747177106	0.0038	319.2548	0.0092
04AUG18	GD	64.119327504	0.0030	-19.747177039	0.0041	319.2551	0.0098
04AUG19	GD	64.119327507	0.0038	-19.747177038	0.0055	319.2588	0.0122
04AUG24	GD	64.119327479	0.0083	-19.747176978	0.0099	319.2708	0.0241
04AUG25	GD	64.119327476	0.0036	-19.747177054	0.0049	319.2529	0.0128
04SEP06	GD	64.119327514	0.0059	-19.747177062	0.0086	319.2652	0.0183
04SEP07	GD	64.119327463	0.0030	-19.747177160	0.0043	319.2646	0.0096
04SEP08	GD	64.119327527	0.0027	-19.747177214	0.0038	319.2676	0.0087
04SEP09	GD	64.119327479	0.0026	-19.747177188	0.0036	319.2564	0.0082
04SEP10	GD	64.119327467	0.0027	-19.747177134	0.0038	319.2595	0.0088
04SEP11	GD	64.119327453	0.0027	-19.747177056	0.0040	319.2689	0.0092

```
04SEP12 GD   64.119327485 0.0028   -19.747177086 0.0039   319.2648 0.0091
04SEP13 GD   64.119327484 0.0027   -19.747177149 0.0036   319.2613 0.0085
04SEP14 GD   64.119327486 0.0030   -19.747177116 0.0044   319.2646 0.0088
04SEP15 GD   64.119327459 0.0028   -19.747177016 0.0041   319.2695 0.0093
04SEP16 GD   64.119327543 0.0029   -19.747177111 0.0043   319.2972 0.0095
04SEP17 GD   64.119327503 0.0031   -19.747177150 0.0043   319.2703 0.0097
04SEP18 GD   64.119327496 0.0029   -19.747177111 0.0036   319.2595 0.0084
04SEP19 GD   64.119327477 0.0027   -19.747177114 0.0037   319.2665 0.0082
04SEP20 GD   64.119327493 0.0026   -19.747177088 0.0036   319.2583 0.0080
04SEP21 GD   64.119327506 0.0030   -19.747177046 0.0043   319.2688 0.0097
04SEP22 GD   64.119327486 0.0030   -19.747177137 0.0043   319.2735 0.0096
04SEP23 GD   64.119327517 0.0026   -19.747177100 0.0036   319.2624 0.0082
04SEP24 GD   64.119327512 0.0028   -19.747177336 0.0040   319.2750 0.0090
04SEP25 GD   64.119327500 0.0029   -19.747177085 0.0044   319.2678 0.0097
04SEP26 GD   64.119327474 0.0027   -19.747177134 0.0039   319.2673 0.0089
04SEP27 GD   64.119327500 0.0026   -19.747177098 0.0036   319.2631 0.0082
04SEP28 GD   64.119327488 0.0028   -19.747177134 0.0042   319.2680 0.0095
04SEP29 GD   64.119327501 0.0028   -19.747177176 0.0043   319.2786 0.0096
04SEP30 GD   64.119327509 0.0027   -19.747177051 0.0039   319.2703 0.0092
04OCT01 GD   64.119327510 0.0028   -19.747176976 0.0039   319.2712 0.0091
04OCT02 GD   64.119327506 0.0027   -19.747177099 0.0038   319.2686 0.0089
04OCT03 GD   64.119327490 0.0028   -19.747176996 0.0041   319.2658 0.0091
04OCT04 GD   64.119327508 0.0027   -19.747176928 0.0040   319.2670 0.0087
04OCT05 GD   64.119327440 0.0026   -19.747177071 0.0036   319.2714 0.0084
04OCT06 GD   64.119327543 0.0026   -19.747177146 0.0036   319.2598 0.0082
04OCT07 GD   64.119327513 0.0026   -19.747177083 0.0035   319.2724 0.0081
04OCT08 GD   64.119327517 0.0029   -19.747177082 0.0045   319.2618 0.0100
04OCT09 GD   64.119327489 0.0029   -19.747177035 0.0044   319.2618 0.0100
04OCT10 GD   64.119327524 0.0030   -19.747177097 0.0042   319.2521 0.0097
04OCT11 GD   64.119327500 0.0030   -19.747177118 0.0048   319.2621 0.0108
04OCT12 GD   64.119327507 0.0029   -19.747177170 0.0042   319.2678 0.0095
04OCT13 GD   64.119327518 0.0032   -19.747177156 0.0044   319.2666 0.0094
04OCT14 GD   64.119327509 0.0029   -19.747177159 0.0043   319.2564 0.0097
04OCT15 GD   64.119327510 0.0029   -19.747177069 0.0041   319.2633 0.0094
04OCT16 GD   64.119327505 0.0027   -19.747177070 0.0040   319.2604 0.0094
04OCT17 GD   64.119327489 0.0028   -19.747177150 0.0041   319.2643 0.0095
04OCT18 GD   64.119327533 0.0030   -19.747177073 0.0047   319.2626 0.0103
04OCT19 GD   64.119327513 0.0030   -19.747177148 0.0042   319.2570 0.0100
04OCT20 GD   64.119327488 0.0028   -19.747177086 0.0039   319.2712 0.0090
04OCT21 GD   64.119327506 0.0027   -19.747177082 0.0037   319.2650 0.0084
04OCT22 GD   64.119327537 0.0028   -19.747177103 0.0039   319.2703 0.0090
04OCT23 GD   64.119327524 0.0026   -19.747177137 0.0036   319.2683 0.0084
04OCT24 GD   64.119327510 0.0028   -19.747177143 0.0040   319.2657 0.0091
04OCT25 GD   64.119327528 0.0028   -19.747177149 0.0037   319.2680 0.0090
04OCT26 GD   64.119327505 0.0031   -19.747177153 0.0046   319.2637 0.0105
04OCT27 GD   64.119327500 0.0028   -19.747177124 0.0040   319.2711 0.0094
04OCT28 GD   64.119327488 0.0033   -19.747177090 0.0049   319.2788 0.0107
04OCT29 GD   64.119327503 0.0030   -19.747177151 0.0043   319.2715 0.0098
04OCT30 GD   64.119327489 0.0032   -19.747177044 0.0048   319.2665 0.0111
04NOV03 GD   64.119327521 0.0077   -19.747177095 0.0104   319.2709 0.0172
04NOV04 GD   64.119327498 0.0030   -19.747177061 0.0041   319.2749 0.0096
04NOV05 GD   64.119327491 0.0031   -19.747177123 0.0043   319.2776 0.0106
04NOV06 GD   64.119327498 0.0028   -19.747177086 0.0038   319.2689 0.0092
04NOV07 GD   64.119327492 0.0029   -19.747177054 0.0042   319.2746 0.0093
04NOV08 GD   64.119327524 0.0043   -19.747177106 0.0059   319.2707 0.0127
04NOV09 GD   64.119327497 0.0043   -19.747177011 0.0065   319.2885 0.0122
04NOV10 GD   64.119327533 0.0070   -19.747177110 0.0090   319.2714 0.0181
04NOV11 GD   64.119327515 0.0030   -19.747177007 0.0043   319.2747 0.0097
04NOV12 GD   64.119327515 0.0034   -19.747177037 0.0046   319.2686 0.0108
04NOV13 GD   64.119327491 0.0029   -19.747177104 0.0041   319.2709 0.0096
04NOV14 GD   64.119327502 0.0029   -19.747176998 0.0041   319.2642 0.0095
04NOV15 GD   64.119327509 0.0030   -19.747177091 0.0043   319.2643 0.0100
04NOV16 GD   64.119327535 0.0029   -19.747177099 0.0041   319.2628 0.0095
04NOV17 GD   64.119327535 0.0030   -19.747177041 0.0042   319.2634 0.0097
04NOV18 GD   64.119327529 0.0031   -19.747177066 0.0044   319.2602 0.0102
04NOV19 GD   64.119327538 0.0032   -19.747177116 0.0052   319.2678 0.0113
04NOV20 GD   64.119327533 0.0032   -19.747177080 0.0059   319.2754 0.0116
04NOV21 GD   64.119327542 0.0031   -19.747177063 0.0044   319.2655 0.0101
04NOV22 GD   64.119327541 0.0031   -19.747177151 0.0046   319.2677 0.0102
04NOV23 GD   64.119327571 0.0030   -19.747177212 0.0040   319.2778 0.0099
04NOV24 GD   64.119327529 0.0029   -19.747177097 0.0041   319.2754 0.0099
04NOV25 GD   64.119327510 0.0032   -19.747177132 0.0043   319.2757 0.0102
04NOV26 GD   64.119327538 0.0030   -19.747177020 0.0040   319.2608 0.0094
04NOV27 GD   64.119327536 0.0029   -19.747176983 0.0042   319.2733 0.0094
```

04NOV28	GD	64.119327544	0.0030	-19.747177117	0.0040	319.2602 0.0095
04NOV29	GD	64.119327519	0.0030	-19.747177068	0.0040	319.2618 0.0095
04NOV30	GD	64.119327534	0.0030	-19.747177113	0.0041	319.2661 0.0098
04DEC01	GD	64.119327552	0.0030	-19.747177093	0.0044	319.2710 0.0100
04DEC02	GD	64.119327532	0.0030	-19.747177057	0.0042	319.2613 0.0096
04DEC03	GD	64.119327540	0.0031	-19.747177029	0.0041	319.2638 0.0099
04DEC04	GD	64.119327526	0.0032	-19.747177109	0.0042	319.2759 0.0104
04DEC05	GD	64.119327504	0.0032	-19.747176954	0.0042	319.2759 0.0097
04DEC06	GD	64.119327548	0.0034	-19.747177044	0.0044	319.2837 0.0101
04DEC07	GD	64.119327556	0.0034	-19.747177000	0.0043	319.2758 0.0105
04DEC08	GD	64.119327543	0.0032	-19.747177073	0.0043	319.2705 0.0103
04DEC09	GD	64.119327524	0.0032	-19.747177134	0.0039	319.2676 0.0099
04DEC10	GD	64.119327535	0.0031	-19.747177118	0.0041	319.2804 0.0101
04DEC11	GD	64.119327533	0.0035	-19.747176979	0.0044	319.2694 0.0101
04DEC12	GD	64.119327520	0.0034	-19.747177045	0.0040	319.2698 0.0097
04DEC13	GD	64.119327536	0.0031	-19.747177071	0.0042	319.2651 0.0099
04DEC14	GD	64.119327547	0.0032	-19.747177114	0.0042	319.2736 0.0105
04DEC15	GD	64.119327545	0.0036	-19.747177125	0.0044	319.2685 0.0111
04DEC16	GD	64.119327539	0.0033	-19.747177085	0.0041	319.2740 0.0102
04DEC17	GD	64.119327541	0.0035	-19.747177102	0.0043	319.2699 0.0104
04DEC18	GD	64.119327544	0.0034	-19.747177113	0.0042	319.2733 0.0102
04DEC19	GD	64.119327538	0.0034	-19.747177130	0.0041	319.2738 0.0103
04DEC20	GD	64.119327546	0.0032	-19.747177122	0.0039	319.2628 0.0100
04DEC21	GD	64.119327544	0.0031	-19.747177111	0.0036	319.2641 0.0093
04DEC22	GD	64.119327534	0.0035	-19.747177023	0.0043	319.2771 0.0101
04DEC23	GD	64.119327554	0.0036	-19.747177116	0.0047	319.2676 0.0107
04DEC24	GD	64.119327526	0.0038	-19.747177149	0.0048	319.2639 0.0111
04DEC25	GD	64.119327553	0.0033	-19.747176995	0.0040	319.2725 0.0104
04DEC26	GD	64.119327510	0.0031	-19.747177099	0.0036	319.2728 0.0093
04DEC27	GD	64.119327525	0.0031	-19.747177059	0.0037	319.2761 0.0094
04DEC28	GD	64.119327540	0.0037	-19.747177086	0.0047	319.2645 0.0102
04DEC29	GD	64.119327533	0.0032	-19.747177037	0.0042	319.2668 0.0097
04DEC30	GD	64.119327524	0.0031	-19.747177127	0.0042	319.2711 0.0095
04DEC31	GD	64.119327558	0.0033	-19.747176979	0.0041	319.2739 0.0095
05JAN01	GD	64.119327557	0.0036	-19.747177052	0.0044	319.2696 0.0102
05JAN02	GD	64.119327574	0.0040	-19.747177046	0.0055	319.2503 0.0118
05JAN03	GD	64.119327558	0.0031	-19.747177123	0.0041	319.2806 0.0097
05JAN04	GD	64.119327549	0.0034	-19.747177116	0.0042	319.2703 0.0100
05JAN05	GD	64.119327544	0.0031	-19.747177009	0.0039	319.2697 0.0094
05JAN06	GD	64.119327544	0.0035	-19.747176982	0.0043	319.2732 0.0099
05JAN07	GD	64.119327553	0.0037	-19.747177121	0.0045	319.2663 0.0104
05JAN08	GD	64.119327584	0.0037	-19.747177136	0.0051	319.2623 0.0117
05JAN09	GD	64.119327552	0.0033	-19.747177223	0.0045	319.2744 0.0109
05JAN10	GD	64.119327556	0.0031	-19.747177151	0.0039	319.2636 0.0099
05JAN11	GD	64.119327555	0.0035	-19.747177061	0.0041	319.2786 0.0107
05JAN12	GD	64.119327576	0.0033	-19.747177234	0.0048	319.2652 0.0102
05JAN13	GD	64.119327547	0.0035	-19.747177068	0.0045	319.2623 0.0107
05JAN14	GD	64.119327543	0.0034	-19.747177040	0.0038	319.2842 0.0098
05JAN15	GD	64.119327521	0.0031	-19.747177061	0.0040	319.2708 0.0093
05JAN16	GD	64.119327559	0.0033	-19.747177038	0.0037	319.2805 0.0096
05JAN17	GD	64.119327521	0.0040	-19.747177073	0.0054	319.2729 0.0108
05JAN18	GD	64.119327564	0.0049	-19.747177060	0.0060	319.2748 0.0131
05JAN19	GD	64.119327556	0.0043	-19.747177180	0.0056	319.2686 0.0132
05JAN20	GD	64.119327548	0.0033	-19.747177169	0.0043	319.2670 0.0102
05JAN21	GD	64.119327544	0.0037	-19.747177201	0.0045	319.2594 0.0107
05JAN22	GD	64.119327551	0.0033	-19.747177200	0.0046	319.2686 0.0109
05JAN23	GD	64.119327567	0.0029	-19.747177138	0.0040	319.2662 0.0097
05JAN24	GD	64.119327564	0.0031	-19.747177200	0.0038	319.2647 0.0093
05JAN25	GD	64.119327550	0.0028	-19.747177100	0.0034	319.2679 0.0087
05JAN26	GD	64.119327563	0.0028	-19.747177183	0.0037	319.2770 0.0090
05JAN27	GD	64.119327561	0.0028	-19.747177106	0.0037	319.2765 0.0094
05JAN28	GD	64.119327537	0.0027	-19.747177092	0.0035	319.2684 0.0084
05JAN29	GD	64.119327527	0.0028	-19.747177103	0.0034	319.2574 0.0086
05JAN30	GD	64.119327557	0.0027	-19.747177113	0.0035	319.2689 0.0088
05JAN31	GD	64.119327562	0.0028	-19.747177013	0.0039	319.2773 0.0089
05FEB01	GD	64.119327560	0.0026	-19.747177155	0.0033	319.2739 0.0082
05FEB02	GD	64.119327573	0.0027	-19.747177081	0.0034	319.2750 0.0085
05FEB03	GD	64.119327568	0.0027	-19.747177110	0.0034	319.2592 0.0086
05FEB04	GD	64.119327577	0.0026	-19.747177088	0.0034	319.2649 0.0085
05FEB05	GD	64.119327586	0.0029	-19.747177173	0.0039	319.2647 0.0099
05FEB06	GD	64.119327591	0.0027	-19.747177283	0.0035	319.2681 0.0084
05FEB07	GD	64.119327591	0.0032	-19.747177179	0.0038	319.2583 0.0092
05FEB08	GD	64.119327568	0.0029	-19.747177239	0.0038	319.2678 0.0089
05FEB09	GD	64.119327541	0.0030	-19.747177126	0.0043	319.2678 0.0096

05FEB10	GD	64.119327572	0.0030	-19.747177171	0.0040	319.2655 0.0095
05FEB11	GD	64.119327548	0.0027	-19.747177181	0.0034	319.2678 0.0086
05FEB12	GD	64.119327550	0.0027	-19.747177005	0.0035	319.2590 0.0088
05FEB13	GD	64.119327601	0.0029	-19.747177132	0.0038	319.2726 0.0094
05FEB14	GD	64.119327563	0.0027	-19.747177098	0.0036	319.2805 0.0088
05FEB15	GD	64.119327543	0.0026	-19.747177040	0.0033	319.2823 0.0081
05FEB16	GD	64.119327582	0.0030	-19.747177100	0.0038	319.2630 0.0093
05FEB17	GD	64.119327602	0.0027	-19.747177060	0.0036	319.2672 0.0085
05FEB18	GD	64.119327616	0.0028	-19.747177046	0.0040	319.2827 0.0086
05FEB19	GD	64.119327572	0.0028	-19.747177132	0.0037	319.2626 0.0090
05FEB20	GD	64.119327598	0.0027	-19.747177126	0.0035	319.2703 0.0084
05FEB21	GD	64.119327594	0.0026	-19.747177110	0.0036	319.2741 0.0081
05FEB22	GD	64.119327625	0.0025	-19.747177160	0.0034	319.2707 0.0077
05FEB23	GD	64.119327589	0.0027	-19.747177173	0.0035	319.2680 0.0088
05FEB24	GD	64.119327594	0.0027	-19.747177133	0.0038	319.2659 0.0091
05FEB25	GD	64.119327597	0.0027	-19.747177158	0.0036	319.2752 0.0080
05FEB26	GD	64.119327580	0.0028	-19.747177150	0.0037	319.2688 0.0089
05FEB27	GD	64.119327583	0.0028	-19.747177118	0.0039	319.2642 0.0096
05FEB28	GD	64.119327584	0.0027	-19.747177038	0.0036	319.2669 0.0081
05MAR01	GD	64.119327589	0.0026	-19.747177170	0.0035	319.2712 0.0079
05MAR02	GD	64.119327602	0.0028	-19.747177095	0.0038	319.2659 0.0092
05MAR03	GD	64.119327595	0.0026	-19.747176969	0.0035	319.2726 0.0080
05MAR04	GD	64.119327605	0.0028	-19.747177151	0.0037	319.2694 0.0091
05MAR05	GD	64.119327613	0.0030	-19.747177154	0.0038	319.2723 0.0090
05MAR06	GD	64.119327636	0.0033	-19.747177259	0.0042	319.2652 0.0090
05MAR07	GD	64.119327639	0.0032	-19.747177163	0.0045	319.2624 0.0094
05MAR08	GD	64.119327621	0.0032	-19.747177197	0.0041	319.2609 0.0093
05MAR09	GD	64.119327590	0.0032	-19.747177092	0.0041	319.2666 0.0094
05MAR10	GD	64.119327618	0.0028	-19.747176989	0.0036	319.2667 0.0086
05MAR11	GD	64.119327576	0.0026	-19.747177151	0.0034	319.2768 0.0078
05MAR12	GD	64.119327594	0.0027	-19.747177178	0.0036	319.2744 0.0085
05MAR13	GD	64.119327609	0.0028	-19.747177200	0.0037	319.2639 0.0086
05MAR14	GD	64.119327600	0.0030	-19.747177130	0.0040	319.2662 0.0087
05MAR15	GD	64.119327622	0.0027	-19.747177137	0.0035	319.2657 0.0084
05MAR16	GD	64.119327628	0.0030	-19.747177135	0.0042	319.2727 0.0103
05MAR17	GD	64.119327606	0.0033	-19.747177161	0.0045	319.2744 0.0106
05MAR18	GD	64.119327636	0.0030	-19.747177213	0.0039	319.2741 0.0089
05MAR19	GD	64.119327637	0.0029	-19.747177122	0.0038	319.2678 0.0093
05MAR20	GD	64.119327648	0.0026	-19.747177067	0.0034	319.2852 0.0082
05MAR21	GD	64.119327644	0.0028	-19.747177111	0.0036	319.2716 0.0088
05MAR22	GD	64.119327625	0.0026	-19.747177120	0.0033	319.2745 0.0079
05MAR23	GD	64.119327628	0.0028	-19.747177236	0.0037	319.2688 0.0090
05MAR24	GD	64.119327621	0.0026	-19.747177220	0.0035	319.2803 0.0081
05MAR25	GD	64.119327633	0.0028	-19.747177147	0.0040	319.2837 0.0083
05MAR26	GD	64.119327652	0.0026	-19.747177175	0.0034	319.2837 0.0080
05MAR27	GD	64.119327623	0.0026	-19.747177087	0.0034	319.2752 0.0078
05MAR28	GD	64.119327618	0.0026	-19.747177149	0.0033	319.2727 0.0077
05MAR29	GD	64.119327624	0.0026	-19.747177109	0.0034	319.2728 0.0082
05MAR30	GD	64.119327632	0.0027	-19.747177107	0.0035	319.2693 0.0087
05MAR31	GD	64.119327636	0.0028	-19.747177106	0.0036	319.2750 0.0087
05APR01	GD	64.119327635	0.0026	-19.747177106	0.0035	319.2750 0.0080
05APR02	GD	64.119327631	0.0027	-19.747177140	0.0034	319.2674 0.0078
05APR03	GD	64.119327623	0.0027	-19.747177099	0.0034	319.2744 0.0082
05APR04	GD	64.119327619	0.0030	-19.747177233	0.0039	319.2709 0.0084
05APR05	GD	64.119327660	0.0034	-19.747177148	0.0046	319.2751 0.0106
05APR06	GD	64.119327617	0.0029	-19.747177208	0.0041	319.2692 0.0095
05APR07	GD	64.119327611	0.0027	-19.747177286	0.0036	319.2795 0.0079
05APR08	GD	64.119327581	0.0029	-19.747177152	0.0039	319.2755 0.0092
05APR09	GD	64.119327578	0.0028	-19.747177143	0.0037	319.2845 0.0093
05APR10	GD	64.119327603	0.0027	-19.747177191	0.0035	319.2801 0.0084
05APR11	GD	64.119327639	0.0030	-19.747177089	0.0040	319.2777 0.0089
05APR12	GD	64.119327626	0.0031	-19.747177174	0.0043	319.2687 0.0086
05APR13	GD	64.119327626	0.0030	-19.747177210	0.0041	319.2731 0.0083
05APR14	GD	64.119327620	0.0028	-19.747177171	0.0038	319.2796 0.0080
05APR15	GD	64.119327626	0.0028	-19.747177103	0.0037	319.2809 0.0088
05APR16	GD	64.119327698	0.0027	-19.747177096	0.0035	319.2928 0.0085
05APR17	GD	64.119327677	0.0029	-19.747177110	0.0037	319.2805 0.0090
05APR18	GD	64.119327662	0.0027	-19.747176969	0.0035	319.2908 0.0082
05APR19	GD	64.119327607	0.0029	-19.747177216	0.0036	319.2816 0.0087
05APR20	GD	64.119327649	0.0028	-19.747177098	0.0037	319.2690 0.0084
05APR21	GD	64.119327643	0.0026	-19.747177107	0.0033	319.2820 0.0078
05APR22	GD	64.119327638	0.0027	-19.747177202	0.0034	319.2768 0.0080
05APR23	GD	64.119327621	0.0027	-19.747177162	0.0034	319.2786 0.0082
05APR24	GD	64.119327592	0.0027	-19.747177156	0.0034	319.2787 0.0079

05APR25	GD	64.119327604	0.0026	-19.747177200	0.0034	319.2763 0.0079
05APR26	GD	64.119327606	0.0026	-19.747177120	0.0034	319.2763 0.0077
05APR27	GD	64.119327643	0.0027	-19.747177149	0.0034	319.2785 0.0081
05APR28	GD	64.119327644	0.0027	-19.747177154	0.0036	319.2695 0.0084
05APR29	GD	64.119327642	0.0027	-19.747177151	0.0038	319.2701 0.0080
05APR30	GD	64.119327646	0.0031	-19.747177150	0.0040	319.2798 0.0089
05MAY01	GD	64.119327651	0.0032	-19.747177161	0.0044	319.2785 0.0100
05MAY02	GD	64.119327643	0.0028	-19.747177112	0.0036	319.2762 0.0085
05MAY03	GD	64.119327652	0.0028	-19.747177105	0.0036	319.2738 0.0083
05MAY04	GD	64.119327623	0.0028	-19.747177154	0.0035	319.2723 0.0086
05MAY05	GD	64.119327663	0.0028	-19.747177168	0.0034	319.2691 0.0081
05MAY06	GD	64.119327610	0.0027	-19.747177173	0.0034	319.2745 0.0079
05MAY07	GD	64.119327624	0.0028	-19.747177187	0.0037	319.2756 0.0080
05MAY08	GD	64.119327674	0.0042	-19.747177188	0.0050	319.2605 0.0102
05MAY09	GD	64.119327614	0.0032	-19.747177139	0.0041	319.2711 0.0100
05MAY10	GD	64.119327654	0.0030	-19.747177089	0.0040	319.2818 0.0094
05MAY11	GD	64.119327639	0.0029	-19.747177142	0.0036	319.2687 0.0084
05MAY12	GD	64.119327637	0.0028	-19.747177125	0.0038	319.2726 0.0082
05MAY13	GD	64.119327625	0.0031	-19.747177144	0.0040	319.2817 0.0099
05MAY14	GD	64.119327662	0.0027	-19.747177111	0.0034	319.2669 0.0079
05MAY15	GD	64.119327662	0.0034	-19.747177197	0.0055	319.2679 0.0094
05MAY16	GD	64.119327657	0.0040	-19.747177172	0.0052	319.2667 0.0105
05MAY17	GD	64.119327648	0.0030	-19.747177130	0.0041	319.2653 0.0086
05MAY18	GD	64.119327648	0.0029	-19.747177132	0.0038	319.2689 0.0086
05MAY19	GD	64.119327663	0.0028	-19.747177138	0.0035	319.2701 0.0081
05MAY20	GD	64.119327646	0.0032	-19.747177058	0.0045	319.2774 0.0095
05MAY21	GD	64.119327630	0.0034	-19.747177153	0.0050	319.2754 0.0093
05MAY22	GD	64.119327637	0.0031	-19.747177224	0.0041	319.2689 0.0087
05MAY23	GD	64.119327646	0.0029	-19.747177184	0.0037	319.2699 0.0086
05MAY24	GD	64.119327648	0.0028	-19.747177147	0.0036	319.2685 0.0082
05MAY25	GD	64.119327657	0.0028	-19.747177115	0.0037	319.2756 0.0086
05MAY26	GD	64.119327661	0.0028	-19.747177183	0.0036	319.2698 0.0082
05MAY27	GD	64.119327644	0.0028	-19.747177169	0.0035	319.2660 0.0081
05MAY28	GD	64.119327644	0.0030	-19.747177170	0.0039	319.2712 0.0087
05MAY29	GD	64.119327645	0.0029	-19.747177171	0.0037	319.2684 0.0083
05MAY30	GD	64.119327666	0.0046	-19.747177097	0.0061	319.2747 0.0106
05MAY31	GD	64.119327629	0.0029	-19.747177208	0.0038	319.2720 0.0085
05JUN01	GD	64.119327653	0.0027	-19.747177089	0.0034	319.2737 0.0081
05JUN02	GD	64.119327646	0.0029	-19.747177127	0.0036	319.2668 0.0082
05JUN03	GD	64.119327649	0.0029	-19.747177106	0.0036	319.2678 0.0085
05JUN04	GD	64.119327629	0.0029	-19.747177056	0.0037	319.2672 0.0086
05JUN05	GD	64.119327665	0.0029	-19.747177134	0.0037	319.2692 0.0087
05JUN06	GD	64.119327634	0.0031	-19.747177109	0.0041	319.2724 0.0100
05JUN07	GD	64.119327621	0.0031	-19.747177247	0.0043	319.2675 0.0099
05JUN08	GD	64.119327654	0.0029	-19.747177076	0.0038	319.2641 0.0093
05JUN09	GD	64.119327635	0.0029	-19.747177227	0.0037	319.2714 0.0090
05JUN10	GD	64.119327663	0.0028	-19.747177128	0.0035	319.2684 0.0084
05JUN11	GD	64.119327657	0.0028	-19.747177094	0.0035	319.2663 0.0084
05JUN12	GD	64.119327711	0.0032	-19.747177119	0.0041	319.2703 0.0096
05JUN13	GD	64.119327651	0.0029	-19.747177282	0.0040	319.2686 0.0088
05JUN14	GD	64.119327689	0.0029	-19.747177274	0.0037	319.2698 0.0084
05JUN15	GD	64.119327649	0.0028	-19.747177166	0.0036	319.2669 0.0081
05JUN16	GD	64.119327672	0.0029	-19.747177090	0.0036	319.2704 0.0083
05JUN17	GD	64.119327660	0.0029	-19.747177191	0.0036	319.2664 0.0085
05JUN18	GD	64.119327665	0.0027	-19.747177183	0.0034	319.2658 0.0081
05JUN19	GD	64.119327681	0.0028	-19.747177186	0.0036	319.2680 0.0087
05JUN20	GD	64.119327653	0.0027	-19.747177180	0.0034	319.2667 0.0083
05JUN21	GD	64.119327650	0.0030	-19.747177153	0.0038	319.2747 0.0096
05JUN22	GD	64.119327653	0.0027	-19.747177221	0.0034	319.2640 0.0081
05JUN23	GD	64.119327673	0.0037	-19.747177179	0.0056	319.2744 0.0098
05JUN24	GD	64.119327654	0.0029	-19.747177174	0.0041	319.2788 0.0097
05JUN25	GD	64.119327663	0.0028	-19.747177147	0.0037	319.2785 0.0091
05JUN26	GD	64.119327647	0.0027	-19.747177179	0.0034	319.2783 0.0081
05JUN27	GD	64.119327650	0.0028	-19.747177065	0.0037	319.2689 0.0091
05JUN28	GD	64.119327651	0.0026	-19.747177094	0.0034	319.2724 0.0081
05JUN29	GD	64.119327672	0.0026	-19.747177121	0.0033	319.2763 0.0080
05JUN30	GD	64.119327689	0.0027	-19.747177295	0.0036	319.2888 0.0087
05JUL01	GD	64.119327650	0.0029	-19.747177183	0.0037	319.2758 0.0085
05JUL02	GD	64.119327680	0.0027	-19.747177153	0.0035	319.2684 0.0083
05JUL03	GD	64.119327661	0.0029	-19.747177146	0.0038	319.2738 0.0095
05JUL04	GD	64.119327659	0.0026	-19.747177192	0.0032	319.2698 0.0077
05JUL05	GD	64.119327675	0.0026	-19.747177147	0.0033	319.2722 0.0078
05JUL06	GD	64.119327674	0.0027	-19.747177255	0.0035	319.2728 0.0086
05JUL07	GD	64.119327677	0.0027	-19.747177197	0.0035	319.2776 0.0084

05JUL08	GD	64.119327644	0.0026	-19.747177177	0.0033	319.2744 0.0080
05JUL09	GD	64.119327685	0.0030	-19.747177204	0.0039	319.2785 0.0085
05JUL10	GD	64.119327685	0.0032	-19.747177091	0.0049	319.2757 0.0089
05JUL11	GD	64.119327661	0.0029	-19.747177215	0.0040	319.2797 0.0088
05JUL12	GD	64.119327659	0.0030	-19.747177258	0.0043	319.2869 0.0091
05JUL13	GD	64.119327669	0.0027	-19.747177155	0.0035	319.2743 0.0082
05JUL14	GD	64.119327694	0.0026	-19.747177165	0.0033	319.2781 0.0080
05JUL15	GD	64.119327671	0.0027	-19.747177233	0.0034	319.2824 0.0081
05JUL16	GD	64.119327660	0.0028	-19.747177252	0.0038	319.2729 0.0085
05JUL17	GD	64.119327687	0.0028	-19.747177228	0.0035	319.2717 0.0082
05JUL18	GD	64.119327660	0.0032	-19.747177230	0.0044	319.2822 0.0090
05JUL19	GD	64.119327686	0.0028	-19.747177275	0.0036	319.2799 0.0085
05JUL20	GD	64.119327674	0.0026	-19.747177195	0.0033	319.2777 0.0078
05JUL21	GD	64.119327696	0.0029	-19.747177278	0.0040	319.2749 0.0089
05JUL22	GD	64.119327664	0.0027	-19.747177280	0.0035	319.2734 0.0081
05JUL23	GD	64.119327691	0.0026	-19.747177183	0.0034	319.2741 0.0080
05JUL24	GD	64.119327669	0.0027	-19.747177115	0.0034	319.2799 0.0081
05JUL25	GD	64.119327669	0.0028	-19.747177212	0.0036	319.2871 0.0082
05JUL26	GD	64.119327689	0.0029	-19.747177172	0.0037	319.2773 0.0085
05JUL27	GD	64.119327670	0.0029	-19.747177182	0.0038	319.2796 0.0084
05JUL28	GD	64.119327665	0.0030	-19.747177206	0.0044	319.2832 0.0086
05JUL29	GD	64.119327664	0.0029	-19.747177182	0.0038	319.2843 0.0084
05JUL30	GD	64.119327649	0.0029	-19.747177246	0.0039	319.2854 0.0084
05JUL31	GD	64.119327670	0.0027	-19.747177267	0.0035	319.2827 0.0080
05AUG01	GD	64.119327673	0.0029	-19.747177192	0.0038	319.2700 0.0088
05AUG02	GD	64.119327656	0.0028	-19.747177195	0.0038	319.2663 0.0084
05AUG03	GD	64.119327663	0.0027	-19.747177240	0.0036	319.2735 0.0083
05AUG04	GD	64.119327676	0.0028	-19.747177132	0.0036	319.2758 0.0082
05AUG05	GD	64.119327640	0.0026	-19.747177197	0.0035	319.2871 0.0080
05AUG06	GD	64.119327679	0.0032	-19.747177133	0.0045	319.2805 0.0089
05AUG07	GD	64.119327670	0.0029	-19.747177206	0.0038	319.2829 0.0093
05AUG08	GD	64.119327668	0.0027	-19.747177145	0.0035	319.2823 0.0081
05AUG09	GD	64.119327653	0.0027	-19.747177144	0.0036	319.2828 0.0081
05AUG10	GD	64.119327682	0.0027	-19.747177114	0.0035	319.2775 0.0080
05AUG11	GD	64.119327679	0.0028	-19.747177196	0.0035	319.2828 0.0084
05AUG12	GD	64.119327708	0.0027	-19.747177223	0.0036	319.2759 0.0084
05AUG13	GD	64.119327655	0.0029	-19.747177165	0.0040	319.2796 0.0086
05AUG14	GD	64.119327682	0.0027	-19.747177094	0.0037	319.2780 0.0086
05AUG15	GD	64.119327674	0.0026	-19.747177213	0.0034	319.2679 0.0080
05AUG16	GD	64.119327718	0.0029	-19.747177430	0.0041	319.3020 0.0093
05AUG17	GD	64.119327674	0.0027	-19.747177347	0.0037	319.2861 0.0084
05AUG18	GD	64.119327674	0.0027	-19.747177331	0.0036	319.2763 0.0084
05AUG19	GD	64.119327674	0.0027	-19.747177260	0.0036	319.2852 0.0085
05AUG20	GD	64.119327665	0.0027	-19.747177259	0.0036	319.2858 0.0084
05AUG21	GD	64.119327663	0.0028	-19.747177223	0.0037	319.2865 0.0082
05AUG22	GD	64.119327627	0.0026	-19.747177245	0.0034	319.2767 0.0078
05AUG23	GD	64.119327662	0.0026	-19.747177168	0.0034	319.2821 0.0081
05AUG24	GD	64.119327628	0.0032	-19.747177059	0.0049	319.2907 0.0092
05AUG25	GD	64.119327613	0.0028	-19.747177295	0.0039	319.3036 0.0085
05AUG26	GD	64.119327667	0.0026	-19.747177123	0.0034	319.2861 0.0079
05AUG27	GD	64.119327674	0.0026	-19.747177185	0.0035	319.2792 0.0079
05AUG28	GD	64.119327665	0.0028	-19.747177194	0.0038	319.2866 0.0092
05AUG29	GD	64.119327690	0.0029	-19.747177167	0.0040	319.2765 0.0091
05AUG30	GD	64.119327649	0.0030	-19.747177238	0.0041	319.2771 0.0098
05AUG31	GD	64.119327682	0.0033	-19.747177202	0.0043	319.2758 0.0098
05SEP01	GD	64.119327692	0.0028	-19.747177242	0.0039	319.2747 0.0092
05SEP02	GD	64.119327694	0.0028	-19.747177180	0.0040	319.2767 0.0084
05SEP03	GD	64.119327703	0.0029	-19.747177317	0.0041	319.2735 0.0089
05SEP04	GD	64.119327706	0.0029	-19.747177261	0.0039	319.2833 0.0086
05SEP05	GD	64.119327701	0.0026	-19.747177198	0.0034	319.2819 0.0081
05SEP06	GD	64.119327696	0.0027	-19.747177174	0.0036	319.2722 0.0083
05SEP07	GD	64.119327673	0.0027	-19.747177257	0.0038	319.2793 0.0081
05SEP08	GD	64.119327683	0.0029	-19.747177235	0.0042	319.2744 0.0087
05SEP09	GD	64.119327680	0.0030	-19.747177223	0.0041	319.2753 0.0098
05SEP10	GD	64.119327713	0.0031	-19.747177286	0.0044	319.2781 0.0095
05SEP12	GD	64.119327708	0.0033	-19.747177348	0.0045	319.2814 0.0099
05SEP13	GD	64.119327736	0.0031	-19.747177239	0.0042	319.2819 0.0084
05SEP14	GD	64.119327725	0.0030	-19.747177245	0.0042	319.2773 0.0091
05SEP15	GD	64.119327707	0.0030	-19.747177299	0.0040	319.2780 0.0091
05SEP16	GD	64.119327695	0.0030	-19.747177273	0.0040	319.2725 0.0095
05SEP17	GD	64.119327711	0.0027	-19.747177229	0.0036	319.2820 0.0084
05SEP18	GD	64.119327669	0.0029	-19.747177163	0.0039	319.2869 0.0093
05SEP19	GD	64.119327668	0.0028	-19.747177222	0.0037	319.2837 0.0089
05SEP20	GD	64.119327674	0.0028	-19.747177180	0.0038	319.2741 0.0087

05SEP21	GD	64.119327673	0.0027	-19.747177187	0.0036	319.2767 0.0083
05SEP22	GD	64.119327688	0.0026	-19.747177166	0.0036	319.2772 0.0081
05SEP23	GD	64.119327690	0.0026	-19.747177211	0.0034	319.2748 0.0079
05SEP24	GD	64.119327683	0.0026	-19.747177213	0.0034	319.2805 0.0078
05SEP25	GD	64.119327684	0.0026	-19.747177165	0.0034	319.2803 0.0082
05SEP26	GD	64.119327681	0.0031	-19.747177300	0.0047	319.2794 0.0103
05SEP27	GD	64.119327687	0.0029	-19.747177248	0.0039	319.2759 0.0091
05SEP28	GD	64.119327687	0.0031	-19.747177220	0.0043	319.2817 0.0097
05SEP29	GD	64.119327693	0.0029	-19.747177174	0.0039	319.2862 0.0091
05SEP30	GD	64.119327685	0.0028	-19.747177189	0.0038	319.2873 0.0089
05OCT01	GD	64.119327690	0.0030	-19.747177249	0.0042	319.2897 0.0099
05OCT02	GD	64.119327655	0.0030	-19.747177178	0.0041	319.2885 0.0097
05OCT03	GD	64.119327699	0.0029	-19.747177254	0.0041	319.2852 0.0092
05OCT04	GD	64.119327704	0.0028	-19.747177198	0.0037	319.2900 0.0091
05OCT05	GD	64.119327676	0.0029	-19.747177246	0.0037	319.2863 0.0091
05OCT06	GD	64.119327714	0.0028	-19.747177201	0.0039	319.3021 0.0091
05OCT07	GD	64.119327710	0.0027	-19.747177174	0.0037	319.2815 0.0084
05OCT08	GD	64.119327660	0.0031	-19.747177265	0.0042	319.2854 0.0095
05OCT09	GD	64.119327689	0.0026	-19.747177238	0.0035	319.2861 0.0080
05OCT10	GD	64.119327668	0.0027	-19.747177210	0.0034	319.2859 0.0083
05OCT11	GD	64.119327685	0.0030	-19.747177223	0.0044	319.2877 0.0099
05OCT12	GD	64.119327684	0.0030	-19.747177253	0.0042	319.2825 0.0098
05OCT13	GD	64.119327694	0.0029	-19.747177246	0.0040	319.2803 0.0093
05OCT14	GD	64.119327728	0.0030	-19.747177280	0.0042	319.2909 0.0099
05OCT15	GD	64.119327709	0.0028	-19.747177196	0.0037	319.2865 0.0087
05OCT16	GD	64.119327720	0.0028	-19.747177231	0.0036	319.2839 0.0086
05OCT17	GD	64.119327739	0.0027	-19.747177112	0.0036	319.2942 0.0084
05OCT18	GD	64.119327698	0.0026	-19.747177224	0.0034	319.2864 0.0078
05OCT19	GD	64.119327701	0.0029	-19.747177192	0.0041	319.2782 0.0092
05OCT20	GD	64.119327693	0.0028	-19.747177188	0.0035	319.2811 0.0085
05OCT21	GD	64.119327708	0.0027	-19.747177188	0.0035	319.2776 0.0082
05OCT22	GD	64.119327696	0.0027	-19.747177229	0.0035	319.2798 0.0084
05OCT23	GD	64.119327697	0.0030	-19.747177250	0.0043	319.2786 0.0099
05OCT24	GD	64.119327702	0.0027	-19.747177152	0.0036	319.2786 0.0086
05OCT25	GD	64.119327711	0.0032	-19.747177215	0.0042	319.2806 0.0091
05OCT26	GD	64.119327695	0.0029	-19.747177235	0.0038	319.2817 0.0090
05OCT27	GD	64.119327702	0.0031	-19.747177225	0.0047	319.2895 0.0105
05OCT28	GD	64.119327676	0.0031	-19.747177160	0.0045	319.2894 0.0100
05OCT29	GD	64.119327682	0.0029	-19.747177193	0.0038	319.2890 0.0089
05OCT30	GD	64.119327680	0.0031	-19.747177252	0.0044	319.2861 0.0101
05OCT31	GD	64.119327702	0.0031	-19.747177184	0.0045	319.2981 0.0098
05NOV01	GD	64.119327703	0.0029	-19.747177211	0.0041	319.2849 0.0098
05NOV02	GD	64.119327704	0.0031	-19.747177211	0.0047	319.2892 0.0107
05NOV03	GD	64.119327718	0.0036	-19.747177075	0.0052	319.2883 0.0116
05NOV04	GD	64.119327727	0.0033	-19.747177201	0.0049	319.2954 0.0119
05NOV05	GD	64.119327746	0.0032	-19.747177309	0.0047	319.3078 0.0109
05NOV06	GD	64.119327745	0.0032	-19.747177208	0.0045	319.2862 0.0105
05NOV07	GD	64.119327711	0.0030	-19.747177200	0.0044	319.2838 0.0103
05NOV08	GD	64.119327732	0.0031	-19.747177212	0.0045	319.2823 0.0104
05NOV09	GD	64.119327741	0.0032	-19.747177317	0.0047	319.2828 0.0109
05NOV10	GD	64.119327717	0.0030	-19.747177240	0.0043	319.2828 0.0102
05NOV11	GD	64.119327710	0.0031	-19.747177264	0.0045	319.2756 0.0105
05NOV12	GD	64.119327732	0.0031	-19.747177235	0.0048	319.2824 0.0111
05NOV13	GD	64.119327706	0.0029	-19.747177289	0.0042	319.2923 0.0098
05NOV14	GD	64.119327721	0.0031	-19.747177215	0.0044	319.2910 0.0105
05NOV15	GD	64.119327709	0.0029	-19.747177264	0.0042	319.2993 0.0099
05NOV16	GD	64.119327708	0.0031	-19.747177211	0.0044	319.2905 0.0102
05NOV17	GD	64.119327698	0.0029	-19.747177153	0.0039	319.2865 0.0093
05NOV18	GD	64.119327700	0.0030	-19.747177074	0.0040	319.2908 0.0095
05NOV19	GD	64.119327742	0.0030	-19.747177168	0.0040	319.3081 0.0094
05NOV20	GD	64.119327702	0.0029	-19.747177119	0.0039	319.2812 0.0093
05NOV21	GD	64.119327744	0.0029	-19.747177210	0.0039	319.2707 0.0095
05NOV22	GD	64.119327722	0.0030	-19.747177094	0.0038	319.2822 0.0093
05NOV23	GD	64.119327736	0.0030	-19.747177082	0.0039	319.2692 0.0096
05NOV24	GD	64.119327760	0.0031	-19.747177187	0.0041	319.2755 0.0100
05NOV25	GD	64.119327759	0.0032	-19.747177220	0.0044	319.2767 0.0102
05NOV26	GD	64.119327749	0.0029	-19.747177224	0.0038	319.2836 0.0094
05NOV27	GD	64.119327774	0.0030	-19.747177241	0.0038	319.2795 0.0095
05NOV28	GD	64.119327727	0.0036	-19.747177171	0.0048	319.2814 0.0116
05NOV29	GD	64.119327734	0.0030	-19.747177148	0.0038	319.2799 0.0095
05NOV30	GD	64.119327739	0.0030	-19.747177145	0.0038	319.2741 0.0096
05DEC01	GD	64.119327739	0.0034	-19.747177259	0.0039	319.2868 0.0101
05DEC02	GD	64.119327719	0.0034	-19.747177286	0.0043	319.2738 0.0104
05DEC03	GD	64.119327757	0.0031	-19.747177236	0.0038	319.2799 0.0095

05DEC04	GD	64.119327747	0.0031	-19.747177219	0.0038	319.2739 0.0096
05DEC05	GD	64.119327740	0.0029	-19.747177189	0.0037	319.2793 0.0092
05DEC06	GD	64.119327760	0.0030	-19.747177223	0.0038	319.2804 0.0097
05DEC07	GD	64.119327761	0.0030	-19.747177256	0.0037	319.2837 0.0093
05DEC08	GD	64.119327716	0.0029	-19.747177150	0.0035	319.2876 0.0091
05DEC09	GD	64.119327743	0.0031	-19.747177095	0.0036	319.2772 0.0093
05DEC10	GD	64.119327743	0.0030	-19.747177162	0.0036	319.2792 0.0091
05DEC11	GD	64.119327751	0.0033	-19.747177076	0.0042	319.2774 0.0095
05DEC12	GD	64.119327729	0.0030	-19.747177173	0.0037	319.2726 0.0090
05DEC13	GD	64.119327749	0.0029	-19.747177186	0.0035	319.2769 0.0089
05DEC14	GD	64.119327751	0.0029	-19.747177143	0.0036	319.2720 0.0089
05DEC15	GD	64.119327743	0.0029	-19.747177158	0.0035	319.2834 0.0090
05DEC16	GD	64.119327755	0.0031	-19.747177154	0.0038	319.2738 0.0096
05DEC17	GD	64.119327722	0.0028	-19.747177171	0.0035	319.2901 0.0090
05DEC18	GD	64.119327743	0.0028	-19.747177188	0.0034	319.2986 0.0090
05DEC19	GD	64.119327729	0.0028	-19.747177196	0.0035	319.2968 0.0089
05DEC20	GD	64.119327728	0.0031	-19.747177173	0.0038	319.2811 0.0095
05DEC21	GD	64.119327754	0.0028	-19.747177203	0.0038	319.2839 0.0095
05DEC22	GD	64.119327720	0.0028	-19.747177195	0.0037	319.2832 0.0095
05DEC23	GD	64.119327753	0.0029	-19.747177212	0.0037	319.2832 0.0097
05DEC24	GD	64.119327783	0.0029	-19.747177280	0.0036	319.2888 0.0095
05DEC25	GD	64.119327728	0.0028	-19.747177321	0.0035	319.3016 0.0088
05DEC26	GD	64.119327711	0.0027	-19.747177202	0.0033	319.2796 0.0086
05DEC27	GD	64.119327747	0.0034	-19.747177107	0.0039	319.2730 0.0095
05DEC28	GD	64.119327786	0.0032	-19.747177135	0.0038	319.2812 0.0100
05DEC29	GD	64.119327737	0.0029	-19.747177157	0.0037	319.2848 0.0098
05DEC30	GD	64.119327739	0.0028	-19.747177270	0.0034	319.2944 0.0089
05DEC31	GD	64.119327754	0.0030	-19.747177189	0.0036	319.2801 0.0096
06JAN01	GD	64.119327738	0.0029	-19.747177167	0.0035	319.2857 0.0091
06JAN02	GD	64.119327705	0.0028	-19.747177254	0.0034	319.3047 0.0090
06JAN03	GD	64.119327726	0.0029	-19.747177148	0.0036	319.2877 0.0092
06JAN04	GD	64.119327711	0.0027	-19.747177125	0.0033	319.2947 0.0082
06JAN05	GD	64.119327731	0.0028	-19.747177162	0.0036	319.2870 0.0088
06JAN06	GD	64.119327707	0.0028	-19.747177091	0.0034	319.2861 0.0089
06JAN07	GD	64.119327722	0.0028	-19.747177171	0.0034	319.2870 0.0089
06JAN08	GD	64.119327749	0.0028	-19.747177231	0.0034	319.2880 0.0089
06JAN09	GD	64.119327742	0.0028	-19.747177110	0.0034	319.2902 0.0089
06JAN10	GD	64.119327744	0.0028	-19.747177211	0.0035	319.2841 0.0089
06JAN11	GD	64.119327716	0.0029	-19.747177179	0.0035	319.2768 0.0090
06JAN12	GD	64.119327716	0.0028	-19.747177202	0.0035	319.2899 0.0090
06JAN13	GD	64.119327734	0.0028	-19.747177177	0.0034	319.2798 0.0090
06JAN14	GD	64.119327701	0.0029	-19.747177116	0.0035	319.2771 0.0094
06JAN15	GD	64.119327706	0.0031	-19.747177107	0.0036	319.2747 0.0098
06JAN16	GD	64.119327715	0.0029	-19.747177125	0.0035	319.2810 0.0093
06JAN17	GD	64.119327703	0.0030	-19.747177145	0.0036	319.2804 0.0096
06JAN18	GD	64.119327724	0.0028	-19.747177184	0.0034	319.2926 0.0092
06JAN19	GD	64.119327746	0.0028	-19.747177188	0.0036	319.2893 0.0090
06JAN20	GD	64.119327719	0.0028	-19.747177171	0.0037	319.3003 0.0094
06JAN21	GD	64.119327942	0.0028	-19.747187826	0.0035	319.3200 0.0089
06JAN22	GD	64.119328022	0.0028	-19.747187199	0.0034	319.3162 0.0089
06JAN23	GD	64.119327743	0.0029	-19.747177139	0.0037	319.2877 0.0091
06JAN24	GD	64.119327758	0.0028	-19.747177158	0.0035	319.2933 0.0095
06JAN25	GD	64.119327790	0.0028	-19.747177265	0.0034	319.2916 0.0088
06JAN26	GD	64.119327779	0.0031	-19.747177262	0.0039	319.2891 0.0087
06JAN27	GD	64.119327757	0.0027	-19.747177213	0.0034	319.2880 0.0084
06JAN28	GD	64.119327767	0.0027	-19.747177290	0.0034	319.2863 0.0084
06JAN29	GD	64.119327740	0.0026	-19.747177283	0.0033	319.2894 0.0080
06JAN30	GD	64.119327733	0.0027	-19.747177249	0.0034	319.2856 0.0083
06JAN31	GD	64.119327718	0.0027	-19.747177225	0.0034	319.2859 0.0086
06FEB01	GD	64.119327729	0.0027	-19.747177217	0.0033	319.3058 0.0084
06FEB02	GD	64.119327776	0.0028	-19.747177188	0.0034	319.2892 0.0084
06FEB03	GD	64.119327755	0.0027	-19.747177248	0.0034	319.2940 0.0086
06FEB04	GD	64.119327755	0.0027	-19.747177206	0.0034	319.2952 0.0081
06FEB05	GD	64.119327752	0.0026	-19.747177163	0.0033	319.2950 0.0080
06FEB06	GD	64.119327768	0.0027	-19.747177231	0.0035	319.2917 0.0081
06FEB07	GD	64.119327766	0.0026	-19.747177188	0.0034	319.2902 0.0086
06FEB08	GD	64.119327756	0.0026	-19.747177246	0.0033	319.2902 0.0082
06FEB09	GD	64.119327758	0.0027	-19.747177241	0.0036	319.2814 0.0089
06FEB10	GD	64.119327753	0.0026	-19.747177158	0.0034	319.2932 0.0081
06FEB11	GD	64.119327772	0.0026	-19.747177198	0.0034	319.2873 0.0080
06FEB12	GD	64.119327759	0.0027	-19.747177177	0.0036	319.2984 0.0082
06FEB13	GD	64.119327765	0.0026	-19.747177214	0.0035	319.2873 0.0082
06FEB14	GD	64.119327758	0.0026	-19.747177217	0.0034	319.2942 0.0080
06FEB15	GD	64.119327736	0.0026	-19.747177243	0.0036	319.2980 0.0080

06FEB16	GD	64.119327746	0.0028	-19.747177299	0.0036	319.2923 0.0088
06FEB17	GD	64.119327766	0.0026	-19.747177279	0.0034	319.2985 0.0078
06FEB18	GD	64.119327776	0.0026	-19.747177256	0.0034	319.2930 0.0082
06FEB19	GD	64.119327764	0.0026	-19.747177267	0.0034	319.2920 0.0080
06FEB20	GD	64.119327765	0.0027	-19.747177137	0.0038	319.2910 0.0085
06FEB21	GD	64.119327794	0.0026	-19.747177268	0.0035	319.2971 0.0079
06FEB22	GD	64.119327803	0.0027	-19.747177427	0.0036	319.3003 0.0082
06FEB23	GD	64.119327795	0.0026	-19.747177238	0.0033	319.2812 0.0080
06FEB24	GD	64.119327801	0.0026	-19.747177222	0.0034	319.2853 0.0080
06FEB25	GD	64.119327780	0.0026	-19.747177232	0.0033	319.2894 0.0079
06FEB26	GD	64.119327802	0.0027	-19.747177234	0.0035	319.2809 0.0086
06FEB27	GD	64.119327804	0.0026	-19.747177274	0.0035	319.2927 0.0079
06FEB28	GD	64.119327787	0.0027	-19.747177280	0.0037	319.2894 0.0083
06MAR01	GD	64.119327744	0.0026	-19.747177317	0.0035	319.2898 0.0084
06MAR02	GD	64.119327758	0.0027	-19.747177257	0.0035	319.2886 0.0081
06MAR03	GD	64.119327759	0.0027	-19.747177262	0.0035	319.2953 0.0086
06MAR04	GD	64.119327784	0.0025	-19.747177274	0.0034	319.2913 0.0078
06MAR05	GD	64.119327794	0.0025	-19.747177221	0.0034	319.2941 0.0077
06MAR06	GD	64.119327796	0.0027	-19.747177177	0.0037	319.3045 0.0090
06MAR07	GD	64.119327785	0.0027	-19.747177254	0.0035	319.3004 0.0085
06MAR08	GD	64.119327794	0.0026	-19.747177181	0.0034	319.2906 0.0081
06MAR09	GD	64.119327790	0.0027	-19.747177253	0.0036	319.2865 0.0088
06MAR10	GD	64.119327765	0.0026	-19.747177248	0.0036	319.2798 0.0086
06MAR11	GD	64.119327800	0.0025	-19.747177178	0.0033	319.2934 0.0081
06MAR12	GD	64.119327800	0.0026	-19.747177226	0.0034	319.2908 0.0081
06MAR13	GD	64.119327783	0.0025	-19.747177258	0.0034	319.2943 0.0078
06MAR14	GD	64.119327787	0.0026	-19.747177265	0.0034	319.2932 0.0081
06MAR15	GD	64.119327776	0.0027	-19.747177249	0.0035	319.2904 0.0083
06MAR16	GD	64.119327814	0.0028	-19.747177301	0.0036	319.2904 0.0087
06MAR17	GD	64.119327820	0.0028	-19.747177289	0.0036	319.2905 0.0087
06MAR18	GD	64.119327816	0.0029	-19.747177269	0.0039	319.2964 0.0087
06MAR19	GD	64.119327807	0.0029	-19.747177230	0.0039	319.2927 0.0091
06MAR20	GD	64.119327792	0.0030	-19.747177185	0.0042	319.2815 0.0097
06MAR21	GD	64.119327798	0.0027	-19.747177268	0.0038	319.2854 0.0087
06MAR22	GD	64.119327804	0.0028	-19.747177294	0.0036	319.2829 0.0083
06MAR23	GD	64.119327805	0.0028	-19.747177331	0.0037	319.2912 0.0089
06MAR24	GD	64.119327790	0.0027	-19.747177294	0.0037	319.2905 0.0084
06MAR25	GD	64.119327797	0.0027	-19.747177265	0.0036	319.2969 0.0080
06MAR26	GD	64.119327816	0.0027	-19.747177307	0.0036	319.2863 0.0082
06MAR27	GD	64.119327833	0.0028	-19.747177295	0.0037	319.2843 0.0084
06MAR28	GD	64.119327775	0.0029	-19.747177223	0.0040	319.2971 0.0096
06MAR29	GD	64.119327761	0.0027	-19.747177272	0.0037	319.2986 0.0088
06MAR30	GD	64.119327777	0.0026	-19.747177312	0.0033	319.2893 0.0078
06MAR31	GD	64.119327794	0.0025	-19.747177331	0.0033	319.2881 0.0077
06APR01	GD	64.119327793	0.0026	-19.747177290	0.0034	319.2832 0.0079
06APR02	GD	64.119327781	0.0026	-19.747177325	0.0034	319.2868 0.0078
06APR03	GD	64.119327796	0.0026	-19.747177237	0.0034	319.2940 0.0079
06APR04	GD	64.119327787	0.0029	-19.747177245	0.0039	319.2909 0.0090
06APR05	GD	64.119327810	0.0033	-19.747177239	0.0046	319.2936 0.0100
06APR06	GD	64.119327783	0.0027	-19.747177302	0.0035	319.2943 0.0081
06APR07	GD	64.119327786	0.0027	-19.747177408	0.0035	319.2968 0.0083
06APR08	GD	64.119327798	0.0027	-19.747177283	0.0034	319.2863 0.0081
06APR09	GD	64.119327750	0.0034	-19.747177321	0.0053	319.2958 0.0110
06APR10	GD	64.119327778	0.0028	-19.747177243	0.0037	319.2943 0.0088
06APR11	GD	64.119327777	0.0027	-19.747177308	0.0034	319.2973 0.0079
06APR12	GD	64.119327786	0.0027	-19.747177258	0.0035	319.2996 0.0080
06APR13	GD	64.119327755	0.0027	-19.747177291	0.0035	319.2899 0.0078
06APR14	GD	64.119327746	0.0043	-19.747177269	0.0070	319.3050 0.0130
06APR15	GD	64.119327802	0.0030	-19.747177235	0.0041	319.2916 0.0084
06APR16	GD	64.119327789	0.0028	-19.747177212	0.0037	319.2933 0.0089
06APR17	GD	64.119327795	0.0026	-19.747177306	0.0033	319.2888 0.0077
06APR18	GD	64.119327816	0.0029	-19.747177284	0.0038	319.2899 0.0090
06APR19	GD	64.119327795	0.0028	-19.747177195	0.0036	319.2940 0.0087
06APR20	GD	64.119327809	0.0027	-19.747177227	0.0034	319.2909 0.0080
06APR21	GD	64.119327829	0.0028	-19.747177235	0.0038	319.2866 0.0090
06APR22	GD	64.119327792	0.0029	-19.747177213	0.0037	319.2985 0.0084
06APR23	GD	64.119327818	0.0028	-19.747177243	0.0038	319.2925 0.0090
06APR24	GD	64.119327828	0.0027	-19.747177265	0.0033	319.2933 0.0077
06APR25	GD	64.119327813	0.0026	-19.747177248	0.0033	319.2883 0.0078
06APR26	GD	64.119327800	0.0027	-19.747177334	0.0035	319.2829 0.0082
06APR27	GD	64.119327789	0.0027	-19.747177231	0.0034	319.2907 0.0080
06APR28	GD	64.119327791	0.0028	-19.747177255	0.0037	319.2870 0.0079
06APR29	GD	64.119327779	0.0027	-19.747177288	0.0035	319.2903 0.0085
06APR30	GD	64.119327809	0.0027	-19.747177240	0.0034	319.2954 0.0081

06MAY01	GD	64.119327801	0.0027	-19.747177180	0.0033	319.2889 0.0080
06MAY02	GD	64.119327830	0.0027	-19.747177280	0.0035	319.2948 0.0083
06MAY03	GD	64.119327826	0.0027	-19.747177178	0.0037	319.3033 0.0088
06MAY04	GD	64.119327865	0.0027	-19.747177226	0.0035	319.2886 0.0083
06MAY05	GD	64.119327830	0.0029	-19.747177327	0.0036	319.2967 0.0087
06MAY06	GD	64.119327827	0.0027	-19.747177162	0.0036	319.2865 0.0080
06MAY07	GD	64.119327818	0.0028	-19.747177222	0.0037	319.2832 0.0082
06MAY08	GD	64.119326981	0.0026	-19.747181444	0.0033	319.3125 0.0076
06MAY09	GD	64.119327832	0.0026	-19.747177221	0.0033	319.2869 0.0078
06MAY10	GD	64.119327835	0.0027	-19.747177236	0.0034	319.2834 0.0081
06MAY11	GD	64.119327831	0.0029	-19.747177244	0.0038	319.2789 0.0086
06MAY12	GD	64.119327828	0.0028	-19.747177265	0.0036	319.2826 0.0083
06MAY13	GD	64.119327819	0.0027	-19.747177289	0.0034	319.2865 0.0078
06MAY14	GD	64.119327807	0.0027	-19.747177191	0.0034	319.2880 0.0079
06MAY15	GD	64.119327808	0.0026	-19.747177243	0.0034	319.2852 0.0079
06MAY16	GD	64.119327826	0.0028	-19.747177240	0.0035	319.2846 0.0084
06MAY17	GD	64.119327811	0.0027	-19.747177220	0.0034	319.2888 0.0080
06MAY18	GD	64.119327846	0.0030	-19.747177189	0.0041	319.2879 0.0087
06MAY19	GD	64.119327833	0.0027	-19.747177168	0.0034	319.2844 0.0081
06MAY20	GD	64.119327829	0.0028	-19.747177197	0.0035	319.2923 0.0083
06MAY21	GD	64.119327835	0.0028	-19.747177227	0.0036	319.2871 0.0085
06MAY22	GD	64.119327814	0.0028	-19.747177251	0.0036	319.2854 0.0085
06MAY23	GD	64.119327826	0.0028	-19.747177348	0.0037	319.2825 0.0085
06MAY24	GD	64.119327820	0.0028	-19.747177329	0.0035	319.2868 0.0087
06MAY25	GD	64.119327821	0.0029	-19.747177306	0.0035	319.2751 0.0086
06MAY26	GD	64.119327836	0.0030	-19.747177258	0.0037	319.2860 0.0091
06MAY27	GD	64.119327825	0.0029	-19.747177243	0.0038	319.2838 0.0089
06MAY28	GD	64.119327838	0.0027	-19.747177271	0.0034	319.2833 0.0084
06MAY29	GD	64.119327811	0.0027	-19.747177291	0.0034	319.2811 0.0081
06MAY30	GD	64.119327825	0.0028	-19.747177239	0.0034	319.2904 0.0082
06MAY31	GD	64.119327829	0.0029	-19.747177276	0.0038	319.2886 0.0093
06JUN01	GD	64.119327819	0.0028	-19.747177287	0.0035	319.2818 0.0085
06JUN02	GD	64.119327847	0.0027	-19.747177180	0.0035	319.2925 0.0082
06JUN03	GD	64.119327849	0.0027	-19.747177229	0.0034	319.2868 0.0080
06JUN04	GD	64.119327863	0.0029	-19.747177186	0.0037	319.2912 0.0087
06JUN05	GD	64.119327861	0.0029	-19.747177232	0.0037	319.2929 0.0090
06JUN06	GD	64.119327828	0.0031	-19.747177204	0.0040	319.2789 0.0092
06JUN07	GD	64.119327815	0.0031	-19.747177250	0.0041	319.2808 0.0098
06JUN08	GD	64.119327821	0.0028	-19.747177289	0.0037	319.2803 0.0084
06JUN09	GD	64.119327854	0.0027	-19.747177251	0.0035	319.2827 0.0081
06JUN10	GD	64.119327844	0.0027	-19.747177212	0.0034	319.2906 0.0081
06JUN11	GD	64.119327840	0.0028	-19.747177149	0.0035	319.2910 0.0085
06JUN12	GD	64.119327843	0.0029	-19.747177310	0.0037	319.2820 0.0088
06JUN13	GD	64.119327846	0.0026	-19.747177426	0.0034	319.2881 0.0079
06JUN14	GD	64.119327816	0.0028	-19.747177207	0.0037	319.3062 0.0088
06JUN17	GD	64.119327837	0.0028	-19.747177268	0.0036	319.2906 0.0086
06JUN18	GD	64.119327855	0.0026	-19.747177292	0.0033	319.2872 0.0079
06JUN19	GD	64.119327837	0.0027	-19.747177153	0.0035	319.2874 0.0082
06JUN20	GD	64.119327846	0.0028	-19.747177241	0.0037	319.2831 0.0091
06JUN21	GD	64.119327845	0.0027	-19.747177271	0.0034	319.2934 0.0082
06JUN22	GD	64.119327861	0.0027	-19.747177313	0.0035	319.2921 0.0083
06JUN23	GD	64.119327855	0.0027	-19.747177304	0.0035	319.2890 0.0082
06JUN24	GD	64.119327857	0.0026	-19.747177300	0.0035	319.2929 0.0081
06JUN25	GD	64.119327862	0.0027	-19.747177309	0.0035	319.2849 0.0082
06JUN26	GD	64.119327855	0.0027	-19.747177245	0.0035	319.2815 0.0083
06JUN27	GD	64.119327857	0.0028	-19.747177245	0.0035	319.2901 0.0084
06JUN28	GD	64.119327849	0.0028	-19.747177334	0.0035	319.2912 0.0084
06JUN29	GD	64.119327849	0.0028	-19.747177253	0.0035	319.3030 0.0084
06JUN30	GD	64.119327866	0.0028	-19.747177230	0.0035	319.2987 0.0083
06JUL01	GD	64.119327867	0.0027	-19.747177246	0.0034	319.2864 0.0080
06JUL02	GD	64.119327854	0.0028	-19.747177276	0.0035	319.2817 0.0085
06JUL03	GD	64.119327861	0.0027	-19.747177318	0.0034	319.2934 0.0081
06JUL04	GD	64.119327847	0.0029	-19.747177329	0.0037	319.2967 0.0088
06JUL05	GD	64.119327832	0.0030	-19.747177303	0.0041	319.2903 0.0090
06JUL06	GD	64.119327847	0.0027	-19.747177291	0.0035	319.2916 0.0085
06JUL07	GD	64.119327867	0.0027	-19.747177323	0.0035	319.2880 0.0084
06JUL08	GD	64.119327846	0.0027	-19.747177302	0.0035	319.2960 0.0083
06JUL09	GD	64.119327844	0.0027	-19.747177354	0.0035	319.2903 0.0083
06JUL10	GD	64.119327832	0.0028	-19.747177332	0.0036	319.2888 0.0084
06JUL11	GD	64.119327838	0.0030	-19.747177280	0.0039	319.2876 0.0092
06JUL12	GD	64.119327836	0.0028	-19.747177273	0.0036	319.2958 0.0085
06JUL13	GD	64.119327830	0.0028	-19.747177301	0.0036	319.2968 0.0087
06JUL14	GD	64.119327838	0.0029	-19.747177273	0.0039	319.2979 0.0089
06JUL16	GD	64.119327852	0.0029	-19.747177304	0.0038	319.2811 0.0089

06JUL17	GD	64.119327843	0.0028	-19.747177272	0.0036	319.2929	0.0088
06JUL18	GD	64.119327872	0.0027	-19.747177228	0.0034	319.2900	0.0082

KGIL

DATE	GD	Lat(deg)+/-Sigma(m)		Lon(deg)+/-Sigma(m)		Height(m)+/-Sigma(m)	
01AUG14	GD	63.859385248	0.0066	-18.974041675	0.0078	669.0634	0.0212
01AUG15	GD	63.859385220	0.0040	-18.974041731	0.0050	669.0739	0.0135
01AUG16	GD	63.859385252	0.0039	-18.974041734	0.0047	669.0863	0.0131
01AUG17	GD	63.859385241	0.0056	-18.974041663	0.0064	669.0853	0.0180
02AUG19	GD	63.859385400	0.0086	-18.974041746	0.0096	669.0489	0.0232
02AUG20	GD	63.859385334	0.0050	-18.974041663	0.0070	669.0779	0.0163
02AUG21	GD	63.859385362	0.0047	-18.974041687	0.0071	669.0541	0.0162
02AUG22	GD	63.859385374	0.0075	-18.974041614	0.0101	669.0950	0.0218
03AUG26	GD	63.859385524	0.0040	-18.974041489	0.0055	669.0639	0.0138
03AUG27	GD	63.859385535	0.0039	-18.974041409	0.0049	669.0806	0.0131
03AUG28	GD	63.859385534	0.0061	-18.974041482	0.0120	669.0748	0.0206
04SEP15	GD	63.859385651	0.0075	-18.974041365	0.0101	669.0906	0.0235
04SEP16	GD	63.859385579	0.0055	-18.974040955	0.0101	669.1097	0.0222
04SEP17	GD	63.859385623	0.0087	-18.974041190	0.0184	669.0949	0.0289
04SEP18	GD	63.859385571	0.0116	-18.974040958	0.0162	669.1270	0.0295
04SEP19	GD	63.859385682	0.0060	-18.974041098	0.0104	669.1019	0.0241
05OCT27	GD	63.859385780	0.0064	-18.974041232	0.0062	669.1231	0.0176
05OCT28	GD	63.859385753	0.0030	-18.974041183	0.0038	669.1259	0.0092
05OCT29	GD	63.859385808	0.0031	-18.974041266	0.0040	669.1182	0.0093
05OCT30	GD	63.859385784	0.0030	-18.974041169	0.0038	669.1209	0.0092
05OCT31	GD	63.859385785	0.0034	-18.974041129	0.0049	669.1249	0.0106
05NOV01	GD	63.859385785	0.0032	-18.974041253	0.0042	669.1186	0.0099
05NOV02	GD	63.859385771	0.0031	-18.974041164	0.0042	669.1169	0.0100
05NOV03	GD	63.859385754	0.0043	-18.974041192	0.0073	669.1428	0.0145
05NOV04	GD	63.859385791	0.0033	-18.974041129	0.0043	669.1130	0.0104
05NOV05	GD	63.859385759	0.0032	-18.974041165	0.0041	669.1139	0.0100
05NOV06	GD	63.859385852	0.0032	-18.974041120	0.0043	669.1516	0.0100
05NOV07	GD	63.859385787	0.0030	-18.974041191	0.0041	669.1081	0.0096
05NOV08	GD	63.859385825	0.0030	-18.974041222	0.0040	669.1148	0.0095
05NOV09	GD	63.859385794	0.0031	-18.974041118	0.0040	669.1197	0.0097
06SEP25	GD	63.859385925	0.0052	-18.974040995	0.0060	669.1253	0.0143
06SEP26	GD	63.859385950	0.0030	-18.974041070	0.0039	669.1300	0.0091
06SEP27	GD	63.859385935	0.0044	-18.974041024	0.0069	669.1423	0.0135

KKLO

DATE	GD	Lat(deg)+/-Sigma(m)		Lon(deg)+/-Sigma(m)		Height(m)+/-Sigma(m)	
01AUG11	GD	63.863596754	0.0062	-19.053767538	0.0075	710.1459	0.0202
01AUG12	GD	63.863596752	0.0041	-19.053767534	0.0047	710.1506	0.0135
01AUG13	GD	63.863596747	0.0040	-19.053767639	0.0050	710.1518	0.0140
01AUG14	GD	63.863596770	0.0057	-19.053767486	0.0059	710.1683	0.0180
02AUG16	GD	63.863597044	0.0057	-19.053767302	0.0076	710.1244	0.0193
02AUG17	GD	63.863596988	0.0038	-19.053767433	0.0049	710.1461	0.0124
02AUG18	GD	63.863596989	0.0043	-19.053767423	0.0060	710.1364	0.0141
02AUG19	GD	63.863596944	0.0083	-19.053767208	0.0137	710.1537	0.0274
05OCT27	GD	63.863597397	0.0072	-19.053767065	0.0065	710.1930	0.0189
05OCT28	GD	63.863597362	0.0032	-19.053766972	0.0038	710.1949	0.0104
05OCT29	GD	63.863597359	0.0033	-19.053766986	0.0040	710.1918	0.0103
05OCT30	GD	63.863597399	0.0033	-19.053766976	0.0039	710.1830	0.0106
06SEP25	GD	63.863597524	0.0056	-19.053766889	0.0060	710.1752	0.0150
06SEP26	GD	63.863597522	0.0028	-19.053766925	0.0036	710.1858	0.0087
06SEP27	GD	63.863597526	0.0039	-19.053766953	0.0056	710.2035	0.0122

KROK

DATE	GD	Lat(deg)+/-Sigma(m)		Lon(deg)+/-Sigma(m)		Height(m)+/-Sigma(m)	
01AUG18	GD	64.06606566	0.0068	-19.39605171	0.0081	584.8967	0.022
01AUG19	GD	64.06606565	0.0044	-19.39605175	0.0050	584.9082	0.0141
01AUG20	GD	64.06606562	0.0040	-19.39605174	0.0046	584.9184	0.0137
01AUG21	GD	64.06606550	0.0089	-19.39605186	0.0075	584.9183	0.0232
02AUG21	GD	64.06606585	0.0050	-19.39605160	0.0068	584.9452	0.0172
02AUG22	GD	64.06606586	0.0044	-19.39605153	0.0060	584.9739	0.0144
02AUG23	GD	64.06606575	0.0080	-19.39605166	0.0082	584.975	0.023
03AUG26	GD	64.06606602	0.0041	-19.39605163	0.0051	584.9218	0.0136
03AUG27	GD	64.06606601	0.0041	-19.39605158	0.0048	584.9353	0.0131
03AUG28	GD	64.06606600	0.0075	-19.39605178	0.0140	584.9378	0.0246
06SEP26	GD	64.06606646	0.0047	-19.39605150	0.0050	584.9969	0.0134
06SEP27	GD	64.06606648	0.0028	-19.39605149	0.0034	585.0119	0.009

```
06SEP28 GD   64.06606648 0.0042   -19.3960515  0.0059    585.0093    0.0136
```

LIHO

DATE	GD	Lat(deg)+/-Sigma(m)		Lon(deg)+/-Sigma(m)		Height(m)+/-Sigma(m)	
01AUG19	GD	63.990480396	0.0040	-19.263350542	0.0048	1053.1557	0.0134
01AUG20	GD	63.990480347	0.0038	-19.263350518	0.0044	1053.1654	0.0133
01AUG21	GD	63.990480368	0.0060	-19.263350446	0.0068	1053.1514	0.0189
02AUG20	GD	63.990480465	0.0073	-19.263350476	0.0092	1053.1905	0.0197
02AUG21	GD	63.990480493	0.0035	-19.263350405	0.0054	1053.1696	0.0110
02AUG22	GD	63.990480483	0.0031	-19.263350178	0.0049	1053.1812	0.0092
02AUG23	GD	63.990480481	0.0055	-19.263350189	0.0064	1053.1784	0.0148
03AUG14	GD	63.990480669	0.0063	-19.263350330	0.0079	1053.1690	0.0173
03AUG15	GD	63.990480716	0.0031	-19.263350143	0.0045	1053.1851	0.0103
03AUG16	GD	63.990480722	0.0030	-19.263350227	0.0041	1053.1962	0.0101
03AUG17	GD	63.990480696	0.0042	-19.263350237	0.0063	1053.1976	0.0144
04SEP20	GD	63.990480819	0.0048	-19.263350119	0.0056	1053.2144	0.0146
04SEP21	GD	63.990480833	0.0030	-19.263350087	0.0041	1053.2095	0.0092
06SEP23	GD	63.990481112	0.0027	-19.263350008	0.0036	1053.2470	0.0082
06SEP24	GD	63.990481094	0.0056	-19.263350094	0.0085	1053.2405	0.0147

LAUF

DATE	GD	Lat(deg)+/-Sigma(m)		Lon(deg)+/-Sigma(m)		Height(m)+/-Sigma(m)	
01AUG17	GD	63.904280871	0.0046	-19.368294873	0.0061	709.4113	0.0149
01AUG18	GD	63.904280965	0.0046	-19.368295040	0.0057	709.3921	0.0139
01AUG19	GD	63.904280948	0.0055	-19.368294770	0.0073	709.4017	0.0179
02AUG15	GD	63.904281176	0.0046	-19.368294907	0.0056	709.4169	0.0144
02AUG16	GD	63.904281174	0.0043	-19.368294887	0.0055	709.4226	0.0137
02AUG17	GD	63.904281206	0.0075	-19.368295089	0.0083	709.4134	0.0211
03AUG12	GD	63.904281263	0.0043	-19.368294904	0.0059	709.4304	0.0143
03AUG13	GD	63.904281278	0.0042	-19.368294900	0.0053	709.4265	0.0134
03AUG14	GD	63.904281242	0.0075	-19.368294727	0.0102	709.4121	0.0229
04SEP14	GD	63.904281306	0.0056	-19.368294672	0.0084	709.4614	0.0156
04SEP15	GD	63.904281345	0.0033	-19.368294761	0.0046	709.4719	0.0104
04SEP16	GD	63.904281321	0.0049	-19.368294722	0.0090	709.4662	0.0178

LAHR

DATE	GD	Lat(deg)+/-Sigma(m)		Lon(deg)+/-Sigma(m)		Height(m)+/-Sigma(m)	
01AUG19	GD	63.987935857	0.0041	-19.059802909	0.0049	666.8851	0.0137
01AUG20	GD	63.987935825	0.0037	-19.059803046	0.0045	666.8856	0.0135
01AUG21	GD	63.987935801	0.0070	-19.059802920	0.0072	666.8960	0.0208
02AUG19	GD	63.987935997	0.0051	-19.059802932	0.0070	666.8943	0.0170
02AUG20	GD	63.987936003	0.0051	-19.059802898	0.0072	666.8805	0.0175
02AUG21	GD	63.987936182	0.0170	-19.059802585	0.0277	666.8861	0.0435
03AUG16	GD	63.987936169	0.0072	-19.059803082	0.0097	666.8892	0.0232
03AUG17	GD	63.987936171	0.0043	-19.059802848	0.0052	666.9038	0.0141
03AUG18	GD	63.987936203	0.0101	-19.059802909	0.0145	666.9206	0.0319
03AUG19	GD	63.987936195	0.0064	-19.059802866	0.0110	666.9033	0.0235
04SEP16	GD	63.987936222	0.0069	-19.059802768	0.0091	666.9150	0.0217
05OCT27	GD	63.987936484	0.0068	-19.059802855	0.0064	666.9734	0.0187
05OCT28	GD	63.987936488	0.0032	-19.059802690	0.0038	666.9756	0.0104
05OCT29	GD	63.987936477	0.0033	-19.059802806	0.0040	666.9770	0.0104
05OCT30	GD	63.987936474	0.0032	-19.059802764	0.0039	666.9755	0.0105
05OCT31	GD	63.987936506	0.0035	-19.059802669	0.0048	666.9719	0.0114
05NOV01	GD	63.987936504	0.0034	-19.059802787	0.0043	666.9685	0.0117
05NOV02	GD	63.987936500	0.0033	-19.059802735	0.0042	666.9677	0.0115
05NOV03	GD	63.987936482	0.0037	-19.059802663	0.0051	666.9604	0.0124
05NOV04	GD	63.987936542	0.0035	-19.059802762	0.0043	666.9727	0.0116
05NOV05	GD	63.987936569	0.0036	-19.059802480	0.0047	666.9972	0.0119
05NOV06	GD	63.987936444	0.0034	-19.059802706	0.0042	666.9746	0.0113
05NOV07	GD	63.987936456	0.0033	-19.059802746	0.0041	666.9700	0.0113
05NOV08	GD	63.987936465	0.0033	-19.059802706	0.0041	666.9689	0.0113
05NOV09	GD	63.987936482	0.0033	-19.059802667	0.0042	666.9653	0.0112
05NOV10	GD	63.987936459	0.0045	-19.059802273	0.0071	666.9946	0.0158
06SEP24	GD	63.987936640	0.0043	-19.059802676	0.0050	666.9712	0.0140
06SEP25	GD	63.987936620	0.0055	-19.059802586	0.0088	666.9606	0.0195

SATU

DATE	GD	Lat(deg)+/-Sigma(m)	Lon(deg)+/-Sigma(m)	Height(m)+/-Sigma(m)
01AUG11	GD	63.880737802 0.0053	-19.250156743 0.0066	734.5542 0.0178
01AUG12	GD	63.880737804 0.0041	-19.250156744 0.0046	734.5579 0.0132
01AUG13	GD	63.880737810 0.0041	-19.250156712 0.0052	734.5523 0.0141
01AUG14	GD	63.880737840 0.0063	-19.250156681 0.0061	734.5766 0.0190
02AUG16	GD	63.880738086 0.0054	-19.250156495 0.0066	734.5654 0.0168
02AUG17	GD	63.880738031 0.0040	-19.250156636 0.0054	734.5781 0.0128
02AUG18	GD	63.880738012 0.0042	-19.250156603 0.0056	734.5802 0.0134
02AUG19	GD	63.880738002 0.0154	-19.250156568 0.0155	734.5756 0.0318
03AUG22	GD	63.880738059 0.0034	-19.250156621 0.0049	734.5863 0.0105
03AUG23	GD	63.880738136 0.0033	-19.250156630 0.0047	734.5836 0.0105
03AUG24	GD	63.880738135 0.0047	-19.250156584 0.0072	734.5915 0.0156
04SEP16	GD	63.880738354 0.0046	-19.250156477 0.0064	734.6628 0.0167
04SEP17	GD	63.880738318 0.0061	-19.250156474 0.0080	734.6324 0.0184
04SEP18	GD	63.880738295 0.0061	-19.250156515 0.0076	734.6432 0.0189
04SEP19	GD	63.880738249 0.0049	-19.250156331 0.0067	734.6418 0.0174
04SEP20	GD	63.880738273 0.0049	-19.250156343 0.0068	734.6332 0.0178
06SEP24	GD	63.880738587 0.0043	-19.250156217 0.0051	734.6489 0.0120
06SEP25	GD	63.880738613 0.0026	-19.250156097 0.0034	734.6418 0.0078
06SEP26	GD	63.880738580 0.0040	-19.250156141 0.0067	734.6547 0.0121

SNAE

DATE	GD	Lat(deg)+/-Sigma(m)	Lon(deg)+/-Sigma(m)	Height(m)+/-Sigma(m)
01AUG03	GD	63.736314948 0.0037	-18.632458205 0.0043	332.3445 0.0128
01AUG04	GD	63.736314925 0.0038	-18.632458166 0.0045	332.3505 0.0127
01AUG06	GD	63.736314918 0.0039	-18.632458096 0.0048	332.3436 0.0130
01AUG07	GD	63.736314965 0.0039	-18.632458190 0.0045	332.3325 0.0135
01AUG08	GD	63.736314941 0.0041	-18.632458111 0.0048	332.3454 0.0141
01AUG09	GD	63.736314910 0.0039	-18.632458113 0.0044	332.3460 0.0131
01AUG10	GD	63.736314935 0.0038	-18.632458112 0.0043	332.3467 0.0129
01AUG11	GD	63.736314932 0.0038	-18.632458140 0.0044	332.3430 0.0129
01AUG12	GD	63.736314916 0.0066	-18.632458164 0.0072	332.3537 0.0201
01AUG13	GD	63.736314926 0.0040	-18.632458171 0.0049	332.3499 0.0136
01AUG14	GD	63.736314941 0.0037	-18.632458170 0.0043	332.3445 0.0125
01AUG15	GD	63.736314953 0.0042	-18.632458170 0.0047	332.3402 0.0131
01AUG16	GD	63.736314967 0.0039	-18.632458208 0.0046	332.3460 0.0128
01AUG17	GD	63.736314914 0.0043	-18.632458125 0.0056	332.3533 0.0142
01AUG18	GD	63.736314939 0.0043	-18.632458159 0.0049	332.3444 0.0135
01AUG20	GD	63.736314948 0.0037	-18.632458147 0.0043	332.3517 0.0128
01AUG21	GD	63.736314951 0.0039	-18.632458174 0.0047	332.3532 0.0133
01AUG22	GD	63.736314877 0.0065	-18.632458213 0.0065	332.3570 0.0199
02AUG17	GD	63.736315109 0.0041	-18.632458006 0.0049	332.3629 0.0128
02AUG18	GD	63.736315111 0.0044	-18.632457982 0.0058	332.3589 0.0141
02AUG19	GD	63.736315087 0.0049	-18.632457957 0.0066	332.3654 0.0154
02AUG20	GD	63.736315101 0.0050	-18.632457990 0.0069	332.3577 0.0162
02AUG21	GD	63.736315092 0.0050	-18.632458073 0.0076	332.3562 0.0171
02AUG22	GD	63.736315101 0.0044	-18.632457932 0.0057	332.3613 0.0141
02AUG23	GD	63.736315095 0.0040	-18.632457939 0.0051	332.3610 0.0134
02AUG24	GD	63.736315134 0.0060	-18.632457917 0.0078	332.3543 0.0199
03AUG02	GD	63.736315218 0.0040	-18.632457690 0.0055	332.3747 0.0141
03AUG03	GD	63.736315244 0.0042	-18.632457755 0.0061	332.3778 0.0144
03AUG04	GD	63.736315245 0.0039	-18.632457772 0.0050	332.3687 0.0137
03AUG05	GD	63.736315251 0.0038	-18.632457802 0.0045	332.3704 0.0125
03AUG06	GD	63.736315235 0.0043	-18.632457837 0.0061	332.3696 0.0151
03AUG07	GD	63.736315232 0.0041	-18.632457876 0.0048	332.3713 0.0134
03AUG08	GD	63.736315246 0.0045	-18.632457838 0.0066	332.3589 0.0154
03AUG09	GD	63.736315253 0.0038	-18.632457840 0.0047	332.3573 0.0128
03AUG10	GD	63.736315226 0.0038	-18.632457754 0.0048	332.3702 0.0126
03AUG11	GD	63.736315224 0.0041	-18.632457753 0.0049	332.3613 0.0131
03AUG12	GD	63.736315261 0.0043	-18.632457767 0.0060	332.3712 0.0143
03AUG13	GD	63.736315256 0.0042	-18.632457727 0.0051	332.3682 0.0132
03AUG14	GD	63.736315233 0.0042	-18.632457855 0.0052	332.3751 0.0135
03AUG15	GD	63.736315279 0.0038	-18.632457716 0.0046	332.3811 0.0128
03AUG16	GD	63.736315229 0.0038	-18.632457781 0.0048	332.3770 0.0127
03AUG17	GD	63.736315237 0.0042	-18.632457795 0.0049	332.3728 0.0137
04SEP14	GD	63.736315301 0.0082	-18.632457657 0.0155	332.4099 0.0220
04SEP15	GD	63.736315285 0.0063	-18.632457434 0.0110	332.4050 0.0204
04SEP16	GD	63.736315251 0.0058	-18.632457495 0.0089	332.4283 0.0196
04SEP17	GD	63.736315314 0.0066	-18.632457470 0.0118	332.4243 0.0215
04SEP18	GD	63.736315340 0.0070	-18.632457586 0.0114	332.4124 0.0214
04SEP19	GD	63.736315299 0.0054	-18.632457360 0.0080	332.4318 0.0174

05OCT27	GD	63.736315467	0.0038	-18.632457505	0.0044	332.4374	0.0124
05OCT28	GD	63.736315444	0.0037	-18.632457381	0.0042	332.4428	0.0122
05OCT29	GD	63.736315440	0.0038	-18.632457290	0.0043	332.4402	0.0121
05OCT30	GD	63.736315466	0.0038	-18.632457445	0.0042	332.4429	0.0122
05OCT31	GD	63.736315430	0.0043	-18.632457504	0.0057	332.4429	0.0143

THRA

DATE	GD	Lat(deg)+/-Sigma(m)		Lon(deg)+/-Sigma(m)		Height(m)+/-Sigma(m)	
00JUL10	GD	63.820692100	0.0105	-19.198106184	0.0122	642.8951	0.0314
00JUL11	GD	63.820692120	0.0052	-19.198106473	0.0071	642.8979	0.0162
03AUG24	GD	63.820692478	0.0045	-19.198105762	0.0058	642.9215	0.0129
03AUG25	GD	63.820692506	0.0032	-19.198105737	0.0045	642.9267	0.0099
03AUG26	GD	63.820692535	0.0031	-19.198105717	0.0044	642.9308	0.0100
03AUG27	GD	63.820692522	0.0037	-19.198105670	0.0058	642.9453	0.0126
06SEP26	GD	63.820693004	0.0036	-19.198105354	0.0043	642.9973	0.0118
06SEP27	GD	63.820693002	0.0048	-19.198105406	0.0060	643.0018	0.0159

THVE

DATE	GD	Lat(deg)+/-Sigma(m)		Lon(deg)+/-Sigma(m)		Height(m)+/-Sigma(m)	
01AUG14	GD	63.861050863	0.0070	-18.742426232	0.0085	644.0538	0.0220
01AUG15	GD	63.861050858	0.0039	-18.742426264	0.0047	644.0625	0.0132
01AUG16	GD	63.861050877	0.0039	-18.742426244	0.0047	644.0754	0.0129
01AUG17	GD	63.861050860	0.0065	-18.742426251	0.0065	644.0784	0.0193
02AUG19	GD	63.861050985	0.0085	-18.742426085	0.0095	644.0851	0.0170
02AUG20	GD	63.861050932	0.0037	-18.742426142	0.0059	644.0952	0.0107
02AUG21	GD	63.861050947	0.0035	-18.742426153	0.0055	644.0772	0.0111
02AUG22	GD	63.861051002	0.0047	-18.742426011	0.0082	644.1011	0.0146
03AUG22	GD	63.861051098	0.0034	-18.742426015	0.0053	644.0943	0.0109
03AUG23	GD	63.861051122	0.0034	-18.742426015	0.0050	644.0958	0.0110
03AUG24	GD	63.861051106	0.0040	-18.742426005	0.0074	644.0979	0.0146
06SEP24	GD	63.861051518	0.0030	-18.742425644	0.0036	644.1629	0.0084
06SEP25	GD	63.861051547	0.0036	-18.742425509	0.0053	644.1611	0.0110

APPENDIX 2: Response due to a tensile fault

```
function [Ux,Uy,Uz,Ur]=Dyke_Model_red(extension,depth);

% Program Written by: Stephanie Scheiber
% Date: 2007-2008
% Reference: Okada, Y. (1985). Surface Deformation due to Shear and
% Tensile Faults in a Half-Space. Bull. Seis. Soc. Amer. 75, 4, 1135-
% 1154pp.
% Description: Models vertical and horizontal ground deformation on the
% surface of the Earth surface (2-D grid) due to the implacement of a
% dyke. Locking depth, length, width, extension and dip of dyke may be
% varied.


% User inputted values
L=1000; % Length of dyke (km). Large value is used to reduce edge effects
W=1000; % Width of dyke (km). Large value is used to reduce edge effects
d=1000+depth; % Depth to the bottom of dyke (km). "depth" is the locking
depth. Large value is used to reduce edge effects
extens=extension; % Dyke-normal rate  (mm/yr)
dip=89.9; % Dip of dyke (degrees). Cannot be vertical as causes division
by zero and therefore an undefined solution
rdist2=500; % Length of grid area (km)
sspace=1; % Grid spacing(km)
mu=1; % Medium constant assumed to be equal to one
lamda=1; % Medium constant assumed to be equal to one

% Converting from kilometres to metres
L = L*10^3;
W = W*10^3;
d = d*10^3;
extens = extens/10^3;
rdist2 = rdist2*10^3;
sspace = sspace*10^3;
% Converting from degrees to radians
dip2 = dip*pi/180;

% MESHGRID generates X and Y matrices for the grid area. Here the
% x and y values for one profile through the grid area (over the
% centre of the dyke) are generated
% in order to save computation time
[x,y]=meshgrid(1,(-1*rdist2/2):sspace:(rdist2/2)+1);

%%%%%%%%%%%%%%%%%%%%%%%%%%%%%%%%%%%%%%%%%%%%%%%%%%%%%%%%%%%%%%%%%%%%%%%

% NEAR VERTICAL DYKE - Equations from Okada (1985) for a tensile fault:

% For E=x-L and n=p (Chinnery's notation)
Ea=x-L;
pa=(y*cos(dip2))+(d*sin(dip2));
na=pa;
qa=(y*sin(dip2))-(d*cos(dip2));
Ya=(na*cos(dip2))+(qa*sin(dip2));
Da=(na*sin(dip2))-(qa*cos(dip2));
Ra=sqrt((Ea.*Ea)+(na.*na)+(qa.*qa));
Xa=sqrt((Ea.*Ea)+(qa.*qa));

const1a=(mu/(lamda+mu));
denoma=Ra+Da;
num4a=1/cos(dip2);
```

```
num5a=sin(dip2)/cos(dip2);
num6a=log(Ra+na);
num7a=log(Ra+Da);
num8a=na.*(Xa+(qa*cos(dip2)));
num9a=Xa.*(Ra+Xa)*sin(dip2);
num10a=(Ea.*(Ra+Xa)*cos(dip2))+0.000000000000000001;
I4a=const1a*num4a*(num7a-(sin(dip2)*num6a));
I5a=const1a*2*num4a*atan((num8a+num9a)./(num10a));
I1a=((-1*const1a*num4a*Ea)./denoma)-(num5a*I5a);
I3a=(const1a*(((num4a*Ya)./denoma)-num6a))+(num5a*I4a);

const2a=extens/(2*pi);
num1a=qa./(Ra.*(Ra+na));
num2a=qa./(Ra.*(Ra+Ea));
num3a=(Ea.*na)./(qa.*Ra);
Uxa=const2a*((qa.*num1a)-(I3a*((sin(dip2))^2)));
Uya=const2a*((-Da.*num2a)-(sin(dip2)*((Ea.*num1a)-atan(num3a)))-
(I1a*((sin(dip2))^2)));
Uza=const2a*((Ya.*num2a)+(cos(dip2)*((Ea.*num1a)-atan(num3a)))-
(I5a*((sin(dip2))^2)));

% For E=x-L and n=p-W (Chinnery's notation)
Eb=x-L;
pb=(y*cos(dip2))+(d*sin(dip2));
nb=pb-W;
qb=(y*sin(dip2))-(d*cos(dip2));
Yb=(nb*cos(dip2))+(qb*sin(dip2));
Db=(nb*sin(dip2))-(qb*cos(dip2));
Rb=sqrt((Eb.*Eb)+(nb.*nb)+(qb.*qb));
Xb=sqrt((Eb.*Eb)+(qb.*qb));

const1b=(mu/(lamda+mu));
denomb=Rb+Db;
num4b=1/cos(dip2);
num5b=sin(dip2)/cos(dip2);
num6b=log(Rb+nb);
num7b=log(Rb+Db);
num8b=nb.*(Xb+(qb*cos(dip2)));
num9b=Xb.*(Rb+Xb)*sin(dip2);
num10b=(Eb.*(Rb+Xb)*cos(dip2))+0.000000000000000001;
I4b=const1b*num4b*(num7b-(sin(dip2)*num6b));
I5b=const1b*2*num4b*atan((num8b+num9b)./(num10b));
I1b=((-1*const1b*num4b*Eb)./denomb)-(num5b*I5b);
I3b=(const1b*(((num4b*Yb)./denomb)-num6b))+(num5b*I4b);

const2b=extens/(2*pi);
num1b=qb./(Rb.*(Rb+nb));
num2b=qb./(Rb.*(Rb+Eb));
num3b=(Eb.*nb)./(qb.*Rb);
Uxb=const2b*((qb.*num1b)-(I3b*((sin(dip2))^2)));
Uyb=const2b*((-Db.*num2b)-(sin(dip2)*((Eb.*num1b)-atan(num3b)))-
(I1b*((sin(dip2))^2)));
Uzb=const2b*((Yb.*num2b)+(cos(dip2)*((Eb.*num1b)-atan(num3b)))-
(I5b*((sin(dip2))^2)));

% For E=x+L and n=p (Chinnery's notation)
Ec=x+L;
pc=(y*cos(dip2))+(d*sin(dip2));
nc=pc;
qc=(y*sin(dip2))-(d*cos(dip2));
Yc=(nc*cos(dip2))+(qc*sin(dip2));
Dc=(nc*sin(dip2))-(qc*cos(dip2));
Rc=sqrt((Ec.*Ec)+(nc.*nc)+(qc.*qc));
Xc=sqrt((Ec.*Ec)+(qc.*qc));
```

```
const1c=(mu/(lamda+mu));
denomc=Rc+Dc;
num4c=1/cos(dip2);
num5c=sin(dip2)/cos(dip2);
num6c=log(Rc+nc);
num7c=log(Rc+Dc);
num8c=nc.*(Xc+(qc*cos(dip2)));
num9c=Xc.*(Rc+Xc)*sin(dip2);
num10c=(Ec.*(Rc+Xc)*cos(dip2))+0.000000000000000001;
I4c=const1c*num4c*(num7c-(sin(dip2)*num6c));
I5c=const1c*2*num4c*atan((num8c+num9c)./(num10c));
I1c=((-1*const1c*num4c*Ec)./denomc)-(num5c*I5c);
I3c=(const1c*(((num4c*Yc)./denomc)-num6c))+(num5c*I4c);

const2c=extens/(2*pi);
num1c=qc./(Rc.*(Rc+nc));
num2c=qc./(Rc.*(Rc+Ec));
num3c=(Ec.*nc)./(qc.*Rc);
Uxc=const2c*((qc.*num1c)-(I3c*((sin(dip2))^2)));
Uyc=const2c*((-Dc.*num2c)-(sin(dip2)*((Ec.*num1c)-atan(num3c)))-
(I1c*((sin(dip2))^2)));
Uzc=const2c*((Yc.*num2c)+(cos(dip2)*((Ec.*num1c)-atan(num3c)))-
(I5c*((sin(dip2))^2)));

% For E=x+L and n=p-W (Chinnery's notation)
Ed=x+L;
pd=(y*cos(dip2))+(d*sin(dip2));
nd=pd-W;
qd=(y*sin(dip2))-(d*cos(dip2));
Yd=(nd*cos(dip2))+(qd*sin(dip2));
Dd=(nd*sin(dip2))-(qd*cos(dip2));
Rd=sqrt((Ed.*Ed)+(nd.*nd)+(qd.*qd));
Xd=sqrt((Ed.*Ed)+(qd.*qd));

const1d=(mu/(lamda+mu));
denomd=Rd+Dd;
num4d=1/cos(dip2);
num5d=sin(dip2)/cos(dip2);
num6d=log(Rd+nd);
num7d=log(Rd+Dd);
num8d=nd.*(Xd+(qd*cos(dip2)));
num9d=Xd.*(Rd+Xd)*sin(dip2);
num10d=(Ed.*(Rd+Xd)*cos(dip2))+0.000000000000000001;
I4d=const1d*num4d*(num7d-(sin(dip2)*num6d));
I5d=const1d*2*num4d*atan((num8d+num9d)./(num10d));
I1d=((-1*const1d*num4d*Ed)./denomd)-(num5d*I5d);
I3d=(const1d*(((num4d*Yd)./denomd)-num6d))+(num5d*I4d);

const2d=extens/(2*pi);
num1d=qd./(Rd.*(Rd+nd));
num2d=qd./(Rd.*(Rd+Ed));
num3d=(Ed.*nd)./(qd.*Rd);
Uxd=const2d*((qd.*num1d)-(I3d*((sin(dip2))^2)));
Uyd=const2d*((-Dd.*num2d)-(sin(dip2)*((Ed.*num1d)-atan(num3d)))-
(I1d*((sin(dip2))^2)));
Uzd=const2d*((Yd.*num2d)+(cos(dip2)*((Ed.*num1d)-atan(num3d)))-
(I5d*((sin(dip2))^2)));

% Calculating the Total Vertical (Uz) and Horizontal (Ur) Displacement
% along the profile
Ux=zeros(501,1); % Ux component is zero along the profile
Uy=Uyc-Uyd-Uya+Uyb;
Uz=Uzc-Uzd-Uza+Uzb;
Ur=sqrt((Ux.*Ux)+(Uy.*Uy));
```

APPENDIX 3: Response due to Hekla Mogi source between 2001 and 2006

```
function [TOTAL0106]=Mogi_Hekla_01_06(VCh01_06,dpth01_06,q);

% Program written by: Stephanie Scheiber
% Date: 2007-2008
% Input and output values: Volume change (VCh01_06) and depth (dpth01_06)
% of Hekla source; Time period over which inflation/deflation of Mogi
% source has occurred (q); Rate of deformation at each site (TOTAL0106,
% horizontal deformation is the component parallel to spreading (N78W))
% Reference: Mogi, K. (1958). "Relations between the eruptions of various
% volcanoes and the deformations of the ground surfaces around them."Bull
% of Earthquake Research Institute 36: 99-134.
% Description: Horizontal and vertical displacements and rates (for 2001-
% 2006) over a Mogi source

% User inputted values
VChange=VCh01_06; % Volume Change (km3)
depth=dpth01_06; % Chamber depth (km)
rdist=108; % Length of grid area (km)
sspace=200; % Grid spacing (km)

% Converting from kilometres to metres
depth2 = depth*10^3;
VChange2 = VChange*10^9;
rdist2 = rdist*10^3;

% MESHGRID generates X and Y matrices for the grid area
[x,y]=meshgrid((-1*rdist2/2):sspace:(rdist2/2));

% Radial Distance
r = sqrt(x.^2+y.^2);

% Vertical displacement due to a Mogi source
const = 3/(4*pi);
Uz = (const*VChange2*depth2)./((depth2^2+r.^2).^(3/2));

% Horizontal displacement due to a Mogi source
Ur = (const*VChange2*r)./((depth2^2+r.^2).^(3/2));

% Site and Mogi source locations in WGS84, UTM Zone 27N
mogix=565000.4372-000;
mogiy=7096999.581-000;

ISAKx=560874.8819;
KROKx=578057.3671;
LIHOx=585129.5376;
BLAUx=580352.5266;
LAUFx=580005.0291;
HRAFx=587179.4827;
HRASx=588221.7342;
DOMAx=591324.9819;
FROSx=595822.0785;
LAHRx=594912.3594;
SATUx=585955.0103;
THRAx=588598.9273;
KKLOx=595844.3353;
KGILx=599775.4237;
```

```
ISAKy=7110983.683;
KROKy=7105794.749;
LIHOy=7097061.677;
BLAUy=7092475.799;
LAUFy=7086893.04;
HRAFy=7093773.73;
HRASy=7091573.266;
DOMAy=7102811.594;
FROSy=7099601.906;
LAHRy=7097344.121;
SATUy=7084821.087;
THRAy=7078205.599;
KKLOy=7082878.089;
KGILy=7083000.709;

% Determining the calculated displacement at each site due to the Mogi
% source deformation.

%UTM co-ordinates are transformed into grid co-ordinates (column and row
values).
ISAKcoly=int16(271-((ISAKy-mogiy)/200));
ISAKrowx=int16(271-((ISAKx-mogix)/200));
KROKcoly=int16(271-((KROKy-mogiy)/200));
KROKrowx=int16(271-((KROKx-mogix)/200));
FROScoly=int16(271-((FROSy-mogiy)/200));
FROSrowx=int16(271-((FROSx-mogix)/200));
LAHRcoly=int16(271-((LAHRy-mogiy)/200));
LAHRrowx=int16(271-((LAHRx-mogix)/200));
SAcoly=int16(271-((SATUy-mogiy)/200));
SArowx=int16(271-((SATUx-mogix)/200));
TAcoly=int16(271-((THRAy-mogiy)/200));
TArowx=int16(271-((THRAx-mogix)/200));
KKcoly=int16(271-((KKLOy-mogiy)/200));
KKrowx=int16(271-((KKLOx-mogix)/200));
KGcoly=int16(271-((KGILy-mogiy)/200));
KGrowx=int16(271-((KGILx-mogix)/200));
Lcoly=int16(271-((LIHOy-mogiy)/200));
Lrowx=int16(271-((LIHOx-mogix)/200));
Bcoly=int16(271-((BLAUy-mogiy)/200));
Browx=int16(271-((BLAUx-mogix)/200));
LFcoly=int16(271-((LAUFy-mogiy)/200));
LFrowx=int16(271-((LAUFx-mogix)/200));
HFcoly=int16(271-((HRAFy-mogiy)/200));
HFrowx=int16(271-((HRAFx-mogix)/200));
HScoly=int16(271-((HRASy-mogiy)/200));
HSrowx=int16(271-((HRASx-mogix)/200));
Dcoly=int16(271-((DOMAy-mogiy)/200));
Drowx=int16(271-((DOMAx-mogix)/200));

% Angle between the site and Mogi source relative to an east-west axis
ISAKangle=atan((ISAKy-mogiy)/(ISAKx-mogix))*180/pi;
KROKangle=atan((KROKy-mogiy)/(KROKx-mogix))*180/pi;
FROSangle=atan((FROSy-mogiy)/(FROSx-mogix))*180/pi;
LAHRangle=atan((LAHRy-mogiy)/(LAHRx-mogix))*180/pi;
SAangle=atan((SATUy-mogiy)/(SATUx-mogix))*180/pi;
TAangle=atan((THRAy-mogiy)/(THRAx-mogix))*180/pi;
KKangle=atan((KKLOy-mogiy)/(KKLOx-mogix))*180/pi;
KGangle=atan((KGILy-mogiy)/(KGILx-mogix))*180/pi;
Langle=atan((LIHOy-mogiy)/(LIHOx-mogix))*180/pi;
Bangle=atan((BLAUy-mogiy)/(BLAUx-mogix))*180/pi;
LAangle=atan((LAUFy-mogiy)/(LAUFx-mogix))*180/pi;
HFangle=atan((HRAFy-mogiy)/(HRAFx-mogix))*180/pi;
HSangle=atan((HRASy-mogiy)/(HRASx-mogix))*180/pi;
Dangle=atan((DOMAy-mogiy)/(DOMAx-mogix))*180/pi;
```

```
% Determining the exact location of the site relative to the Mogi source
in
% order to determine the signs (positive or negative) of the x and y
% displacement components for each site. Also determining the
displacement
% experienced at each site due to Mogi deformation [in m]
if mogix>=560874.8819 && mogiy<=7110983.683;
    ISAK=Ur(ISAKrowx,ISAKcoly);
elseif mogix<=560874.8819 && mogiy>=7110983.683;
    ISAK=Ur(ISAKrowx,ISAKcoly)*-1;
elseif mogix>=560874.8819 && mogiy>=7110983.683;
    ISAK=Ur(ISAKrowx,ISAKcoly);
else
    ISAK=Ur(ISAKrowx,ISAKcoly)*-1;
end;
if mogix>=578057.3671 && mogiy<=7105794.749;
    KROK=Ur(KROKrowx,KROKcoly)*-1;
elseif mogix<=578057.3671 && mogiy>=7105794.749;
    KROK=Ur(KROKrowx,KROKcoly);
elseif mogix>=578057.3671 && mogiy>=7105794.749;
    KROK=Ur(KROKrowx,KROKcoly)*-1;
else
    KROK=Ur(KROKrowx,KROKcoly);
end;
if mogix>=595822.0785 && mogiy<=7099601.906;
    FROS=Ur(FROSrowx,FROScoly)*-1;
elseif mogix<=595822.0785 && mogiy>=7099601.906;
    FROS=Ur(FROSrowx,FROScoly);
elseif mogix>=595822.0785 && mogiy>=7099601.906;
    FROS=Ur(FROSrowx,FROScoly)*-1;
else
    FROS=Ur(FROSrowx,FROScoly);
end;
if mogix>=591324.9819 && mogiy<=7102811.594;
    DOMA=Ur(Drowx,Dcoly)*-1;
elseif mogix<=591324.9819 && mogiy>=7102811.594;
    DOMA=Ur(Drowx,Dcoly);
elseif mogix>=591324.9819 && mogiy>=7102811.594;
    DOMA=Ur(Drowx,Dcoly)*-1;
else
    DOMA=Ur(Drowx,Dcoly);
end;
if mogix>=594912.3594 && mogiy<=7097344.121;
    LAHR=Ur(LAHRrowx,LAHRcoly)*-1;
elseif mogix<=594912.3594 && mogiy>=7097344.121;
    LAHR=Ur(LAHRrowx,LAHRcoly);
elseif mogix>=594912.3594 && mogiy>=7097344.121;
    LAHR=Ur(LAHRrowx,LAHRcoly)*-1;
else
    LAHR=Ur(LAHRrowx,LAHRcoly);
end;
if mogix>=588598.9273 && mogiy<=7078205.599;
    THRA=Ur(TArowx,TAcoly)*-1;
elseif mogix<=588598.9273 && mogiy>=7078205.599;
    THRA=Ur(TArowx,TAcoly);
elseif mogix>=588598.9273 && mogiy>=7078205.599;
    THRA=Ur(TArowx,TAcoly)*-1;
else
    THRA=Ur(TArowx,TAcoly);
end;
if mogix>=595844.3353 && mogiy<=7082878.089;
    KKLO=Ur(KKrowx,KKcoly)*-1;
elseif mogix<=595844.3353 && mogiy>=7082878.089;
    KKLO=Ur(KKrowx,KKcoly);
elseif mogix>=595844.3353 && mogiy>=7082878.089;
```

```
    KKLO=Ur(KKrowx,KKcoly)*-1;
else
    KKLO=Ur(KKrowx,KKcoly);
end;
if mogix>=599775.4237 && mogiy<=7083000.709;
    KGIL=Ur(KGrowx,KGcoly)*-1;
elseif mogix<=599775.4237 && mogiy>=7083000.709;
    KGIL=Ur(KGrowx,KGcoly);
elseif mogix>=599775.4237 && mogiy>=7083000.709;
    KGIL=Ur(KGrowx,KGcoly)*-1;
else
    KGIL=Ur(KGrowx,KGcoly);
end;
if mogix>=588221.7342 && mogiy<=7091573.266;
    SATU=Ur(SArowx,SAcoly)*-1;
elseif mogix<=588221.7342 && mogiy>=7091573.266;
    SATU=Ur(SArowx,SAcoly);
elseif mogix>=588221.7342 && mogiy>=7091573.266;
    SATU=Ur(SArowx,SAcoly)*-1;
else
    SATU=Ur(SArowx,SAcoly);
end;
if mogix>=585129.5376 && mogiy<=7097061.677;
    LIHO=Ur(Lrowx,Lcoly)*-1;
elseif mogix<=585129.5376 && mogiy>=7097061.677;
    LIHO=Ur(Lrowx,Lcoly);
elseif mogix>=585129.5376 && mogiy>=7097061.677;
    LIHO=Ur(Lrowx,Lcoly)*-1;
else
    LIHO=Ur(Lrowx,Lcoly);
end;
if mogix>=580352.5266 && mogiy<=7092475.799;
    BLAU=Ur(Browx,Bcoly)*-1;
elseif mogix<=580352.5266 && mogiy>=7092475.799;
    BLAU=Ur(Browx,Bcoly);
elseif mogix>=580352.5266 && mogiy>=7092475.799;
    BLAU=Ur(Browx,Bcoly)*-1;
else
    BLAU=Ur(Browx,Bcoly);
end;
if mogix>=580005.0291 && mogiy<=7086893.04;
    LAUF=Ur(LFrowx,LFcoly)*-1;
elseif mogix<=580005.0291 && mogiy>=7086893.04;
    LAUF=Ur(LFrowx,LFcoly);
elseif mogix>=580005.0291 && mogiy>=7086893.04;
    LAUF=Ur(LFrowx,LFcoly)*-1;
else
    LAUF=Ur(LFrowx,LFcoly);
end;
if mogix>=587179.4827 && mogiy<=7093773.73;
    HRAF=Ur(HFrowx,HFcoly)*-1;
elseif mogix<=587179.4827 && mogiy>=7093773.73;
    HRAF=Ur(HFrowx,HFcoly);
elseif mogix>=587179.4827 && mogiy>=7093773.73;
    HRAF=Ur(HFrowx,HFcoly)*-1;
else
    HRAF=Ur(HFrowx,HFcoly);
end;
if mogix>=588221.7342 && mogiy<=7091573.266;
    HRAS=Ur(HSrowx,HScoly)*-1;
elseif mogix<=588221.7342 && mogiy>=7091573.266;
    HRAS=Ur(HSrowx,HScoly);
elseif mogix>=588221.7342 && mogiy>=7091573.266;
    HRAS=Ur(HSrowx,HScoly)*-1;
else
```

```
    HRAS=Ur(HSrowx,HScoly);
end;

% Calculating the x and y components of the horizontal displacements [in
m]
ISAKx=ISAK*cos(ISAKangle*pi/180);
ISAKy=ISAK*sin(ISAKangle*pi/180);
KROKx=KROK*cos(KROKangle*pi/180);
KROKy=KROK*sin(KROKangle*pi/180);
FROSx=FROS*cos(FROSangle*pi/180);
FROSy=FROS*sin(FROSangle*pi/180);
LAHRx=LAHR*cos(LAHRangle*pi/180);
LAHRy=LAHR*sin(LAHRangle*pi/180);
SATUx=SATU*cos(SAangle*pi/180);
SATUy=SATU*sin(SAangle*pi/180);
THRAx=THRA*cos(TAangle*pi/180);
THRAy=THRA*sin(TAangle*pi/180);
KKLOx=KKLO*cos(KKangle*pi/180);
KKLOy=KKLO*sin(KKangle*pi/180);
KGILx=KGIL*cos(KGangle*pi/180);
KGILy=KGIL*sin(KGangle*pi/180);
LIHOx=LIHO*cos(Langle*pi/180);
LIHOy=LIHO*sin(Langle*pi/180);
BLAUx=BLAU*cos(Bangle*pi/180);
BLAUy=BLAU*sin(Bangle*pi/180);
LAUFx=LAUF*cos(LAangle*pi/180);
LAUFy=LAUF*sin(LAangle*pi/180);
HRAFx=HRAF*cos(HFangle*pi/180);
HRAFy=HRAF*sin(HFangle*pi/180);
HRASx=HRAS*cos(HSangle*pi/180);
HRASy=HRAS*sin(HSangle*pi/180);
DOMAx=DOMA*cos(Dangle*pi/180);
DOMAy=DOMA*sin(Dangle*pi/180);

% Vertical displacements for each site
ISAKz=Uz(ISAKrowx,ISAKcoly);
KROKz=Uz(KROKrowx,KROKcoly);
FROSz=Uz(FROSrowx,FROScoly);
LAHRz=Uz(LAHRrowx,LAHRcoly);
SATUz=Uz(SArowx,SAcoly);
THRAz=Uz(TArowx,TAcoly);
KKLOz=Uz(KKrowx,KKcoly);
KGILz=Uz(KGrowx,KGcoly);
LIHOz=Uz(Lrowx,Lcoly);
BLAUz=Uz(Browx,Bcoly);
LAUFz=Uz(LFrowx,LFcoly);
HRAFz=Uz(HFrowx,HFcoly);
HRASz=Uz(HSrowx,HScoly);
DOMAz=Uz(Drowx,Dcoly);

% Table of horizontal (x, y, and radial) and vertical displacements
KROK1=[KROK,KROKx,KROKy,KROKz];
ISAK1=[ISAK,ISAKx,ISAKy,ISAKz];
BLAU1=[BLAU,BLAUx,BLAUy,BLAUz];
LIHO1=[LIHO,LIHOx,LIHOy,LIHOz];
LAUF1=[LAUF,LAUFx,LAUFy,LAUFz];
HRAS1=[HRAS,HRASx,HRASy,HRASz];
HRAF1=[HRAF,HRAFx,HRAFy,HRAFz];
DOMA1=[DOMA,DOMAx,DOMAy,DOMAz];
FROS1=[FROS,FROSx,FROSy,FROSz];
LAHR1=[LAHR,LAHRx,LAHRy,LAHRz];
SATU1=[SATU,SATUx,SATUy,SATUz];
THRA1=[THRA,THRAx,THRAy,THRAz];
KKLO1=[KKLO,KKLOx,KKLOy,KKLOz];
KGIL1=[KGIL,KGILx,KGILy,KGILz];
```

```
TOTAL=[ISAK1;KROK1;BLAU1;LIHO1;LAUF1;HRAS1;HRAF1;DOMA1;FROS1;LAHR1;SATU1;
THRA1;KKLO1;KGIL1];

% Calculating the rate of deformation due to the Mogi source for each
site [in m/yr]
% (i.e., Displacement divided by "q" years, inputted at the start)
KROK_v=KROK/q;
KROKx_v=KROKx/q;
KROKy_v=KROKy/q;
ISAK_v=ISAK/q;
ISAKx_v=ISAKx/q;
ISAKy_v=ISAKy/q;
BLAU_v=BLAU/q;
BLAUx_v=BLAUx/q;
BLAUy_v=BLAUy/q;
LIHO_v=LIHO/q;
LIHOx_v=LIHOx/q;
LIHOy_v=LIHOy/q;
LAUF_v=LAUF/q;
LAUFx_v=LAUFx/q;
LAUFy_v=LAUFy/q;
HRAS_v=HRAS/q;
HRASx_v=HRASx/q;
HRASy_v=HRASy/q;
HRAF_v=HRAF/q;
HRAFx_v=HRAFx/q;
HRAFy_v=HRAFy/q;
DOMA_v=DOMA/q;
DOMAx_v=DOMAx/q;
DOMAy_v=DOMAy/q;
FROS_v=FROS/q;
FROSx_v=FROSx/q;
FROSy_v=FROSy/q;
LAHR_v=LAHR/q;
LAHRx_v=LAHRx/q;
LAHRy_v=LAHRy/q;
SATU_v=SATU/q;
SATUx_v=SATUx/q;
SATUy_v=SATUy/q;
THRA_v=THRA/q;
THRAx_v=THRAx/q;
THRAy_v=THRAy/q;
KKLO_v=KKLO/q;
KKLOx_v=KKLOx/q;
KKLOy_v=KKLOy/q;
KGIL_v=KGIL/q;
KGILx_v=KGILx/q;
KGILy_v=KGILy/q;

% Vertical velocities
KROKz_v=KROKz/q;
ISAKz_v=ISAKz/q;
BLAUz_v=BLAUz/q;
LIHOz_v=LIHOz/q;
LAUFz_v=LAUFz/q;
HRASz_v=HRASz/q;
HRAFz_v=HRAFz/q;
DOMAz_v=DOMAz/q;
FROSz_v=FROSz/q;
LAHRz_v=LAHRz/q;
SATUz_v=SATUz/q;
THRAz_v=THRAz/q;
KKLOz_v=KKLOz/q;
KGILz_v=KGILz/q;
```

```
% Table of horizontal (x, y, and radial) and vertical velocities
KROK2=[KROK_v,KROKx_v,KROKy_v,KROKz_v];
ISAK2=[ISAK_v,ISAKx_v,ISAKy_v,ISAKz_v];
BLAU2=[BLAU_v,BLAUx_v,BLAUy_v,BLAUz_v];
LIHO2=[LIHO_v,LIHOx_v,LIHOy_v,LIHOz_v];
LAUF2=[LAUF_v,LAUFx_v,LAUFy_v,LAUFz_v];
HRAS2=[HRAS_v,HRASx_v,HRASy_v,HRASz_v];
HRAF2=[HRAF_v,HRAFx_v,HRAFy_v,HRAFz_v];
DOMA2=[DOMA_v,DOMAx_v,DOMAy_v,DOMAz_v];
FROS2=[FROS_v,FROSx_v,FROSy_v,FROSz_v];
LAHR2=[LAHR_v,LAHRx_v,LAHRy_v,LAHRz_v];
SATU2=[SATU_v,SATUx_v,SATUy_v,SATUz_v];
THRA2=[THRA_v,THRAx_v,THRAy_v,THRAz_v];
KKLO2=[KKLO_v,KKLOx_v,KKLOy_v,KKLOz_v];
KGIL2=[KGIL_v,KGILx_v,KGILy_v,KGILz_v];
TOTALv=[ISAK2;KROK2;BLAU2;LIHO2;LAUF2;HRAS2;HRAF2;DOMA2;FROS2;LAHR2;SATU2
;THRA2;KKLO2;KGIL2];

% Calculating the component of the horizontal velocity parallel to
spreading
% (i.e. N78E) for each site [in m/yr]
angleK=(atan(KROKy_v/KROKx_v))*180/pi;
TangleK=360+(90-angleK);
DiffK=abs(282-TangleK);
comptK=KROK_v*cos(DiffK*pi/180);
comptxK=comptK*cos((282-270)*pi/180)*-1*1000;
comptyK=comptK*sin((282-270)*pi/180)*1000;

angleI=(atan(ISAKy_v/ISAKx_v))*180/pi;
TangleI=270-angleI;
DiffI=abs(282-TangleI);
comptI=ISAK_v*cos(DiffI*pi/180);
comptxI=comptI*cos((282-270)*pi/180)*-1*1000;
comptyI=comptI*sin((282-270)*pi/180)*1000;

angleB=(atan(BLAUy_v/BLAUx_v))*180/pi;
TangleB=90-angleB;
DiffB=abs(282-TangleB);
comptB=BLAU_v*cos(DiffB*pi/180);
comptxB=comptB*cos((282-270)*pi/180)*-1*1000;
comptyB=comptB*sin((282-270)*pi/180)*1000;

angleL=(atan(LIHOy_v/LIHOx_v))*180/pi;
TangleL=360+(90-angleL);
DiffL=abs(282-TangleL);
comptL=LIHO_v*cos(DiffL*pi/180);
comptxL=comptL*cos((282-270)*pi/180)*-1*1000;
comptyL=comptL*sin((282-270)*pi/180)*1000;

angleLA=(atan(LAUFy_v/LAUFx_v))*180/pi;
TangleLA=90-angleLA;
DiffLA=abs(282-TangleLA);
comptLA=LAUF_v*cos(DiffLA*pi/180);
comptxLA=comptLA*cos((282-270)*pi/180)*-1*1000;
comptyLA=comptLA*sin((282-270)*pi/180)*1000;

angleH=(atan(HRASy_v/HRASx_v))*180/pi;
TangleH=90-angleH;
DiffH=abs(282-TangleH);
comptH=HRAS_v*cos(DiffH*pi/180);
comptxH=comptH*cos((282-270)*pi/180)*-1*1000;
comptyH=comptH*sin((282-270)*pi/180)*1000;

angleHF=(atan(HRAFy_v/HRAFx_v))*180/pi;
```

```
TangleHF=90-angleHF;
DiffHF=abs(282-TangleHF);
comptHF=HRAF_v*cos(DiffHF*pi/180);
comptxHF=comptHF*cos((282-270)*pi/180)*-1*1000;
comptyHF=comptHF*sin((282-270)*pi/180)*1000;

angleD=(atan(DOMAy_v/DOMAx_v))*180/pi;
TangleD=90-angleD;
DiffD=abs(282-TangleD);
comptD=DOMA_v*cos(DiffD*pi/180);
comptxD=comptD*cos((282-270)*pi/180)*-1*1000;
comptyD=comptD*sin((282-270)*pi/180)*1000;

angleF=(atan(FROSy_v/FROSx_v))*180/pi;
TangleF=90-angleF;
DiffF=abs(282-TangleF);
comptF=FROS_v*cos(DiffF*pi/180);
comptxF=comptF*cos((282-270)*pi/180)*-1*1000;
comptyF=comptF*sin((282-270)*pi/180)*1000;

angleLH=(atan(LAHRy_v/LAHRx_v))*180/pi;
TangleLH=90-angleLH;
DiffLH=abs(282-TangleLH);
comptLH=LAHR_v*cos(DiffLH*pi/180);
comptxLH=comptLH*cos((282-270)*pi/180)*-1*1000;
comptyLH=comptLH*sin((282-270)*pi/180)*1000;

angleS=(atan(SATUy_v/SATUx_v))*180/pi;
TangleS=90-angleS;
DiffS=abs(282-TangleS);
comptS=SATU_v*cos(DiffS*pi/180);
comptxS=comptS*cos((282-270)*pi/180)*-1*1000;
comptyS=comptS*sin((282-270)*pi/180)*1000;

angleT=(atan(THRAy_v/THRAx_v))*180/pi;
TangleT=90-angleT;
DiffT=abs(282-TangleT);
comptT=THRA_v*cos(DiffT*pi/180);
comptxT=comptT*cos((282-270)*pi/180)*-1*1000;
comptyT=comptT*sin((282-270)*pi/180)*1000;

DiffKK=abs(282-(360+(90-KKangle)));
comptKK=KKLO_v*cos(DiffKK*pi/180);
comptxKK=comptKK*cos((282-270)*pi/180)*-1*1000;
comptyKK=comptKK*sin((282-270)*pi/180)*1000;

DiffKG=abs(282-(360+(90-KGangle)));
comptKG=KGIL_v*cos(DiffKG*pi/180);
comptxKG=comptKG*cos((282-270)*pi/180)*-1*1000;
comptyKG=comptKG*sin((282-270)*pi/180)*1000;

% Table of components of the horizontal velocities parallel to plate
% spreading
TOTAL0106=[comptxI,comptyI;comptxK,comptyK;comptxL,comptyL;comptxD,compty
D;comptxF,comptyF;comptxLH,comptyLH;comptxB,comptyB;comptxHF,comptyHF;com
ptxH,comptyH;comptxLA,comptyLA;comptxS,comptyS;comptxT,comptyT;comptxKK,c
omptyKK;comptxKG,comptyKG];
```

APPENDIX 4: Response due to Hekla Mogi source between 1994 and 2003

```
function [TOTAL9403]=Mogi_Hekla_94_03(VCh94_03,dpth94_03);

% Program written by: Stephanie Scheiber
% Date: 2007-2008
% Input and output values: Volume change (VCh94_03) and depth (dpth94_03)
% of Hekla source; Rate of deformation at each site (TOTAL9403,horizontal
% deformation is the component parallel to spreading (N78W))
% Reference: Mogi, K. (1958). "Relations between the eruptions of various
% volcanoes and the deformations of the ground surfaces around them."Bull
% of Earthquake Research Institute 36: 99-134.
% Description: Horizontal and vertical displacements and rates (for 1994-
% 2003) over a Mogi source

% User inputted values
VChange=VCh94_03; % Volume Change (km3)
depth=dpth94_03; % Chamber depth (km)
rdist=108; % Length of grid area (km)
sspace=200; % Grid spacing (km)

% Converting from kilometres to metres
depth2 = depth*10^3;
VChange2 = VChange*10^9;
rdist2 = rdist*10^3;

% MESHGRID generates X and Y matrices for the grid area
[x,y]=meshgrid((-1*rdist2/2):sspace:(rdist2/2));

% Radial Distance
r = sqrt(x.^2+y.^2);

% Vertical displacement due to a Mogi source
const = 3/(4*pi);
Uz = (const*VChange2*depth2)./((depth2^2+r.^2).^(3/2));

% Horizontal displacement due to a Mogi source
Ur = (const*VChange2*r)./((depth2^2+r.^2).^(3/2));

% Site and Mogi source locations in WGS84, UTM Zone 27N
mogix=565000.4372;
mogiy=7096999.581;

D353x=580323.0411;
D356x=587262.2914;
D359x=592590.3579;
D361x=595094.6002;
ISAKx=560874.8819;
VALAx=572178.0131;
KROKx=578057.3671;
D364x=595822.0785;
D365x=596868.8406;
SKHRx=555092.5163;
PALAx=562381.5899;
SATUx=585955.0103;
KGILx=599775.4237;
BRSKx=571560.1012;
DROPx=570164.8208;
THRAx=588598.9273;
```

```
D353y=7112541.316;
D356y=7108269.393;
D359y=7109538.698;
D361y=7107384.464;
ISAKy=7110983.683;
VALAy=7106767.333;
KROKy=7105794.749;
D364y=7099601.906;
D365y=7097404.294;
SKHRy=7079668.451;
PALAy=7084263.139;
SATUy=7084821.087;
KGILy=7083000.709;
BRSKy=7091147.335;
DROPy=7087771.71;
THRAy=7078205.599;

% Determining the calculated displacement at each site due to the Mogi
% source deformation.

%UTM co-ordinates are transformed into grid co-ordinates (column and row
values).
D353coly=int16(271-((D353y-mogiy)/200));
D353rowx=int16(271-((D353x-mogix)/200));
D356coly=int16(271-((D356y-mogiy)/200));
D356rowx=int16(271-((D356x-mogix)/200));
D359coly=int16(271-((D359y-mogiy)/200));
D359rowx=int16(271-((D359x-mogix)/200));
D361coly=int16(271-((D361y-mogiy)/200));
D361rowx=int16(271-((D361x-mogix)/200));
ISAKcoly=int16(271-((ISAKy-mogiy)/200));
ISAKrowx=int16(271-((ISAKx-mogix)/200));
VALAcoly=int16(271-((VALAy-mogiy)/200));
VALArowx=int16(271-((VALAx-mogix)/200));
KROKcoly=int16(271-((KROKy-mogiy)/200));
KROKrowx=int16(271-((KROKx-mogix)/200));
D364coly=int16(271-((D364y-mogiy)/200));
D364rowx=int16(271-((D364x-mogix)/200));
D365coly=int16(271-((D365y-mogiy)/200));
D365rowx=int16(271-((D365x-mogix)/200));
SKHRcoly=int16(271-((SKHRy-mogiy)/200));
SKHRrowx=int16(271-((SKHRx-mogix)/200));
PALAcoly=int16(271-((PALAy-mogiy)/200));
PALArowx=int16(271-((PALAx-mogix)/200));
SAcoly=int16(271-((SATUy-mogiy)/200));
SArowx=int16(271-((SATUx-mogix)/200));
KGcoly=int16(271-((KGILy-mogiy)/200));
KGrowx=int16(271-((KGILx-mogix)/200));
BRcoly=int16(271-((BRSKy-mogiy)/200));
BRrowx=int16(271-((BRSKx-mogix)/200));
DRcoly=int16(271-((DROPy-mogiy)/200));
DRrowx=int16(271-((DROPx-mogix)/200));
TAcoly=int16(271-((THRAy-mogiy)/200));
TArowx=int16(271-((THRAx-mogix)/200));

% Angle between the site and Mogi source relative to an east-west axis
D353angle=atan((D353y-mogiy)/(D353x-mogix))*180/pi;
D356angle=atan((D356y-mogiy)/(D356x-mogix))*180/pi;
D359angle=atan((D359y-mogiy)/(D359x-mogix))*180/pi;
D361angle=atan((D361y-mogiy)/(D361x-mogix))*180/pi;
ISAKangle=atan((ISAKy-mogiy)/(ISAKx-mogix))*180/pi;
VALAangle=atan((VALAy-mogiy)/(VALAx-mogix))*180/pi;
KROKangle=atan((KROKy-mogiy)/(KROKx-mogix))*180/pi;
D364angle=atan((D364y-mogiy)/(D364x-mogix))*180/pi;
```

```
D365angle=atan((D365y-mogiy)/(D365x-mogix))*180/pi;
SKHRangle=atan((SKHRy-mogiy)/(SKHRx-mogix))*180/pi;
PALAangle=atan((PALAy-mogiy)/(PALAx-mogix))*180/pi;
SAangle=atan((SATUy-mogiy)/(SATUx-mogix))*180/pi;
KGangle=atan((KGILy-mogiy)/(KGILx-mogix))*180/pi;
BRangle=atan((BRSKy-mogiy)/(BRSKx-mogix))*180/pi;
DRangle=atan((DROPy-mogiy)/(DROPx-mogix))*180/pi;
TAangle=atan((THRAy-mogiy)/(THRAx-mogix))*180/pi;

% The horizontal displacement experienced at each site
% due to Mogi deformation [in m]
D353=Ur(D353rowx,D353coly);
D356=Ur(D356rowx,D356coly);
D359=Ur(D359rowx,D359coly);
D361=Ur(D361rowx,D361coly);
ISAK=Ur(ISAKrowx,ISAKcoly);
VALA=Ur(VALArowx,VALAcoly);
KROK=Ur(KROKrowx,KROKcoly);
D364=Ur(D364rowx,D364coly);
D365=Ur(D365rowx,D365coly);
SKHR=Ur(SKHRrowx,SKHRcoly);
PALA=Ur(PALArowx,PALAcoly);
SATU=Ur(SArowx,SAcoly);
KGIL=Ur(KGrowx,KGcoly);
BRSK=Ur(BRrowx,BRcoly);
DROP=Ur(DRrowx,DRcoly);
THRA=Ur(TArowx,TAcoly);

% Calculating the x and y components of the horizontal displacements [in
m]
D353x=D353*cos(D353angle*pi/180);
D353y=D353*sin(D353angle*pi/180);
D356x=D356*cos(D356angle*pi/180);
D356y=D356*sin(D356angle*pi/180);
D359x=D359*cos(D359angle*pi/180);
D359y=D359*sin(D359angle*pi/180);
D361x=D361*cos(D361angle*pi/180);
D361y=D361*sin(D361angle*pi/180);
ISAKx=ISAK*cos(ISAKangle*pi/180);
ISAKy=ISAK*sin(ISAKangle*pi/180);
VALAx=VALA*cos(VALAangle*pi/180);
VALAy=VALA*sin(VALAangle*pi/180);
KROKx=KROK*cos(KROKangle*pi/180);
KROKy=KROK*sin(KROKangle*pi/180);
D364x=D364*cos(D364angle*pi/180);
D364y=D364*sin(D364angle*pi/180);
D365x=D365*cos(D365angle*pi/180);
D365y=D365*sin(D365angle*pi/180);
SKHRx=SKHR*cos(SKHRangle*pi/180);
SKHRy=SKHR*sin(SKHRangle*pi/180);
PALAx=PALA*cos(PALAangle*pi/180);
PALAy=PALA*sin(PALAangle*pi/180);
SATUx=SATU*cos(SAangle*pi/180);
SATUy=SATU*sin(SAangle*pi/180);
KGILx=KGIL*cos(KGangle*pi/180);
KGILy=KGIL*sin(KGangle*pi/180);
BRSKx=BRSK*cos(BRangle*pi/180);
BRSKy=BRSK*sin(BRangle*pi/180);
DROPx=DROP*cos(DRangle*pi/180);
DROPy=DROP*sin(DRangle*pi/180);
THRAx=THRA*cos(TAangle*pi/180);
THRAy=THRA*sin(TAangle*pi/180);

% Vertical displacements for each site
D353z=Uz(D353rowx,D353coly);
```

```
D356z=Uz(D356rowx,D356coly);
D359z=Uz(D359rowx,D359coly);
D361z=Uz(D361rowx,D361coly);
ISAKz=Uz(ISAKrowx,ISAKcoly);
VALAz=Uz(VALArowx,VALAcoly);
KROKz=Uz(KROKrowx,KROKcoly);
D364z=Uz(D364rowx,D364coly);
D365z=Uz(D365rowx,D365coly);
SKHRz=Uz(SKHRrowx,SKHRcoly);
PALAz=Uz(PALArowx,PALAcoly);
SATUz=Uz(SArowx,SAcoly);
KGILz=Uz(KGrowx,KGcoly);
BRSKz=Uz(BRrowx,BRcoly);
DROPz=Uz(DRrowx,DRcoly);
THRAz=Uz(TArowx,TAcoly);

% Table of horizontal (x and y) and vertical displacements
D3531=[D353x,D353y,D353z];
D3561=[D356x,D356y,D356z];
D3591=[D359x,D359y,D359z];
D3611=[D361x,D361y,D361z];
ISAK1=[ISAKx,ISAKy,ISAKz];
VALA1=[VALAx,VALAy,VALAz];
KROK1=[KROKx,KROKy,KROKz];
D3641=[D364x,D364y,D364z];
D3651=[D365x,D365y,D365z];
SKHR1=[SKHRx,SKHRy,SKHRz];
PALA1=[PALAx,PALAy,PALAz];
SATU1=[SATUx,SATUy,SATUz];
KGIL1=[KGILx,KGILy,KGILz];
BRSK1=[BRSKx,BRSKy,BRSKz];
DROP1=[DROPx,DROPy,DROPz];
THRA1=[THRAx,THRAy,THRAz];
TOTAL=[D3531;D3561;D3591;D3611;ISAK1;VALA1;KROK1;D3641;D3651;SKHR1;PALA1;
SATU1;KGIL1;BRSK1;DROP1;THRA1];

% Calculating the rate of deformation due to the Mogi source for each
site [in m/yr]
% (i.e., Displacement divided by 9 years [1994-2003])
D353_v=D353/9;
D353x_v=D353x/9;
D353y_v=D353y/9;
D356_v=D356/9;
D356x_v=D356x/9;
D356y_v=D356y/9;
D359_v=D359/9;
D359x_v=D359x/9;
D359y_v=D359y/9;
D361_v=D361/9;
D361x_v=D361x/9;
D361y_v=D361y/9;
ISAK_v=ISAK/9;
ISAKx_v=ISAKx/9;
ISAKy_v=ISAKy/9;
VALA_v=VALA/9;
VALAx_v=VALAx/9;
VALAy_v=VALAy/9;
KROK_v=KROK/9;
KROKx_v=KROKx/9;
KROKy_v=KROKy/9;
D364_v=D364/9;
D364x_v=D364x/9;
D364y_v=D364y/9;
D365_v=D365/9;
D365x_v=D365x/9;
```

```
D365y_v=D365y/9;
SKHR_v=SKHR/9;
SKHRx_v=SKHRx/9;
SKHRy_v=SKHRy/9;
PALA_v=PALA/9;
PALAx_v=PALAx/9;
PALAy_v=PALAy/9;
SATU_v=SATU/9;
SATUx_v=SATUx/9;
SATUy_v=SATUy/9;
KGIL_v=KGIL/9;
KGILx_v=KGILx/9;
KGILy_v=KGILy/9;
BRSK_v=BRSK/9;
BRSKx_v=BRSKx/9;
BRSKy_v=BRSKy/9;
DROP_v=DROP/9;
DROPx_v=DROPx/9;
DROPy_v=DROPy/9;
THRA_v=THRA/9;
THRAx_v=THRAx/9;
THRAy_v=THRAy/9;

% Vertical velocities
D353z_v=D353z/9;
D356z_v=D356z/9;
D359z_v=D359z/9;
D361z_v=D361z/9;
ISAKz_v=ISAKz/9;
VALAz_v=VALAz/9;
KROKz_v=KROKz/9;
D364z_v=D364z/9;
D365z_v=D365z/9;
SKHRz_v=SKHRz/9;
PALAz_v=PALAz/9;
SATUz_v=SATUz/9;
KGILz_v=KGILz/9;
BRSKz_v=BRSKz/9;
DROPz_v=DROPz/9;
THRAz_v=THRAz/9;

% Table of horizontal (x, y, and radial) and vertical velocities
D3532=[D353x_v,D353y_v,D353z_v];
D3562=[D356x_v,D356y_v,D356z_v];
D3592=[D359x_v,D359y_v,D359z_v];
D3612=[D361x_v,D361y_v,D361z_v];
ISAK2=[ISAKx_v,ISAKy_v,ISAKz_v];
VALA2=[VALAx_v,VALAy_v,VALAz_v];
KROK2=[KROKx_v,KROKy_v,KROKz_v];
D3642=[D364x_v,D364y_v,D364z_v];
D3652=[D365x_v,D365y_v,D365z_v];
SKHR2=[SKHRx_v,SKHRy_v,SKHRz_v];
PALA2=[PALAx_v,PALAy_v,PALAz_v];
SATU2=[SATUx_v,SATUy_v,SATUz_v];
KGIL2=[KGILx_v,KGILy_v,KGILz_v];
BRSK2=[BRSKx_v,BRSKy_v,BRSKz_v];
DROP2=[DROPx_v,DROPy_v,DROPz_v];
THRA2=[THRAx_v,THRAy_v,THRAz_v];
TOTALv=[D3532;D3562;D3592;D3612;ISAK2;VALA2;KROK2;D3642;D3652;SKHR2;PALA2
;SATU2;KGIL2;BRSK2;DROP2;THRA2];

% Calculating the component of the horizontal velocity parallel to
spreading
% (i.e. N78E) for each site [in m/yr]
DiffD353=abs(282-(360+(90-D353angle)));
```

```
comptD353=D353_v*cos(DiffD353*pi/180);
comptxD353=comptD353*cos((282-270)*pi/180)*-1*1000;
comptyD353=comptD353*sin((282-270)*pi/180)*1000;

DiffD356=abs(282-(360+(90-D356angle)));
comptD356=D356_v*cos(DiffD356*pi/180);
comptxD356=comptD356*cos((282-270)*pi/180)*-1*1000;
comptyD356=comptD356*sin((282-270)*pi/180)*1000;

DiffD359=abs(282-(360+(90-D359angle)));
comptD359=D359_v*cos(DiffD359*pi/180);
comptxD359=comptD359*cos((282-270)*pi/180)*-1*1000;
comptyD359=comptD359*sin((282-270)*pi/180)*1000;

DiffD361=abs(282-(360+(90-D361angle)));
comptD361=D361_v*cos(DiffD361*pi/180);
comptxD361=comptD361*cos((282-270)*pi/180)*-1*1000;
comptyD361=comptD361*sin((282-270)*pi/180)*1000;

DiffISAK=abs(282-(360+(90-ISAKangle)));
comptISAK=ISAK_v*cos(DiffISAK*pi/180);
comptxISAK=comptISAK*cos((282-270)*pi/180)*1000;
comptyISAK=comptISAK*sin((282-270)*pi/180)*-1*1000;

DiffVALA=abs(282-(360+(90-VALAangle)));
comptVALA=VALA_v*cos(DiffVALA*pi/180);
comptxVALA=comptVALA*cos((282-270)*pi/180)*-1*1000;
comptyVALA=comptVALA*sin((282-270)*pi/180)*1000;

DiffKROK=abs(282-(360+(90-KROKangle)));
comptKROK=KROK_v*cos(DiffKROK*pi/180);
comptxKROK=comptKROK*cos((282-270)*pi/180)*-1*1000;
comptyKROK=comptKROK*sin((282-270)*pi/180)*1000;

DiffD364=abs(282-(360+(90-D364angle)));
comptD364=D364_v*cos(DiffD364*pi/180);
comptxD364=comptD364*cos((282-270)*pi/180)*-1*1000;
comptyD364=comptD364*sin((282-270)*pi/180)*1000;

DiffD365=abs(282-(360+(90-D365angle)));
comptD365=D365_v*cos(DiffD365*pi/180);
comptxD365=comptD365*cos((282-270)*pi/180)*-1*1000;
comptyD365=comptD365*sin((282-270)*pi/180)*1000;

DiffSKHR=abs(282-(360+(90-SKHRangle)));
comptSKHR=SKHR_v*cos(DiffSKHR*pi/180);
comptxSKHR=comptSKHR*cos((282-270)*pi/180)*1000;
comptySKHR=comptSKHR*sin((282-270)*pi/180)*-1*1000;

DiffPALA=abs(282-(360+(90-PALAangle)));
comptPALA=PALA_v*cos(DiffPALA*pi/180);
comptxPALA=comptPALA*cos((282-270)*pi/180)*1000;
comptyPALA=comptPALA*sin((282-270)*pi/180)*-1*1000;

DiffSA=abs(282-(360+(90-SAangle)));
comptSA=SATU_v*cos(DiffSA*pi/180);
comptxSA=comptSA*cos((282-270)*pi/180)*-1*1000;
comptySA=comptSA*sin((282-270)*pi/180)*1000;

DiffKG=abs(282-(360+(90-KGangle)));
comptKG=KGIL_v*cos(DiffKG*pi/180);
comptxKG=comptKG*cos((282-270)*pi/180)*-1*1000;
comptyKG=comptKG*sin((282-270)*pi/180)*1000;
```

```
DiffBR=abs(282-(360+(90-BRangle)));
comptBR=BRSK_v*cos(DiffBR*pi/180);
comptxBR=comptBR*cos((282-270)*pi/180)*-1*1000;
comptyBR=comptBR*sin((282-270)*pi/180)*1000;

DiffDR=abs(282-(360+(90-DRangle)));
comptDR=DROP_v*cos(DiffDR*pi/180);
comptxDR=comptDR*cos((282-270)*pi/180)*-1*1000;
comptyDR=comptDR*sin((282-270)*pi/180)*1000;

DiffTA=abs(282-(360+(90-TAangle)));
comptTA=THRA_v*cos(DiffTA*pi/180);
comptxTA=comptTA*cos((282-270)*pi/180)*-1*1000;
comptyTA=comptTA*sin((282-270)*pi/180)*1000;

% Table of components of the horizontal velocities parallel to plate
% spreading
TOTAL9403=[comptxD353,comptyD353;comptxD356,comptyD356;comptxD359,comptyD
359;comptxD361,comptyD361;comptxISAK,comptyISAK;comptxVALA,comptyVALA;com
ptxKROK,comptyKROK;comptxD364,comptyD364;comptxD365,comptyD365;comptxSKHR
,comptySKHR;comptxPALA,comptyPALA;comptxSA,comptySA;comptxKG,comptyKG;com
ptxBR,comptyBR;comptxDR,comptyDR;comptxTA,comptyTA];
```

APPENDIX 5: Response due to Torfajökull Mogi source between 2001 and 2006

```
function [TOTAL_Torf]=Mogi_Torf(VChT,dT,mogx,mogy);

% Program written by: Stephanie Scheiber
% Date: 2007-2008
% Input and output values: Volume change (VChT) and depth (dT) of
% Torfajokull source; Mogi source location (mogx and mogy); Rate of
% deformation at each site (TOTAL_Torf, horizontal deformation is the
% component parallel to spreading (N78W))
% Reference: Mogi, K. (1958). "Relations between the eruptions of various
% volcanoes and the deformations of the ground surfaces around them."Bull
% of Earthquake Research Institute 36: 99-134.
% Description: Horizontal and vertical displacements and rates (for 2001-
% 2006) over a Mogi source

% User inputted values
VChange=VChT; % Volume Change (km3)
depth=dT; % Chamber depth (km)
rdist=108; % Length of grid area (km)
sspace=200; % Grid spacing (km)

% Converting from kilometres to metres
depth2 = depth*10^3;
VChange2 = VChange*10^9;
rdist2 = rdist*10^3;

% MESHGRID generates X and Y matrices for the grid area
[x,y]=meshgrid((-1*rdist2/2):sspace:(rdist2/2));

% Radial Distance
r = sqrt(x.^2+y.^2);

% Vertical displacement due to a Mogi source
const = 3/(4*pi);
Uz = (const*VChange2*depth2)./((depth2^2+r.^2).^(3/2));

% Horizontal displacement due to a Mogi source
Ur = (const*VChange2*r)./((depth2^2+r.^2).^(3/2));

% Site and Mogi source locations in WGS84, UTM Zone 27N
mogix=580000+mogx;
mogiy=7087000+mogy;

LIHOx=585129.5376;
BLAUx=580352.5266;
LAUFx=580005.0291;
HRAFx=587179.4827;
HRASx=588221.7342;
SATUx=585955.0103;
LIHOy=7097061.677;
BLAUy=7092475.799;
LAUFy=7086893.04;
HRAFy=7093773.73;
HRASy=7091573.266;
SATUy=7084821.087;

% Determining the calculated displacement at each site due to the Mogi
% source deformation.
```

```
%UTM co-ordinates are transformed into grid co-ordinates (column and row
values).
Lcoly=int16(271-((LIHOy-mogiy)/200));
Lrowx=int16(271-((LIHOx-mogix)/200));
Bcoly=int16(271-((BLAUy-mogiy)/200));
Browx=int16(271-((BLAUx-mogix)/200));
LFcoly=int16(271-((LAUFy-mogiy)/200));
LFrowx=int16(271-((LAUFx-mogix)/200));
HFcoly=int16(271-((HRAFy-mogiy)/200));
HFrowx=int16(271-((HRAFx-mogix)/200));
HScoly=int16(271-((HRASy-mogiy)/200));
HSrowx=int16(271-((HRASx-mogix)/200));
SAcoly=int16(271-((SATUy-mogiy)/200));
SArowx=int16(271-((SATUx-mogix)/200));

% Angle between the site and Mogi source relative to an east-west axis
Langle=atan((LIHOy-mogiy)/(LIHOx-mogix))*180/pi;
Bangle=atan((BLAUy-mogiy)/(BLAUx-mogix))*180/pi;
LAangle=atan((LAUFy-mogiy)/(LAUFx-mogix))*180/pi;
HFangle=atan((HRAFy-mogiy)/(HRAFx-mogix))*180/pi;
HSangle=atan((HRASy-mogiy)/(HRASx-mogix))*180/pi;
SAangle=atan((SATUy-mogiy)/(SATUx-mogix))*180/pi;

% Determining the exact location of the site relative to the Mogi source
in
% order to determine the signs (positive or negative) of the x and y
% displacement components for each site. Also determining the
displacement
% experienced at each site due to Mogi deformation [in m]
if mogix>=585129.5376 && mogiy<=7097061.677;
    LIHO=Ur(Lrowx,Lcoly)*-1;
elseif mogix<=585129.5376 && mogiy>=7097061.677;
    LIHO=Ur(Lrowx,Lcoly);
elseif mogix>=585129.5376 && mogiy>=7097061.677;
    LIHO=Ur(Lrowx,Lcoly)*-1;
else
    LIHO=Ur(Lrowx,Lcoly);
end;
if mogix>=580352.5266 && mogiy<=7092475.799;
    BLAU=Ur(Browx,Bcoly)*-1;
elseif mogix<=580352.5266 && mogiy>=7092475.799;
    BLAU=Ur(Browx,Bcoly);
elseif mogix>=580352.5266 && mogiy>=7092475.799;
    BLAU=Ur(Browx,Bcoly)*-1;
else
    BLAU=Ur(Browx,Bcoly);
end;
if mogix>=580005.0291 && mogiy<=7086893.04;
    LAUF=Ur(LFrowx,LFcoly)*-1;
elseif mogix<=580005.0291 && mogiy>=7086893.04;
    LAUF=Ur(LFrowx,LFcoly);
elseif mogix>=580005.0291 && mogiy>=7086893.04;
    LAUF=Ur(LFrowx,LFcoly)*-1;
else
    LAUF=Ur(LFrowx,LFcoly);
end;
if mogix>=587179.4827 && mogiy<=7093773.73;
    HRAF=Ur(HFrowx,HFcoly)*-1;
elseif mogix<=587179.4827 && mogiy>=7093773.73;
    HRAF=Ur(HFrowx,HFcoly);
elseif mogix>=587179.4827 && mogiy>=7093773.73;
    HRAF=Ur(HFrowx,HFcoly)*-1;
else
    HRAF=Ur(HFrowx,HFcoly);
```

```
end;
if mogix>=588221.7342 && mogiy<=7091573.266;
    HRAS=Ur(HSrowx,HScoly)*-1;
elseif mogix<=588221.7342 && mogiy>=7091573.266;
    HRAS=Ur(HSrowx,HScoly);
elseif mogix>=588221.7342 && mogiy>=7091573.266;
    HRAS=Ur(HSrowx,HScoly)*-1;
else
    HRAS=Ur(HSrowx,HScoly);
end;
if mogix>=588221.7342 && mogiy<=7091573.266;
    SATU=Ur(SArowx,SAcoly)*-1;
elseif mogix<=588221.7342 && mogiy>=7091573.266;
    SATU=Ur(SArowx,SAcoly);
elseif mogix>=588221.7342 && mogiy>=7091573.266;
    SATU=Ur(SArowx,SAcoly)*-1;
else
    SATU=Ur(SArowx,SAcoly);
end;

% Calculating the x and y components of the horizontal displacements [in
m]
LIHOx=LIHO*cos(Langle*pi/180);
LIHOy=LIHO*sin(Langle*pi/180);
BLAUx=BLAU*cos(Bangle*pi/180);
BLAUy=BLAU*sin(Bangle*pi/180);
LAUFx=LAUF*cos(LAangle*pi/180);
LAUFy=LAUF*sin(LAangle*pi/180);
HRAFx=HRAF*cos(HFangle*pi/180);
HRAFy=HRAF*sin(HFangle*pi/180);
HRASx=HRAS*cos(HSangle*pi/180);
HRASy=HRAS*sin(HSangle*pi/180);
SATUx=SATU*cos(SAangle*pi/180);
SATUy=SATU*sin(SAangle*pi/180);

% Vertical displacements for each site
LIHOz=Uz(Lrowx,Lcoly);
BLAUz=Uz(Browx,Bcoly);
HRAFz=Uz(HFrowx,HFcoly);
HRASz=Uz(HSrowx,HScoly);
SATUz=Uz(SArowx,SAcoly);
LAUFz=Uz(LFrowx,LFcoly);

% Table of horizontal (x, y, and radial) and vertical displacements
HRAS1=[HRAS,HRASx,HRASy,HRASz];
BLAU1=[BLAU,BLAUx,BLAUy,BLAUz];
LIHO1=[LIHO,LIHOx,LIHOy,LIHOz];
HRAF1=[HRAF,HRAFx,HRAFy,HRAFz];
LAUF1=[LAUF,LAUFx,LAUFy,LAUFz];
SATU1=[SATU,SATUx,SATUy,SATUz];
TOTAL=[BLAU1;LIHO1;HRAF1;HRAS1;LAUF1;SATU1];

% Calculating the rate of deformation due to the Mogi source for each
site [in m/yr]
% (i.e., Displacement divided by 5.93 years [2000-2006])
HRAS_v=HRAS/5.93;
HRASx_v=HRASx/5.93;
HRASy_v=HRASy/5.93;
HRASz_v=HRASz/5.93;
BLAU_v=BLAU/5.93;
BLAUx_v=BLAUx/5.93;
BLAUy_v=BLAUy/5.93;
BLAUz_v=BLAUz/5.93;
LIHO_v=LIHO/5.93;
LIHOx_v=LIHOx/5.93;
```

```
LIHOy_v=LIHOy/5.93;
LIHOz_v=LIHOz/5.93;
HRAF_v=HRAF/5.93;
HRAFx_v=HRAFx/5.93;
HRAFy_v=HRAFy/5.93;
HRAFz_v=HRAFz/5.93;
LAUF_v=LAUF/5.93;
LAUFx_v=LAUFx/5.93;
LAUFy_v=LAUFy/5.93;
LAUFz_v=LAUFz/5.93;
SATU_v=SATU/5.93;
SATUx_v=SATUx/5.93;
SATUy_v=SATUy/5.93;
SATUz_v=SATUz/5.93;

% Table of horizontal (x, y, and radial) and vertical velocities
HRASv=[HRAS_v,HRASx_v,HRASy_v,HRASz_v];
BLAUv=[BLAU_v,BLAUx_v,BLAUy_v,BLAUz_v];
LIHOv=[LIHO_v,LIHOx_v,LIHOy_v,LIHOz_v];
HRAFv=[HRAF_v,HRAFx_v,HRAFy_v,HRAFz_v];
LAUFv=[LAUF_v,LAUFx_v,LAUFy_v,LAUFz_v];
SATUv=[SATU_v,SATUx_v,SATUy_v,SATUz_v];
TOTALv=[BLAUv;LIHOv;HRAFv;HRASv;LAUFv;SATUv];

% Calculating the component of the horizontal velocity parallel to
spreading
% (i.e. N78E) for each site [in m/yr]. Provision is made for the Mogi
% source location to be varied as a source location for Torfajokull is
not
% well constrained. The "if...elseif" statements below allow for correct
% determination of the angle between the site and Mogi source, and the
% signs (positive or negative) for the x and y velocity components
if mogix>=585129.5376;
    TangleL=90-Langle;
elseif mogix<=585129.5376;
    TangleL=270-Langle;
end;
if mogix>=585129.5376 && TangleL>=12;
DiffL=abs(282-TangleL);
comptL=LIHO_v*cos(DiffL*pi/180);
comptxL=comptL*cos((282-270)*pi/180)*-1*1000;
comptyL=comptL*sin((282-270)*pi/180)*1000;
else
DiffL=abs(282-TangleL);
comptL=LIHO_v*cos(DiffL*pi/180);
comptxL=comptL*cos((282-270)*pi/180)*1000;
comptyL=comptL*sin((282-270)*pi/180)*-1*1000;
end;

if mogix>=580352.5266;
    TangleB=90-Bangle;
elseif mogix<=580352.5266;
    TangleB=270-Bangle;
end;
if mogix>=580352.5266 && TangleB>=12;
DiffB=abs(282-TangleB);
comptB=BLAU_v*cos(DiffB*pi/180);
comptxB=comptB*cos((282-270)*pi/180)*-1*1000;
comptyB=comptB*sin((282-270)*pi/180)*1000;
else
DiffB=abs(282-TangleB);
comptB=BLAU_v*cos(DiffB*pi/180);
comptxB=comptB*cos((282-270)*pi/180)*1000;
comptyB=comptB*sin((282-270)*pi/180)*-1*1000;
end;
```

```
if mogix>=580005.0291;
    TangleLA=90-LAangle;
elseif mogix<=580005.0291;
    TangleLA=270-LAangle;
end;
if mogix>=580005.0291 && TangleLA>=12;
DiffLA=abs(282-TangleLA);
comptLA=LAUF_v*cos(DiffLA*pi/180);
comptxLA=comptLA*cos((282-270)*pi/180)*-1*1000;
comptyLA=comptLA*sin((282-270)*pi/180)*1000;
else
DiffLA=abs(282-TangleLA);
comptLA=LAUF_v*cos(DiffLA*pi/180);
comptxLA=comptLA*cos((282-270)*pi/180)*1000;
comptyLA=comptLA*sin((282-270)*pi/180)*-1*1000;
end;

if mogix>=587179.4827;
    TangleHF=90-HFangle;
elseif mogix<=587179.4827;
    TangleHF=270-HFangle;
end;
if mogix>=587179.4827 && TangleHF>=12;
DiffHF=abs(282-TangleHF);
comptHF=HRAF_v*cos(DiffHF*pi/180);
comptxHF=comptHF*cos((282-270)*pi/180)*-1*1000;
comptyHF=comptHF*sin((282-270)*pi/180)*1000;
else
DiffHF=abs(282-TangleHF);
comptHF=HRAF_v*cos(DiffHF*pi/180);
comptxHF=comptHF*cos((282-270)*pi/180)*1000;
comptyHF=comptHF*sin((282-270)*pi/180)*-1*1000;
end;

if mogix>=588221.7342;
    TangleHS=90-HSangle;
elseif mogix<=588221.7342;
    TangleHS=270-HSangle;
end;
if mogix>=588221.7342 && TangleHS>-12;
DiffHS=abs(282-TangleHS);
comptHS=HRAS_v*cos(DiffHS*pi/180);
comptxHS=comptHS*cos((282-270)*pi/180)*-1*1000;
comptyHS=comptHS*sin((282-270)*pi/180)*1000;
else
DiffHS=abs(282-TangleHS);
comptHS=HRAS_v*cos(DiffHS*pi/180);
comptxHS=comptHS*cos((282-270)*pi/180)*1000;
comptyHS=comptHS*sin((282-270)*pi/180)*-1*1000;
end;

if mogix>=588221.7342;
    TangleSA=90-SAangle;
elseif mogix<=588221.7342;
    TangleSA=270-SAangle;
end;
if mogix>=588221.7342 && TangleSA>-12;
DiffSA=abs(282-TangleSA);
comptSA=SATU_v*cos(DiffSA*pi/180);
comptxSA=comptSA*cos((282-270)*pi/180)*-1*1000;
comptySA=comptSA*sin((282-270)*pi/180)*1000;
else
DiffSA=abs(282-TangleSA);
comptSA=SATU_v*cos(DiffSA*pi/180);
```

```
comptxSA=comptSA*cos((282-270)*pi/180)*1000;
comptySA=comptSA*sin((282-270)*pi/180)*-1*1000;
end;

% Table of components of the horizontal velocities parallel to plate
% spreading
TOTAL_Torf=[comptxB,comptyB;comptxL,comptyL;comptxHF,comptyHF;comptxHS,co
mptyHS;comptxLA,comptyLA;comptxSA,comptySA];
```

APPENDIX 6: Response due to Katla Mogi source between 1999 and 2004

```
function [TOTAL,TOTALv,TOTAL_K]=Mogi_Katla(VCh_Katla,dpth_Katla);

% Program written by: Stephanie Scheiber
% Date: 2007-2008
% Input and output values: Volume change (VCh_Kalta) and depth
% (dpth_Katla) of Hekla source; Displacement (TOTAL) and rate of
% deformation at each site (TOTALv and TOTAL_K, horizontal deformation is
% the component parallel to spreading (N78W))
% Reference: Mogi, K. (1958). "Relations between the eruptions of various
% volcanoes and the deformations of the ground surfaces around them."Bull
% of Earthquake Research Institute 36: 99-134.
% Description: Horizontal and vertical displacements and rates (for 1999-
% 2004) over a Mogi source

% User inputted values
VChange=VCh_Katla; % Volume Change (km3)
depth=dpth_Katla; % Chamber depth (km)
rdist=108; % Length of grid area (km)
sspace=200; % Grid spacing (km)

% Converting from kilometres to metres
depth2 = depth*10^3;
VChange2 = VChange*10^9;
rdist2 = rdist*10^3;

% MESHGRID generates X and Y matrices for the grid area
[x,y]=meshgrid((-1*rdist2/2):sspace:(rdist2/2));

% Radial Distance
r = sqrt(x.^2+y.^2);

% Vertical displacement due to a Mogi source
const = 3/(4*pi);
Uz = (const*VChange2*depth2)./((depth2^2+r.^2).^(3/2));

% Horizontal displacement due to a Mogi source
Ur = (const*VChange2*r)./((depth2^2+r.^2).^(3/2));

% IMPROFILE computes pixel-value cross-sections along a specified line
% segment. Here the profile is taken across the centre of the image
profz = improfile(Uz,[1 (rdist2/sspace)+1],[((rdist2/2)/sspace)+1
(((rdist2/2)-1)/sspace)+1]);
profr = improfile(Ur,[1 (rdist2/sspace)+1],[((rdist2/2)/sspace)+1
(((rdist2/2)-1)/sspace)+1]);
%ratio=abs(profr/profz);

% Site and Mogi source locations in WGS84, UTM Zone 27N
mogix=592587.28;
mogiy=7059739.21;

MAELx=599988.028;
THRAx=588598.9273;
SNAEx=616977.467;

MAELy=7076317.465;
THRAy=7078205.599;
SNAEy=7070212.261;
```

```
% Determining the calculated displacement at each site due to the Mogi
% source deformation.

%UTM co-ordinates are transformed into grid co-ordinates (column and row
values).
MAELcoly=int16(271-((MAELy-mogiy)/200));
MAELrowx=int16(271-((MAELx-mogix)/200));
THRAcoly=int16(271-((THRAy-mogiy)/200));
THRArowx=int16(271-((THRAx-mogix)/200));
SNAEcoly=int16(271-((SNAEy-mogiy)/200));
SNAErowx=int16(271-((SNAEx-mogix)/200));

% Angle between the site and Mogi source relative to an east-west axis
MAELangle=atan((MAELy-mogiy)/(MAELx-mogix))*180/pi;
THRAangle=atan((THRAy-mogiy)/(THRAx-mogix))*180/pi;
SNAEangle=atan((SNAEy-mogiy)/(SNAEx-mogix))*180/pi;

% The horizontal displacement experienced at each site due to Mogi
deformation [in m]
MAEL=Ur(MAELrowx,MAELcoly);
THRA=Ur(THRArowx,THRAcoly);
SNAE=Ur(SNAErowx,SNAEcoly);

% Calculating the x and y components of the horizontal displacements [in
m]
MAELx=MAEL*cos(MAELangle*pi/180);
THRAx=THRA*cos(THRAangle*pi/180)*-1;
SNAEx=SNAE*cos(SNAEangle*pi/180);
MAELy=MAEL*sin(MAELangle*pi/180);
THRAy=THRA*sin(THRAangle*pi/180)*-1;
SNAEy=SNAE*sin(SNAEangle*pi/180);

% Vertical displacements for each site
MAELz=Uz(MAELrowx,MAELcoly);
THRAz=Uz(THRArowx,THRAcoly);
SNAEz=Uz(SNAErowx,SNAEcoly);

% Table of horizontal (x, y, and radial) and vertical displacements
TOTAL=[MAEL,MAELx,MAELy,MAELz;THRA,THRAx,THRAy,THRAz;SNAE,SNAEx,SNAEy,SNA
Ez];

% Calculating the rate of deformation due to the Mogi source for each
site [in m/yr]
% (i.e., Displacement divided by 5 years, 1999-2004)
MAEL_v=MAEL/5;
THRA_v=THRA/5;
SNAE_v=SNAE/5;
MAELz_v=MAELz/5;
THRAz_v=THRAz/5;
SNAEz_v=SNAEz/5;
MAELx_v=MAELx/5;
THRAx_v=THRAx/5;
SNAEx_v=SNAEx/5;
MAELy_v=MAELy/5;
THRAy_v=THRAy/5;
SNAEy_v=SNAEy/5;

% Table of horizontal (x, y, and radial) and vertical velocities
TOTALv=[MAEL_v,MAELx_v,MAELy_v,MAELz_v;THRA_v,THRAx_v,THRAy_v,THRAz_v;SNA
E_v,SNAEx_v,SNAEy_v,SNAEz_v];
```

```
% Calculating the component of the horizontal velocity parallel to
spreading
% (i.e. N78E) for each site [in m/yr]
DiffMAEL=abs(282-(360+(90-MAELangle)));
comptMAEL=MAEL_v*cos(DiffMAEL*pi/180);
comptxMAEL=comptMAEL*cos((282-270)*pi/180)*-1*1000;
comptyMAEL=comptMAEL*sin((282-270)*pi/180)*1000;

DiffTHRA=abs(282-(360+(90-THRAangle)));
comptTHRA=THRA_v*cos(DiffTHRA*pi/180);
comptxTHRA=comptTHRA*cos((282-270)*pi/180)*1000;
comptyTHRA=comptTHRA*sin((282-270)*pi/180)*-1*1000;

DiffSNAE=abs(282-(360+(90-SNAEangle)));
comptSNAE=SNAE_v*cos(DiffSNAE*pi/180);
comptxSNAE=comptSNAE*cos((282-270)*pi/180)*-1*1000;
comptySNAE=comptSNAE*sin((282-270)*pi/180)*1000;

% Table of components of the horizontal velocities parallel to plate
% spreading
TOTAL_K=[comptxMAEL,comptyMAEL;comptxTHRA,comptyTHRA;comptxSNAE,comptySNA
E];

% Generating vectors that will be used for plotting profile and 2-D
images
x2 = [(-1*rdist2/2):sspace:((rdist2/2)-1)];
y2 = [(-1*rdist2/2):sspace:((rdist2/2)-1)];

figure(1); % Vertical Displacement
% A plot of the above-mentioned profile across the centre of the image:
subplot(3,1,1); plot(x2,profz); axis tight; xlabel('x'); ylabel('Vert
Disp (m)'); title('Vertical Displacement over Mogi Source');
% A 2-D image of the data:
subplot(3,1,2); imagesc(x2,y2,Uz), colorbar; axis tight; axis equal;
xlabel('x'); ylabel('y');
% A 3-D image of the data:
subplot(3,1,3); mesh(x,y,Uz); xlabel('x'); ylabel('y'); zlabel('Vert Disp
(m)');

figure(2); % Horizontal Displacement
% A plot of the above-mentioned profile across the centre of the image:
subplot(3,1,2); plot(x2,profr); axis tight; xlabel('x'); ylabel('Horiz
Disp (m)'); title('Horizontal Displacement over Mogi Source');
% A 2-D image of the data:
subplot(3,1,2); imagesc(x2,y2,Ur), colorbar; axis tight; axis equal;
xlabel('x'); ylabel('y');
% A 3-D image of the data:
subplot(3,1,3); mesh(x,y,Ur); xlabel('x'); ylabel('y'); zlabel('Horiz
Disp (m)');
```

APPENDIX 7: Determining best-fit model to 1994-2003 and 2001-2006 GPS-derived velocities along profile 1

```
function [chi95Pd,chi95Sd,param1]=P1_depth_ext;

% Program written by: Stephanie Scheiber
% Date: 2007-2008
% Input and output values: 95% confidence level for model fit to 1994-
% 2003 dataset along profile 1 (chi95d) and 2001-2006 dataset along
% profile 1 (chi95Sd); Best-fit model parameters (param1)
% Description: Modelling 1994-2003 and 2001-2006 GPS-derived site
% velocities. Components of modelling:
% 1) Mid-Atlantic Ridge - Tensile fault (Okada, 1985)
% 2) Hekla - Spherical source (Mogi, 1958) (at depth 11 km (Sturkell et
% al. (2006)), experiencing volume change determined from "dry-tilt"
% data)
% 3) Torfajokull - Spherical source (Mogi, 1958) (location determined
% from area of maximum subsidence on 1993-2000 InSAR image)
% In this program locking depth and extension rate is varied
% independently while holding horizontal the x location of the dyke
% constant

% User inputted values
% Dyke parameters
a=2; % horizontal shift of dyke
b=-3; % vertical shift of dyke   - P1

% Hekla parameters (2001-2006) - VChange and depth
dpth1=11;
VCh1=0.04;
VCh3=0.06;
VCh4=VCh3;
VCh5=VCh1;

% Hekla parameters (1994-2003) - VChange and depth
VCh94_03=0.03;
dpth94_03=11;

% Preallocating matrices to their maximum possible size to save
computation
% time
g=25; % same as v below
h=25; % same as w below
isakMr=zeros(g,h);
isakMx=zeros(g,h);
isakMy=zeros(g,h);
VALAMr=zeros(g,h);
VALAMx=zeros(g,h);
VALAMy=zeros(g,h);
D353Mr=zeros(g,h);
D353Mx=zeros(g,h);
D353My=zeros(g,h);
krokMr=zeros(g,h);
krokMx=zeros(g,h);
krokMy=zeros(g,h);
D356Mr=zeros(g,h);
D356Mx=zeros(g,h);
D356My=zeros(g,h);
D359Mr=zeros(g,h);
D359Mx=zeros(g,h);
D359My=zeros(g,h);
```

```
D361Mr=zeros(g,h);
D361Mx=zeros(g,h);
D361My=zeros(g,h);
domaMr=zeros(g,h);
domaMx=zeros(g,h);
domaMy=zeros(g,h);
frosMr=zeros(g,h);
frosMx=zeros(g,h);
frosMy=zeros(g,h);
lahrMr=zeros(g,h);
lahrMx=zeros(g,h);
lahrMy=zeros(g,h);
D369Mr=zeros(g,h);
D369Mx=zeros(g,h);
D369My=zeros(g,h);
D371Mr=zeros(g,h);
D371Mx=zeros(g,h);
D371My=zeros(g,h);
D372Mr=zeros(g,h);
D372Mx=zeros(g,h);
D372My=zeros(g,h);
GALTMr=zeros(g,h);
GALTMx=zeros(g,h);
GALTMy=zeros(g,h);
chiir=zeros(g,h);
chiIr=zeros(g,h);
chiVr=zeros(g,h);
chiD3r=zeros(g,h);
chikr=zeros(g,h);
chiKr=zeros(g,h);
chiD6r=zeros(g,h);
chiD9r=zeros(g,h);
chiD1r=zeros(g,h);
chidr=zeros(g,h);
chifr=zeros(g,h);
chiD4r=zeros(g,h);
chilhr=zeros(g,h);
chiD5r=zeros(g,h);
chiD69r=zeros(g,h);
chiD71r=zeros(g,h);
chiD2r=zeros(g,h);
chiGr=zeros(g,h);
chi1P=zeros(g,h);
chi1S=zeros(g,h);
ext2=zeros(g,h);
dep2=zeros(g,h);
min1P=zeros(g,h);
min1S=zeros(g,h);

% Hekla Correction (2000-2006)
[TOTAL1]=Mogi_Hekla_01_06(VCh1,dpth1,4.95); % For site KROK
%[TOTAL2]=Mogi_Hekla_01_06(VCh2,dpth1,6.43); % THRA
[TOTAL3]=Mogi_Hekla_01_06(VCh3,dpth1,5.93); % FROS and HRAF
[TOTAL4]=Mogi_Hekla_01_06(VCh4,dpth1,5.93); % ISAK
[TOTAL5]=Mogi_Hekla_01_06(VCh5,dpth1,4.95); %
BLAU,DOMA,HRAS,KGIL,KKLO,LIHO,LAUF,LAHR,SATU,SNAE,THVE


% Hekla Correction (1994-2003)
[TOTAL9403]=Mogi_Hekla_94_03(VCh94_03,dpth94_03);


% GPS-derived horizontal velocities
%% Profile 1
% 2001-2006 dataset(x and y component of 2001-2006 velocity component
```

```
% parallel to spreading direction)
isakx=-15.86059145;
ix=isakx-TOTAL4(1,1); % Removing the effect due to Hekla inflation
krokx=-6.991547449;
kx=krokx-TOTAL1(2,1);
domax=-6.996722031;
dx=domax-TOTAL5(4,1);
frosx=-5.2505;
fx=frosx-TOTAL3(5,1);
lahrx=-5.934617716;
lhx=lahrx-TOTAL5(6,1);
isaky=3.371272785;
iy=isaky-TOTAL4(1,2);
kroky=1.486099287;
ky=kroky-TOTAL1(2,2);
domay=1.487199178;
dy=domay-TOTAL5(4,2);
frosy=1.116;
fy=frosy-TOTAL3(5,2);
lahry=1.261441936;
lhy=lahry-TOTAL5(6,2);
isakO=sqrt(ix^2+iy^2); % Calculating the overall velocity value
krokO=sqrt(kx^2+ky^2);
domaO=sqrt(dx^2+dy^2);
frosO=sqrt(fx^2+fy^2);
lahrO=sqrt(lhx^2+lhy^2);

% 1994-2003 dataset (LaFemina et al, 2005)
ISAKx=-12.59786657;
Ix=ISAKx-TOTAL9403(5,1);  % Removing the effect due to Hekla inflation
VALAx=-9.957499615;
Vx=VALAx-TOTAL9403(6,1);
D353x=-9.312901047;
D3x=D353x-TOTAL9403(1,1);
KROKx=-8.553359872;
Kx=KROKx-TOTAL9403(7,1);
D356x=-7.836192691;
D6x=D356x-TOTAL9403(2,1);
D359x=-8.214009685;
D9x=D359x-TOTAL9403(3,1);
D361x=-8.288148749;
D1x=D361x-TOTAL9403(4,1);
D364x=-7.195068376;
D4x=D364x-TOTAL9403(8,1);
D365x=-6.848270732;
D5x=D365x-TOTAL9403(9,1);
ISAKy=2.677759202;
Iy=ISAKy-TOTAL9403(5,2);
VALAy=2.116531881;
Vy=VALAy-TOTAL9403(6,2);
D353y=1.979518226;
D3y=D353y-TOTAL9403(1,2);
KROKy=1.818072765;
Ky=KROKy-TOTAL9403(7,2);
D356y=1.665634175;
D6y=D356y-TOTAL9403(2,2);
D359y=1.745941656;
D9y=D359y-TOTAL9403(3,2);
D361y=1.761700401;
D1y=D361y-TOTAL9403(4,2);
D364y=1.529358995;
D4y=D364y-TOTAL9403(8,2);
D365y=1.45564488;
D5y=D365y-TOTAL9403(9,2);
ISAKO=sqrt(Ix^2+Iy^2); % Calculating the overall velocity value
```

```
VALAO=sqrt(Vx^2+Vy^2);
D353O=sqrt(D3x^2+D3y^2);
KROKO=sqrt(Kx^2+Ky^2);
D356O=sqrt(D6x^2+D6y^2);
D359O=sqrt(D9x^2+D9y^2);
D361O=sqrt(D1x^2+D1y^2);
D364O=sqrt(D4x^2+D4y^2);
D365O=sqrt(D5x^2+D5y^2);
D369O=(2.85548062); % No correction is needed at these sites due to Hekla
inflation due to distance from source
D371O=(3.073041005);
D372O=(3.392189323);
GALTO=(4.568711674);

 % Calculating the Chi-squared for each site
ISAKerrx=0.62; % uncertainty in east velocity value for site
VALAerrx=1.81;
D353errx=0.81;
KROKerrx=0.91;
D356errx=0.93;
D359errx=0.62;
D361errx=0.62;
D364errx=0.91;
D365errx=2.1;
D369errx=1.11;
D371errx=0.64;
D372errx=1.11;
GALTerrx=1.22;
isakerrx=0.25;
krokerrx=0.71;
domaerrx=2.3;
froserrx=2;
lahrerrx=0.71;

ISAKerry=0.46;% uncertainty in north velocity value for site
VALAerry=1.32;
D353erry=0.64;
KROKerry=0.83;
D356erry=0.61;
D359erry=0.46;
D361erry=0.55;
D364erry=0.46;
D365erry=1.52;
D369erry=0.37;
D371erry=0.61;
D372erry=0.83;
GALTerry=0.52;
isakerry=0.16;
krokerry=0.64;
domaerry=1.71;
froserry=1.61;
lahrerry=0.55;

ISAKerrr=sqrt(ISAKerrx^2+ISAKerry^2); % Overall error for each site
VALAerrr=sqrt(VALAerrx^2+VALAerry^2);
D353errr=sqrt(D353errx^2+D353erry^2);
KROKerrr=sqrt(KROKerrx^2+KROKerry^2);
D356errr=sqrt(D356errx^2+D356erry^2);
D359errr=sqrt(D359errx^2+D359erry^2);
D361errr=sqrt(D361errx^2+D361erry^2);
D364errr=sqrt(D364errx^2+D364erry^2);
D365errr=sqrt(D365errx^2+D365erry^2);
D369errr=sqrt(D369errx^2+D369erry^2);
D371errr=sqrt(D371errx^2+D371erry^2);
D372errr=sqrt(D372errx^2+D372erry^2);
```

```
GALTerrr=sqrt(GALTerrx^2+GALTerry^2);
isakerrr=sqrt(isakerrx^2+isakerry^2);
krokerrr=sqrt(krokerrx^2+krokerry^2);
domaerrr=sqrt(domaerrx^2+domaerry^2);
froserrr=sqrt(froserrx^2+froserry^2);
lahrerrr=sqrt(lahrerrx^2+lahrerry^2);
%_____________________________________________________________________________
_
% Ridge parameters - Profile 1

for v=1:25; % extension
    for w=1:25; % depth
extension1=0+v; % [in mm]
depth1=0+w; % [in km]

[profUx1,profUy1,profz1,profr1]=Dyke_Model_red(extension1,depth1);
Ux1=profUy1; % Swop because of matlab axes system
Uy1=profUx1;
% Rotation of the x and y components of displacement in line with the
plane
% spreading direction (N78W)
Ux_rot1=(Ux1*cos(12*pi/180))+(Uy1*sin(12*pi/180));
Uy_rot1=(-1*Ux1*sin(12*pi/180))+(Uy1*cos(12*pi/180));
maxUy1=max(Uy_rot1);
maxUx1=min(Ux_rot1);
Ux_arct1=Ux_rot1+maxUx1; % Converting from a ridge-centred reference from
to stable Eurasia frame
Uy_arct1=Uy_rot1+maxUy1;
Ur_arct1=(sqrt(Ux_arct1.^2+Uy_arct1.^2)*1000)+b; % Plate spreading model
relative to stable Eu

% Modelled plate spreading value at each site
% Profile 1 - x values for each site (relative to 500 km long dyke
profile)
isakX=212+a;
VALAX=225+a;
D353X=227+a;
krokX=231+a;
D356X=237+a;
D359X=240+a;
D361X=245+a;
domaX=246+a;
frosX=251+a;
lahrX=254+a;
D369X=266+a;
D371X=271+a;
D372X=276+a;
GALTX=284+a;

% Modelled plate spreading value at each site
isakMr(v,w)=Ur_arct1(isakX,1);
isakMx(v,w)=isakMr(v,w)*cos(12*pi/180)*-1;
isakMy(v,w)=isakMr(v,w)*sin(12*pi/180);
VALAMr(v,w)=Ur_arct1(VALAX,1);
VALAMx(v,w)=VALAMr(v,w)*cos(12*pi/180)*-1;
VALAMy(v,w)=VALAMr(v,w)*sin(12*pi/180);
D353Mr(v,w)=Ur_arct1(D353X,1);
D353Mx(v,w)=D353Mr(v,w)*cos(12*pi/180)*-1;
D353My(v,w)=D353Mr(v,w)*sin(12*pi/180);
krokMr(v,w)=Ur_arct1(krokX,1);
krokMx(v,w)=krokMr(v,w)*cos(12*pi/180)*-1;
krokMy(v,w)=krokMr(v,w)*sin(12*pi/180);
D356Mr(v,w)=Ur_arct1(D356X,1);
D356Mx(v,w)=D356Mr(v,w)*cos(12*pi/180)*-1;
D356My(v,w)=D356Mr(v,w)*sin(12*pi/180);
```

```
D359Mr(v,w)=Ur_arct1(D359X,1);
D359Mx(v,w)=D359Mr(v,w)*cos(12*pi/180)*-1;
D359My(v,w)=D359Mr(v,w)*sin(12*pi/180);
D361Mr(v,w)=Ur_arct1(D361X,1);
D361Mx(v,w)=D361Mr(v,w)*cos(12*pi/180)*-1;
D361My(v,w)=D361Mr(v,w)*sin(12*pi/180);
domaMr(v,w)=Ur_arct1(domaX,1);
domaMx(v,w)=domaMr(v,w)*cos(12*pi/180)*-1;
domaMy(v,w)=domaMr(v,w)*sin(12*pi/180);
frosMr(v,w)=Ur_arct1(frosX,1);
frosMx(v,w)=frosMr(v,w)*cos(12*pi/180)*-1;
frosMy(v,w)=frosMr(v,w)*sin(12*pi/180);
lahrMr(v,w)=Ur_arct1(lahrX,1);
lahrMx(v,w)=lahrMr(v,w)*cos(12*pi/180)*-1;
lahrMy(v,w)=lahrMr(v,w)*sin(12*pi/180);
D369Mr(v,w)=Ur_arct1(D369X,1);
D369Mx(v,w)=D369Mr(v,w)*cos(12*pi/180)*-1;
D369My(v,w)=D369Mr(v,w)*sin(12*pi/180);
D371Mr(v,w)=Ur_arct1(D371X,1);
D371Mx(v,w)=D371Mr(v,w)*cos(12*pi/180)*-1;
D371My(v,w)=D371Mr(v,w)*sin(12*pi/180);
D372Mr(v,w)=Ur_arct1(D372X,1);
D372Mx(v,w)=D372Mr(v,w)*cos(12*pi/180)*-1;
D372My(v,w)=D372Mr(v,w)*sin(12*pi/180);
GALTMr(v,w)=Ur_arct1(GALTX,1);
GALTMx(v,w)=GALTMr(v,w)*cos(12*pi/180)*-1;
GALTMy(v,w)=GALTMr(v,w)*sin(12*pi/180);

% Chi-squared values
%% 1994-2003 data
chiIr(v,w)=(isakMr(v,w)-ISAKO).^2/(ISAKerrr^2);
chiVr(v,w)=(VALAMr(v,w)-VALAO).^2/(VALAerrr^2);
chiD3r(v,w)=(D353Mr(v,w)-D353O).^2/(D353errr^2);
chiKr(v,w)=(krokMr(v,w)-KROKO).^2/(KROKerrr^2);
chiD6r(v,w)=(D356Mr(v,w)-D356O).^2/(D356errr^2);
chiD9r(v,w)=(D359Mr(v,w)-D359O).^2/(D359errr^2);
chiD1r(v,w)=(D361Mr(v,w)-D361O).^2/(D361errr^2);
chiD4r(v,w)=(frosMr(v,w)-D364O).^2/(D364errr^2);
chiD5r(v,w)=(lahrMr(v,w)-D365O).^2/(D365errr^2);
chiD69r(v,w)=(D369Mr(v,w)-D369O).^2/(D369errr^2);
chiD71r(v,w)=(D371Mr(v,w)-D371O).^2/(D371errr^2);
chiD2r(v,w)=(D372Mr(v,w)-D372O).^2/(D372errr^2);
chiGr(v,w)=(GALTMr(v,w)-GALTO).^2/(GALTerrr^2);

%% 2001-2006 data
chiir(v,w)=(isakMr(v,w)-isakO).^2/(isakerrr^2);
chikr(v,w)=(krokMr(v,w)-krokO).^2/(krokerrr^2);
chidr(v,w)=(domaMr(v,w)-domaO).^2/(domaerrr^2);
chifr(v,w)=(frosMr(v,w)-frosO).^2/(froserrr^2);
chilhr(v,w)=(lahrMr(v,w)-lahrO).^2/(lahrerrr^2);

% Overall chi-squared value
chi1P(v,w)=chiIr(v,w)+chiVr(v,w)+chiD3r(v,w)+chiKr(v,w)+chiD6r(v,w)+chiD9
r(v,w)+chiD1r(v,w)+chiD4r(v,w)+chiD5r(v,w)+chiD69r(v,w)+chiD71r(v,w)+chiD
2r(v,w)+chiGr(v,w);
chi1S(v,w)=chiir(v,w)+chikr(v,w)+chidr(v,w)+chifr(v,w)+chilhr(v,w);

    end;
end;


% Determining model parameters for minimum chi-squared model
min1P20=min(min(chi1P));
min1S20=min(min(chi1S));
```

```
[y1P,x1P]=find(chi1P==min1P20);
[y1S,x1S]=find(chi1S==min1S20);
x1P20=0+x1P;      % depth
y1P20=0+y1P;      % extension
x1S20=0+x1S;
y1S20=0+y1S;

% F test and 95% confidence level
% NP=13; % Number of data points
% NS=5;
% vP=2; % Number adjustable parameters (Dyke - rate and depth)
% vS=2;
FP=2.94; % F value for degrees of freedom (11,11) for probability of 0.05
FS=19.2; % F value for degrees of freedom (3,3) for probability of 0.05

% For chi-squared versus depth plots
chi1Pd=interp(chi1P(y1P,:),100); % depth
chi1Sd=interp(chi1S(y1S,:),100);
chi95Pd=FP*(min1P20); % 95% confidence interval
chi95Sd=FS*(min1S20);
% Determining model parameters at which the 95% confidence level
intersects
% the chi-squared curves. These values provide a measure of the
uncertainty
% level for a parameters. NB! The current value of 0.1 subtracted from
the
% 95% confidence values can be varied in order to determine a x and y
value
[y95Pd,x95Pd]=find((chi95Pd-0.05)<chi1Pd & chi1Pd<(chi95Pd+0.05));
[y95Sd,x95Sd]=find((chi95Sd-0.5)<chi1Sd & chi1Sd<(chi95Sd+0.5));
x95Pd=1+((x95Pd)/100);
x95Sd=1+((x95Sd)/100);

% For chi-squared versus extension plots
chi1Pe=interp(chi1P(:,x1P),100); % extension
chi1Se=interp(chi1S(:,x1S),100);
chi95Pe=FP*(min1P20);
chi95Se=FS*(min1S20);
% NB! The current value of 0.1 subtracted from the 95% confidence values
% can be varied in order to determine a x and y value
[y95Pe,x95Pe]=find((chi95Pe-0.1)<chi1Pe & chi1Pe<(chi95Pe+0.1));
[y95Se,x95Se]=find((chi95Se-0.5)<chi1Se & chi1Se<(chi95Se+0.5));
x95Pe=1+((y95Pe)/100);
x95Se=1+((y95Se)/100);

% Parameter uncertainties
%Pem=y1P20-x95Pe(1,1);
%Pep=x95Pe(2,1)-y1P20;
Sem=y1S20-x95Se(1,1);
Sep=x95Se(2,1)-y1S20;
%Pdm=x1P20-x95Pd(1,1);
%Pdp=x95Pd(1,2)-x1P20;
Sdm=x1S20-x95Sd(1,1);
Sdp=x95Sd(1,2)-x1S20;

% Table of best-fit models, chi-squared values and uncertainties
%param1=[y1P20,Pem,Pep,x1P20,Pdm,Pdp,min1P20;y1S20,Sem,Sep,x1S20,Sdm,Sdp,
min1S20];
param1=[y1P20,0,0,x1P20,0,0,min1P20;y1S20,Sem,Sep,x1S20,Sdm,Sdp,min1S20];


% Plot of chi-sq versus depth for different extension rates
for e=1:25; % v
```

```
ext1=0+e; % extension [in mm]
min1P(e,1)=min(chi1P(e,:)); % minimum chi-squared values
min1S(e,1)=min(chi1S(e,:));
min1P2=min1P(e,1);
min1S2=min1S(e,1);
[y1P,x1P]=find(chi1P==min1P2); % best-fit model parameters for minimum
chi-squared value
[y1S,x1S]=find(chi1S==min1S2);
x1P=0+x1P; % best-fit locking depth
y1P=min1P2;  % minimum chi-squared values
x1S=0+x1S;
y1S=min1S2;

% 1994-2003 dataset
figure(1); subplot(5,5,e); hold on; plot(1:25,chi1P(e,:),'b');
title(['Extension Rate:',num2str(ext1),'mm/yr'],'FontWeight','bold');
xlabel('depth (km)'); ylabel('\chi^2','Rotation',360);axis([0 25 0 100])
plot(x1P,y1P,'pk');text(x1P+1,y1P,['(',num2str(x1P),',',num2str(min1P2,'%
3.2f'),')']);
% 95% confidence level is plotted and the x values at the intersection
with the curve
%if ext1==y1P20; line(1:25,chi95Pd,'LineStyle','-');
line(x95Pd(1,1),1:chi95Pd);
line(x95Pd(1,2),1:chi95Pd);end;%plot(x95P,[:],'pr');

% 2001-2006 dataset
figure(2); subplot(5,5,e); hold on; plot(1:25,chi1S(e,:),'r');
title(['Extension
Rate:',num2str(ext1),'mm/yr'],'FontWeight','bold');xlabel('depth (km)');
ylabel('\chi^2','Rotation',360);axis([0 25 0 50])
plot(x1S,y1S,'pk');text(x1S+1,y1S,['(',num2str(x1S),',',num2str(min1S2,'%
3.2f'),')']);
% 95% confidence level is plotted and the x values at the intersection
with the curve
if ext1==y1S20; line(1:25,chi95Sd,'LineStyle','-');
line(x95Sd(1,1),1:chi95Sd); line(x95Sd(1,2),1:chi95Sd);
end;%plot(x95S,[:],'pr');

end;


% Plot of chi-sq versus extension rate for different depths
for f=1:25; % v

dep1=0+f; % locking depth [in km]
min1P2(1,f)=min(chi1P(:,f)); % minimum chi-squared values
min1S2(1,f)=min(chi1S(:,f));
min1P3=min1P2(1,f);
min1S3=min1S2(1,f);
[y1P2,x1P2]=find(chi1P==min1P3);% best-fit model parameters for minimum
chi-squared value
[y1S2,x1S2]=find(chi1S==min1S3);
x1P2=0+y1P2; % best-fit extension rate
y1P2=min1P3; % minimum chi-squared values
x1S2=0+y1S2;
y1S2=min1S3;

% 1994-2003 dataset
figure(3); subplot(5,5,f); hold on; plot(1:25,chi1P(:,f),'b');
title(['Depth:',num2str(dep1),'km'],'FontWeight','bold');xlabel('Rate
(mm/yr)'); ylabel('\chi^2','Rotation',360);axis([0 25 0 100])
plot(x1P2,y1P2,'pk');text(x1P2+1,y1P2,['(',num2str(x1P2),',',num2str(min1
P3,'%3.2f'),')']);
```

```
% 95% confidence level is plotted and the x values at the intersection
with the curve
%if dep1==x1P20; line(1:25,chi95Pe,'LineStyle','-');
line(x95Pe(1,1),1:chi95Pe); line(x95Pe(2,1),1:chi95Pe);end;

% 2001-2006 dataset
figure(4); subplot(5,5,f); hold on; plot(1:25,chi1S(:,f),'r');
title(['Depth:',num2str(dep1),'km'],'FontWeight','bold');xlabel('Rate
(mm/yr)'); ylabel('\chi^2','Rotation',360);axis([0 25 0 50])
plot(x1S2,y1S2,'pk');text(x1S2+1,y1S2,['(',num2str(x1S2),',',num2str(min1
S3,'%3.2f'),')']);
% 95% confidence level is plotted and the x values at the intersection
with the curve
if dep1==x1S20; line(1:25,chi95Se,'LineStyle','-');
line(x95Se(1,1),1:chi95Se); line(x95Se(2,1),1:chi95Se);end;

end;

for e=1:25;
ext2(1,e)=0+e;
dep2(1,e)=0+e;
end;

% Correlation plot of extension rate versus locking depth
% 1994-2003 dataset
figure(5);
subplot(2,1,1);hold on;
% Contour intervals of 40, minimum contour is the 95% confidence level
colormap hot; % or 'cool'
contour(dep2,ext2,chi1P,[chi95Pe chi95Pe+40 chi95Pe+80 chi95Pe+120
chi95Pe+160 chi95Pe+200 chi95Pe+240 chi95Pe+280 chi95Pe+320 chi95Pe+360
chi95Pe+400 chi95Pe+440 chi95Pe+480 chi95Pe+520 chi95Pe+560 chi95Pe+600
chi95Pe+640 chi95Pe+680 chi95Pe+720 chi95Pe+760 chi95Pe+800]);
colorbar;
plot(x1P20,y1P20,'pk');text(x1P20+1,y1P20,num2str(min1P20,'%3.2f'));
axis square;  ylabel('extension (mm/yr)','FontSize',11); xlabel('depth
(km)','FontSize',11);
title('1994-2003 Dataset','FontWeight','bold','FontSize',12)

% 2001-2006 dataset
subplot(2,1,2);hold on;
% Contour intervals of 40, minimum contour is the 95% confidence level
contour(dep2,ext2,chi1S,[chi95Se chi95Se+40 chi95Se+80 chi95Se+120
chi95Se+160 chi95Se+200 chi95Se+240 chi95Se+280 chi95Se+320 chi95Se+360
chi95Se+400 chi95Se+440 chi95Se+480 chi95Se+520 chi95Se+560 chi95Se+600
chi95Se+640 chi95Se+680 chi95Se+720 chi95Se+760 chi95Se+800]);
colorbar;
plot(x1S20,y1S20,'pk');text(x1S20+1,y1S20,num2str(min1S20,'%3.2f'));
axis square;  ylabel('extension (mm/yr)','FontSize',11); xlabel('depth
(km)','FontSize',11);
title('2001-2006 Dataset','FontWeight','bold','FontSize',12)
hold off;
```

APPENDIX 8: Determining best-fit model to 1994-2003 and 2001-2006 GPS-derived velocities along profile 3

```
function [param3,chi95Pd,chi95Sd]=P3_depth_ext;

% Program written by: Stephanie Scheiber
% Date: 2007-2008
% Input and output values: 95% confidence level for model fit to 1994-
% 2003 dataset along profile 3 (chi95d) and 2001-2006 dataset along
% profile 3 (chi95Sd); Best-fit model parameters (param3)
% Description: Modelling 1994-2003 and 2001-2006 GPS-derived site
% velocities. Components of modelling:
% 1) Mid-Atlantic Ridge - Tensile fault (Okada, 1985)
% 2) Hekla - Spherical source (Mogi, 1958) (at depth 11 km (Sturkell et
% al. (2006)), experiencing volume change determined from "dry-tilt"
% data)
% 3) Torfajokull - Spherical source (Mogi, 1958) (location determined
% from area of maximum subsidence on 1993-2000 InSAR image)
% In this program locking depth and extension rate is varied
% independently while holding horizontal the x location of the dyke
% constant

% User inputted values
% Dyke parameters
t=-18; % horizontal shift of dyke
u=0;% vertical shift of dyke   - P3

% Hekla parameters (2001-2006) - VChange and depth
dpth1=11;
VCh1=0.04;
VCh2=0.07;
VCh3=0.06;
VCh4=VCh3;
VCh5=VCh1;

% Hekla parameters (1994-2003) - VChange and depth
VCh94_03=0.03;
dpth94_03=11;

% Torf parameters
VChT=0;
dT=4;
mogx=7500; % m Location of Mogi source - InSAR
mogy=2000; % m

% Preallocating matrices to their maximum possible size to save
computation
% time
g=25; % same as v below
h=25; % same as w below
satuMr=zeros(g,h);
satuMx=zeros(g,h);
satuMy=zeros(g,h);
kkloMr=zeros(g,h);
kkloMx=zeros(g,h);
kkloMy=zeros(g,h);
kgilMr=zeros(g,h);
kgilMx=zeros(g,h);
kgilMy=zeros(g,h);
BULAMr=zeros(g,h);
BULAMx=zeros(g,h);
```

```
BULAMy=zeros(g,h);
SKHRMr=zeros(g,h);
SKHRMx=zeros(g,h);
SKHRMy=zeros(g,h);
PALAMr=zeros(g,h);
PALAMx=zeros(g,h);
PALAMy=zeros(g,h);
thraMr=zeros(g,h);
thraMx=zeros(g,h);
thraMy=zeros(g,h);
MAELMr=zeros(g,h);
MAELMx=zeros(g,h);
MAELMy=zeros(g,h);
snaeMr=zeros(g,h);
snaeMx=zeros(g,h);
snaeMy=zeros(g,h);
ELDHMr=zeros(g,h);
ELDHMx=zeros(g,h);
ELDHMy=zeros(g,h);
chisar=zeros(g,h);
chikkr=zeros(g,h);
chikgr=zeros(g,h);
chiBr=zeros(g,h);
chiSr=zeros(g,h);
chiPr=zeros(g,h);
chitar=zeros(g,h);
chiTAr=zeros(g,h);
chiMr=zeros(g,h);
chisnr=zeros(g,h);
chiSNr=zeros(g,h);
chiEr=zeros(g,h);
chi3P=zeros(g,h);
chi3S=zeros(g,h);
BRSKMr=zeros(g,h);
DROPMr=zeros(g,h);
BRSKMx=zeros(g,h);
BRSKMy=zeros(g,h);
DROPMx=zeros(g,h);
DROPMy=zeros(g,h);
chiSAr=zeros(g,h);
chiKGr=zeros(g,h);
chiBRr=zeros(g,h);
chiDRr=zeros(g,h);

% Hekla Correction (2000-2006)
[TOTAL1]=Mogi_Hekla_01_06(VCh1,dpth1,4.95); % KROK
[TOTAL2]=Mogi_Hekla_01_06(VCh2,dpth1,6.43); % THRA
[TOTAL3]=Mogi_Hekla_01_06(VCh3,dpth1,5.93); % FROS and HRAF
[TOTAL4]=Mogi_Hekla_01_06(VCh4,dpth1,5.93); % ISAK
[TOTAL5]=Mogi_Hekla_01_06(VCh5,dpth1,4.95); %
BLAU,DOMA,HRAS,KGIL,KKLO,LIHO,LAUF,LAHR,SATU,SNAE,THVE

% Hekla Correction (1994-2003)
[TOTAL9403]=Mogi_Hekla_94_03(VCh94_03,dpth94_03);

% Torfajokull Correction
[TOTAL2Torf]=Mogi_Torf(VChT,dT,mogx,mogy);

% MODELLED VALUES for dyke

% GPS-derived horizontal velocities
%% Profile 3
% 2001-2006 dataset(x and y component of 2001-2006 velocity component
% parallel to spreading direction)
```

```
thrax=-2.1506;
tax=thrax-TOTAL2(12,1); % Removing the effect due to Hekla inflation
snaex=0.035448;
thray=0.45712;
tay=thray-TOTAL2(12,2);
snaey=-0.0075348;
thraO=sqrt(tax^2+tay^2);
snaeO=sqrt((snaex^2)+(snaey^2));
satux=-3.557015838;
sax=satux-TOTAL5(11,1)-TOTAL2Torf(6,1);% Removing the effect due to Hekla
and Torfajokull deformation
kklox=-2.827422515;
kkx=kklox-TOTAL5(13,1);
kgilx=-2.472171935;
kgx=kgilx-TOTAL5(14,1);
satuy=0.756067056;
say=satuy-TOTAL5(11,2)-TOTAL2Torf(6,2);
kkloy=0.600987208;
kky=kkloy-TOTAL5(13,2);
kgily=0.525476366;
kgy=kgily-TOTAL5(14,2);
satuO=sqrt(sax^2+say^2); % Calculating the overall velocity value
kkloO=sqrt(kkx^2+kky^2);
kgilO=sqrt(kgx^2+kgy^2);

% 1994-2003 dataset (LaFemina et al, 2005)
SKHRx=-6.985084903;
Sx=SKHRx-TOTAL9403(10,1); % Removing the effect due to Hekla inflation
SKHRy=1.48472563;
Sy=SKHRy-TOTAL9403(10,2);
PALAx=-6.902536196;
Px=PALAx-TOTAL9403(11,1);
PALAy=1.467179361;
Py=PALAy-TOTAL9403(11,2);
SATUx=-5.4345;
SAx=SATUx-TOTAL9403(12,1);
SATUy=1.1551;
SAy=SATUy-TOTAL9403(12,2);
KGILx=-4.0354;
KGx=KGILx-TOTAL9403(13,1);
KGILy=0.85774;
KGy=KGILy-TOTAL9403(13,2);
BRSKx=-3.0889;
BRx=BRSKx-TOTAL9403(14,1);
BRSKy=0.65656;
BRy=BRSKy-TOTAL9403(14,2);
DROPx=-3.9273;
DRx=DROPx-TOTAL9403(15,1);
DROPy=0.83477;
DRy=DROPy-TOTAL9403(15,2);
THRAx=(-5.56628);
TAx=THRAx-TOTAL9403(16,1);
THRAy=1.18315;
TAy=THRAy-TOTAL9403(16,2);
SKHRO=sqrt(Sx^2+Sy^2); % Calculating the overall velocity value
PALAO=sqrt(Px^2+Py^2);
SATUO=sqrt(SAx^2+SAy^2);
KGILO=sqrt(KGx^2+KGy^2);
BRSKO=sqrt(BRx^2+BRy^2);
DROPO=sqrt(DRx^2+DRy^2);
THRAO=sqrt(TAx^2+TAy^2);
BULAO=(0.339096331); % No correction is needed at these sites due to
Hekla inflation due to distance from source
MAELO=(3.343);
SNAEO=(0.448290357);
```

```
ELDHO=(1.207568579);

% Calculating the Chi-squared for each site
SKHRerrx=1.21; % uncertainty in east velocity value for site
PALAerrx=1.12;
THRAerrx=1.02;
MAELerrx=1.02;
SNAEerrx=0.91;
ELDHerrx=0.62;
BULAerrx=1.31;
thraerrx=1.01;
snaeerrx=0.52;
satuerrx=0.71;
kkloerrx=0.62;
kgilerrx=0.62;
SATUerrx=3.51;
KGILerrx=3.9;
BRSKerrx=1.52;
DROPerrx=1.21;

SKHRerry=1.12; % uncertainty in north velocity value for site
PALAerry=0.91;
THRAerry=0.61;
MAELerry=0.81;
SNAEerry=0.83;
ELDHerry=0.45;
BULAerry=0.83;
thraerry=0.73;
snaeerry=0.83;
satuerry=0.55;
kkloerry=0.55;
kgilerry=0.55;
SATUerry=0.81;
KGILerry=1.02;
BRSKerry=0.91;
DROPerry=1.12;

SKHRerrr=sqrt(SKHRerrx^2+SKHRerry^2); % Overall error for each site
PALAerrr=sqrt(PALAerrx^2+PALAerry^2);
THRAerrr=sqrt(THRAerrx^2+THRAerry^2);
MAELerrr=sqrt(MAELerrx^2+MAELerry^2);
SNAEerrr=sqrt(SNAEerrx^2+SNAEerry^2);
ELDHerrr=sqrt(ELDHerrx^2+ELDHerry^2);
BULAerrr=sqrt(BULAerrx^2+BULAerry^2);
thraerrr=sqrt(thraerrx^2+thraerry^2);
snaeerrr=sqrt(snaeerrx^2+snaeerry^2);
satuerrr=sqrt(satuerrx^2+satuerry^2);
kkloerrr=sqrt(kkloerrx^2+kkloerry^2);
kgilerrr=sqrt(kgilerrx^2+kgilerry^2);
SATUerrr=sqrt(SATUerrx^2+SATUerry^2);
KGILerrr=sqrt(KGILerrx^2+KGILerry^2);
BRSKerrr=sqrt(BRSKerrx^2+BRSKerry^2);
DROPerrr=sqrt(DROPerrx^2+DROPerry^2);

%_____________________________________________________________________
_
% Ridge parameters - Profile 3

for e=1:25; % extension
    for f=1:25; % depth
extension3=0+e; % [in mm]
depth3=0+f; % [in km]

[profUx3,profUy3,profz3,profr3]=Dyke_Model_red(extension3,depth3);
```

```
Ux3=profUy3; % Swop because of matlab axes system
Uy3=profUx3;
% Rotation of the x and y components of displacement in line with the
plane
% spreading direction (N78W)
Ux_rot3=(Ux3*cos(12*pi/180))+(Uy3*sin(12*pi/180));
Uy_rot3=(-1*Ux3*sin(12*pi/180))+(Uy3*cos(12*pi/180));
maxUy3=max(Uy_rot3);
maxUx3=min(Ux_rot3);
Ux_arct3=Ux_rot3+maxUx3; % Converting from a ridge-centred reference from
to stable Eurasia frame
Uy_arct3=Uy_rot3+maxUy3;
Ur_arct3=(sqrt(Ux_arct3.^2+Uy_arct3.^2)*1000)+u; % Plate spreading model
relative to stable Eu

% Modelled plate spreading value at each site
% Profile 3 - x values for each site (relative to 500 km long dyke
profile)
SKHRX=232+t;
PALAX=235+t;
thraX=263+t;
MAELX=274+t;
snaeX=294+t;
ELDHX=311+t;
satuX=255+t;
kkloX=265+t;
kgilX=268+t;
BULAX=291+t;
BRSKX=237+t;
DROPX=237+t;

% Modelled plate spreading value at each site
SKHRMr(e,f)=Ur_arct3(SKHRX,1);
SKHRMx(e,f)=SKHRMr(e,f)*cos(12*pi/180)*-1;
SKHRMy(e,f)=SKHRMr(e,f)*sin(12*pi/180);
PALAMr(e,f)=Ur_arct3(PALAX,1);
PALAMx(e,f)=PALAMr(e,f)*cos(12*pi/180)*-1;
PALAMy(e,f)=PALAMr(e,f)*sin(12*pi/180);
thraMr(e,f)=Ur_arct3(thraX,1);
thraMx(e,f)=thraMr(e,f)*cos(12*pi/180)*-1;
thraMy(e,f)=thraMr(e,f)*sin(12*pi/180);
MAELMr(e,f)=Ur_arct3(MAELX,1);
MAELMx(e,f)=MAELMr(e,f)*cos(12*pi/180)*-1;
MAELMy(e,f)=MAELMr(e,f)*sin(12*pi/180);
snaeMr(e,f)=Ur_arct3(snaeX,1);
snaeMx(e,f)=snaeMr(e,f)*cos(12*pi/180)*-1;
snaeMy(e,f)=snaeMr(e,f)*sin(12*pi/180);
ELDHMr(e,f)=Ur_arct3(ELDHX,1);
ELDHMx(e,f)=ELDHMr(e,f)*cos(12*pi/180)*-1;
ELDHMy(e,f)=ELDHMr(e,f)*sin(12*pi/180);
satuMr(e,f)=Ur_arct3(satuX,1);
satuMx(e,f)=satuMr(e,f)*cos(12*pi/180)*-1;
satuMy(e,f)=satuMr(e,f)*sin(12*pi/180);
kkloMr(e,f)=Ur_arct3(kkloX,1);
kkloMx(e,f)=kkloMr(e,f)*cos(12*pi/180)*-1;
kkloMy(e,f)=kkloMr(e,f)*sin(12*pi/180);
kgilMr(e,f)=Ur_arct3(kgilX,1);
kgilMx(e,f)=kgilMr(e,f)*cos(12*pi/180)*-1;
kgilMy(e,f)=kgilMr(e,f)*sin(12*pi/180);
BULAMr(e,f)=Ur_arct3(BULAX,1);
BULAMx(e,f)=BULAMr(e,f)*cos(12*pi/180)*-1;
BULAMy(e,f)=BULAMr(e,f)*sin(12*pi/180);
BRSKMr(e,f)=Ur_arct3(BRSKX,1);
BRSKMx(e,f)=BRSKMr(e,f)*cos(12*pi/180)*-1;
BRSKMy(e,f)=BRSKMr(e,f)*sin(12*pi/180);
```

```
DROPMr(e,f)=Ur_arct3(DROPX,1);
DROPMx(e,f)=DROPMr(e,f)*cos(12*pi/180)*-1;
DROPMy(e,f)=DROPMr(e,f)*sin(12*pi/180);

% Chi-squared values - Profile 3
%% 1994-2003 data
chiSr(e,f)=(SKHRMr(e,f)-SKHRO).^2/(SKHRerrr^2);
chiPr(e,f)=(PALAMr(e,f)-PALAO).^2/(PALAerrr^2);
chiTAr(e,f)=(thraMr(e,f)-THRAO).^2/(THRAerrr^2);
chiMr(e,f)=(MAELMr(e,f)-MAELO).^2/(MAELerrr^2);
chiSNr(e,f)=(snaeMr(e,f)-SNAEO).^2/(SNAEerrr^2);
chiEr(e,f)=(ELDHMr(e,f)-ELDHO).^2/(ELDHerrr^2);
chiBr(e,f)=(BULAMr(e,f)-BULAO).^2/(BULAerrr^2);
chiSAr(e,f)=(satuMr(e,f)-SATUO).^2/(SATUerrr^2);
chiKGr(e,f)=(kgilMr(e,f)-KGILO).^2/(KGILerrr^2);
chiBRr(e,f)=(BRSKMr(e,f)-BRSKO).^2/(BRSKerrr^2);
chiDRr(e,f)=(DROPMr(e,f)-DROPO).^2/(DROPerrr^2);

%% 2001-2006 data
chitar(e,f)=(thraMr(e,f)-thraO).^2/(thraerrr^2);
chisnr(e,f)=(snaeMr(e,f)-snaeO).^2/(snaeerrr^2);
chisar(e,f)=(satuMr(e,f)-satuO).^2/(satuerrr^2);
chikkr(e,f)=(kkloMr(e,f)-kkloO).^2/(kkloerrr^2);
chikgr(e,f)=(kgilMr(e,f)-kgilO).^2/(kgilerrr^2);

% Overall chi-squared value
chi3P(e,f)=chiSr(e,f)+chiPr(e,f)+chiTAr(e,f)+chiMr(e,f)+chiSNr(e,f)+chiEr
(e,f)+chiBr(e,f)+chiSAr(e,f)+chiKGr(e,f)+chiBRr(e,f)+chiDRr(e,f);
chi3S(e,f)=chitar(e,f)+chisnr(e,f)+chisar(e,f)+chikkr(e,f)+chikgr(e,f);

    end;
end;

% Determining model parameters for minimum chi-squared model
min1P30=min(min(chi3P));
min1S30=min(min(chi3S));
[y3P,x3P]=find(chi3P==min1P30);
[y3S,x3S]=find(chi3S==min1S30);
x3P30=0+x3P;     % depth
y3P30=0+y3P;     % extension
x3S30=0+x3S;
y3S30=0+y3S;

% F test and 95% confidence level
% NP=11; % Number of data points
% NS=5;
% vP=2; % Number adjustable parameters (Dyke - rate and depth)
% vS=2;
FP=3.39; % F value for degrees of freedom (9,9) for probability of 0.05
FS=19.2; % F value for degrees of freedom (3,3) for probability of 0.05

% For chi-squared versus depth plots
chi3Pd=interp(chi3P(y3P,:),100); % depth
chi3Sd=interp(chi3S(y3S,:),100);
chi95Pd=FP*(min1P30); % 95% confidence interval
chi95Sd=FS*(min1S30);
% Determining model parameters at which the 95% confidence level
intersects
% the chi-squared curves. These values provide a measure of the
uncertainty
% level for a parameters. NB! The current value of 0.1 subtracted from
the
% 95% confidence values can be varied in order to determine a x and y
value
```

```
[y95Pd,x95Pd]=find((chi95Pd-0.1)<chi3Pd & chi3Pd<(chi95Pd+0.1));
[y95Sd,x95Sd]=find((chi95Sd-0.1)<chi3Sd & chi3Sd<(chi95Sd+0.1));
x95Pd=1+((x95Pd)/100);
x95Sd=1+((x95Sd)/100);

% For chi-squared versus extension plots
chi3Pe=interp(chi3P(:,x3P),100); % extension
chi3Se=interp(chi3S(:,x3S),100);
chi95Pe=FP*(min1P30);
chi95Se=FS*(min1S30);
% NB! The current value of 0.1 subtracted from the 95% confidence values
% can be varied in order to determine a x and y value
[y95Pe,x95Pe]=find((chi95Pe-0.05)<chi3Pe & chi3Pe<(chi95Pe+0.05));
[y95Se,x95Se]=find((chi95Se-0.5)<chi3Se & chi3Se<(chi95Se+0.5));
x95Pe=1+((y95Pe)/100);
x95Se=1+((y95Se)/100);

% Parameter uncertainties
Pem=y3P30-x95Pe(1,1);
Pep=x95Pe(2,1)-y3P30;
Pdm=x3P30-x95Pd(1,1);
Pdp=x95Pd(1,2)-x3P30;
Sem=y3S30-x95Se(1,1);
Sep=x95Se(2,1)-y3S30;
Sdm=x3S30-x95Sd(1,1);
Sdp=x95Sd(1,2)-x3S30;

% Table of best-fit models, chi-squared values and uncertainties
param3=[y3P30,Pem,Pep,x3P30,Pdm,Pdp,min1P30;y3S30,Sem,Sep,x3S30,Sdm,Sdp,m
in1S30];

% Plot of chi-sq versus depth for different extension rates
for v=1:20; % v

ext1=0+v; % extension [in mm]
min1P(v,1)=min(chi3P(v,:)); % minimum chi-squared values
min1S(v,1)=min(chi3S(v,:));
min1P20=min1P(v,1);
min1S20=min1S(v,1);
[y0P,x0P]=find(chi3P==min1P20); % best-fit model parameters for minimum
chi-squared value
[y0S,x0S]=find(chi3S==min1S20);
x1P=0+x0P; % best-fit locking depth
y1P=min1P20;   % minimum chi-squared values
x1S=0+x0S;
y1S=min1S20;

% 1994-2003 dataset
figure(1); subplot(4,5,v); hold on; plot(1:25,chi3P(v,:),'b');
title(['Extension
Rate:',num2str(ext1),'mm/yr'],'FontWeight','bold');xlabel('depth (km)');
ylabel('\chi^2','Rotation',360);axis([0 20 0 50])
plot(x1P,y1P,'pk');text(x1P+1,y1P,['(',num2str(x1P),',',num2str(min1P20,'
%3.2f'),')']); hold off;
% 95% confidence level is plotted and the x values at the intersection
with the curve
if ext1==y3P30; line(1:25,chi95Pd,'LineStyle','-');
line(x95Pd(1,1),1:chi95Pd);
line(x95Pd(1,2),1:chi95Pd);end;%plot(x95P,[:],'pr');

% 2001-2006 dataset
figure(2); subplot(4,5,v); hold on; plot(1:25,chi3S(v,:),'r');
```

```
title(['Extension
Rate:',num2str(ext1),'mm/yr'],'FontWeight','bold');xlabel('depth (km)');
ylabel('\chi^2','Rotation',360);axis([0 20 0 20])
plot(x1S,y1S,'pk');text(x1S+1,y1S,['(',num2str(x1S),',',num2str(min1S20,'
%3.2f'),')']); hold off;
% 95% confidence level is plotted and the x values at the intersection
with the curve
if ext1==y3S30; line(1:25,chi95Sd,'LineStyle','-');
line(x95Sd(1,1),1:chi95Sd); line(x95Sd(1,2),1:chi95Sd);
end;%plot(x95S,[:],'pr');

end;

% Plot of chi-sq versus extension rate for different depths
for w=1:20; % v

dep1=0+w; % locking depth [in km]
min1P2(1,w)=min(chi3P(:,w));% minimum chi-squared values
min1S2(1,w)=min(chi3S(:,w));
min1P3=min1P2(1,w);
min1S3=min1S2(1,w);
[y1P2,x1P2]=find(chi3P==min1P3);% best-fit model parameters for minimum
chi-squared value
[y1S2,x1S2]=find(chi3S==min1S3);
x1P2=0+y1P2;     % best-fit extension rate
y1P2=min1P3;     % minimum chi-squared values
x1S2=0+y1S2;
y1S2=min1S3;

% 1994-2003 dataset
figure(3); subplot(4,5,w); hold on; plot(1:25,chi3P(:,w),'b');
title(['Depth:',num2str(dep1),'km'],'FontWeight','bold');xlabel('Rate
(mm/yr)'); ylabel('\chi^2','Rotation',360);axis([0 20 0 50])
plot(x1P2,y1P2,'pk');text(x1P2+1,y1P2,['(',num2str(x1P2),',',num2str(min1
P3,'%3.2f'),')']); hold off;
% 95% confidence level is plotted and the x values at the intersection
with the curve
if dep1==x3P30; line(1:25,chi95Pe,'LineStyle','-');
line(x95Pe(1,1),1:chi95Pe); line(x95Pe(2,1),1:chi95Pe);end;

% 2001-2006 dataset
figure(4); subplot(4,5,w); hold on; plot(1:25,chi3S(:,w),'r');
title(['Depth:',num2str(dep1),'km'],'FontWeight','bold');xlabel('Rate
(mm/yr)'); ylabel('\chi^2','Rotation',360);axis([0 20 0 50])
plot(x1S2,y1S2,'pk');text(x1S2+1,y1S2,['(',num2str(x1S2),',',num2str(min1
S3,'%3.2f'),')']); hold off;
% 95% confidence level is plotted and the x values at the intersection
with the curve
if dep1==x3S30; line(1:25,chi95Se,'LineStyle','-');
line(x95Se(1,1),1:chi95Se); line(x95Se(2,1),1:chi95Se);end;

end;

for e=1:25;
ext5(1,e)=0+e;
dep5(1,e)=0+e;
end;

% Correlation plot of extension rate versus locking depth
% 1994-2003 dataset
figure(5);
subplot(2,1,1);hold on;
% Contour intervals of 40, minimum contour is the 95% confidence level
```

```
contour(dep5,ext5,chi3P,[chi95Pe chi95Pe+40 chi95Pe+80 chi95Pe+120
chi95Pe+160 chi95Pe+200 chi95Pe+240 chi95Pe+280 chi95Pe+320 chi95Pe+360
chi95Pe+400 chi95Pe+440 chi95Pe+480 chi95Pe+520 chi95Pe+560 chi95Pe+600
chi95Pe+640 chi95Pe+680 chi95Pe+720 chi95Pe+760 chi95Pe+800]);
colormap hot; % or 'cool'
colorbar;
plot(x3P30,y3P30,'pk');text(x3P30+1,y3P30,num2str(min1P30,'%3.2f'));
axis square;  ylabel('extension (mm/yr)','FontSize',11); xlabel('depth
(km)','FontSize',11);
title('1994-2003 Dataset','FontWeight','bold','FontSize',12)
hold off;

% 2001-2006 dataset
subplot(2,1,2);hold on;
% Contour intervals of 40, minimum contour is the 95% confidence level
contour(dep5,ext5,chi3S,[chi95Se chi95Pe+40 chi95Pe+80 chi95Pe+120
chi95Pe+160 chi95Pe+200 chi95Pe+240 chi95Pe+280 chi95Pe+320 chi95Pe+360
chi95Pe+400 chi95Pe+440 chi95Pe+480 chi95Pe+520 chi95Pe+560 chi95Pe+600
chi95Pe+640 chi95Pe+680 chi95Pe+720 chi95Pe+760 chi95Pe+800]);
colorbar;
plot(x3S30,y3S30,'pk');text(x3S30+1,y3S30,num2str(min1S30,'%3.2f'));
axis square;  ylabel('extension (mm/yr)','FontSize',11); xlabel('depth
(km)','FontSize',11);
title('2001-2006 Dataset','FontWeight','bold','FontSize',12)
hold off;
```

APPENDIX 9: Profile plots of the best-fit plate spreading models to the 1994-2003 and 2001-2006 GPS-derived velocities along profile 1, 2 and 3

```
function [chi]=Plate_spreading_profiles;

% Program written by: Stephanie Scheiber
% Date: 2007-2008
% Input and output values: Volume change (VCh01_06) and depth
% (dpth01_06) of Hekla source; Time period over which
% inflation/deflation of Mogi source has occurred (q); Rate of
% deformation at each site (TOTAL0106, horizontal deformation is
% the component parallel to spreading (N78W))

% Description: Modelling 1994-2003 and 2001-2006 GPS-derived site
% velocities. Components of modelling:
% 1) Mid-Atlantic Ridge - Tensile fault (Okada, 1985)
% 2) Hekla - Spherical source (Mogi, 1958) (at depth 11 km
% (Sturkell et al. (2006)),
% experiencing volume change determined from "dry-tilt" data)
% 3) Torfajokull - Spherical source (Mogi, 1958) (location
% determined from area of maximum subsidence on 1993-2000 InSAR
% image)
% 4) Katla - Modelled at spherical source, but effect is removed
% from data, and corrected data used in this program (0.01 km3
% volume change btn 1999 and 2004 at depth of 4.9 km, Sturkell et
% al. (2008))

% Output: chi - chi squared value for each profile, for each
% dataset. Chi-squared value is a measure of goodness-of-fit of a
% model to data

% User inputted values
% Hekla parameters (2000-2006) - VChange and depth
dpth1=11;
VCh1=0.04; % Data collected from Aug 2001, tilt shows 3.7 microrad change
from 01-06
          % BLAU,DOMA,HRAS,ISAK, KGIL,KKLO,KROK,
LIHO,LAUF,LAHR,SATU,SNAE,THVE
VCh2=0.07; % Data collected from April 2000, tilt shows 7.1 microrad
change from 01-06 - THRA
VCh3=0.06; % Data collected from Oct 2000, tilt shows 6.1 microrad change
from 01-06 - FROS and HRAF
VCh4=VCh3;
VCh5=VCh1;

% Hekla parameters (1994-2003) - VChange and depth
VCh94_03=0.03;
dpth94_03=11;

% Torfajokull parameters - VChange and depth and location
VChT=-0.005;
dT=4;
mogx=7500+0.001; % Location of Mogi source - In area of maximum
subsidence seen on 93-00 InSAR [in m]
mogy=2000+0.001; %

% Hekla Correction (2000-2006)
[TOTAL1]=Mogi_Hekla_01_06(VCh1,dpth1,4.95); % For site KROK
[TOTAL2]=Mogi_Hekla_01_06(VCh2,dpth1,6.43); % THRA
[TOTAL3]=Mogi_Hekla_01_06(VCh3,dpth1,5.93); % FROS and HRAF
[TOTAL4]=Mogi_Hekla_01_06(VCh4,dpth1,5.93); % ISAK
```

```
[TOTAL5]=Mogi_Hekla_01_06(VCh5,dpth1,4.95); %
BLAU,DOMA,HRAS,KGIL,KKLO,LIHO,LAUF,LAHR,SATU,SNAE,THVE

% Hekla Correction (1994-2003)
[TOTAL9403]=Mogi_Hekla_94_03(VCh94_03,dpth94_03);

% Torfajokull Correction
[TOTAL2Torf]=Mogi_Torf(VChT,dT,mogx,mogy);

% Modelling of spreading ridge
% Ridge parameters - Profile 1
extension1=10; % in mm
depth1=5; % in km
a1=2; % horizontal shift of dyke
b1=2.4; % vertical shift of dyke

% Ridge parameters - Profile 2
extension2=9; % in mm
depth2=3; % in km
a2=-2; % horizontal shift of dyke
b2=2; % vertical shift of dyke (reference frame shift)

% Ridge parameters - Profile 3
extension3=7; % in mm
depth3=4; % in km
a3=-18; % horizontal shift of dyke
b3=0; % vertical shift of dyke

% Ridge Model for Profile 1
[profUx1,profUy1,profz1,profr1]=Dyke_Model_red(extension1,depth1); %
Response due to tensile fault
Ux1=profUy1; % Swop because of matlab axes system
Uy1=profUx1;
% Rotation of the x and y components of displacement in line with the
plane
% spreading direction (N78W)
Ux_rot1=(Ux1*cos(12*pi/180))+(Uy1*sin(12*pi/180));
Uy_rot1=(-1*Ux1*sin(12*pi/180))+(Uy1*cos(12*pi/180));
maxUy1=max(Uy_rot1);
maxUx1=min(Ux_rot1);
Ux_arct1=Ux_rot1+maxUx1; % Converting from a ridge-centred reference from
to stable Eurasia frame
Uy_arct1=Uy_rot1+maxUy1;
Ur_arct1=(sqrt(Ux_arct1.^2+Uy_arct1.^2)*1000)+b1; % Plate spreading model
relative to stable Eu
x1=1:501; % To plot profile across dyke

% Ridge Model for Profile 2
[profUx2,profUy2,profz2,profr2]=Dyke_Model_red(extension2,depth2);
Ux2=profUy2;
Uy2=profUx2;
Ux_rot2=(Ux2*cos(12*pi/180))+(Uy2*sin(12*pi/180));
Uy_rot2=(-1*Ux2*sin(12*pi/180))+(Uy2*cos(12*pi/180));
maxUy2=max(Uy_rot2);
maxUx2=min(Ux_rot2);
Ux_arct2=Ux_rot2+maxUx2;
Uy_arct2=Uy_rot2+maxUy2;
Ur_arct2=(sqrt(Ux_arct2.^2+Uy_arct2.^2)*1000)+b2;
x2=1:501;

% Ridge Model for Profile 3
[profUx3,profUy3,profz3,profr3]=Dyke_Model_red(extension3,depth3);
Ux3=profUy3;
Uy3=profUx3;
Ux_rot3=(Ux3*cos(12*pi/180))+(Uy3*sin(12*pi/180));
```

```
Uy_rot3=(-1*Ux3*sin(12*pi/180))+(Uy3*cos(12*pi/180));
maxUy3=max(Uy_rot3);
maxUx3=min(Ux_rot3);
Ux_arct3=Ux_rot3+maxUx3;
Uy_arct3=Uy_rot3+maxUy3;
Ur_arct3=(sqrt(Ux_arct3.^2+Uy_arct3.^2)*1000)+b3;
x3=1:501;

% GPS-derived horizontal velocities
%% Profile 1
% 2001-2006 dataset(x and y component of 2001-2006 velocity component
% parallel to spreading direction)
isakx=-15.86059145;
ix=isakx-TOTAL4(1,1); % Removing the effect due to Hekla inflation
krokx=-6.991547449;
kx=krokx-TOTAL1(2,1);
domax=-6.996722031;
dx=domax-TOTAL5(4,1);
frosx=-5.2505;
fx=frosx-TOTAL3(5,1);
lahrx=-5.934617716;
lhx=lahrx-TOTAL5(6,1);
isaky=3.371272785;
iy=isaky-TOTAL4(1,2);
kroky=1.486099287;
ky=kroky-TOTAL1(2,2);
domay=1.487199178;
dy=domay-TOTAL5(4,2);
frosy=1.116;
fy=frosy-TOTAL3(5,2);
lahry=1.261441936;
lhy=lahry-TOTAL5(6,2);
isakO=sqrt(ix^2+iy^2); % Calculating the overall velocity value
krokO=sqrt(kx^2+ky^2);
domaO=sqrt(dx^2+dy^2);
frosO=sqrt(fx^2+fy^2);
lahrO=sqrt(lhx^2+lhy^2);

% 1994-2003 dataset (LaFemina et al, 2005)
ISAKx=-12.59786657;
Ix=ISAKx-TOTAL9403(5,1);  % Removing the effect due to Hekla inflation
VALAx=-9.957499615;
Vx=VALAx-TOTAL9403(6,1);
D353x=-9.312901047;
D3x=D353x-TOTAL9403(1,1);
KROKx=-8.553359872;
Kx=KROKx-TOTAL9403(7,1);
D356x=-7.836192691;
D6x=D356x-TOTAL9403(2,1);
D359x=-8.214009685;
D9x=D359x-TOTAL9403(3,1);
D361x=-8.288148749;
D1x=D361x-TOTAL9403(4,1);
D364x=-7.195068376;
D4x=D364x-TOTAL9403(8,1);
D365x=-6.848270732;
D5x=D365x-TOTAL9403(9,1);
ISAKy=2.677759202;
Iy=ISAKy-TOTAL9403(5,2);
VALAy=2.116531881;
Vy=VALAy-TOTAL9403(6,2);
D353y=1.979518226;
D3y=D353y-TOTAL9403(1,2);
KROKy=1.818072765;
Ky=KROKy-TOTAL9403(7,2);
```

```
D356y=1.665634175;
D6y=D356y-TOTAL9403(2,2);
D359y=1.745941656;
D9y=D359y-TOTAL9403(3,2);
D361y=1.761700401;
D1y=D361y-TOTAL9403(4,2);
D364y=1.529358995;
D4y=D364y-TOTAL9403(8,2);
D365y=1.45564488;
D5y=D365y-TOTAL9403(9,2);
ISAKO=sqrt(Ix^2+Iy^2); % Calculating the overall velocity value
VALAO=sqrt(Vx^2+Vy^2);
D353O=sqrt(D3x^2+D3y^2);
KROKO=sqrt(Kx^2+Ky^2);
D356O=sqrt(D6x^2+D6y^2);
D359O=sqrt(D9x^2+D9y^2);
D361O=sqrt(D1x^2+D1y^2);
D364O=sqrt(D4x^2+D4y^2);
D365O=sqrt(D5x^2+D5y^2);
D369O=(2.85548062); % No correction is needed at these sites due to Hekla
inflation due to distance from source
D371O=(3.073041005);
D372O=(3.392189323);
GALTO=(4.568711674);


%% Profile 2
% 2001-2006 dataset
blaux=-2.103467009;
bx=blaux-TOTAL5(7,1)-TOTAL2Torf(1,1);  % Removing the effect due to Hekla
and Torfajokull deformation
lihox=-4.520953539;
lx=lihox-TOTAL5(3,1)-TOTAL2Torf(2,1);
hrafx=-4.1646;
hfx=hrafx-TOTAL3(8,1)-TOTAL2Torf(3,1);
hrasx=-4.81158949;
hsx=hrasx-TOTAL5(9,1)-TOTAL2Torf(4,1);
thvex=-2.718899161;  % No correction for volcanic deformation is needed
due to distance from sources
blauy=0.447105715;
by=blauy-TOTAL5(7,2)-TOTAL2Torf(1,2);
lihoy=0.96095834;
ly=lihoy-TOTAL5(3,2)-TOTAL2Torf(2,2);
hrafy=0.88522;
hfy=hrafy-TOTAL3(8,2)-TOTAL2Torf(3,2);
hrasy=1.022734918;
hsy=hrasy-TOTAL5(9,2)-TOTAL2Torf(4,2);
thvey=0.577919857;
blauO=sqrt(bx^2+by^2); % Calculating the overall velocity value
lihoO=sqrt(lx^2+ly^2);
hrafO=sqrt(hfx^2+hfy^2);
hrasO=sqrt(hsx^2+hsy^2);
thveO=sqrt((thvex^2)+(thvey^2));

%% Profile 3
% 2001-2006 dataset
thrax=-2.1506;
tax=thrax-TOTAL2(12,1);  % Removing the effect due to Hekla deformation
snaex=0.035448;
thray=0.45712;
tay=thray-TOTAL2(12,2);
snaey=-0.0075348;
thraO=sqrt(tax^2+tay^2);
snaeO=sqrt((snaex^2)+(snaey^2));
satux=-3.557015838;
```

```
sax=satux-TOTAL5(11,1)-TOTAL2Torf(6,1); % Removing the effect due to
Hekla and Torfajokull deformation
kklox=-2.827422515;
kkx=kklox-TOTAL5(13,1);
kgilx=-2.472171935;
kgx=kgilx-TOTAL5(14,1);
satuy=0.756067056;
say=satuy-TOTAL5(11,2)-TOTAL2Torf(6,2);
kkloy=0.600987208;
kky=kkloy-TOTAL5(13,2);
kgily=0.525476366;
kgy=kgily-TOTAL5(14,2);
satuO=sqrt(sax^2+say^2); % Calculating the overall velocity value
kkloO=sqrt(kkx^2+kky^2);
kgilO=sqrt(kgx^2+kgy^2);

% 1994-2003 dataset
SKHRx=-6.985084903;
Sx=SKHRx-TOTAL9403(10,1);  % Removing the effect due to Hekla deformation
SKHRy=1.48472563;
Sy=SKHRy-TOTAL9403(10,2);
PALAx=-6.902536196;
Px=PALAx-TOTAL9403(11,1);
PALAy=1.467179361;
Py=PALAy-TOTAL9403(11,2);
SATUx=-5.4345;
SAx=SATUx-TOTAL9403(12,1);
SATUy=1.1551;
SAy=SATUy-TOTAL9403(12,2);
KGILx=-4.0354;
KGx=KGILx-TOTAL9403(13,1);
KGILy=0.85774;
KGy=KGILy-TOTAL9403(13,2);
BRSKx=-3.0889;
BRx=BRSKx-TOTAL9403(14,1);
BRSKy=0.65656;
BRy=BRSKy-TOTAL9403(14,2);
DROPx=-3.9273;
DRx=DROPx-TOTAL9403(15,1);
DROPy=0.8347;
DRy=DROPy-TOTAL9403(15,2);
THRAx=(-5.56628);
TAx=THRAx-TOTAL9403(16,1);
THRAy=1.18315;
TAy=THRAy-TOTAL9403(16,2);
SKHRO=sqrt(Sx^2+Sy^2); % Calculating the overall velocity value
PALAO=sqrt(Px^2+Py^2);
SATUO=sqrt(SAx^2+SAy^2);
KGILO=sqrt(KGx^2+KGy^2);
BRSKO=sqrt(BRx^2+BRy^2);
DROPO=sqrt(DRx^2+DRy^2);
THRAO=sqrt(TAx^2+TAy^2);
BULAO=(0.339096331); % No correction for volcanic deformation is needed
due to distance from source
MAELO=(3.343);
SNAEO=(0.448290357);
ELDHO=(1.207568579);


% Modelled plate spreading value at each site
% Profile 1 - x values for each site (relative to 500 km long dyke
profile)
isakX=212+a1;
VALAX=225+a1;
D353X=227+a1;
```

```
krokX=231+a1;
D356X=237+a1;
D359X=240+a1;
D361X=245+a1;
domaX=246+a1;
frosX=251+a1;
lahrX=254+a1;
D369X=266+a1;
D371X=271+a1;
D372X=276+a1;
GALTX=284+a1;

% Profile 2- x values
blauX=243+a2;
lihoX=244+a2;
hrafX=249+a2;
hrasX=251+a2;
thveX=278+a2;

% Profile 3 - x values
SKHRX=232+a3;
PALAX=235+a3;
thraX=263+a3;
MAELX=274+a3;
snaeX=294+a3;
ELDHX=311+a3;
satuX=255+a3;
kkloX=265+a3;
kgilX=268+a3;
BULAX=291+a3;
BRSKX=237+a3;
DROPX=237+a3;

% Modelled plate spreading value at each site
%% Profile 1
isakMr =Ur_arct1(isakX,1);
VALAMr =Ur_arct1(VALAX,1);
D353Mr =Ur_arct1(D353X,1);
krokMr =Ur_arct1(krokX,1);
D356Mr =Ur_arct1(D356X,1);
D359Mr =Ur_arct1(D359X,1);
D361Mr =Ur_arct1(D361X,1);
domaMr =Ur_arct1(domaX,1);
frosMr =Ur_arct1(frosX,1);
lahrMr =Ur_arct1(lahrX,1);
D369Mr =Ur_arct1(D369X,1);
D371Mr =Ur_arct1(D371X,1);
D372Mr =Ur_arct1(D372X,1);
GALTMr =Ur_arct1(GALTX,1);

%% Profile 2
blauMr=Ur_arct2(blauX,1);
lihoMr=Ur_arct2(lihoX,1);
hrafMr=Ur_arct2(hrafX,1);
hrasMr =Ur_arct2(hrasX,1);
thveMr =Ur_arct2(thveX,1);

%% Profile 3
satuMr =Ur_arct3(satuX,1);
kkloMr =Ur_arct3(kkloX,1);
kgilMr =Ur_arct3(kgilX,1);
SKHRMr=Ur_arct3(SKHRX,1);
PALAMr=Ur_arct3(PALAX,1);
thraMr=Ur_arct3(thraX,1);
MAELMr=Ur_arct3(MAELX,1);
```

```
snaeMr=Ur_arct3(snaeX,1);
ELDHMr=Ur_arct3(ELDHX,1);
BULAMr =Ur_arct3(BULAX,1);
SATUMr =Ur_arct3(satuX,1);
KGILMr =Ur_arct3(kgilX,1);
BRSKMr =Ur_arct3(BRSKX,1);
DROPMr =Ur_arct3(DROPX,1);

% Calculating the Chi-squared for each site
% Profile 1
ISAKerrx=0.62; % uncertainty in east velocity value for site
VALAerrx=1.81;
D353errx=0.81;
KROKerrx=0.91;
D356errx=0.93;
D359errx=0.62;
D361errx=0.62;
D364errx=0.91;
D365errx=2.1;
D369errx=1.11;
D371errx=0.64;
D372errx=1.11;
GALTerrx=1.22;
isakerrx=0.25;
krokerrx=0.71;
domaerrx=2.3;
froserrx=2;
lahrerrx=0.71;

% Profile 2
blauerrx=0.71;
lihoerrx=0.81;
hraferrx=2.2;
hraserrx=0.62;
thveerrx=0.81;

% Profile 3
SKHRerrx=1.21;
PALAerrx=1.12;
THRAerrx=1.02;
MAELerrx=1.02;
SNAEerrx=0.91;
ELDHerrx=0.62;
BULAerrx=1.31;
thraerrx=1.01;
snaeerrx=0.52;
satuerrx=0.71;
kkloerrx=0.62;
kgilerrx=0.62;
SATUerrx=3.51;
KGILerrx=3.9;
BRSKerrx=1.52;
DROPerrx=1.21;

% Profile 1
ISAKerry=0.46; % uncertainty in north velocity value for site
VALAerry=1.32;
D353erry=0.64;
KROKerry=0.83;
D356erry=0.61;
D359erry=0.46;
D361erry=0.55;
D364erry=0.46;
D365erry=1.52;
D369erry=0.37;
```

```
D371erry=0.61;
D372erry=0.83;
GALTerry=0.52;
isakerry=0.16;
krokerry=0.64;
domaerry=1.71;
froserry=1.61;
lahrerry=0.55;

% Profile 2
blauerry=0.64;
lihoerry=0.64;
hraferry=1.42;
hraserry=0.55;
thveerry=0.64;

% Profile 3
SKHRerry=1.12;
PALAerry=0.91;
THRAerry=0.61;
MAELerry=0.81;
SNAEerry=0.83;
ELDHerry=0.45;
BULAerry=0.83;
thraerry=0.73;
snaeerry=0.83;
satuerry=0.55;
kkloerry=0.55;
kgilerry=0.55;
SATUerry=0.81;
KGILerry=1.02;
BRSKerry=0.91;
DROPerry=1.12;

% Overall error for each site
% Profile 1
ISAKerrr=sqrt(ISAKerrx^2+ISAKerry^2);
VALAerrr=sqrt(VALAerrx^2+VALAerry^2);
D353errr=sqrt(D353errx^2+D353erry^2);
KROKerrr=sqrt(KROKerrx^2+KROKerry^2);
D356errr=sqrt(D356errx^2+D356erry^2);
D359errr=sqrt(D359errx^2+D359erry^2);
D361errr=sqrt(D361errx^2+D361erry^2);
D364errr=sqrt(D364errx^2+D364erry^2);
D365errr=sqrt(D365errx^2+D365erry^2);
D369errr=sqrt(D369errx^2+D369erry^2);
D371errr=sqrt(D371errx^2+D371erry^2);
D372errr=sqrt(D372errx^2+D372erry^2);
GALTerrr=sqrt(GALTerrx^2+GALTerry^2);
isakerrr=sqrt(isakerrx^2+isakerry^2);
krokerrr=sqrt(krokerrx^2+krokerry^2);
domaerrr=sqrt(domaerrx^2+domaerry^2);
froserrr=sqrt(froserrx^2+froserry^2);
lahrerrr=sqrt(lahrerrx^2+lahrerry^2);

% Profile 2
blauerrr=sqrt(blauerrx^2+blauerry^2);
lihoerrr=sqrt(lihoerrx^2+lihoerry^2);
hraferrr=sqrt(hraferrx^2+hraferry^2);
hraserrr=sqrt(hraserrx^2+hraserry^2);
thveerrr=sqrt(thveerrx^2+thveerry^2);

% Profile 3
BULAerrr=sqrt(BULAerrx^2+BULAerry^2);
SKHRerrr=sqrt(SKHRerrx^2+SKHRerry^2);
```

```
PALAerrr=sqrt(PALAerrx^2+PALAerry^2);
THRAerrr=sqrt(THRAerrx^2+THRAerry^2);
MAELerrr=sqrt(MAELerrx^2+MAELerry^2);
SNAEerrr=sqrt(SNAEerrx^2+SNAEerry^2);
ELDHerrr=sqrt(ELDHerrx^2+ELDHerry^2);
thraerrr=sqrt(thraerrx^2+thraerry^2);
snaeerrr=sqrt(snaeerrx^2+snaeerry^2);
satuerrr=sqrt(satuerrx^2+satuerry^2);
kkloerrr=sqrt(kkloerrx^2+kkloerry^2);
kgilerrr=sqrt(kgilerrx^2+kgilerry^2);
SATUerrr=sqrt(SATUerrx^2+SATUerry^2);
KGILerrr=sqrt(KGILerrx^2+KGILerry^2);
BRSKerrr=sqrt(BRSKerrx^2+BRSKerry^2);
DROPerrr=sqrt(DROPerrx^2+DROPerry^2);

% Chi-squared values
% Profile 1
%% 1994-2003 data
chiIr=(isakMr-ISAKO).^2/(ISAKerrr^2);
chiVr=(VALAMr-VALAO).^2/(VALAerrr^2);
chiD3r=(D353Mr-D353O).^2/(D353errr^2);
chiKr=(krokMr-KROKO).^2/(KROKerrr^2);
chiD6r=(D356Mr-D356O).^2/(D356errr^2);
chiD9r=(D359Mr-D359O).^2/(D359errr^2);
chiD1r=(D361Mr-D361O).^2/(D361errr^2);
chiD4r=(frosMr-D364O).^2/(D364errr^2);
chiD5r=(lahrMr-D365O).^2/(D365errr^2);
chiD69r=(D369Mr-D369O).^2/(D369errr^2);
chiD71r=(D371Mr-D371O).^2/(D371errr^2);
chiD2r=(D372Mr-D372O).^2/(D372errr^2);
chiGr=(GALTMr-GALTO).^2/(GALTerrr^2);

%% 2001-2006 data
chiir=(isakMr-isakO).^2/(isakerrr^2);
chikr=(krokMr-krokO).^2/(krokerrr^2);
chidr=(domaMr-domaO).^2/(domaerrr^2);
chifr=(frosMr-frosO).^2/(froserrr^2);
chilhr=(lahrMr-lahrO).^2/(lahrerrr^2);

% Profile 2
%% 2001-2006 data
chibr=(blauMr-blauO).^2/(blauerrr^2);
chilr=(lihoMr-lihoO).^2/(lihoerrr^2);
chihfr=(hrafMr-hrafO).^2/(hraferrr^2);
chihsr=(hrasMr-hrasO).^2/(hraserrr^2);
chitvr=(thveMr-thveO).^2/(thveerrr^2);

% Profile 3
%% 1994-2003 data
chiSr=(SKHRMr-SKHRO).^2/(SKHRerrr^2);
chiPr=(PALAMr-PALAO).^2/(PALAerrr^2);
chiTAr=(thraMr-THRAO).^2/(THRAerrr^2);
chiMr=(MAELMr-MAELO).^2/(MAELerrr^2);
chiSNr=(snaeMr-SNAEO).^2/(SNAEerrr^2);
chiEr=(ELDHMr-ELDHO).^2/(ELDHerrr^2);
chiBr=(BULAMr-BULAO).^2/(BULAerrr^2);
chiSAr=(SATUMr-SATUO).^2/(SATUerrr^2);
chiKGr=(KGILMr-KGILO).^2/(KGILerrr^2);
chiBRr=(BRSKMr-BRSKO).^2/(BRSKerrr^2);
chiDRr=(DROPMr-DROPO).^2/(DROPerrr^2);

%% 2001-2006 data
chitar=(thraMr-thraO).^2/(thraerrr^2);
chisnr=(snaeMr-snaeO).^2/(snaeerrr^2);
chisar=(satuMr-satuO).^2/(satuerrr^2);
```

```
chikkr=(kkloMr-kkloO).^2/(kkloerrr^2);
chikgr=(kgilMr-kgilO).^2/(kgilerrr^2);

% Overall chi-squared value
chi1P=chiIr+chiVr+chiD3r+chiKr+chiD6r+chiD9r+chiD1r+chiD4r+chiD5r+chiD69r
+chiD71r+chiD2r+chiGr;
chi1S=chiir+chikr+chidr+chifr+chilhr;
chi2S=chibr+chilr+chihfr+chihsr+chitvr;
chi3P=chiSr+chiPr+chiTAr+chiMr+chiSNr+chiEr+chiBr+chiSAr+chiKGr+chiBRr+ch
iDRr;
chi3S=chitar+chisnr+chisar+chikkr+chikgr;
chi=[chi1P,chi1S;chi2S,0;chi3P,chi3S];

% GPS-derived site velocities
obsS1=[isakO;krokO;domaO;frosO;lahrO];
obsP1=[ISAKO;VALAO;D353O;KROKO;D356O;D359O;D361O;D364O;D365O;D369O;D371O;
D372O;GALTO];
obsS2=[blauO;lihoO;hrafO;hrasO;thveO];
obsS3=[thraO;snaeO;satuO;kkloO;kgilO];
obsP3=[SKHRO;PALAO;THRAO;MAELO;SNAEO;ELDHO;BULAO;SATUO;KGILO;BRSKO;DROPO]
;

% x location of sites along profiles
XvalS1=[isakX;krokX;domaX;frosX;lahrX];
XvalP1=[isakX;VALAX;D353X;krokX;D356X;D359X;D361X;frosX;lahrX;D369X;D371X
;D372X;GALTX];
XvalS2=[blauX;lihoX;hrafX;hrasX;thveX];
XvalS3=[thraX;snaeX;satuX;kkloX;kgilX];
XvalP3=[SKHRX;PALAX;thraX;MAELX;snaeX;ELDHX;BULAX;satuX;kgilX;BRSKX;DROPX
];

% Velocity uncertainty for each site
errorS1=[isakerrr;krokerrr;domaerrr;froserrr;lahrerrr];
errorP1=[ISAKerrr;VALAerrr;D353errr;KROKerrr;D356errr;D359errr;D361errr;D
364errr;D365errr;D369errr;D371errr;D372errr;GALTerrr];
errorS2=[blauerrr;lihoerrr;hraferrr;hraserrr;thveerrr];
errorS3=[thraerrr;snaeerrr;satuerrr;kkloerrr;kgilerrr];
errorP3=[SKHRerrr;PALAerrr;THRAerrr;MAELerrr;SNAEerrr;ELDHerrr;BULAerrr;S
ATUerrr;KGILerrr;BRSKerrr;DROPerrr];

% Plotting Profiles - Velocities and Model

% Locations of fissure swarms along each profile - to be plotted
% Profile 1
EVZ1_W1x=253+(-25.78)+a1;
EVZ1_E1x=253+(-21.34)+a1;
EVZ1_W2x=253+(-18.67)+a1;
EVZ1_E2x=253+(-11.56)+a1;
EVZ1_W3x=253+(-8.89)+a1;
EVZ1_E3x=253+3.11+a1;
EVZ1_W5x=253+21.33+a1;
EVZ1_E5x=253+24.44+a1;
EVZ1_W6x=253+25.78+a1;
EVZ1_E6x=253+42.66+a1;

% Profile 2
EVZ2_W1x=253+(-30.22)+a2;
EVZ2_E1x=253+(-20.44)+a2;
EVZ2_W2x=253+(-18.67)+a2;
EVZ2_E2x=253+(-16.00)+a2;
EVZ2_W3x=253+14.22+a2;
EVZ2_W4x=253+19.11+a2;
EVZ2_E4x=253+26.67+a2;

% Profile 3
```

```
EVZ3_W1x=253+(-23.11)+a3;
EVZ3_E1x=253+(-14.22)+a3;
EVZ3_W2x=253+(-10.67)+a3;
EVZ3_E2x=253+11.56+a3;
EVZ3_W3x=253+16.00+a3;
EVZ3_E3x=253+33.78+a3;

% Central sites along each profile - to be plotted
fros_x=251+a1;
hraf_x=249+a2;
thra_x=263+a3;

 % Profile 1 - 2001-2006 dataset
figure(1); hold on;
% Plotting location of fissure swarms
patch([EVZ1_W1x EVZ1_W1x EVZ1_E1x EVZ1_E1x],[-1 20 20 -
1],'y'),plot([EVZ1_W1x EVZ1_W1x EVZ1_E1x EVZ1_E1x],[-1 20 20 -1],'y');
patch([EVZ1_W2x EVZ1_W2x EVZ1_E2x EVZ1_E2x],[-1 20 20 -
1],'y');plot([EVZ1_W2x EVZ1_W2x EVZ1_E2x EVZ1_E2x],[-1 20 20 -1],'y');
patch([EVZ1_W3x EVZ1_W3x EVZ1_E3x EVZ1_E3x],[-1 20 20 -
1],'y');plot([EVZ1_W3x EVZ1_W3x EVZ1_E3x EVZ1_E3x],[-1 20 20 -1],'y');
patch([EVZ1_W5x EVZ1_W5x EVZ1_E5x EVZ1_E5x],[-1 20 20 -
1],'y');plot([EVZ1_W5x EVZ1_W5x EVZ1_E5x EVZ1_E5x],[-1 20 20 -1],'y');
patch([EVZ1_W6x EVZ1_W6x EVZ1_E6x EVZ1_E6x],[-1 20 20 -
1],'y');plot([EVZ1_W6x EVZ1_W6x EVZ1_E6x EVZ1_E6x],[-1 20 20 -1],'y');
% Labelling fissure swarms
text(228.25+a1,0,'H','Fontsize',14);text(236.5+a1,0,'V','Fontsize',14);te
xt(247.5+a1,0,'VV','Fontsize',14);text(274.5+a1,0,'El','Fontsize',14);tex
t(286+a1,0,'L','Fontsize',14);
% Plotting plate spreading model
plot(x1,Ur_arct1,'k');
errorbar(XvalS1,obsS1,errorS1,'rd','MarkerSize',6,'MarkerFaceColor','r');
axis([200 300 -1 20]);
% Labelling axes
xlabel('Distance (km)','Fontsize',14); ylabel('Horizontal Rate
(mm/yr)','Fontsize',14);
% Labelling plot - Profile number and dataset
text(205,19,'Profile 1','Fontsize',16,'FontWeight','bold');
text(205,18,'2001-2006','Fontsize',14);
patch([278 278 298 298 278],[17.7 19.4 19.4 17.7 17.7],'w');plot([278 278
298 298 278],[17.7 19.4 19.4 17.7 17.7],'k');
% Listing the chi-squared value for the model, and model extension rate
and
% locking depth
text(279,18.7,'\chi^2','Fontsize',14);text(283,18.5,'=','Fontsize',14);st
r=num2str(chi1S,4);text(286,18.5,str,'Fontsize',14);
text(276,17,'R','Fontsize',14);text(280.5,17,'=','Fontsize',14);str=num2s
tr(extension1);text(283.5,17,str,'Fontsize',14);text(287.5,17,'
mm/yr','Fontsize',14);
text(276,16,'D','Fontsize',14);text(280.5,16,'=','Fontsize',14);str=num2s
tr(depth1);text(284.5,16,str,'Fontsize',14);text(287,16,'
km','Fontsize',14);
% Listing Hekla volume change
text(274,14.8,'\DeltaV_H','Fontsize',14);text(280.5,15,'=','Fontsize',14)
;str=num2str(VCh5);text(284,15,str,'Fontsize',14);text(292,15.15,'
km^3','Fontsize',14);
text(fros_x,10,'FROS','Fontsize',14,'Rotation',90); % Central site along
profile
set(gca,'XTickLabel',[-50 -40 -30 -20 -10 0 10 20 30 40 50]); %
Relabelling axis

 % Profile 1 - 1994-2003 dataset
figure(2); hold on;
patch([EVZ1_W1x EVZ1_W1x EVZ1_E1x EVZ1_E1x],[-1 20 20 -
1],'y'),plot([EVZ1_W1x EVZ1_W1x EVZ1_E1x EVZ1_E1x],[-1 20 20 -1],'y');
```

```
patch([EVZ1_W2x EVZ1_W2x EVZ1_E2x EVZ1_E2x],[-1 20 20 -
1],'y');plot([EVZ1_W2x EVZ1_W2x EVZ1_E2x EVZ1_E2x],[-1 20 20 -1],'y');
patch([EVZ1_W3x EVZ1_W3x EVZ1_E3x EVZ1_E3x],[-1 20 20 -
1],'y');plot([EVZ1_W3x EVZ1_W3x EVZ1_E3x EVZ1_E3x],[-1 20 20 -1],'y');
patch([EVZ1_W5x EVZ1_W5x EVZ1_E5x EVZ1_E5x],[-1 20 20 -
1],'y');plot([EVZ1_W5x EVZ1_W5x EVZ1_E5x EVZ1_E5x],[-1 20 20 -1],'y');
patch([EVZ1_W6x EVZ1_W6x EVZ1_E6x EVZ1_E6x],[-1 20 20 -
1],'y');plot([EVZ1_W6x EVZ1_W6x EVZ1_E6x EVZ1_E6x],[-1 20 20 -1],'y');
text(228.25+a1,0,'H','Fontsize',14);text(236.5+a1,0,'V','Fontsize',14);te
xt(247.5+a1,0,'VV','Fontsize',14);text(274.5+a1,0,'El','Fontsize',14);tex
t(286+a1,0,'L','Fontsize',14);
plot(x1,Ur_arct1,'k');
errorbar(XvalP1,obsP1,errorP1,'bd','MarkerSize',6,'MarkerFaceColor','b');
axis([200 300 -1 20]);
xlabel('Distance (km)','Fontsize',14); ylabel('Horizontal Rate
(mm/yr)','Fontsize',14);
text(205,19,'Profile 1','Fontsize',16,'FontWeight','bold');
text(205,18,'1994-2003','Fontsize',14);
patch([278 278 298 298 278],[17.7 19.4 19.4 17.7 17.7],'w');plot([278 278
298 298 278],[17.7 19.4 19.4 17.7 17.7],'k');
text(279,18.7,'\chi^2','Fontsize',14);text(283,18.5,'=','Fontsize',14);st
r=num2str(chi1P,4);text(286,18.5,str,'Fontsize',14);
text(276,17,'R','Fontsize',14);text(280.5,17,'=','Fontsize',14);str=num2s
tr(extension1);text(283.5,17,str,'Fontsize',14);text(287.5,17,'
mm/yr','Fontsize',14);
text(276,16,'D','Fontsize',14);text(280.5,16,'=','Fontsize',14);str=num2s
tr(depth1);text(284.5,16,str,'Fontsize',14);text(287,16,'
km','Fontsize',14);
text(274,14.8,'\DeltaV_H','Fontsize',14);text(280.5,15,'=','Fontsize',14)
;str=num2str(VCh94_03);text(284,15,str,'Fontsize',14);text(292,15.15,'
km^3','Fontsize',14);
text(fros_x,9.5,'FROS','Fontsize',14,'Rotation',90);
set(gca,'XTickLabel',[-50 -40 -30 -20 -10 0 10 20 30 40 50]);

 % Profile 2 - 2001-2006 dataset
figure(3); hold on;
patch([EVZ2_W1x EVZ2_W1x EVZ2_E1x EVZ2_E1x],[-1 20 20 -
1],'w'),plot([EVZ2_W1x EVZ2_W1x EVZ2_E1x EVZ2_E1x],[-1 20 20 -1],'y');
patch([EVZ2_W2x EVZ2_W2x EVZ2_E2x EVZ2_E2x],[-1 20 20 -
1],'y');plot([EVZ2_W2x EVZ2_W2x EVZ2_E2x EVZ2_E2x],[-1 20 20 -1],'y');
patch([EVZ2_E2x EVZ2_E2x EVZ2_W3x EVZ2_W3x],[-1 20 20 -
1],'w');plot([EVZ2_W2x EVZ2_W2x EVZ2_E2x EVZ2_E2x],[-1 20 20 -1],'y');
patch([EVZ2_W4x EVZ2_W4x EVZ2_E4x EVZ2_E4x],[-1 20 20 -
1],'y');plot([EVZ2_W4x EVZ2_W4x EVZ2_E4x EVZ2_E4x],[-1 20 20 -1],'y');
plot([EVZ2_W1x EVZ2_W1x EVZ2_E1x EVZ2_E1x EVZ2_W1x],[-1 20 20 -1 -
1],'k');
plot([EVZ2_E2x EVZ2_E2x EVZ2_W3x EVZ2_W3x EVZ2_E2x],[-1 20 20 -1 -
1],'k');
text(226+a2,0,'H','Fontsize',14);text(234+a2,0,'V','Fontsize',14);text(25
1+a2,0,'T','Fontsize',14);text(274.5+a2,0,'El','Fontsize',14);
plot(x2,Ur_arct2,'k');
errorbar(XvalS2,obsS2,errorS2,'rd','MarkerSize',6,'MarkerFaceColor','r');
axis([200 300 -1 20]);
xlabel('Distance (km)','Fontsize',14); ylabel('Horizontal Rate
(mm/yr)','Fontsize',14);
text(205,19,'Profile 2','Fontsize',16,'FontWeight','bold');
text(205,18,'2001-2006','Fontsize',14);
patch([278 278 298 298 278],[17.7 19.4 19.4 17.7 17.7],'w');plot([278 278
298 298 278],[17.7 19.4 19.4 17.7 17.7],'k');
text(279,18.7,'\chi^2','Fontsize',14);text(283,18.5,'=','Fontsize',14);st
r=num2str(chi2S,3);text(286,18.5,str,'Fontsize',14);
text(273,17,'R','Fontsize',14);text(278,17,'=','Fontsize',14);str=num2str
(extension2);text(281.5,17,str,'Fontsize',14);text(285,17,'
mm/yr','Fontsize',14);
```

```
text(273,16,'D','Fontsize',14);text(278,16,'=','Fontsize',14);str=num2str
(depth2);text(281.5,16,str,'Fontsize',14);text(285,16,'
km','Fontsize',14);
text(271,14.8,'\DeltaV_H','Fontsize',14);text(278,15,'=','Fontsize',14);s
tr=num2str(VCh5);text(282,15,str,'Fontsize',14);text(290,15.15,'
km^3','Fontsize',14);
% Listing Torfajokull volume change
text(271,13.3,'\DeltaV_T','Fontsize',14);text(278,13.5,'=','Fontsize',14)
;str=num2str(VChT);text(281,13.5,str,'Fontsize',14);text(292,13.65,'
km^3','Fontsize',14);
text(hraf_x,12,'HRAF','Fontsize',14,'Rotation',90);
set(gca,'XTickLabel',[-50 -40 -30 -20 -10 0 10 20 30 40 50]);

% Profile 3 - 1994-2003 dataset
figure(4); hold on;
patch([EVZ3_W1x EVZ3_W1x EVZ3_E1x EVZ3_E1x],[-1 20 20 -
1],'y'),plot([EVZ3_W1x EVZ3_W1x EVZ3_E1x EVZ3_E1x],[-1 20 20 -1],'y');
patch([EVZ3_W2x EVZ3_W2x EVZ3_E2x EVZ3_E2x],[-1 20 20 -
1],'y');plot([EVZ3_W2x EVZ3_W2x EVZ3_E2x EVZ3_E2x],[-1 20 20 -1],'y');
patch([EVZ3_W3x EVZ3_W3x EVZ3_E3x EVZ3_E3x],[-1 20 20 -
1],'y');plot([EVZ3_W3x EVZ3_W3x EVZ3_E3x EVZ3_E3x],[-1 20 20 -1],'y');
text(233+a3,0,'V','Fontsize',14);text(250+a3,0,'Tfs','Fontsize',14);text(
277+a3,0,'El','Fontsize',14);
plot(x3,Ur_arct3,'k');
errorbar(XvalP3,obsP3,errorP3,'bd','MarkerSize',6,'MarkerFaceColor','b');
axis([200 300 -1 20]);
xlabel('Distance (km)','Fontsize',14); ylabel('Horizontal Rate
(mm/yr)','Fontsize',14);
text(205,19,'Profile 3','Fontsize',16,'FontWeight','bold');
text(205,18,'1994-2003','Fontsize',14);
patch([278 278 298 298 278],[17.7 19.4 19.4 17.7 17.7],'w');plot([278 278
298 298 278],[17.7 19.4 19.4 17.7 17.7],'k');
text(279,18.7,'\chi^2','Fontsize',14);text(283,18.5,'=','Fontsize',14);st
r=num2str(chi3P,3);text(286,18.5,str,'Fontsize',14);
text(275,17,'R','Fontsize',14);text(280,17,'=','Fontsize',14);str=num2str
(extension3);text(284.5,17,str,'Fontsize',14);text(287.5,17,'
mm/yr','Fontsize',14);
text(275,16,'D','Fontsize',14);text(280,16,'=','Fontsize',14);str=num2str
(depth3);text(284.5,16,str,'Fontsize',14);text(287,16,'
km','Fontsize',14);
text(273,14.8,'\DeltaV_H','Fontsize',14);text(280,15,'=','Fontsize',14);s
tr=num2str(VCh94_03);text(284,15,str,'Fontsize',14);text(292,15.15,'
km^3','Fontsize',14);
text(thra_x,9,'THRA','Fontsize',14,'Rotation',90);
set(gca,'XTickLabel',[-50 -40 -30 -20 -10 0 10 20 30 40 50]);

 % Profile 3 - 2001-2006 dataset
figure(5); hold on;
patch([EVZ3_W1x EVZ3_W1x EVZ3_E1x EVZ3_E1x],[-1 20 20 -
1],'y'),plot([EVZ3_W1x EVZ3_W1x EVZ3_E1x EVZ3_E1x],[-1 20 20 -1],'y');
patch([EVZ3_W2x EVZ3_W2x EVZ3_E2x EVZ3_E2x],[-1 20 20 -
1],'y');plot([EVZ3_W2x EVZ3_W2x EVZ3_E2x EVZ3_E2x],[-1 20 20 -1],'y');
patch([EVZ3_W3x EVZ3_W3x EVZ3_E3x EVZ3_E3x],[-1 20 20 -
1],'y');plot([EVZ3_W3x EVZ3_W3x EVZ3_E3x EVZ3_E3x],[-1 20 20 -1],'y');
text(233+a3,0,'V','Fontsize',14);text(250+a3,0,'Tfs','Fontsize',14);text(
277+a3,0,'El','Fontsize',14);
plot(x3,Ur_arct3,'k');
errorbar(XvalS3,obsS3,errorS3,'rd','MarkerSize',6,'MarkerFaceColor','r');
axis([200 300 -1 20]);
xlabel('Distance (km)','Fontsize',14); ylabel('Horizontal Rate
(mm/yr)','Fontsize',14);
text(205,19,'Profile 3','Fontsize',16,'FontWeight','bold');
text(205,18,'2001-2006','Fontsize',14);
patch([278 278 298 298 278],[17.7 19.4 19.4 17.7 17.7],'w');plot([278 278
298 298 278],[17.7 19.4 19.4 17.7 17.7],'k');
```

```
text(279,18.7,'\chi^2','Fontsize',14);text(283,18.5,'=','Fontsize',14);st
r=num2str(chi3S,3);text(286,18.5,str,'Fontsize',14);
text(275,17,'R','Fontsize',14);text(280,17,'=','Fontsize',14);str=num2str
(extension3);text(284.5,17,str,'Fontsize',14);text(287.5,17,'
mm/yr','Fontsize',14);
text(275,16,'D','Fontsize',14);text(280,16,'=','Fontsize',14);str=num2str
(depth3);text(284.5,16,str,'Fontsize',14);text(287,16,'
km','Fontsize',14);
text(273,14.8,'\DeltaV_H','Fontsize',14);text(280,15,'=','Fontsize',14);s
tr=num2str(VCh5);text(284,15,str,'Fontsize',14);text(292,15.15,'
km^3','Fontsize',14);
text(thra_x,7,'THRA','Fontsize',14,'Rotation',90);
set(gca,'XTickLabel',[-50 -40 -30 -20 -10 0 10 20 30 40 50]);
```

APPENDIX 10: Determining the best-fit Mogi model to "dry-tilt" data from NAEF (or HRAF) site

```
function [Vch,dmin,mindiff2]=Tilt_Mogi;

% Program written by: Stephanie Scheiber, taken from Erik
% Sturkells C++tilt code
% Date: 2007-2008
% Description of program: Calculate tilt displacement due to Mogi
% source, and with compared the value with the actual tilt
% measured at NAEF site near Hekla

% Output: Volume change (VCh) and depth (dmin) for best-fit Mogi
% source to the NAEF tilt data; Difference between modelled and
% observed tilt value at NAEF

result=zeros(100); % Preallocation of space

% User inputted values
rdist = 40000; % radial distance of model, [m]
sspace = 100; % station spacing, [m]

% Input values
for n=1:20;
    for m=1:40;

    h0 = -0.26+(n*0.02); % m
    depth = 3000+(m*200); % m

% MESHGRID generates X and Y matrices for three-dimensional plots.
[x,y]=meshgrid((-1*rdist/2):sspace:(rdist/2));

% Radial Distance
r = sqrt(x.^2+y.^2);

% The equation calculating the tilt displacement
tiltd = (h0*(depth^2)*((-
3.0*depth*r)./((depth^2+r.^2).^(5/2))))/0.000001; % in microradians

% Determining the tilt value 11 km west of Hekla (i.e. NAEF site)
% NAEF at x=11.18km (row=89) and y = -0.635km (column=207)
result(n,m)=(tiltd(89,207));
% To determine tilt at HRAF (3.2 km from Mogi source at Torfajokull):
% result=(tiltd(168,201));

% Difference between modelled and observed values (7.2 microrad)
diff=abs(result-7.2);

    end;
end;

% Find model with minimum difference value
mindiff=min(diff);
mindiff2=min(mindiff);

% Determine row and column of minimum difference value so can determine
% depth and h0 value
[r,c]=find((mindiff2-0.00001)<diff & diff<(mindiff2+0.00001));
dmin=(c*200)+3000; % depth value for min difference between model and obs
h0min=(r*0.02)-0.26; % h0 value for min difference between model and obs
Vch=-1*(h0min)*(dmin.^2)*4*pi/(3*10^9); % Change volume of magma chamber
for min h0 and depth values
```

APPENDIX 11: Determining the "dry-tilt response at NAEF (or HRAF) site due to a Mogi source

```
function [result]=Tilt_Mogi_individ(Vch,d);

% Program written by: Stephanie Scheiber, taken from Erik
% Sturkells C++tilt code
% Date: 2007-2008
% Description of program: Calculate tilt displacement due to Mogi
% source, and compared with the value with the actual tilt
% measured at NAEF site near Hekla (or HRAF tilt site within Torfajokull
caldera)

% Input and Output values: Tilt response (result) due to a Mogi
% source at depth (d), experiencing volume change (Vch)

% User inputted values
depth=d*1000; % Depth of Mogi source [m]
h0=((-1*(depth.^2)*4*pi/(3*10^9))^-1)*Vch; % h0 for volume change Vch [in
km3]
rdist = 40000; % radial distance of model, [m]
sspace = 100; % station spacing, [m]

% MESHGRID generates X and Y matrices for three-dimensional plots.
[x,y]=meshgrid((-1*rdist/2):sspace:(rdist/2));

% Radial Distance
r = sqrt(x.^2+y.^2);

% The equation calculating the tilt displacement
tiltd = (h0*(depth^2)*((-
3.0*depth*r)./((depth^2+r.^2).^(5/2))))/0.000001; % in microradians

% Determining the tilt value 11 km west of Hekla (i.e. NAEF site)
% NAEF at x=11.18km (row=89) and y = -0.635km (column=207)
result=(tiltd(89,207));
% To determine tilt at HRAF (3.2 km from Mogi source at Torfajokull):
% result=(tiltd(168,201));

% Plot of tilt response

x2 = [(-1*rdist/2):sspace:((rdist/2)-1)];
y2 = [(-1*rdist/2):sspace:((rdist/2)-1)];

% IMPROFILE computes pixel-value cross-sections along a specified line
% segment. Here the profile is taken across the centre of the image
proft = improfile(tiltd,[1 (rdist/sspace)+1],[((rdist/2)/sspace)+1
(((rdist/2)-1)/sspace)+1]);

figure(1);
% A plot of the above-mentioned profile across the centre of the image:
subplot(3,1,1); plot(x2,proft); axis tight; xlabel('x'); ylabel('Tilt
Disp (microradians)');
% A 2-D image of the data:
subplot(3,1,2); imagesc(x2,y2,tiltd), colorbar; axis tight; axis square;
xlabel('x'); ylabel('y');
% A 3-D image of the data:
subplot(3,1,3); mesh(x,y,tiltd); xlabel('x'); ylabel('y'); zlabel('Tilt
Disp (microradians)');
```